Thermal Mechanical Analyses of Compressed Air Energy Storage Pile Foundations

Madina Bimaganbetova, B. Eng

Submitted in fulfillment of the requirements for the degree of Master of Science in Civil & Environmental Engineering

School of Engineering and Digital Sciences

Department of Civil & Environmental Engineering

Nazarbayev University

53 Kabanbay Batyr Avenue, Astana, Kazakhstan, 010000

Supervisors: Dichuan Zhang, Jong Kim

Date of completion: April 11

Declaration Form

I hereby, declare that this manuscript, entitled “Thermal Mechanical Analyses of Compressed Air Energy Storage Pile Foundations”, is the result of my own work except for quotations and citations which have been duly acknowledged.

I also declare that, to the best of my knowledge and belief, it has not been previously or concurrently submitted, in whole or in part, for any other degree or diploma at Nazarbayev University or any other national or international institution.

Name: Madina Bimaganbetova

Date: 11.04.21

Abstract

Nowadays, renewable energy has become a widely accepted energy source due to the growing interest in environmental issues such as air pollution and greenhouse gas emissions. However, it highly depends on the day and night cycle and has an intermittent nature. Thus, ways of storing the extra energy generated by renewable energy have been developed including pumped hydroelectric, compressed air, solar batteries, and thermal energy storage. An energy storage pile foundation system is being developed through a multidisciplinary research project. The main idea of the proposed system is to store extra energy in hollowed pile foundations by utilizing compressed air energy storage technology.

In previous studies, structural responses of the energy storage pile foundations under internal air pressure were evaluated. These studies were based on an assumption of completely cooling air down to the ambient temperature before entering the pile foundation for storage. This assumption may require additional resources due to the efficiency of the cooling process. Another option is to keep the storage air temperature higher than the ambient temperature, which can be achieved by controlling the cooling process. As a result, thermal mechanical loading will be induced to the pile foundation. However, the stress states in the pile section that originated from the thermal loading are different from the stress states that originated from the internal air pressure. Therefore, it is necessary to investigate the structural response of the pile foundation under the combined air pressure and thermal mechanical loading.

This thesis focuses on analytical investigations of structural responses of the energy storage pile foundations under combined loadings from the internal air pressure and temperature changes. To conduct this study, two steps of analytical research work were performed. In the first step, non-steady state thermal analyses were conducted to identify the temperature distributions inside the pile section. In the second step, the temperature distribution, obtained from the first step, was used as thermal loadings for static thermal mechanical analyses to evaluate the structural responses of the pile. The analyses were performed using general finite element software, Abaqus CAE. Several pile designs with different parameters were studied. These parameters include the geometry of the piles, spacing between them, level of cooling, the thermal expansion coefficient of the pile, and inner diameter of the pile.

From the analytical results, it has been found that the maximum tensile stress originated from the internal air pressure can be reduced by introducing an appropriate level of thermal mechanical loading. The appropriate level can be achieved by adjusting the storage temperature.

Moreover, by limiting the days of continuous usage of the energy storage pile, the thermal mechanical loading can eliminate the state where the entire concrete section is under pure tension, which has been a critical issue for the pile under the internal air pressure. Design recommendations regarding the optimum storage temperature and the number of days of continuous usage were made as follows: the appropriate range of storage temperature lies between 31.5°C to 34°C; it is recommended to pause the air storage one day for every 5-14 days depending on the pile section sizes to avoid the entire pile section transiting to a pure tension state.

Acknowledgements

This thesis became a reality with the help of the kind and supportive people around me. I would like to show my sincere gratitude to these individuals.

First, I would like to express my sincere gratitude towards my supervisor Professor Dichuan Zhang and co-supervisor Professor Jong Kim. This study has been finished under their conscientious supervision. I appreciate all the time they have offered me to discuss the subject of the matter as well as the valuable advice provided.

Second, I am grateful for my family that encouraged me to complete this work throughout my study. Special thanks to my supportive husband, Marsel, and lovable child, Anuar, who motivated and inspired me to complete this endeavor.

My appreciation and gratitude to Dias Bakhtiyarov, Dilnura Sailauova, and Zhamilya Mamesh, who gladly helped me out at the beginning of my journey.

Finally, I would like to pay respect to the administration staff of Nazarbayev University for their assistance throughout the program.

Table of Contents

List of Abbreviations and Symbols

CAES	Compressed air energy storage
UHPC	Ultra-high-performance concrete
d_{in}	Inner diameter
T_1	Ambient air temperature
T_2	Temperature after compression process
T_3	Temperature after heating process
T_{hs}	Heat storage medium temperature
T_s	Storage temperature
P_1	Atmospheric pressure
P_2	Pressure after compression process
P_3	Pressure after heating process
P_s	Storage pressure
w	Work done by compressor
n	Air amount going through compressor
R	Universal gas constant
$\dot{w}_{in}$	Electric power from solar panels
$\dot{n}$	Air flow rate through the compressor
η_1	Efficiency of the compression
t	Compression time
$n_{s,i}$	Initial amount of air in the medium
ρ_i	Initial density of the air
μ	Solar mass of the air
V	Volume of the storage tank
η_2	Efficiency of the cooling
η_3	Efficiency of the heating
η_4	Efficiency of the expansion
$\dot{w}_{out}$	Power generated by turbine
η_T	Total energy efficiency
k	Thermal conductivity
c	Specific heat

N_p	Structural load
s	Pile spacing
r	Radius
T_d	Design temperature
P_d	Design pressure
N	Transition cycle
CTE	Coefficient of thermal expansion
$F(\sigma)$	Yield function
α, β	Dimensionless constants
$\hat{\sigma}_{max}$	Maximum principal stress
I_1	The first invariant in the stress tensor
J_2	The second deviatoric stress invariant
f_{c0}	Initial yield compressive stress
f_{b0}	Biaxial initial yield compressive stress
f_{t0}	Initial yield tensile stress

List of Tables

List of Figures

Chapter 1 – Introduction

1.1.Overview

With growing concerns about environmental issues such as harmful air pollutants and greenhouse gas emissions, renewable energy has become a widely popular source of energy in recent years. It is mostly represented as wind or solar energy with a highly unpredictable and intermittent nature. Such energy grids do not store the energy by themselves. As a result, the extra energy generated by renewable power will not be properly occupied and excess energy will be wasted [1]. Thus, it is crucial to solve this issue with new and innovative technology. One of the solutions for this is the so-called compressed air energy storage (CAES) pile foundations, which utilize hollowed reinforced concrete (RC) piles to store the renewable energy generated from solar panels [2].

These types of pile foundations were developed under a multidisciplinary research program. It suggests storing the renewable energy inside the RC pile foundations using the CAES technology. It is one of the environmentally friendly and highly reputable approaches with good economic feasibility [3,4]. The first study of this multidisciplinary research program evaluated the structural responses of the pile foundations subjected to internal air pressure, structural loads, and soil pressure [2]. To determine the critical tensile stresses, three dimensional (3D) finite element model was used. After a thorough examination of the critical stresses along with the crack patterns in the CAES piles, several conclusions were made. First, it was identified that internal air pressure mostly depends on the energy demand and the inner diameter (d_{in}) of the pile foundation. Second, for the normal strength concrete combination of compressed air pressure and structural loads from the structure causes serious tensile stresses and radial cracks. Also, the same combination of loadings results in high tensile stresses at the bottom of the pile length. Nevertheless, it happens to be less than the tensile strength of chosen concrete. Third, the shaft friction at the top of the pile can be reduced due to compressed air. However, due to the same reason, it can be increased at the bottom of the pile. Finally, thicker piles are recommended for the design of such energy piles with the normal strength concrete [2]. This study is followed by the second paper within this multidisciplinary research program. It investigates the nonlinear structural responses of fiber reinforced concrete piles subjected to high internal pressure [5]. For this research, a two-dimensional (2D) plane strain model with concrete damage plasticity was used. Several parameters including concrete grade, amount of fiber, and thickness of the pile were studied in this paper. It was concluded that with the increase

of d_{in} the pile can resist less applied pressure. Larger d_{in} leads to a more uniform distribution of stresses, resulting in the fast growth of crack propagation speed. On the other hand, resistance to the applied pressure can be compensated by the higher grade of concrete and the content of fiber. As these two parameters increase, more applied pressure can be resisted by the pile foundation. It is related to the slower crack penetration speed and higher ductility [5].

It should be noted that previously mentioned studies had an assumption that the temperature was cooled down till the ambient temperature before entering the pile foundation for storage. This assumption may require additional resources due to the efficiency of the cooling process. Another option is to keep the storage air temperature higher than the ambient temperature, which can be achieved by controlling the cooling process. Further studies have investigated the temperature distributions inside concrete sections of a single energy storage pile [6]. It was needed to examine the possibility of storing the compressed air with a temperature higher than the ambient temperature because complete cooling till the ambient temperature requires more resources due to the cooling efficiency. In this study, a 2D plane strain model was used to conduct non-steady heat transfer analyses. Various parameters such as thermal conductivities of the concrete, specific heat capacities, and the geometry of the pile foundations were evaluated. Several conclusions were deduced at the end of this study. First, the temperature changes inside the concrete pile section became slower as getting closer to the outer skin. Second, the residual temperature effect can be observed at the end of each cycle. This temperature resided at the end of the cycle causes cumulative effect at the last cycle. Third, less time will be needed for heat to travel through the pile if the pile becomes thinner. Finally, an increase in thermal conductivity and a decrease in the specific heat capacity of concrete results in higher temperatures inside the concrete section [6]. This study was extended by investigation of group pile effect on temperature distributions inside energy storage piles [7]. Thus, dynamic heat transfer simulations were conducted to show the effect of temperature changes in one pile on the adjacent piles and surrounding soils. 2D symmetric models were developed for this work. The main parameter of this study is the distance between the piles. It was concluded that additional heat from the adjacent piles plays a major role in increasing the temperature inside concrete and soil as well. Moreover, smaller pile spacings resulted in faster temperature distributions.

One further step is to use the obtained data on temperature distributions inside CAES piles to conduct thermal mechanical analyses of CAES piles. These two studies on thermal analyses were focused on the effects of different thermal parameters, while this thesis adopts

only one set of thermal parameters applicable for ultra-high-performance concrete. As a continuity of the research work, in the current study structural responses under combined internal air pressure and temperature changes were investigated. Thus, the opportunity of storing the compressed air with a temperature higher than the ambient temperature of 20 °C will be explored. This thesis hypothesizes that by adjusting cooling levels the storage temperature can be optimized so that the tensile stresses caused by combined air pressure and temperature changes can be minimized. For this hypothesis to be proven, two studies were performed: (1) thermal analyses and (2) thermal mechanical analyses. The first study is needed to obtain temperature distributions inside the concrete section. The second one is to evaluate the structural responses of the pile foundations under combined loadings. Besides different storage temperatures, the effect of several study parameters such as pile spacing, the inner diameter of the pile foundations, and the coefficient of thermal expansion of concrete was investigated.

1.2.Research hypothesis

The inner air pressure and thermal mechanical loading can generate different stress conditions in the proposed pile foundation. The maximum tensile stresses in the proposed pile foundation that originated from the air pressure might be reduced due to the thermal mechanical stresses. Therefore, it is possible to identify an optimum storage temperature (termed as design temperature) to minimize the stresses in the pile section.

1.3.Thesis problem statement

The focus of this thesis is an investigation of temperature distributions as well as the internal air pressure and thermal induced response in the energy storage pile. For this purpose, a two-step study was performed:

- Thermal analyses in order to obtain temperature distributions inside the concrete section.
- Thermal mechanical analyses to evaluate structural responses of pile foundations.

First, temperature distributions inside the concrete section for the pile foundation through non-steady state heat transfer analyses were studied. Temperature changes due to compressing and releasing air were calculated based on thermal dynamic processes of the CAES. After that, the heat transfer analysis was conducted using an analytical 2D plane strain model. The obtained

temperature distributions, as well as the internal pressure changes, were used for the thermal mechanical analyses using an axisymmetric model of the concrete pile.

1.4.Objectives

The main objectives of this thesis are listed below:

- Determination of temperature changes for the pile foundation by thermal analyses.
- Investigation of structural responses of the pile foundation under temperature changes.
- Investigation of structural responses of the pile foundation under both temperature changes and internal air pressure.
- Identification of an optimal storage temperature (termed here as design temperature) to minimize the tensile stress in the pile section.
- Determination of the number of days until the pile section transits to the pure tension state.

1.5. Outline of the thesis

This thesis consists of seven chapters. First, Chapter 1 introduces the research work, hypothesis, thesis statement, and objectives. It is followed by Chapter 2, which focuses on background information and thermodynamic cycles of CAES. Next, Chapter 3 provides the study description and research methodology. Chapter 4 focuses on the results of thermal analyses about temperature distributions inside the pile section, while Chapter 5 demonstrates the results of thermal mechanical analyses. Discussions of parametric studies and design recommendations can be found in Chapter 6. Finally, conclusions have been drawn in Chapter 7.

Chapter 2 – Background Information

2.1. Applications of CAES technology

Nowadays, renewable energy from solar panels and windmills attached to the buildings has been widely used to supply buildings with electrical power for daily operations [8]. However, the main problem is that it cannot provide it uninterruptedly due to its intermittent nature [9]. A solution to this problem can be storing extra energy for later usage [10]. This can be done by utilizing CAES technology [11]. A reinforced concrete pile foundation with hollowed sections is used as a space for the storage of renewable energy.

The concept of the proposed research can be explained using Figure 2.1. The solar power coming from solar panels at the roof of the building will be divided into two parts: one will be used immediately, and the other part will be converted into compressed air with high pressure through a compressor and stored in the foundation system. Once it is needed, it will be released and converted back into electric power by a turbine and generator.

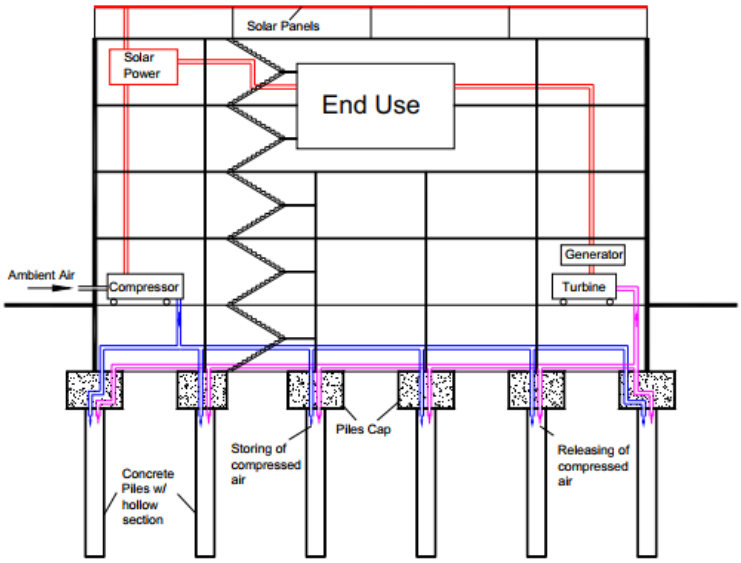

Figure 2.1: Proposed compressed air energy storage system [12].

Currently, only two CAES plants are operating: the Huntorf plant (Germany) and the McIntosh plant (Alabama, USA) [13]. Both use underground salt caverns for large-scale air storage [1]. However, with the rapid growth of wind and solar energy use, CAES becomes an up-and-coming energy storage solution to eliminate drawbacks related to the intermittency nature of renewable energy [14]. There might be challenges associated with the usage of the CAES system in small-scale building structures due to difficulties associated with the safety

and load-carrying capacity of the pile foundations. Under structural loads, soil effects along with the compressed air pressures and temperature loadings the pile foundation may be subjected to complex stresses. Thus, this study will present numerical results on the structural responses of the CAES pile under the combined loadings.

2.2. Studies on thermal induced response on the energy piles

Many studies were conducted to evaluate the response of the single or group of energy piles subjected to thermal or thermo-mechanical loads. Energy piles are pile foundations that have two main functions: structural support and heat exchange to satisfy the energy needs of the buildings [15]. Energy piles and energy storage piles can be differentiated by loading conditions and thermal loadings. Energy piles are usually subjected to structural loads along with temperature changes. Whereas energy storage piles are also subjected to compressed air pressure besides structural loads and temperature changes. Moreover, it should be noted that energy piles are entirely heated up, albeit in energy storage piles temperature distributions might be non-uniform inside the pile section. These differences such as additional loadings as air pressure and non-uniformity of temperature distributions might result in more critical tensile stresses in the energy storage piles.

Di Donna et al. [15] have conducted a study on the response of a group of energy piles subjected to different combinations of thermo-mechanical loads. This study used 3D finite element analyses with real field data to evaluate these responses. This helped to validate numerical simulation with the experimental results. Thus, it shows the trustworthiness of the obtained results. This paper sums up the behavior of the energy piles under traditional as well as extreme thermal loading conditions. Thermally induced vertical stresses and displacement developments in a group of piles are thoroughly analyzed. The study confirmed that there is no critical displacement development or vertical stresses under the operating thermal load. The geotechnical stability of the structure is guaranteed, and it lies within the current standards.

According to the authors, with the increase in temperature increase in displacements and stresses can be observed. The average pile head settlements were about +1.0 mm under mechanical load. It was reduced by -0.1 mm due to the heating under operating thermal load. Whereas under heating of all piles to up to 43°C, it reached a maximum value of -4.0 mm.

Stresses generated under thermal loadings are mainly acceptable. It meets the requirement of the concrete strength and reached a maximum of about 1 MPa under operating conditions. Under more extreme changes such as heating all the piles till 43°C, this value

increased to 4 MPa. However, when some of the piles were heated, thermally induced compressive stress became more considerable with 7 MPa. It is related to the increase of constrained conditions due to the existence of non-heated piles. This happens at the end of the heating phase. After stabilization of temperature, the heat flows towards the non-heated piles leading to the decrease of constrained conditions discussed above. Thus, thermal induced compressive stresses will be reduced. On the other hand, it will lead to thermal deformation and foundation movements.

To wrap it up, it is concluded by authors that currently there are no critical vertical stresses or displacements under operating conditions. However, in the future with the more intense use of energy piles, extreme thermal loadings may induce more critical stresses and thermal deformation.

Another study conducted on an energy pile response under cyclic temperature variations was performed by Faizal et al. [16]. In this paper single pile under a six-story residential building was examined to see the effects of daily changes in temperature. Pile temperature ranged between 10°C to 23°C for this study. It had an initial temperature of 18°C. Axial thermal stress profile along the length of the pile was observed. It has shown higher stresses near the bottom of the pile at the end of cooling. This is associated with the larger temperature changes in the cooling cycle. Radial stresses produced significantly lower stresses and are considered negligible. Thus, radial thermal contraction or expansion of the pile did not generally affect the skin friction of the pile. The temperature distributions inside the pile section at the end of cooling and heating were found to be uniform. However, this was not the case for axial thermal stresses. Nevertheless, it lies below the ultimate capacity of the pile. Furthermore, daily thermal changes did not cause thermally induced plastic deformation for the energy pile installed in the dense sand.

The behavior of the heat exchanger pile was also researched with experimental and numerical methods by Laloui et al. [17]. The objective of this paper is to investigate loads on a pile caused by thermal effects. The maximum thermal loadings applied to this pile is 21°C, whereas the mechanical load reached 1300 kN. Finite element modeling was used to simulate the authentic experimental results. It demonstrates the reliability of the analytical model in the sense of replicating thermo-mechanical effects.

According to the authors, the thermal effect generates larger axial stresses at the toe of the pile in comparison to stresses produced by dead loads from the structure. It is related to the

uniform nature of thermal effects. Besides, the uplift due to thermal effects and settlement due to static loads can be noticed. This difference in the movement direction act so that friction resistance is not affected by the temperature. Despite the thermal stresses that may spread in the soil, the produced strains are limited. Thus, the pore water pressure or the effective stress are not influenced by this.

Another research has evaluated the thermal mechanical behavior of energy pile foundations located in a new building at the US Air Force Academy [18]. To evaluate the structural responses of the foundations during heating and cooling, three of them were equipped with strain gauges and thermistors. At the end of the study, several pertinent conclusions have been deduced. As per the authors, the increase in temperature resulted in expansive thermal axial strains, which mainly occurred near the top and bottom of the pile. Maximum compressive thermal axial stress ranged between 4.0 to 5.1 MPa. It is considered adequate because the compressive strength of the concrete was estimated to be 21 MPa. For the maximum increase of temperature of 18°C, the upward movement of the foundation was calculated to be from -1.3 to -1.7 mm. Consequently, these movements cannot produce any structural or aesthetic destructions to the building. The thermal axial strains and stresses along with the displacements have followed a similar pattern during cooling as well.

2.3. Thermodynamic cycles of CAES

One of the key problems related to compressed air energy storage is that when the air is compressed it heats up. There are three ways of dealing with this heat that emerged during the compression process:

- Adiabatic storage.
- Diabetic storage.
- Isothermal storage.

The heat from compression is retained and reused during the expansion process to produce the power during adiabatic storage, while during diabetic storage the heat is dispersed into the atmosphere. Therefore, when the air is released to go through the turbines it needs to be heated. The third option implies the use of a heat exchanger to retain the interior and exterior temperatures at the nearly same level [19].

In this study, the first option, i.e., the adiabatic method, was used. As it can be seen from Figure 2.2, it consists of four thermodynamic cycles: (1) compression; (2) cooling; (3) heating; (4) expansion. First, the ambient air is compressed by the renewable energy available for

storage. Once it is compressed, the pressure and temperature of the compressed air will drastically raise. Thus, the cooling process is performed as the next step to extract the heat and store it in a heat storage medium. Due to the efficiency of the cooling process, temperature after cooling cannot reduce to the ambient temperature. Finally, the compressed air is released and undergoes the heating and expansion process to produce electric power whenever it is required.

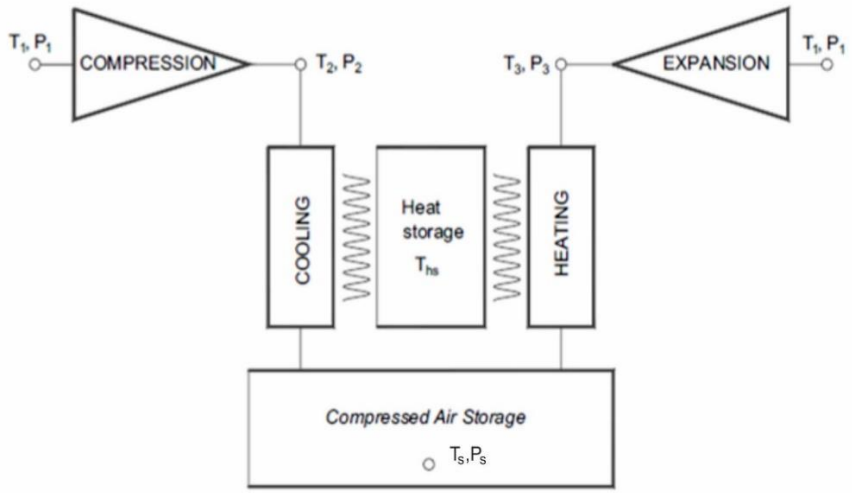

Figure 2.2: Thermodynamic cycles of CAES (Modified from [6]).

A detailed explanation of an advanced adiabatic process and the equations will be demonstrated below.

2.3.1. Compression process

The compression process follows the energy conservation principle. To simplify equations, the assumption of the isentropic adiabatic compression condition was made. According to Al Shemmeri [20], the energy balance for the ideal gas can be stated as follows:

$$w = 3.5nR(T_2 - T_1) \quad [2.1]$$

In this equation *w* is the work done by the compressor (J), *n* is the air amount going through the compressor (mol), *R* is the universal gas constant, i.e. 8.31 J/mol. T_1 and T_2 are the ambient air temperature and temperature after the compression process, respectively. K was selected for this study as a unit of temperature. Based on the principle of energy balance, the following equation can be drawn to represent the electric power coming from the solar panels ($\dot{w}_{in}$) used to power the compressor:

$$\dot{w}_{in} = 3.5\dot{n}R(T_2 - T_1)/\eta_1 \quad [2.2]$$

where $\dot{n}$ is air flow rate through the compressor (mol/s), and η_1 is the efficiency of the compression. The amount of air built up in the storage medium can be expressed as a function of compression time:

$$\dot{n} = n_s - n_{s,i}/t_{in} = \dot{w}_{in}\eta_1/3.5R(T_2 - T_1) \quad [2.3]$$

$$n_{s,i} = \rho_i V/\mu \quad [2.4]$$

where *t* is the compression time (s), $n_{s,i}$ is the initial amount of air in the medium. In the equation [2.4], ρ_i is the initial density of the air (1.2 kg/m^3), μ is the solar mass of the air (0.029 kg/mol), and *V* is the volume of the storage tank (m^3). The adiabatic temperature to pressure relationship is demonstrated below:

$$T_2 = CP_2^{2/7} \quad [2.5]$$

where *C* is a constant value of 10.89 K/Pa$^{2/7}$. By substituting equation [2.5] into equation [2.3], the amount of the air stored in the medium can be calculated, as follows:

$$n_s = \dot{w}_{in}\eta_1 t_{in}/3.5R\left(CP_2^{2/7} - T_1\right) + n_{s,i} \quad [2.6]$$

The following equation can be obtained based on the ideal gas relationship:

$$n_s = P_2 V/RT_2 = VP_2^{5/7}/RC \quad [2.7]$$

By equating equation [2.6] to equation [2.7], the pressure after the compression (P_2) can be estimated using the following relationship:

$$VP_2^{5/7}/RC = \dot{w}_{in}\eta_1 t_{in}/3.5R\left(CP_2^{2/7} - T_1\right) + n_{s,i} \quad [2.8]$$

2.3.2. Cooling process

The heat extracted from the air during the cooling process will be collected in a special heat storage medium (e.g., oil), for the succeeding heating and expansion processes. There might be some heat loss during the extraction of the heat resulting in efficiency, η_2. Therefore, the heat storage medium temperature can be expressed as follows:

$$T_{hs} = \eta_2(T_2 - T_1) \quad [2.9]$$

The storage temperature (T_s) and pressure (P_s) can be determined as follows:

$$T_s = \gamma T_2 \quad [2.10]$$

$$P_s = n_s R T_s / V \quad [2.11]$$

where γ represents the level of cooling in %. In previous study, γ was set as T_1/T_2, while in the current study it is higher than T_1/T_2 and examined as a study parameter.

2.3.3. Heating process

In this process, the stored air consumes the heat from the heat storage medium. However, some heat may be dispersed from the heat storage during this process resulting in efficiency, η_3. A linear increase of both temperature and pressure is expected during the heating process. Therefore, the following expressions can be obtained based on the ideal gas law:

$$T_3 = \eta_3 T_{hs} \quad [2.10]$$

$$P_3 = n_s R T_3 / V \quad [2.11]$$

2.3.4. Expansion process

Inversed compression process for a generation of power at an efficiency, $\eta_{4,}$, can be called the expansion procedure. By substituting η_1 to $1/\eta_4$ in equation [2.8], the relationship between pressure before the expansion, time, and generated power can be obtained, as follows:

$$V P_3^{5/7} / RC = \dot{w}_{out} t_{out} / 3.5 R \eta_4 \left(C P_3^{2/7} - T_1 \right) + n_{s,i} \quad [2.12]$$

where $\dot{w}_{out}$ is the power generated by turbine. The total energy efficiency of the system can be estimated in the following manner:

$$\eta_T = \dot{w}_{out} t_{out} / \dot{w}_{in} t_{in} = \eta_1 \cdot \eta_2 \cdot \eta_3 \cdot \eta_4 \quad [2.13]$$

2.4. Stresses in the pile foundations

The pile foundation is subjected to the structural load (N_p) as well as the internal pressure (P_s) and temperature changes (T_s). Under internal pressure, the tensile stresses will be generated as it is shown in this Figure 2.3. They will gradually decrease as it gets closer to the outer side of the pile. On the other hand, compression stresses will be generated closer to the inner side under temperature changes. As moving away from the center of the pile, these stresses will gradually increase resulting in tension at the outer side. Thus, it is expected that tensile stresses coming from the combined effect of pressure and temperature will be lowered due to opposite stresses.

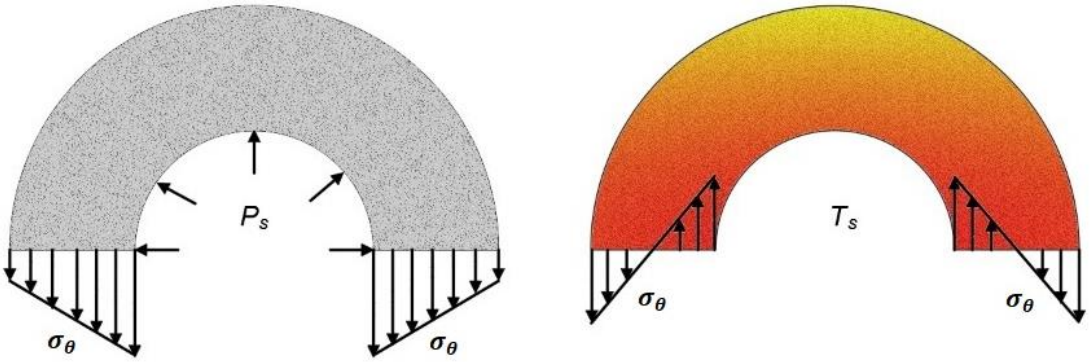

Figure 2.3: Stresses in the pile foundations.

Chapter 3 – Description of the Study

3.1. Variable parameters

Five different designs of the pile, shown in Table 3.1, were chosen so that they could be used to represent different study parameters. Current practice was used as a basis of the pile foundation's design [21]. The number of stories (N) and column spacing plays a major role in this design. The axial force of each column member without factors can be estimated as follows:

$$N_{Ed} = (10 + 3)NA_{tr} \quad [3.1]$$

where 10 kPa and 3 kPa are estimated dead and live loads of each floor, respectively. A_{tr} is the tributary area. Medium dense sand with γ=18 kPa and φ=30° is used for the design of the pile foundation. The bearing capacity (Q_b) and shaft friction capacity (Q_s) are two major sources of pile foundation strength. The pile foundation design follows the allowable stress design method:

$$\frac{N_{Ed}}{n_p} = N_p \leq Q_{all} = \min\left[\frac{Q_b + Q_s}{2}, \frac{Q_b}{3.5} + \frac{Q_s}{1.5}\right] \quad [3.2]$$

Here, n_p is the number of piles and Np is the axial force applied to each pile. L_p, d_o and d_{in} represent the length of the pile, outer diameter, and maximum allowable inner diameter of the pile foundation, respectively.

Table 3.1: Various pile designs used in this study.

Pile design	Column spacing	N	N_{Ed} (kN)	n_p	N_p (kN)	d_o (m)	L_p (m)	Q_b (kN)	Q_s (kN)	Q_{all} (kN)	N_p/Q_{all}	Max. d_{in} (m)
#1 (s=5 m)	7m×7m	2	1274	2	637	1	6	1286	316	639	1.00	0.93
#2 (s=4 m)	7m×7m	4	2548	3	849	1	9	1286	653	864	0.98	0.91
#3 (s=6 m)	6m×6m	2	936	1	936	1	10	1286	791	956	0.98	0.90
#4 (s=3.5 m)	5m×5m	4	1300	2	650	1	6.5	1286	364	671	0.97	0.93
#5 (s=3 m)	5m×5m	6	1950	3	650	1	6.5	1286	364	671	0.97	0.93

Additionally, four different parameters are proposed to be investigated: 1) the inner diameter (d_{in}) of the pile; 2) pile spacing (s); 3) coefficients of thermal expansion; 4) the level of cooling (γ) (Table 3.2). Depending on the pile design (i.e., number of stories, column spacing), spacing between the piles will also change. By running the simulations for five spacing cases its effect on stress distribution along the pile section can be observed. Moreover, with an increase in the inner diameter of the pile, the storage temperature and pressure will reduce due to the enhanced volume of the storage. Thus, this parameter should also be examined. Furthermore, different coefficients of thermal expansion can also be evaluated since their values are ranged between 10 to 15 microstrain/°C for ultra-high-performance concrete

(UHPC) [22]. Storage temperature and pressure differ based on various pile designs and inner diameter as well as the cooling level.

Table 3.2: Study parameters.

d_{in} (mm)	s (m)	Coefficients of thermal expansion (10^{-6}/°C)	γ (%)
200	3	10	1, 1.5, 2
300	3.5	12	1, 1.5, 2
400	4	15	1.5, 2, 2.5
	5		
	6		

3.2. Temperature and pressure loadings

Using the thermodynamic cycles of CAES, the storage temperature (T_s) and pressure (P_s) can be determined. According to Zhang et al. [2], the storage temperature (T_s) can be identified by solving an implicit equation [3.1]. Then, equation [3.2] can be used to calculate storage pressure (P_s).

$$\frac{V_s\left(\frac{\gamma T_2-\eta_2 T_1}{1-\eta_2}\right)^{\frac{5}{2}}}{C^{\frac{7}{2}}}=\frac{\dot{w}_{in}\eta_1 t_{in}}{3.5R\left(\frac{\gamma T_2-\eta_2 T_1}{1-\eta_2}-T_1\right)}+\frac{\rho_i V_s}{\mu} \qquad [3.3]$$

$$P_s=\frac{R\gamma T_2\left(\frac{\gamma T_2-\eta_2 T_1}{1-\eta_2}\right)^{\frac{5}{2}}}{C^{\frac{7}{2}}} \qquad [3.4]$$

where available energy for storage ($\dot{w}_{in}$) and available volumes for storage (V_s) are the input variables. R is the universal gas constant; T_1 is the ambient air temperature; T_2 is the after compression; C is a constant value of 10.89; t_{in} is the time for air compression; ρ_i and μ are the initial density and molar mass of the air, which are 1.2 kg/m^3 and 0.029 kg/mol, respectively. η_1 is the efficiency for the compression and η_2 is the efficiency for the heat exchange.

For this study, several building structures with different design parameters were selected such as the different number of stories, different column and pile spacing, different pile lengths, and different inner diameters. In addition to this, different levels of cooling were considered to find an optimum storage temperature and pressure. Figure 3.1 illustrates the pressure (P_s) and

temperature (T_s) in the stored compressed air for a 24-hour cycle. In this Figure, the case of a 2-story building with 7×7 m column spacing, 5 m pile spacing, and an inner diameter of 200 mm can be observed for different pressure (P_s) and temperature (T_s) storage. As it can be seen, the pressure and temperature start to rise at 7:00, when the energy is available to be stored. It reaches a peak at 19:00 when renewable energy is not available. Thereafter, the compressed air will be released to generate power causing pressure and temperature to decline. These different storage temperatures and pressures were used as an input for thermal and thermal mechanical analyses.

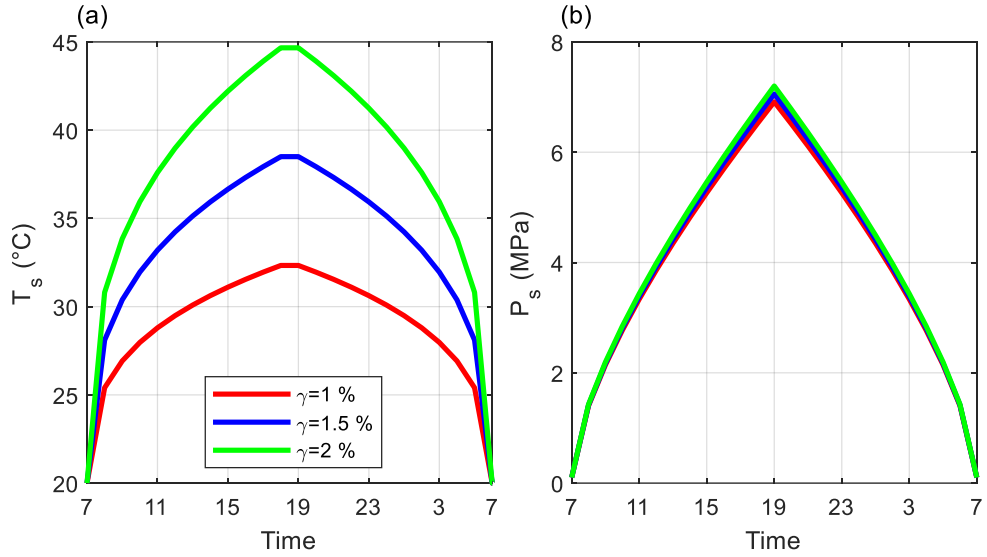

Figure 3.1: (a) Storage temperature and (b) storage pressure for a 24-hour period.

3.3. Model for thermal analyses

The numerical model for the pile foundation and nearby soils was built using the general-purpose finite element software Abaqus. A quarter of the pile is represented as the 2D plane strain model shown in Figure 3.2. No heat flux passes through the symmetrical boundary conditions. Small heat transfer through the bottom of the pile foundation was ignored. The temperature change from the compressed air was applied at the inner surface of the pile foundation. For a concrete section, 10 to 20 mm mesh was applied, while for soils mesh size gradually increases along the radial direction.

Thermal conductivity of k = 2 W/m·°C and specific heat of c = 940 J/kg·°C were assigned to the concrete [23]. For the soil, these values were k = 1.0W/m·°C and c = 1220 J/kg·°C, respectively [24,25]. Considering the impossibility of a perfect connection between

concrete and soil, thermal conductance of 25 W/m^{2}·°C was assigned to an interface element [26]. The density of concrete and soil is 2450 kg/m^{3} and 1600 kg/m^{3}, respectively.

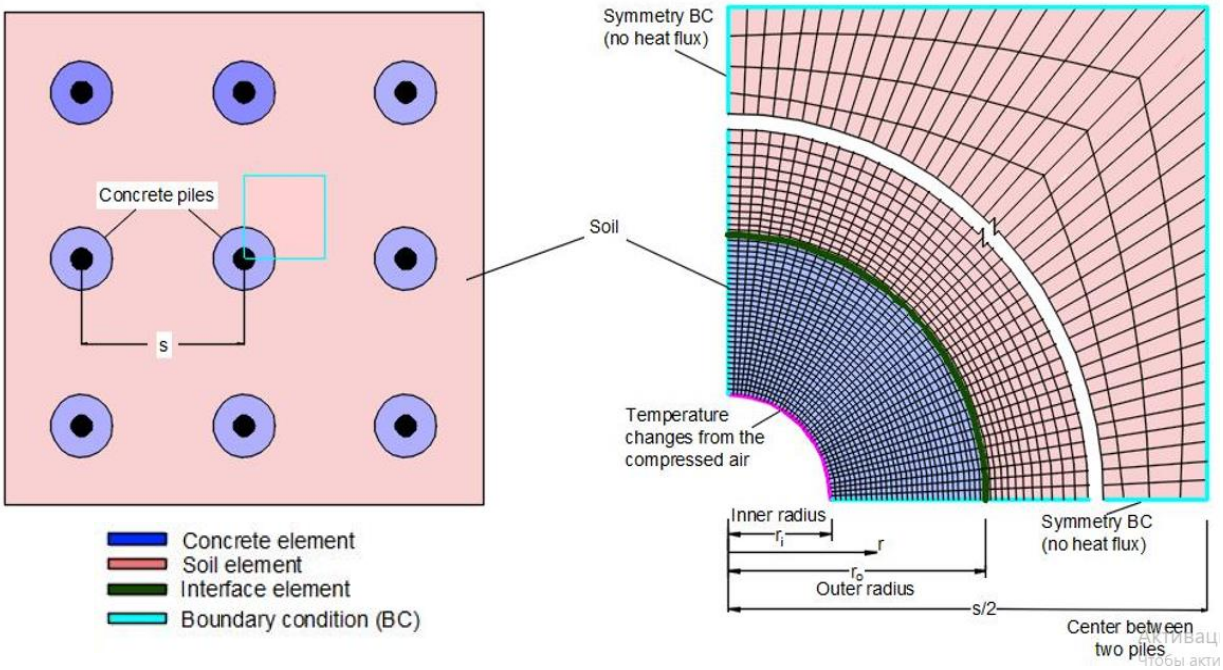

Figure 3.2: The 2D plane strain model.

The non-steady heat transfer analysis was performed by introducing the temperature change varying with time at the inner skin of the pile foundation. Time integration used the backward Euler method with absolute stability. Automatic adjustment of time integration incrementation during the simulation controls the Courant-Friedrichs-Lewy number to be less than 1.0. The proposed pile foundation will be exposed to many temperature loadings cycles throughout its lifecycle. For this study, 365 cycles representing a period of 1-year were applied to each simulation. The initial temperature condition of the soil and concrete pile foundation was expected to be 12 °C as per [27].

3.4. Model for thermal mechanical analyses

An axisymmetric model of the pile foundation was built using the same software (Figure 3.3). For thermal mechanical analyses of energy storage pile, UHPC referred to as C150 was used. The modulus of elasticity and Poisson ratio of C150 concrete were taken to be 45.55 GPa and 0.2, respectively [5]. This type of concrete has a tensile strength of 8.5 MPa and compressive strength of 150 MPa. The coefficient of thermal expansion was chosen to be 15.0·10^{-6}/°C [22]. In addition, a 20 mm steel cap was applied at the top and bottom parts of the pile to reduce localized concentrated stress issue. Its modulus of elasticity is 200 GPa and Poisson ratio is 0.3 [28, 29]. The coefficient of thermal expansion was chosen to be 12.0·10^{-}

^{6}/°C [30]. For a better and more precise representation of stress and strain distribution along the radial and longitudinal direction, a comparatively fine mesh of 20 mm by 20 mm was applied to the model. The structural loads calculated following chosen pile design were applied as a uniformly distributed load at the top of the pile. The temperature distributions inside concrete sections were also applied into corresponding node sets along the radius direction. Internal pressure changes were applied using the surface pressures at the inner surface of the pile foundation.

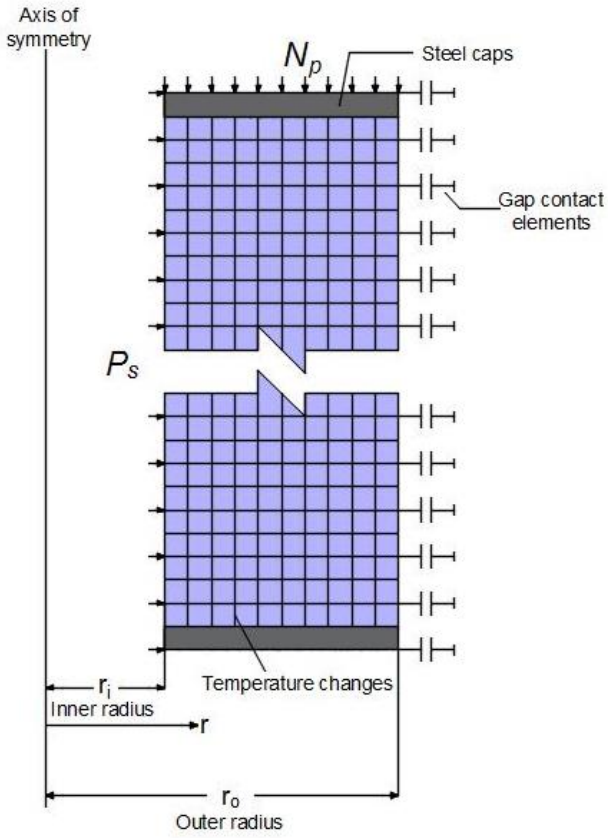

Figure 3.3: The axisymmetric model.

The soil-pile interaction was modeled by using gap contact elements, which can be used to model contact between two nodes in a fixed direction in space. The soil lateral pressure and shaft friction were introduced in the analysis through these contact elements so that coupled behavior of soil lateral pressure and shaft friction can be observed. The gap contact element is defined by the initial separation distance also known as the initial gap. It is needed to consider the initial soil pressure applied to the structure. Moreover, mechanical contact properties were also defined by using a "softened" contact relationship. As per this relationship, the contact pressure is a tabulated function of the space between the surface. It is applied as a data set of pressure against overclosure. This overclosure conforms to a negative clearance. Thus, the soil

is formulated by a series of p-y curves varying with depth, where *p* stands for soil pressure and *y* is the pile deflection (Figure 3.4a). The curve was elaborated on the basis of the API method [31]. Friction properties were also introduced by applying allowable elastic slip coming from simplified soil friction response shown in Figure 3.4b [32]. The coefficient of friction was calculated as $\mu=\tan(\phi'-5°)$, where ϕ' is a friction angle. The end bearing elements were also modeled similarly. The material properties for these elements were determined from the simplified curve of soil bearing response demonstrated in Figure 3.4c [32]. It is crucial to note that pressure and stress values from Figure 3.4 vary depending on the tributary area of each gap contact element.

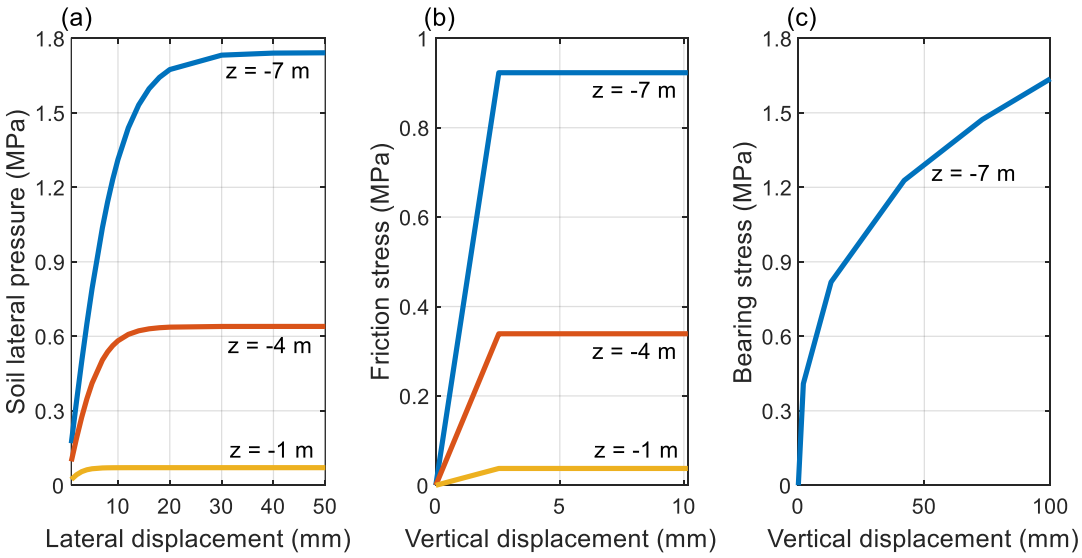

Figure 3.4: Soil model response curves: (a) lateral response; (b) shaft friction response; (c) end bearing response.

Static stress analysis was conducted by applying the temperature loadings, pressure loadings, or combined temperature and pressure loadings at the inner surface of the pile. This option is used to indicate that the step should be analyzed as a static load step. During a static step, a time period should be assigned to the analysis. It is necessary to identify variations of loads and other parameters prescribed to the step. A time varies from 0 to 1 by default unless the time period is specified. The time increments are then formulated by dividing the total period of the step into fractions.

As it was mentioned earlier, three different loadings were applied to the model. They are temperature changes, internal pressure, and structural loads. Storage temperature and pressure calculation were discussed above in Section 3.2. The pressure was applied at the inner surface of the pile, while the temperature was applied at a particular node set. For instance, the

temperature distributions from thermal analyses were extracted for the r=0.1 m. As a result, this data was applied to the node sets with r=0.1 m in the axisymmetric model. Structural loads presented in Table 3.1 were calculated in accordance with the pile design. It was applied at the top of the pile.

3.5. Yield surface function

The yield function is used for better representation of different behaviors in the tensile and compressive region [33]. For frictional materials like concrete, it is given as:

$$F(\sigma) - c = 0 \qquad [3.5]$$

where c is the cohesion and $F(\sigma)$ is a scalar function of invariants of the stress tensor. This function can be calculated as follows:

$$F(\sigma) = \frac{1}{1-\alpha}\left(\alpha I_1 + \sqrt{3J_2} + \beta\langle\hat{\sigma}_{max}\rangle\right) \qquad [3.6]$$

where α and β are the dimensionless constants; and $\hat{\sigma}_{max}$ is algebraically maximum principal stress. I_1 and J_2 in this equation represent the first invariant in the stress tensor and the second deviatoric stress invariants, respectively. Dimensionless constants can be calculated in the following manner:

$$\alpha = \frac{f_{b0} - f_{c0}}{2f_{b0} - f_{c0}} \qquad [3.7]$$

which should lie in the range of 0 to 0.5. Here, f_{c0} is the initial yield compressive stress and f_{b0} is the biaxial initial yield compressive stress. To calculate β, initial yield tensile stress f_{t0} is assumed to be equal to the maximum tensile strength:

$$\beta = \frac{f_{c0}}{f_{t0}}(\alpha - 1) - (1 + \alpha) \qquad [3.8]$$

Chapter 4 – Thermal Analyses

As was mentioned above, this thesis consists of two main parts. The first study is related to temperature distributions inside the concrete section. Thus, in this section, the results obtained from the thermal analyses will be discussed. Obtained results will be further used to explain and correlate with the results obtained from the second part of the study, i.e., thermal mechanical analyses. Each pile design case is investigated separately. The summary is presented at the end of this section.

4.1. Pile design #1

Figure 4.1a shows the temperature changing with time at different points of the pile. As it can be noticed, at the inner side of the pile it follows the storage temperature that was applied to the pile. The temperature reduces as moving away from the pile's inner skin. Also, the temperature gradually increases at the end of the time for the points other than the inner surface. Finally, the outer skin of the pile reaches the lowest temperature due to the lowering effect of temperature. Following Figure 4.1b and 4.1c represent the temperature varying with time at the inner and outer surface of the pile for different d_{in}. Here, D200, D300, and D400 represent the piles with 200-, 300-, and 400-mm inner diameter. At the inner surface of the pile, all of them follow the storage temperature inputted to the model. It happened that the temperature input for the 200-mm pile is higher than the 300-mm pile. Closer to the outer surface, the temperature at the middle of the cycle was lowered from around 32°C to around 14°C for d_{in}=200 mm. For d_{in}=300 mm, this temperature change was lower with around 30°C at the inner surface and 15°C at the outer surface of the pile. For a 400-mm pile, it decreased from 36°C to about 19°C as moving further along the radius of the pile. At the inner surface of the pile, the temperature comes back to the original temperature of 20°C at the end of the cycle for all three cases. It is worth noting that it slightly decreases closer to the outer surface to around 16°C and 18°C for d_{in}=200 mm and d_{in}=300 mm, respectively. However, for a 400-mm pile, this value increases to 22°C. This might be associated with the thickness of the pile and the lowering effect of temperature. For thicker piles, the lowering effect of temperature can be significant. Also, heat transfer appears to be slower in this case. Whereas thinner piles cannot be considerably cooled down due to the shorter distance between the inner and outer surface of the pile.

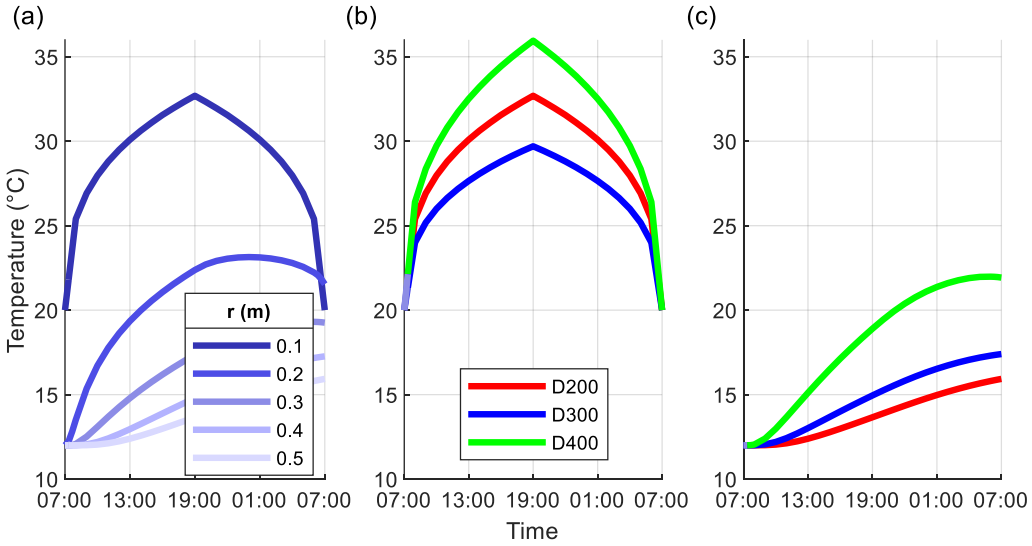

Figure 4.1: Temperature changing with time at (a) different locations; and for various din at (b) inner and (c) outer surface for pile design #1.

The cyclic response of temperature changes for different locations can be observed in Figure 4.2. At r=0.1 m, the pile temperature changes continually due to input storage temperature. The residual temperature effect starts to develop as getting further from the inner skin. The temperature remained from the previous cycles causes cumulative effect for the subsequent cycles. As a result, temperature increases in the pile section. For example, the temperature at the end of the 1st cycle and 10th cycle was approximately 16°C and 22°C at the outer surface, respectively.

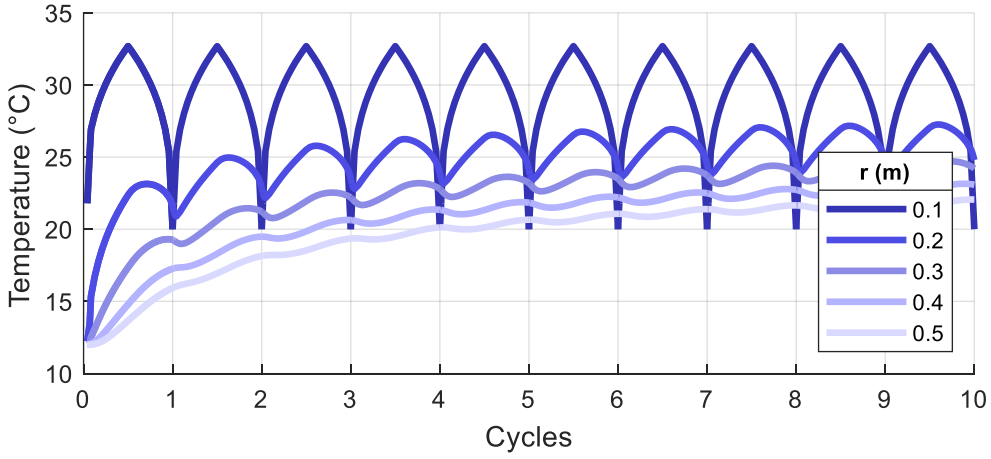

Figure 4.2: Temperature changes for the first 10 cycles for pile design #1.

Figure 4.3a demonstrates maximum temperature at the end of each loading cycle at different locations of the pile. The constant value of around 33°C can be noticed at the inner skin of the pile due to input temperature. It decreases as it gets further due to the lowering effect

of temperature. Also, the gradual increase of temperature with the cycle can be noticed for all locations, except inner skin. This is the residual temperature effect discussed above. In addition, the temperature profile along radial direction for various cycles is presented in Figure 4.3b. It clearly shows that the greater cycle corresponds to the higher temperature. A slight increase closer to the inner skin of the pile can be observed. This is followed by the gradual decrease closer to the outer side, proving the temperature lowering effect.

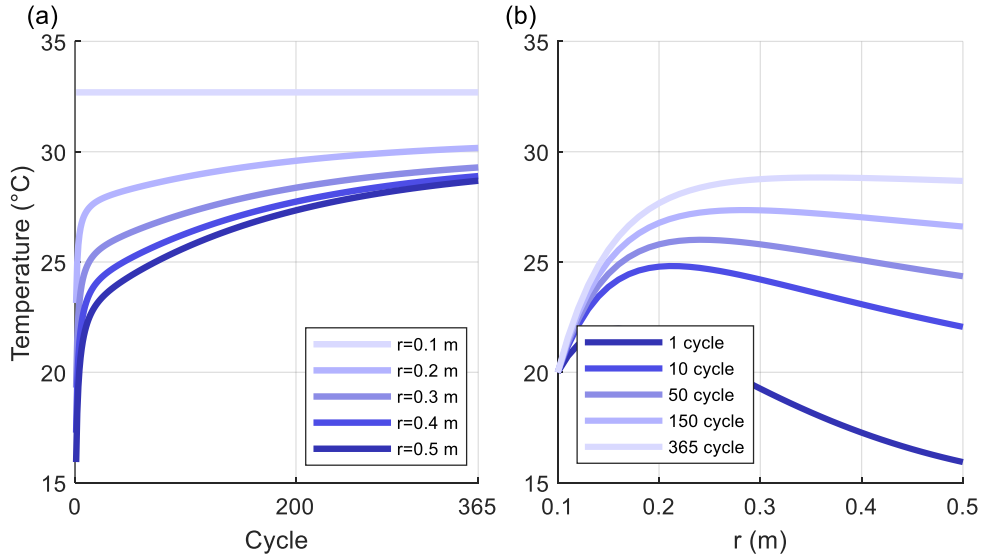

Figure 4.3: (a) Maximum temperature of each loading cycle and (b) temperature profile along radius for different cycles for pile design #1.

4.2. Pile design #2

Figure 4.4a also shows the temperature changing with time at different points of the pile. A similar pattern can be observed for this pile design as well. Figure 4.4b and 4.4c demonstrate the temperature varying with time at the inner and outer surface of the pile for different d_{in}. The storage temperature inputted into the model can be observed in Figure 4.4b. It happened that the temperature input for the 200-mm pile is the highest, followed by the 400- and 300-mm pile. Closer to the outer surface, the temperature at the middle of the cycle was lowered from around 32°C to around 14°C for d_{in}=200 mm. For d_{in}=300 mm, this temperature change was lower with around 29°C at the inner surface and 15°C at the outer surface of the pile. For a 400-mm pile, it decreased from 32°C to about 18°C as moving further along radius of the pile. At the inner surface of the pile, the temperature comes back to the ambient temperature of 20°C at the end of the cycle for all three cases. It is worth noting that it slightly decreases closer to the outer surface to around 15°C and 17°C for d_{in}=200 mm and d_{in}=300 mm,

respectively. However, for a 400-mm pile, this value stays around 20°C. This is due to the inconsiderable temperature lowering effect for thinner piles.

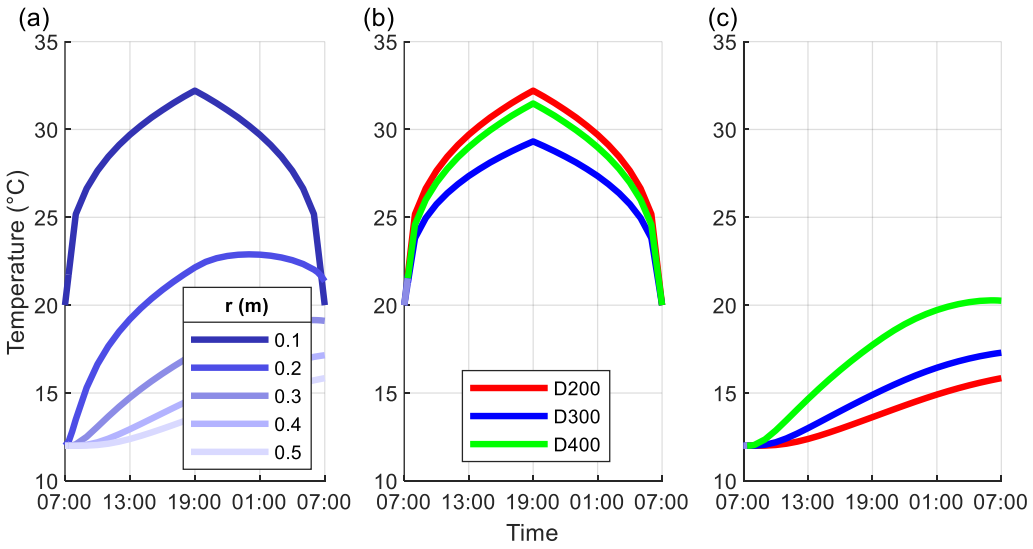

Figure 4.4: Temperature changing with time at (a) different locations; and for various d_{in} at (b) inner and (c) outer surface for pile design #2.

Figure 4.5 shows the temperature changes for the first 10 cycles at different locations of the pile. At r=0.1 m, the pile temperature changes continually due to applied temperature. Moving away from the pile, the temperature change gets lower. The residual temperature effect also comes to pass. Thus, temperature change increases with the loading cycle.

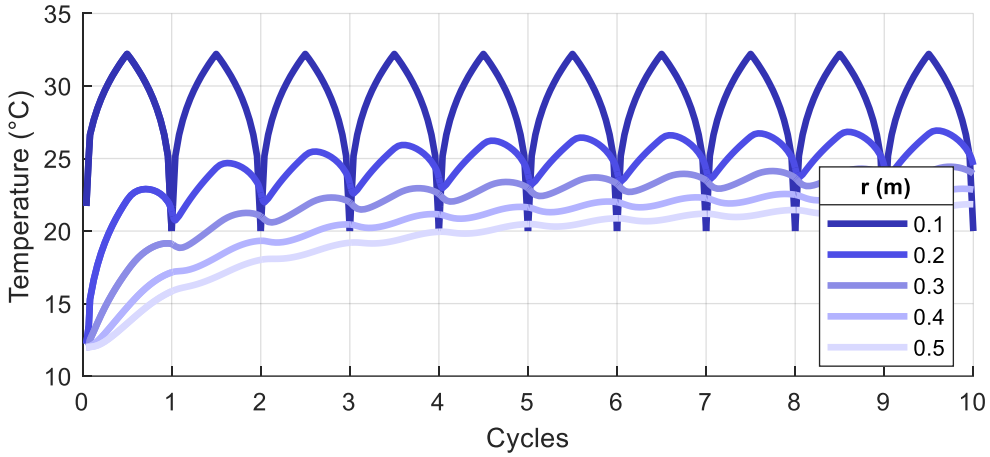

Figure 4.5: Temperature changes for the first 10 cycles for pile design #2.

Figure 4.6a represents the maximum temperature at the end of each loading cycle at different locations of the pile. Also, the temperature profile along radial direction for various cycles is presented in Figure 4.6b. These figures clearly show that the greater cycle corresponds to the higher temperature due to the residual temperature effect.

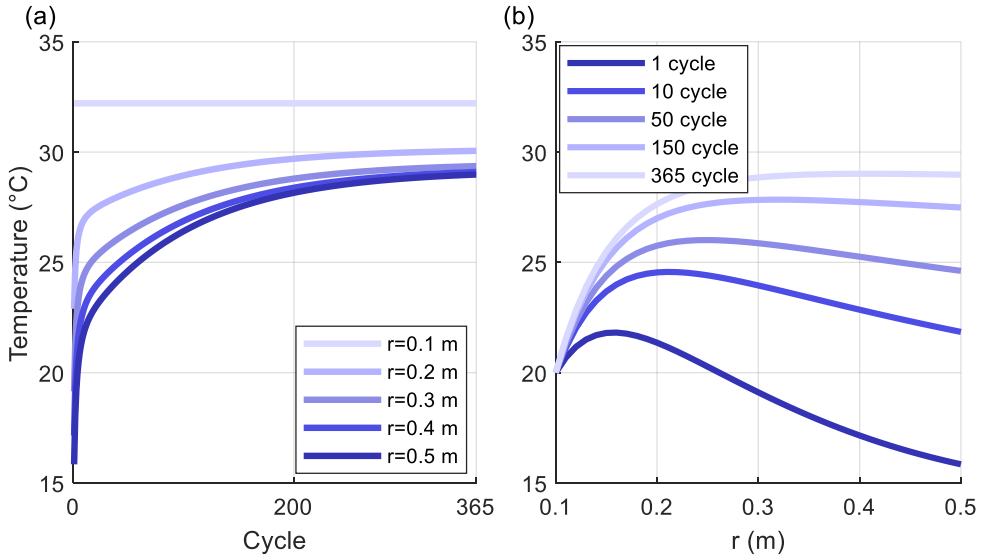

Figure 4.6: (a) Maximum temperature of each loading cycle and (b) temperature profile along radius for different cycles for pile design #2.

4.3. Pile design #3

The temperature changing with time at different points of the pile can be shown in Figure 4.7a. A similar pattern can be observed for this pile design as well. Figures 4.7b and 4.7c demonstrate the temperature varying with time at the inner and outer surface of the pile for different d_{in}. At the inner skin of the pile, the storage temperature applied to this pile design can be noted. It happened that the temperature input for the 200- and 400-mm pile is almost the same. For the 300-mm pile, it is slightly lower. Closer to the outer surface, the temperature at the middle of the cycle was lowered from around 32°C to around 13.5°C for d_{in}=200 mm. For d_{in}=300 mm, this temperature change was lower with around 29°C at the inner surface and 15°C at the outer skin of the pile. For a 400-mm pile, it decreased from 32°C to about 18°C as moving further along the radius of the pile. At the inner face of the pile, the temperature comes back to the original temperature of 20°C at the end of the cycle for all three cases. It is worth noting that it slightly decreases closer to the outer surface to around 16°C and 17°C for d_{in}=200 mm and d_{in}=300 mm, respectively. However, for the 400-mm pile, this value stays around 20°C.

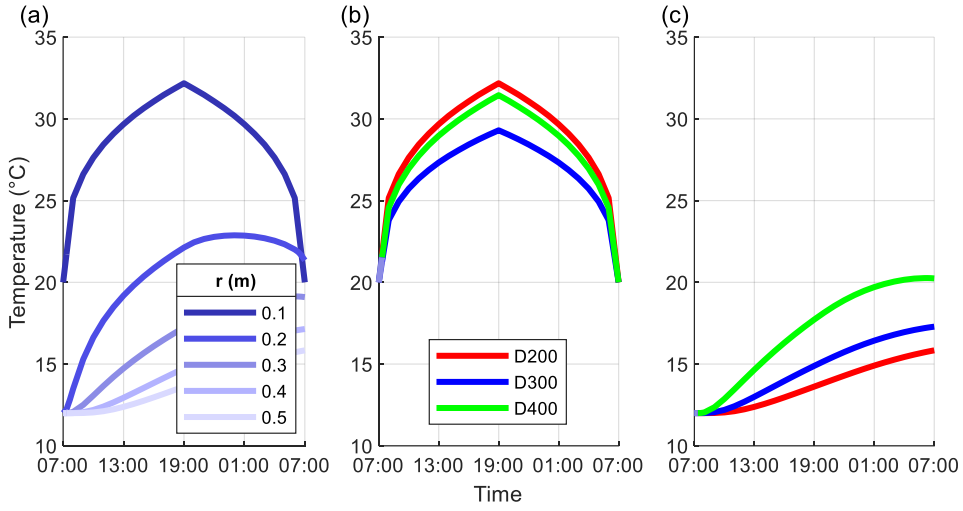

Figure 4.7: Temperature changing with time at (a) different locations; and for various d_{in} at (b) inner and (c) outer surface for pile design #3.

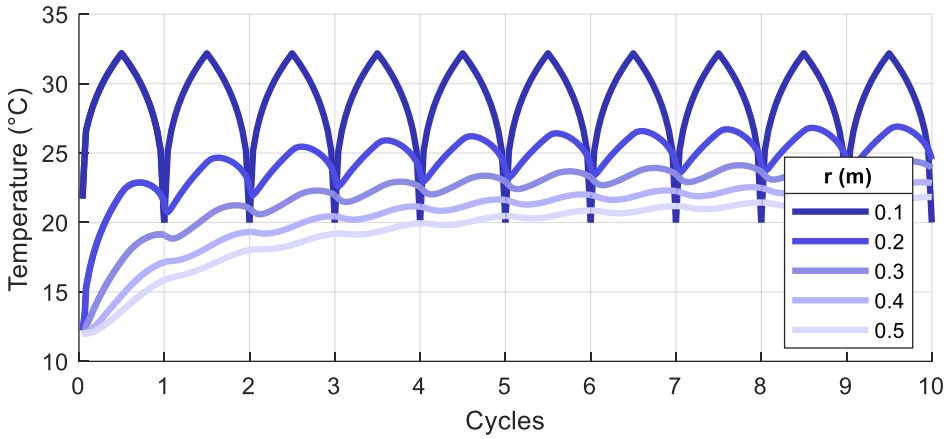

Figure 4.8: Temperature changes for the first 10 cycles for pile design #3.

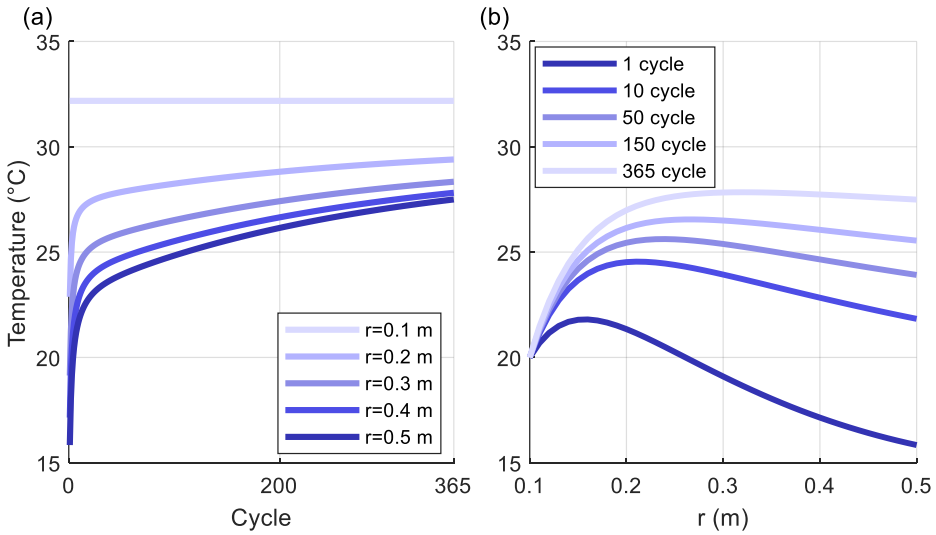

Figure 4.9: (a) Maximum temperature of each loading cycle and (b) temperature profile along radius for different cycles for pile design #3.

Figure 4.8 presents the cyclic response of temperature changes at different locations for pile design #3. It follows a similar pattern as previous cases.

Figure 4.9 also shows that the longer the pile is subjected to the temperature changes, the warmer it gets with the cycle due to the residual temperature effect.

4.4. Pile design #4

The temperature varying with time at different points of the pile can also be observed in Figure 4.10a. A similar pattern can be observed for this pile design also. Figure 4.10b and 4.10c demonstrate the temperature versus time at the inner and outer skin of the pile for different d_{in}. At the inner surface of the pile, the storage temperature inputted to the model is shown. It happened that the temperature input for the 200- and 400-mm pile is almost the same, followed by the 300-mm pile. Closer to the outer surface, it represents the temperature change plot reducing with d_{in}. Thus, the highest temperature changes are observed for d_{in}=400 mm, followed by the descending order of inner diameters. This figure mainly demonstrated the lowering effect of temperature from inner to the outer skin.

Following Figure 4.11 presents the cyclic response of temperature changes at different locations for pile design #4. It follows a similar pattern as previous cases.

Figure 4.12 also proves the point of the cumulative effect of temperature due to the residue from the prior cycles.

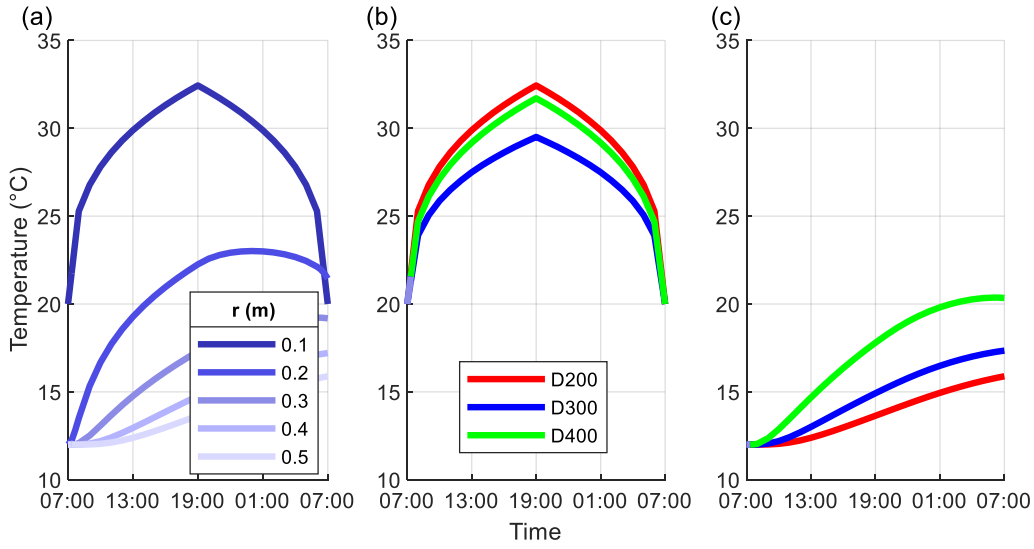

Figure 4.10: Temperature changing with time at (a) different locations; and for various d_{in} at (b) inner and (c) outer surface for pile design #4.

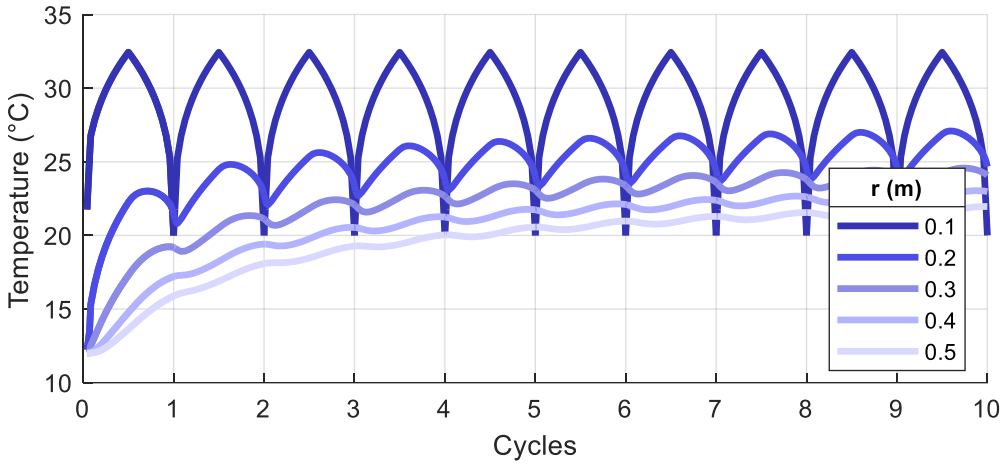

Figure 4.11: Temperature changes for the first 10 cycles for pile design #4.

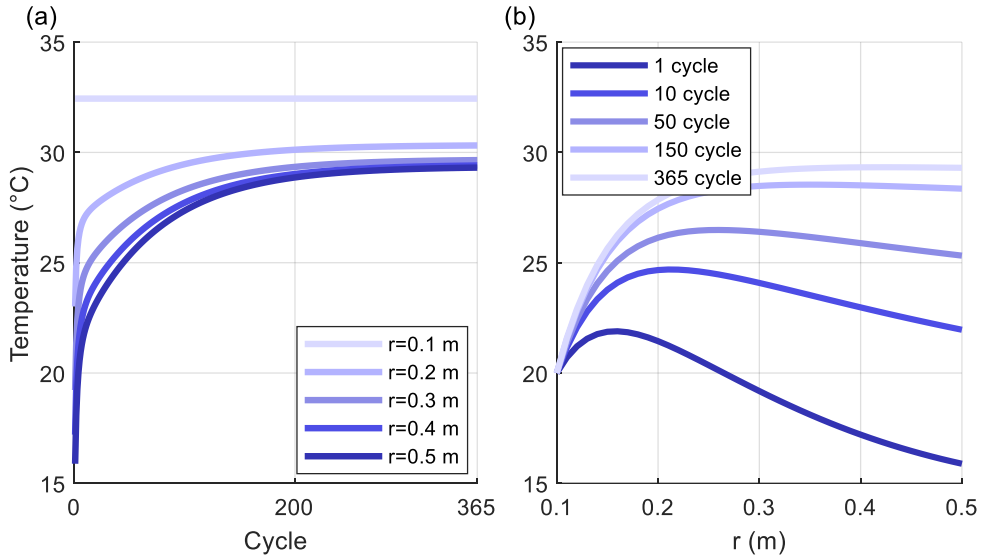

Figure 4.12: (a) Maximum temperature of each loading cycle and (b) temperature profile along radius for different cycles for pile design #4.

4.5. Pile design #5

The temperature varying with time at different points of the pile can be observed in Figure 4.13a as well. The results for this pile design follow a similar pattern as previous examples. Figure 4.13b and 4.13c demonstrate the temperature versus time at the inner and outer skin of the pile for different d_{in}. At the inner surface of the pile, the storage temperature applied to the model is shown. It happened that the temperature input for 200- and 400-mm pile is similar, and the lower temperature is applied to a 300-mm pile. Moving away from the pile, the highest temperature changes are observed for d_{in}=400 mm, followed by the 300- and 200-mm piles.

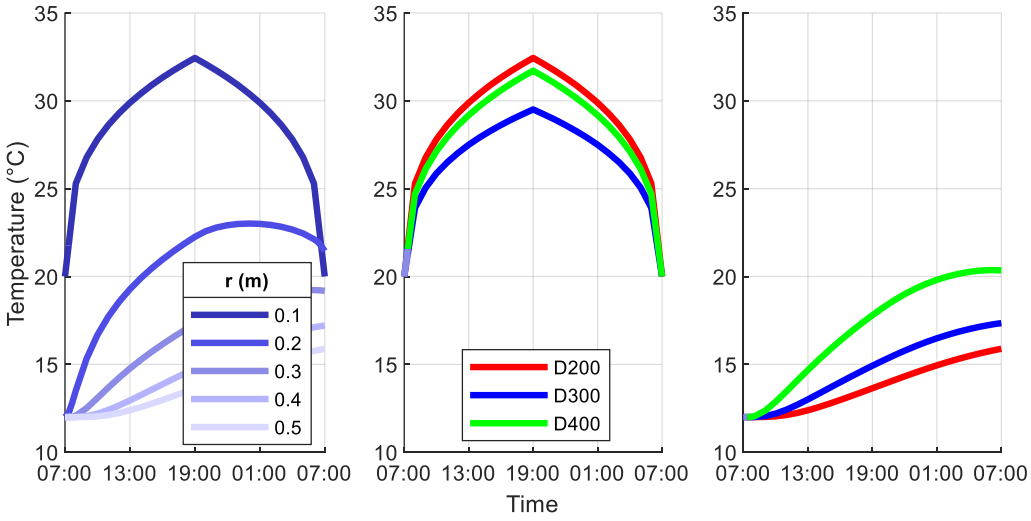

Figure 4.13: Temperature changing with time at (a) different locations; and for various d_{in} at (b) inner and (c) outer surface for pile design #5.

Following Figure 4.14 presents the cyclic response of temperature changes at different locations for pile design #5. It follows a similar trend as in the cases discussed above.

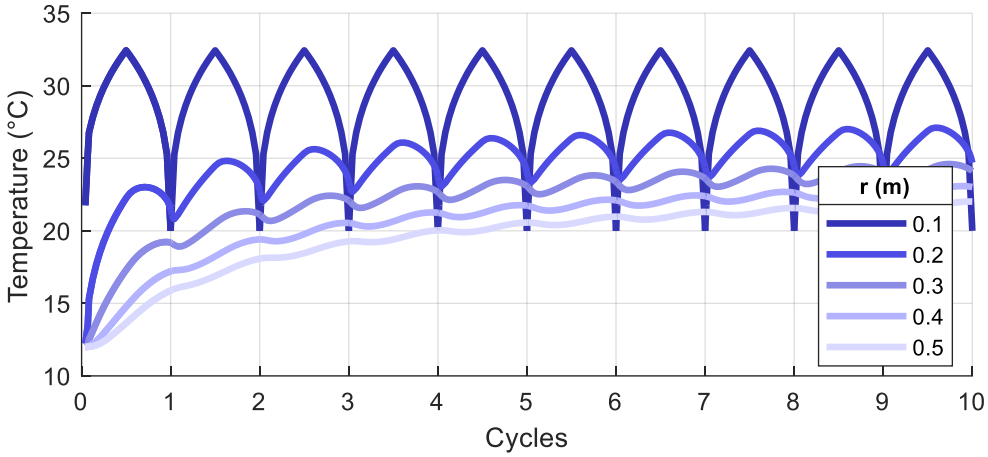

Figure 4.14: Temperature changes for the first 10 cycles for pile design #5.

Figure 4.15 supports the residual temperature effect with increasing cycles for this pile design as well.

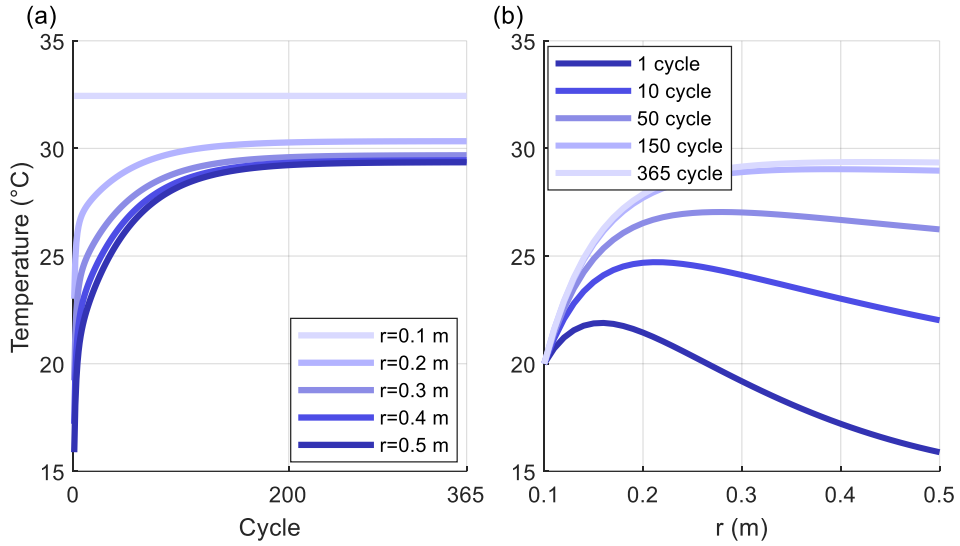

Figure 4.15: (a) Maximum temperature of each loading cycle and (b) temperature profile along radius for different cycles for pile design #5.

4.6. Summary of thermal analyses

In this Figure 4.16, the maximum temperature at the end of each cycle is shown at three different locations of the pile for various d_{in}. As it can be seen, the maximum temperature of around 36°C is applied to a pile with d_{in}=400 mm. It is followed by around 33°C and 30°C to a pile with d_{in}=200 mm and d_{in}=300 mm, respectively. For the middle and outer edge of the pile, a similar arrangement can be noticed. At the middle of the pile, the maximum temperature in the last cycle decreased to 33°C for a pile with d_{in}=400 mm. This value did not significantly reduce at the outer edge of the pile. For the 300-mm and 200-mm piles, it was reduced to 27°C and 29°C, respectively. This happened due to the lowering effect of temperature.

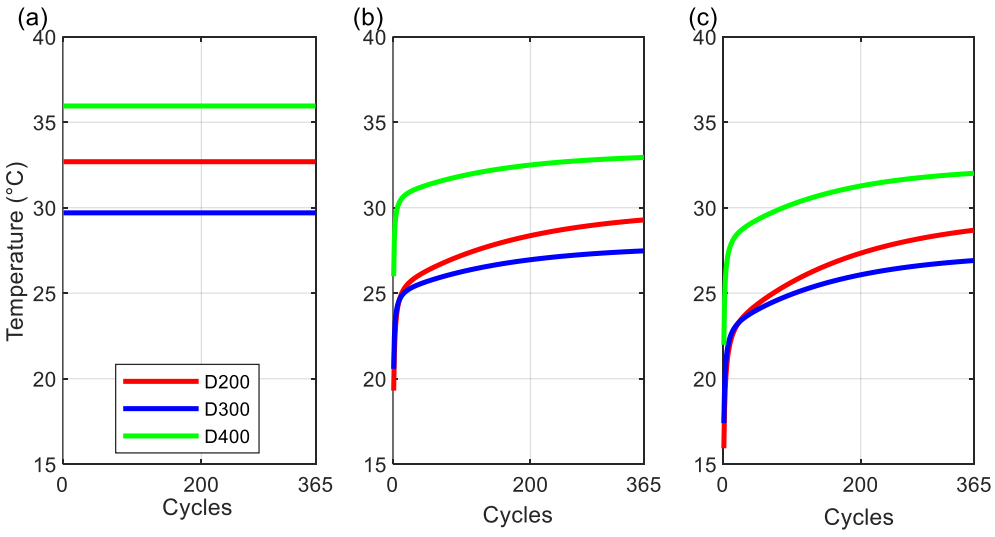

Figure 4.16: Maximum temperature at each loading cycle for various d_{in} at the (a) inner, (b) middle and (c) outer surface of the pile.

Figure 4.17 shows the maximum temperature chnaging with cycles for different T_s at the inner, middle and outer part of the pile. As expected, the highest temperature corresponds to 2% of T_2. It is about 46°C at the inner surface of the pile. It decreases to 39°C as gets further. It is followed by 1.5% of T_2 with about 39°C at the inner surface and 34°C at the outer skin of the pile. The lowest temperature input corresponds to approximately 33°C for 1% of T_2. It reduces to about 29°C as moves away from the pile. To sum up, it can be said the higher the applied temperature, the higher the temperature changes inside the concrete section as well.

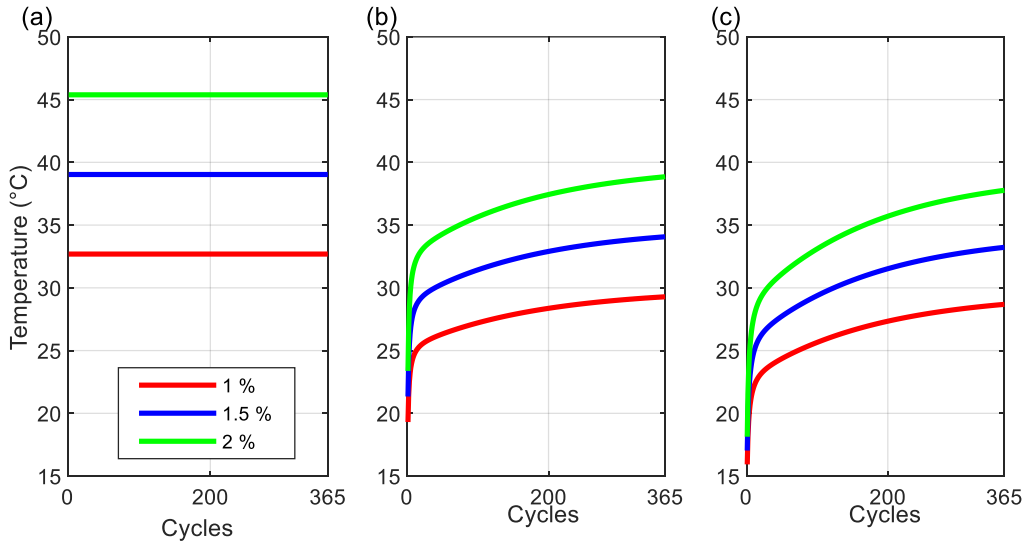

Figure 4.17: Maximum temperature at each loading cycle for various T_s at the (a) inner, (b) middle and (c) outer surface of the pile.

Similar plots are represented in Figure 4.18 as well, but for different pile spacings. As it was noticed above, there is a negligible difference between temperature change at the middle and outer surface of the pile. Also, the maximum temperature is constant at the inner surface of the pile. According to Figure 4.18a, for the same d_{in}, the input temperature for different designs of the pile lies in the range of 32-33°C. Figures 4.18b and 4.18c show lower temperature change for greater pile spacings. The reason for this is the heat produced from adjacent piles. This heat can travel through the soil layer to the adjacent pile via thermal conduction. Hence, the temperature in the pile section, especially for the cases with a small pile spacing, is increased due to the heat transfer.

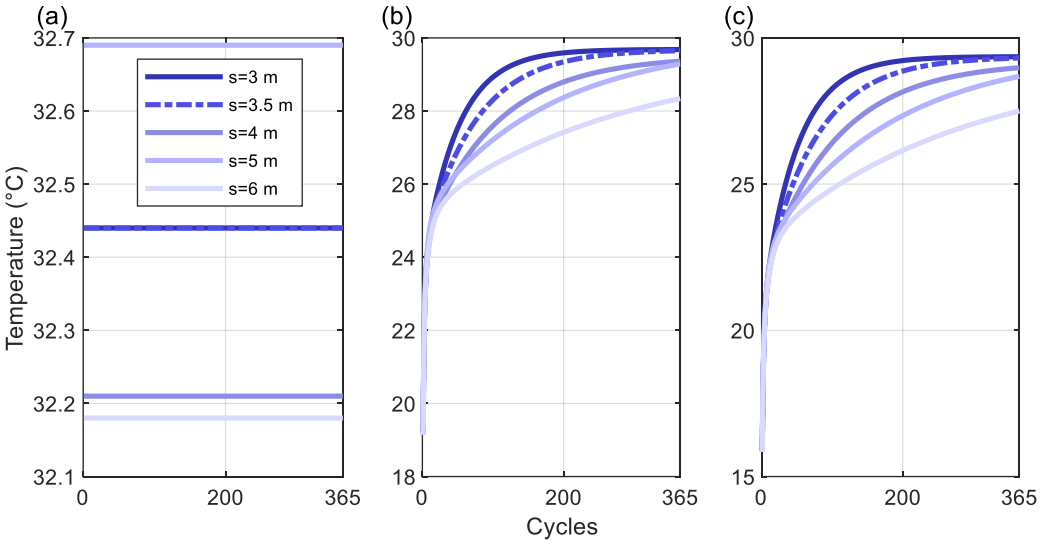

Figure 4.18: Maximum temperature at each loading cycle for various pile spacings at the (a) inner, (b) middle and (c) outer surface of the pile.

Chapter 5 – Thermal Mechanical Analyses

The second part of this study is related to the structural responses of the energy storage piles subjected to temperature changes and internal air pressure. Thus, this section will describe the results obtained from thermal mechanical analyses. Results for various pile dimensions discussed in Section 3.1 are presented below. In this section, figures are presented for γ=1% and d_{in}=200 mm case. Similar figures for other γ and d_{in} cases are presented in Appendix A.

5.1. Pile design #1

Figure 5.1 illustrates the stress changing with one cycle at the inner and outer surface of the pile. Here, the abbreviation "P+T" stands for combined loadings, "T" and "P" means temperature changes and internal air pressure, respectively. All the following data presented in this section are linked to the point, where maximum circumferential stress happens. The reason for this is that circumferential stress is the major source of critical stress in this study. Radial stresses demonstrate compressive stresses at both locations of the pile. At the outer surface of the pile, it reaches a negligible value of -0.05 MPa under combined loadings for γ=1%. At the inner surface, temperature changes result in lower compressive stresses than the internal air pressure. Thus, for γ=1% combination of these two results in -7 MPa of compressive stress at the middle of the cycle. Furthermore, it should be noted that the internal air pressure generates a negligible amount of vertical stress. Thus, stresses due to temperature changes and combined loadings are almost the same. At the inner skin of the pile, it causes compressive stress of around -13 MPa at the middle of the cycle for γ=1%. While at the outer surface, it produces slight tensile stress of around 2 MPa at the middle of the cycle for γ=1%. A major part of tensile stresses come from circumferential stresses at the outer side of the pile. As per Figure 5.1f, the combination of temperature changes and internal air pressure leads to around 3.5 MPa of tensile stresses at the middle of the cycle for γ=1%. Whereas at the inner side, compressive stresses due to temperature changes (around -12 MPa at the middle of the cycle) help to reduce tensile stresses of about 7 MPa coming from pressure. As a result, around -5 MPa of compressive stresses are generated at the middle of the cycle for γ=1%. Overall, a similar trend is followed for other cases of d_{in} and γ.

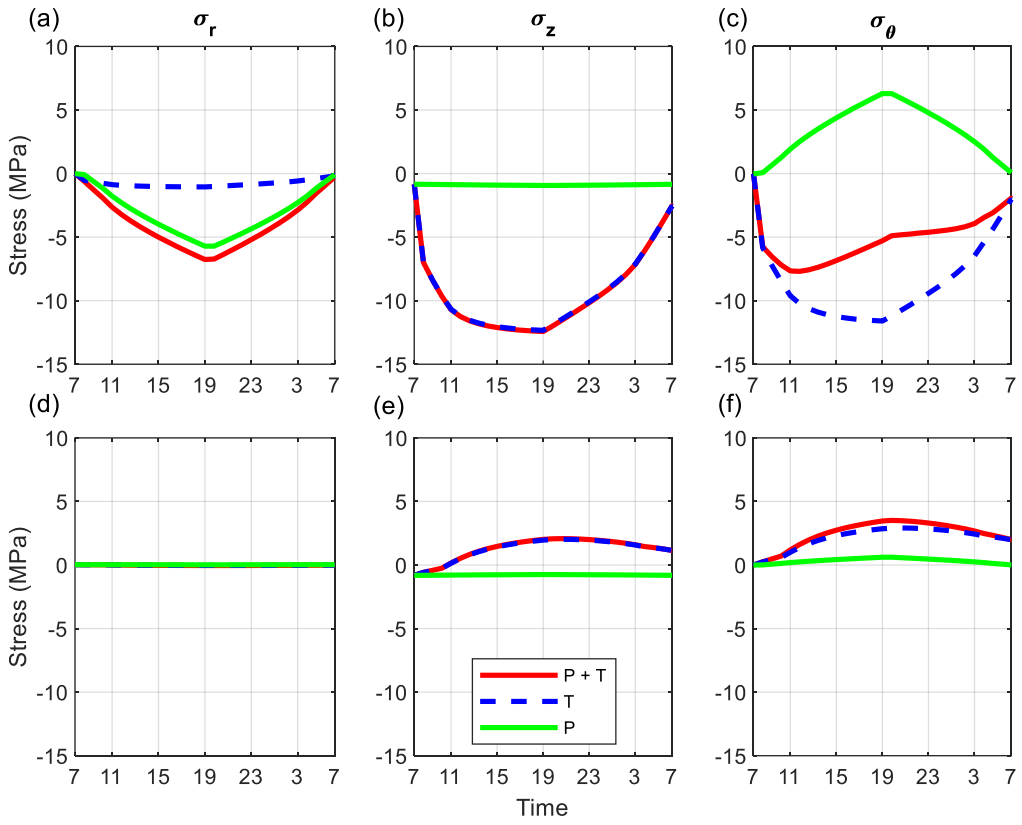

Figure 5.1: Stress varying with 24-hour time at the (a)-(c) inner and (d)-(f) outer surface for the pile design #1.

Stress distribution along the radial direction at the middle and end of the cycle is presented in Figure 5.2 below. At the end of the cycle, a negligible effect of internal air pressure can be observed. Thus, it leads to a similar trend of stress under temperature changes only and combined effect. Radial stresses generate compression with the lowest of around -1 MPa closer to the inner edge of the pile for γ=1%. Others produce compression gradually transiting to tension closer to the outer surface of the pile for d_{in}=200 mm and d_{in}=300 mm. However, for d_{in}=400 mm tension can be observed not only closer to the outer side but at the inner side as well. These tensile stresses are slightly higher than 1 MPa for vertical stresses and about 2 MPa for circumferential stresses at the end of the cycle. The same can be applied for the vertical stress at the middle of the cycle, which reaches a maximum of around 2-5 MPa of tensile stresses for different γ and d_{in} cases. Radial stresses at the middle of the cycle produce compressive stresses under three loadings cases. It is interesting to note that circumferential stresses at the middle of the cycle under internal air pressure generate tensile stresses. It slowly decreases closer to the outer surface of the pile. Whereas temperature changes result in compressive stress gradually transferring to tensile stress after some point. As a result, the maximum circumferential tensile stresses in the pile section under combined loading are

smaller than the case under the internal air pressure. Thus, the effect from combined loadings is minimized. It starts with -4 MPa of compressive stresses at the inner side slowly transiting to around 4 MPa of tensile stresses closer to the outer side for γ=1%. A similar trend can be observed for d_{in}=300 mm and d_{in}=400 mm as well.

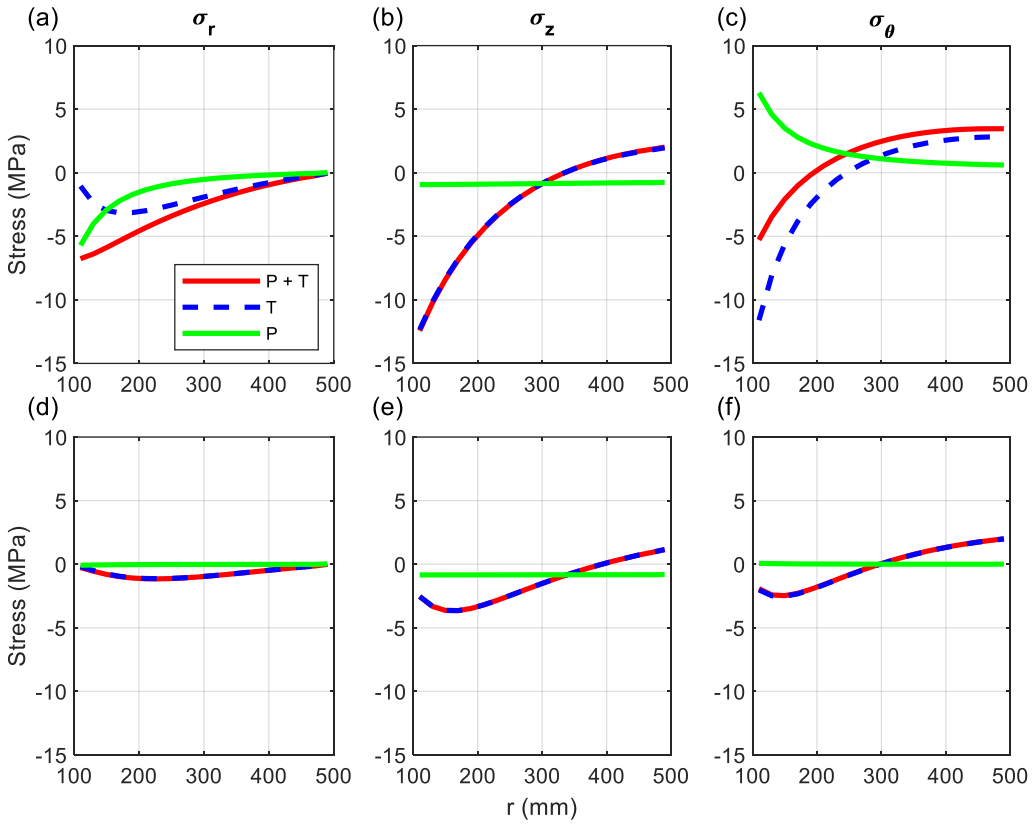

Figure 5.2: Stress distribution along r-direction at the (a)-(c) middle and (d)-(f) end of the cycle for the pile design #1.

Figure 5.3 shows the stress profile along longitudinal direction at different locations. At the inner surface of the pile, circumferential stresses under pressure generate high tensile stresses. This is canceled by compressive stresses coming from the temperature changes. Consequently, adequate compressive stresses of approximately -5 MPa can be observed under combined loadings for γ=1%. At the outer surface of the pile, both stresses presented here produce a negligible amount of stress under internal air pressure. Thus, the stresses under temperature changes and combined loadings are similar. Vertical stresses do not exceed allowable tensile strength with around 3-4 MPa for all γ and d_{in} cases. Circumferential stresses follow a similar trend.

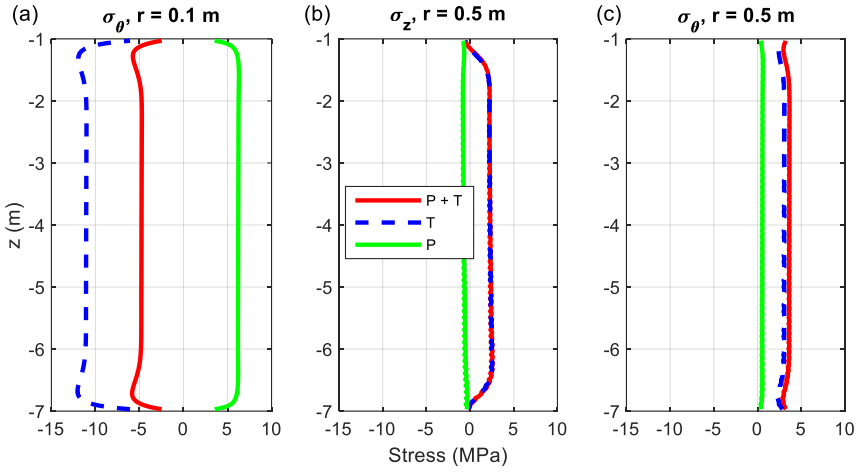

Figure 5.3: Stress distribution along z-direction for the pile design #1: (a) circumferential stress at inner skin; (b) vertical stress and (c) circumferential stress at outer skin.

Stress changing with time for the first 10 cycles at the inner and outer surface of the pile is illustrated in this Figure 5.4. For all three stresses at the inner skin of the pile and radial stress at the outer side of the pile, stresses keep increasing with time. This can be associated with the residual stress effect left from the previous cycles. However, vertical, and circumferential stresses at the outer side of the pile decrease as time goes by. With the increase of loading cycles, the residual effect decreases the compression stress at the inner surface. Eventually, it makes it under tension after the sufficient number of cycles. However, tensile stresses at the outer surface are also reduced due to the residual stress effect. This is the case for different values of γ and d_{in} as well.

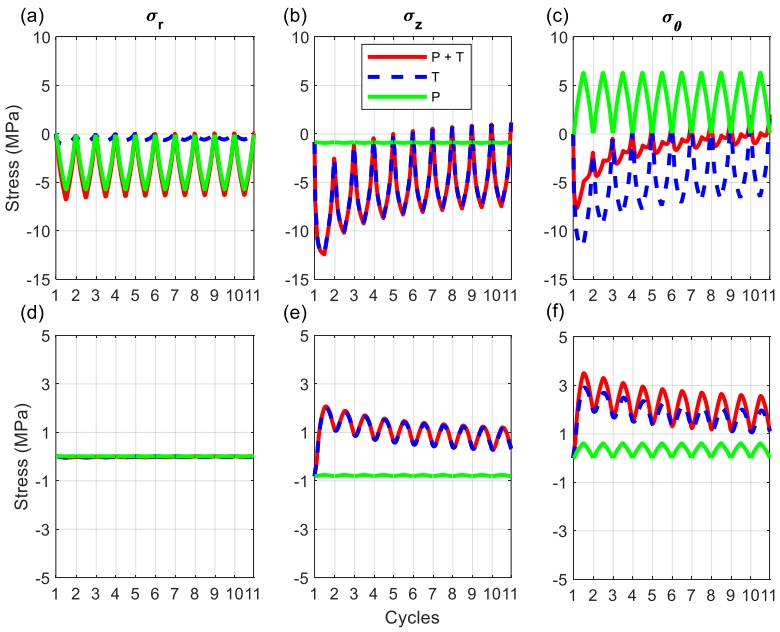

Figure 5.4: Stress varying with 10 cycles for (a)-(c) inner and (d)-(f) outer surface for the pile design #1.

Stress distribution along the radial direction at the middle and end of the different cycles is demonstrated in Figure 5.5. Radial stresses at the middle of all cycles presented produce compressive stresses. It shows a minor increase with the increase in the number of cycles. However, at the end of the cycles, it generates compressive stresses at the 1st cycle only. Starting from the 10th cycle, it induces tension. Tensile stresses keep increasing with the cycle at the inner surface of the pile and go down closer to the outer surface. Vertical stresses produce compressive stresses at the middle of the cycle. Small tensile stresses can be observed at the outer surface of the pile. At the end of the 1st cycle, this tendency is followed. However, starting from the 10th cycle tensile stresses at the inner surface of the pile can be noticed. They keep increasing with the cycle due to the residual stress effect. The same description can be applied to circumferential stresses at the end of the cycle as well. Circumferential stresses at the middle of the 1st cycle start from compression. As moving away from the pile, it gradually increases to tension. After reaching transition cycles, pure tension stresses are generated. A transition cycle (N) is defined here as a cycle in which stress goes from the compression-tension distribution to the pure tension state in the entire pile section. For a pile with d_{in}=200 mm, it is the 10th cycle for γ=1%, the 24th cycle for γ=1.5%, and the 26th cycle for γ=2%. For a pile with d_{in}=300 mm, it is the 9th cycle for γ=1%, the 17th cycle for γ=1.5%, and the 18th cycle for γ=2%. For a pile with d_{in}=400 mm, it is the 5th cycle for γ=1% and γ=1.5%, and the 8th cycle for γ=2%. At the inner side of the pile, higher tensile stresses correspond to a greater cycle. However, it works reversely at the outer surface.

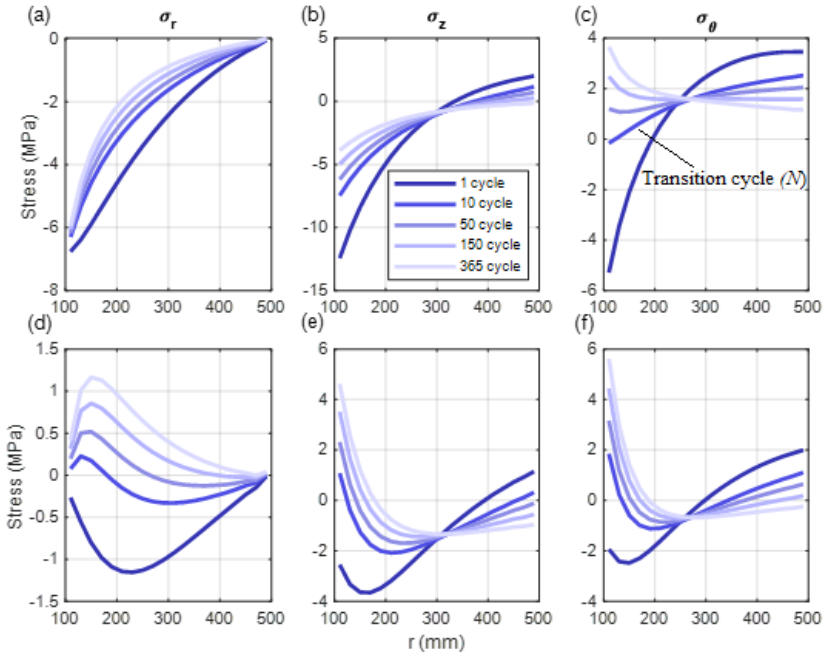

Figure 5.5: Stress distribution along r-direction at the (a)-(c) middle and (d)-(f) end of the different cycles for the pile design #1.

Figure 5.6 represents the stress profile along the length of the pile at the inner and outer face of the pile for various cycles. At the inner skin, compression stresses are generated at the 1st cycle. Then, it is followed by tensile stresses increasing with cycles. This can be associated with the residual stress effect. At the outer face, tensile stresses are produced at first. Starting from the transition cycle, compressive stresses can be observed.

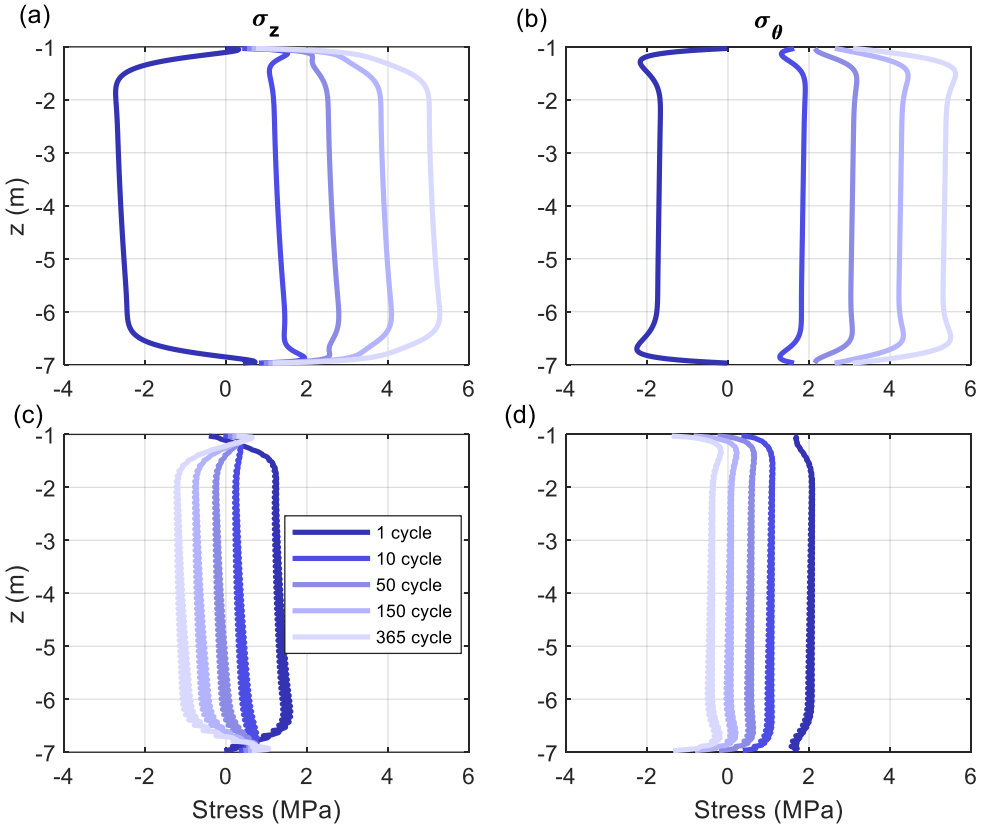

Figure 5.6: Stress distribution along z-direction for various cycles at the (a)-(b) inner and (c)-(d) outer surface for pile design #1.

Figure 5.7 demonstrates soil's stress and displacement profile along longitudinal direction for pile design #1. In this Figure, red dashed line represents the stress under application of structural loads only. It can be noticed that there is not much difference in stress profile between the three different loading cases. Minor increases of lateral and friction stress can be noticed at the bottom of the pile. It keeps increasing with the cycle due to the residual temperature effect. This insignificant increase of stress might be related to the relatively large wall thickness. In addition, temperature changes cause vertical displacement to reduce at the top of the pile from the original position to 1 mm. A similar trend can be observed for other cases of d_{in} and different γ.

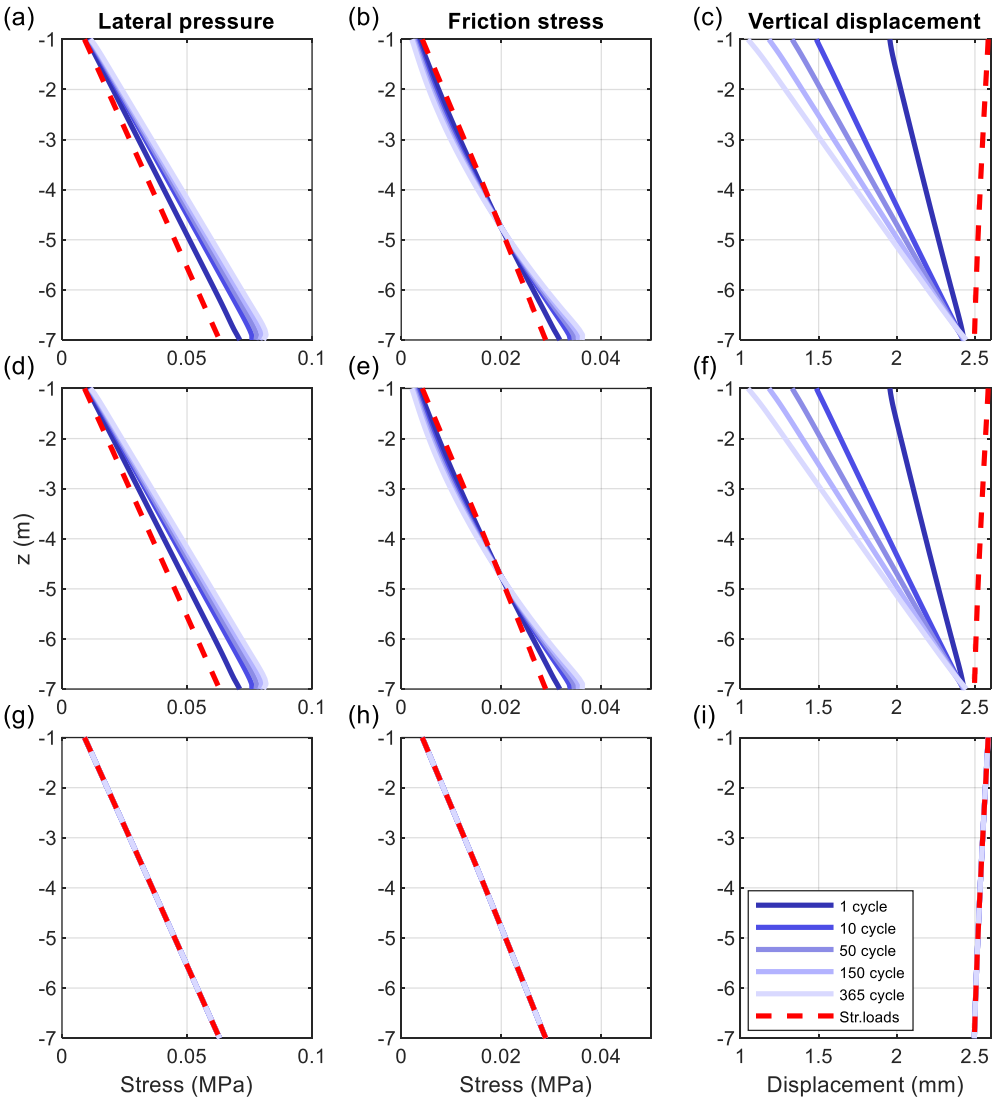

Figure 5.7: Soil stresses and displacement along z-direction for various cycles under (a)-(c) combined loadings; (d)-(f) temperature changes; (g)-(i) internal air pressure for pile design #1.

5.2. Pile design #2

Figure 5.8 shows the stress changing with one cycle at the inner and outer surface of the pile under combined loadings. Radial stresses produce compressive stresses at the inner and outer skin of the pile. At the outer surface, it reaches a negligible value of -0.04 MPa for γ=1% and -0.06 MPa for γ=1.5% under combined loadings. At the inner surface, the combination of two loadings results in approximately -6 MPa of compressive stress at the middle of the cycle for both γ. Furthermore, vertical stress will be discussed. At the inner skin of the pile, it causes compressive stress of around -13 MPa and -16 MPa at the middle of the cycle for γ=1% and γ=1.5%, respectively. While at the outer surface, it produces slight tensile stress of around 1.8

MPa and 2.5 MPa at the middle of the cycle for γ=1% and γ=1.5%, respectively. Tensile stresses come from circumferential stresses at the outer skin of the pile. The combination of temperature changes and internal air pressure leads to around 3.3 MPa of tensile stresses at the middle of the cycle for γ=1%. For γ=1.5%, circumferential tensile stresses reach about 4.2 MPa at the same location. Whereas at the inner side, the minimum compressive stress is around -8 MPa for γ=1% and -10 MPa γ=1.5% at the beginning of the cycle.

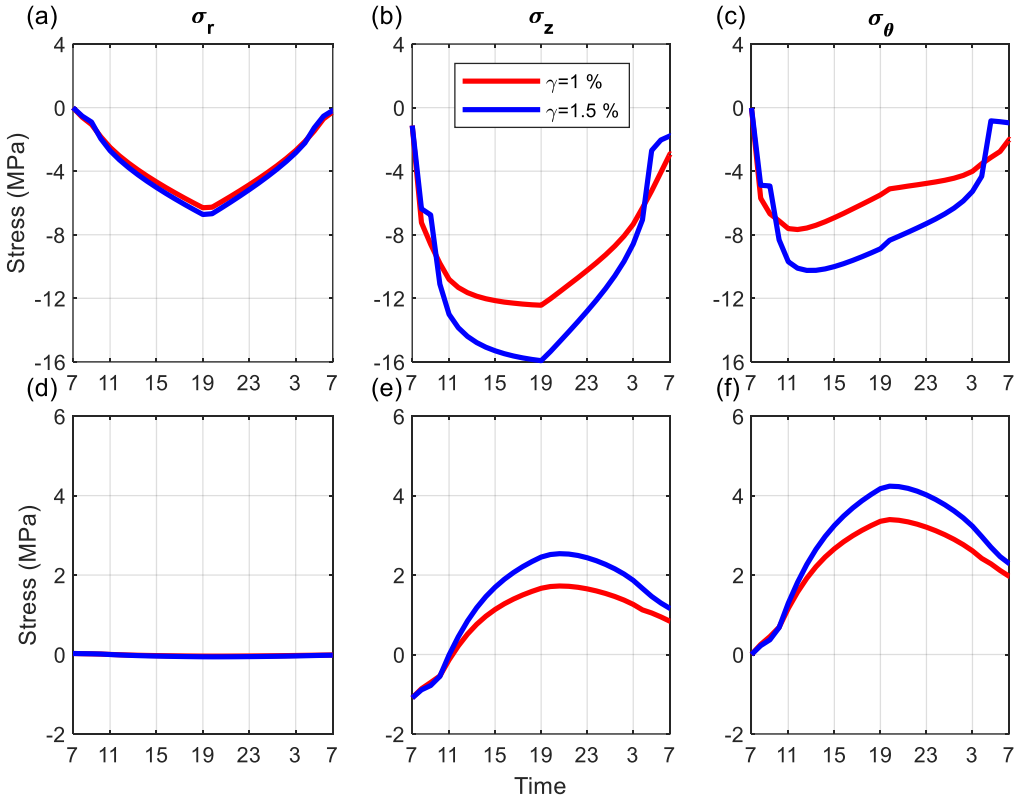

Figure 5.8: Stress varying with 24-hour time at the (a)-(c) inner and (d)-(f) outer surface for the pile design #2.

Stress distribution along the radial direction under combined loadings at the middle and end of the cycle is presented in Figure 5.9 below for pile design #2. At the end of the cycle, radial stresses generate compression with the lowest of -1.2 MPa at the inner surface of the pile. Vertical and circumferential stresses generate compression gradually transiting to tension closer to the outer skin of the pile. The same can be applied for the vertical stress at the middle of the cycle. Radial stresses at the middle of the cycle produce compressive stresses under combined loadings. Circumferential stresses at the middle of the cycle start with -4 MPa of compressive stresses at the inner side slowly transiting to around 4 MPa of tensile stresses closer to the outer side.

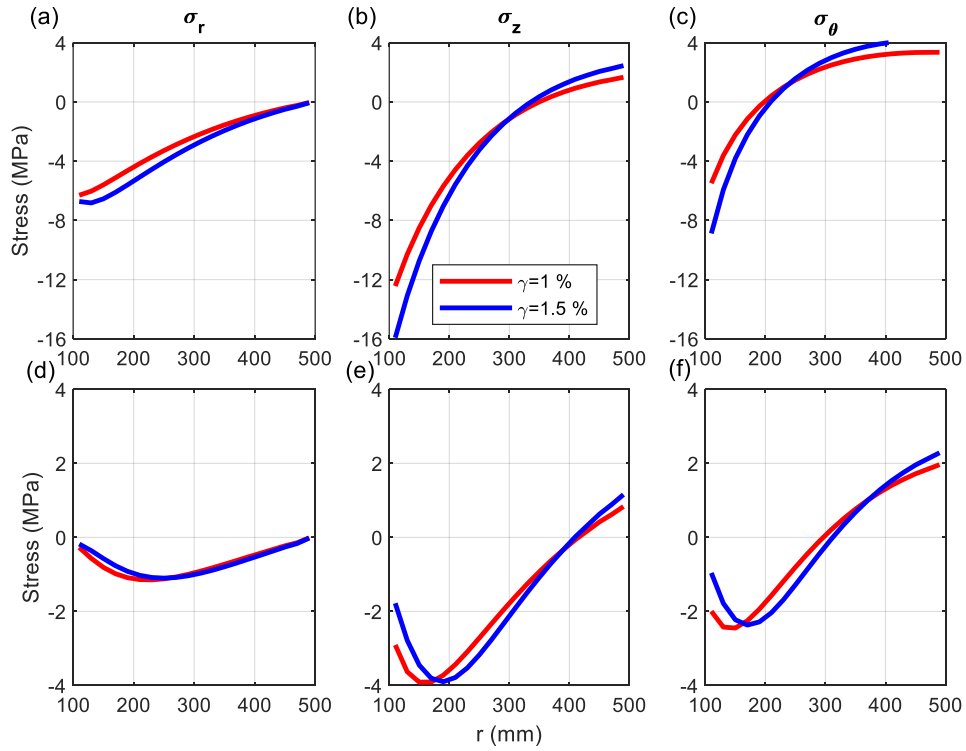

Figure 5.9: Stress distribution along r-direction at the (a)-(c) middle and (d)-(f) end of the cycle for the pile design #2.

Figure 5.10 shows the stress profile along z-direction at different locations under combined effect for pile design #2. At the inner side of the pile, circumferential stresses produce compressive stresses of around -6 MPa at the top and bottom of the pile for γ=1% and about -10 MPa for γ=1.5%. At the outer surface of the pile, for γ=1% vertical and circumferential stresses induce approximately 2 and 3.5 MPa of tensile stresses, respectively. Whereas for γ=1.5%, vertical stresses reach 3.5 MPa and circumferential stresses are 4.5 MPa.

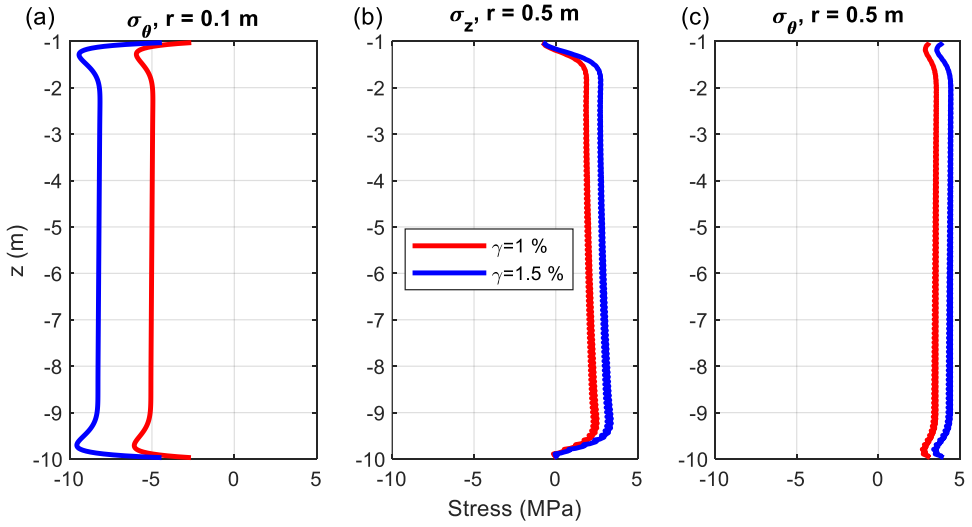

Figure 5.10: Stress distribution along z-direction for the pile design #2: (a) circumferential stress at inner skin; (b) vertical stress and (c) circumferential stress at outer skin.

Stress changing with time for the first 10 cycles at the inner and outer surface of the pile for pile design #2 is illustrated in this Figure 5.11. For all three stresses at the inner skin of the pile and radial stress at the outer side of the pile, stresses increase with time. This can be associated with the residual stress effect left from the previous cycles. While vertical and circumferential stresses at the outer side of the pile decrease as time goes by. This can be related to the lowering effect of temperature and stress at further distances.

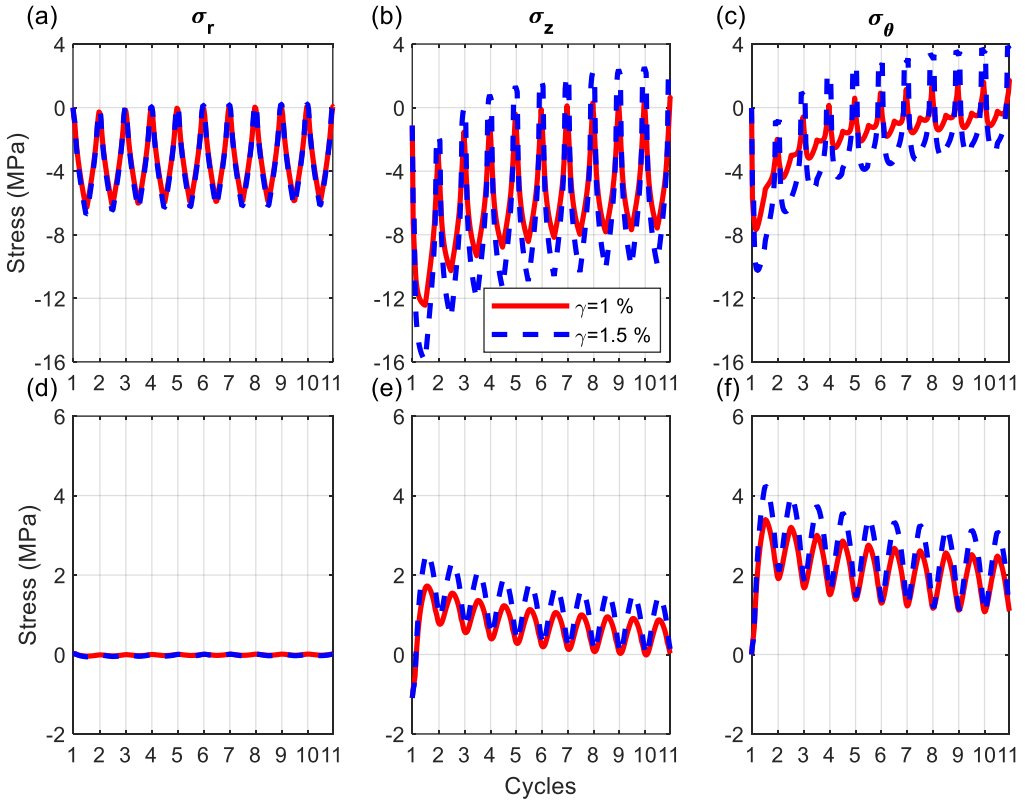

Figure 5.11: Stress varying with 10 cycles for (a)-(c) inner and (d)-(f) outer surface for the pile design #2.

Stress distribution along the radial direction at the middle and end of the different cycles for pile design #2 is shown in Figure 5.12. Radial stresses at the middle of all cycles presented generate compressive stresses. It shows a slight increase with the cycle. However, at the end of the cycles, it generates compressive stresses at the 1st cycle only. Starting from the 13th cycle, it induces tension. Tensile stresses keep increasing with the cycle at the inner surface of the pile and go down closer to the outer surface. Vertical stresses induce compressive stresses at the middle of the cycle. Small tensile stresses can be observed at the outer surface of the pile. At the end of the 1st cycle, this tendency is followed. However, starting from the 13th cycle tensile stresses at the inner surface of the pile can be noticed. They keep increasing with the cycle due to the residual stress effect. The same description can be applied to circumferential stresses at

the end of the cycle as well. Vertical and circumferential stresses reach a maximum of 4 and 6 MPa of tensile stresses at the end of the 365th cycle, respectively. Circumferential stresses at the middle of the 1st cycle start from compression. Getting further from the pile, it gradually increases to tension. After reaching the transition cycle, pure tension stresses are generated. In this case, it is the 13th cycle for γ=1% and the 26th cycle for γ=1.5%. At the inner side of the pile, higher tensile stresses correspond to a greater cycle. However, it works the other way round at the outer surface.

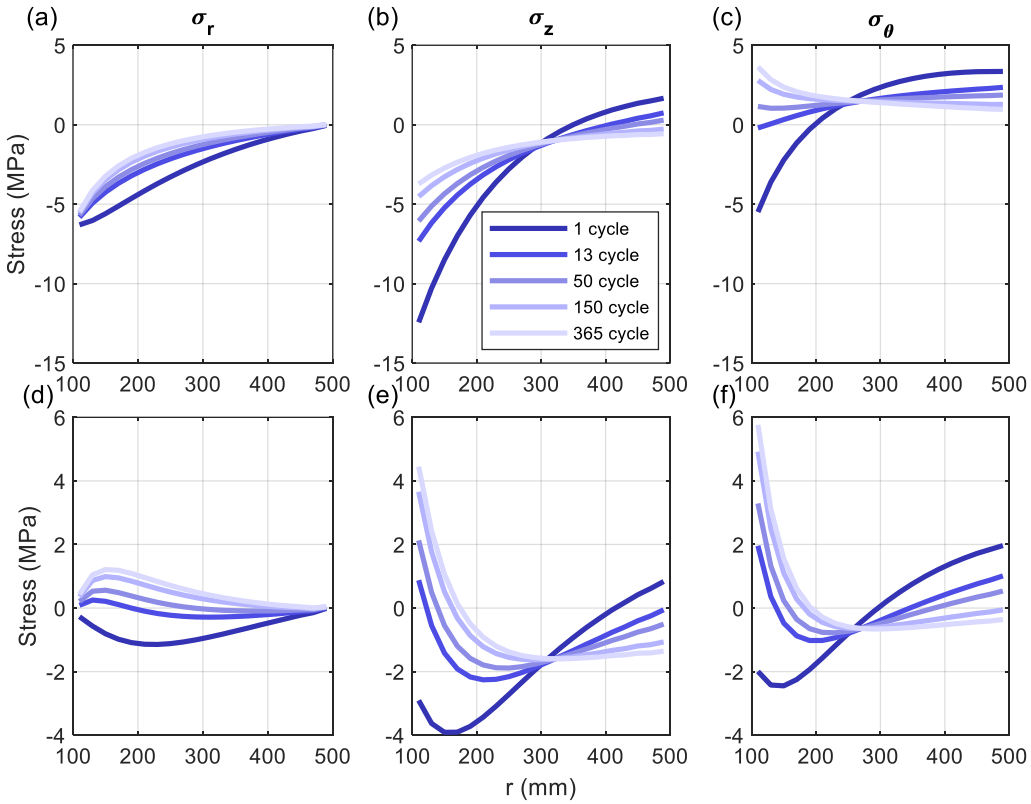

Figure 5.12: Stress distribution along r-direction at the (a)-(c) middle and (d)-(f) end of the different cycles for the pile design #2.

Figure 5.13 represents the stress profile along the longitudinal direction at the inner and outer face of the pile for various cycles for pile design #2. At the inner skin, compressive stresses are generated at the 1st cycle. Then, it is followed by tensile stresses increasing with cycles. It reaches around 6 MPa of tensile stresses for both. This might be due to the residual stress effect. At the outer surface, tensile stresses are produced at the 1st cycle. Starting from the transition cycle, compressive stresses can be noticed.

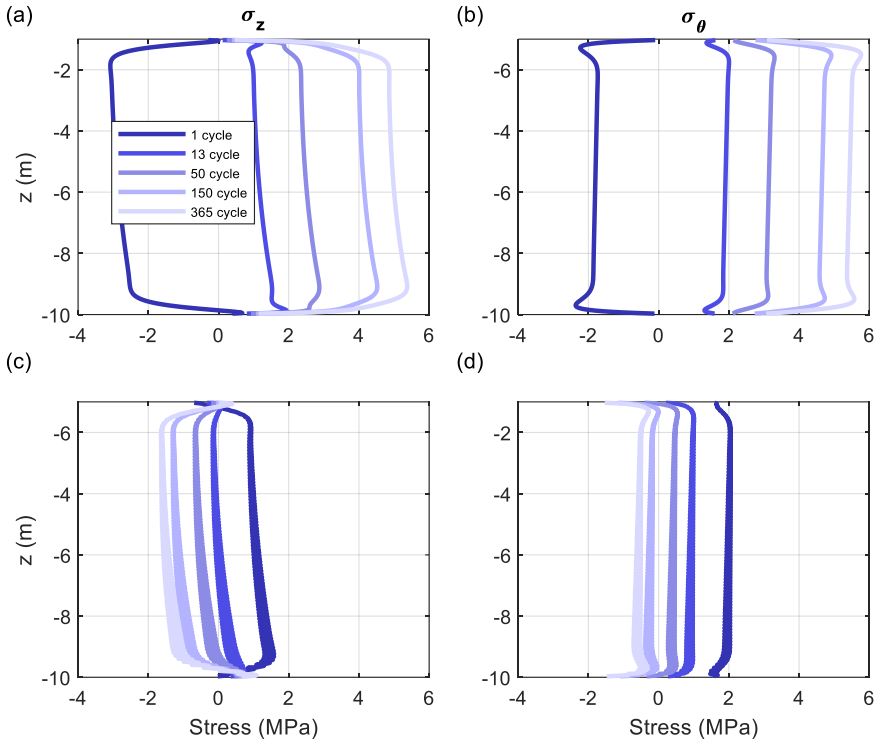

Figure 5.13: Stress distribution along z-direction for various cycles at the (a)-(b) inner and (c)-(d) outer surface for pile design #2.

Figure 5.14 demonstrates soil's stress and displacement profile along longitudinal direction under combined loadings for pile design #2. Minor increase of lateral and friction stress can be noticed at the bottom of the pile in comparison to the original distribution. It keeps increasing with the cycle due to the residual temperature effect. Additionally, vertical displacement is reduced at the top of the pile from the original location to around 0.5 mm by the 365th cycle. At the bottom of the pile, a small increase can be noticed as well.

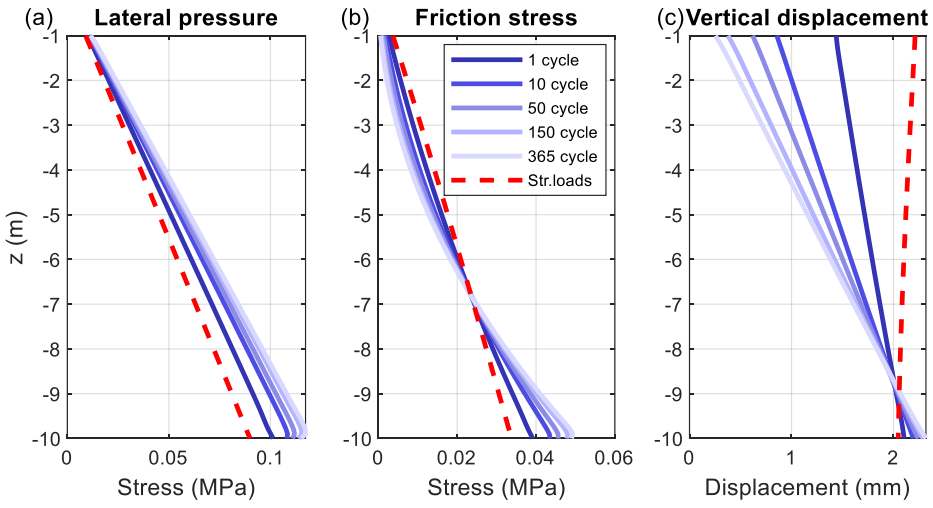

Figure 5.14: Soil stresses and displacement along z-direction for various cycles under (a)-(c) combined loadings for pile design #2.

5.3. Pile design #3

Figure 5.15 shows the stress changing with one cycle at the inner and outer surface of the pile under combined loadings for pile design #3. Similar to the previous cases, radial stresses produce compressive stresses at both locations of the pile. At the outer surface, it reaches a negligible value of -0.05-0.1 MPa. At the inner surface, combined loadings lead to around -6 MPa of compressive stress at the middle of the cycle for both γ. Vertical stress at the inner surface causes compressive stress of around -13 MPa for γ=1% and -16 MPa for γ=1.5% at the middle of the cycle. While at the outer surface, it produces slight tensile stress of around 1.6 MPa and 2.2 MPa for γ=1% and γ=1.5%, respectively. At the outer skin of the pile, circumferential stresses under the combined effect of temperature changes and internal air pressure result in 3.3 MPa and 4.1 MPa of tensile stresses at the middle of the cycle for γ=1% and γ=1.5%, respectively. Whereas at the inner side, the minimum compressive stress is around -8 MPa at the beginning of the cycle for γ=1%. For γ=1.5% this value reached around -10 MPa at the same point. A similar tendency is observed in the case of another d_{in}.

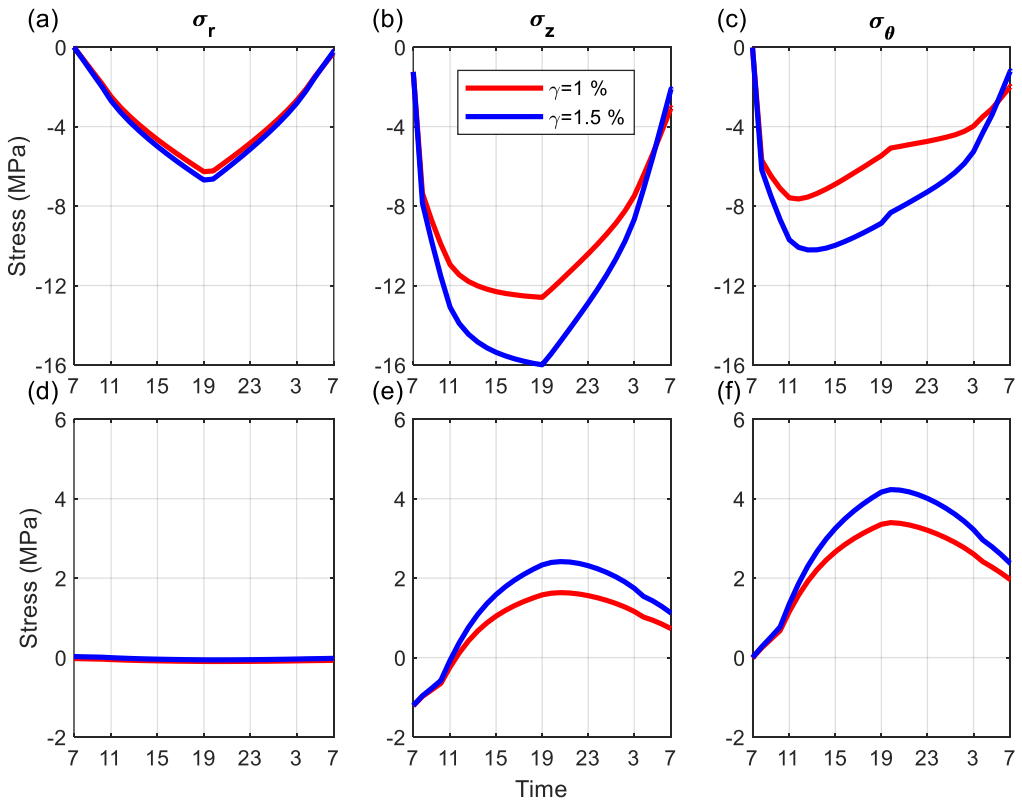

Figure 5.15: Stress varying with 24-hour time at the (a)-(c) inner and (d)-(f) outer surface for the pile design #3.

Figure 5.16 illustrates stress distribution along radial direction under combined loadings at the middle and end of the cycle for pile design #3. At the end of the cycle, radial stresses generate compression with the lowest of -1.2 MPa at the inner surface of the pile. Vertical and circumferential stresses induce compressive stresses steadily transiting to tension closer to the outer skin of the pile. The same trend is followed by the vertical stress at the middle of the cycle. An exception is a pile with d_{in}=400 mm, where tension can be observed at the inner surface of the pile as well. Radial stresses at the middle of the cycle produce compressive stresses under combined loadings. It starts with -6 MPa at the inner surface and reaches 0 MPa at the outer side. Circumferential stresses at the middle of the cycle start with -4 MPa of compressive stresses for γ=1% and -8 MPa for γ=1.5% at the inner side. It gradually transits to about 4 MPa of tensile stresses closer to the outer side for all cases.

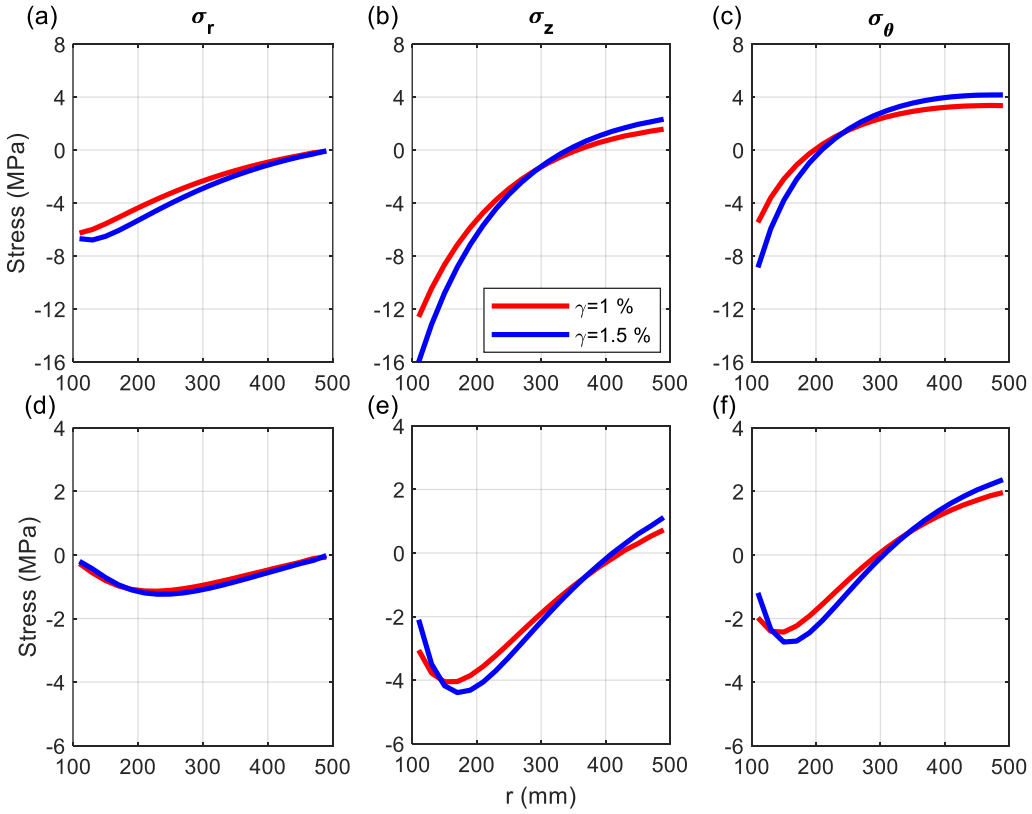

Figure 5.16: Stress distribution along r-direction at the (a)-(c) middle and (d)-(f) end of the cycle for the pile design #3.

Figure 5.17 illustrates the stress profile along the length of the pile at different locations under combined effect for pile design #3. At the inner side of the pile, circumferential stresses produce compressive stresses of around -6 MPa and -10 MPa for γ=1% and γ=1.5%, respectively. At the outer surface of the pile, vertical and circumferential stresses induce approximately 3 and 3.5 MPa of tensile stresses for γ=1%, respectively. These values are

slightly higher for γ=1.5%. A similar pattern of stress distribution can be noticed in the piles with another d_{in}.

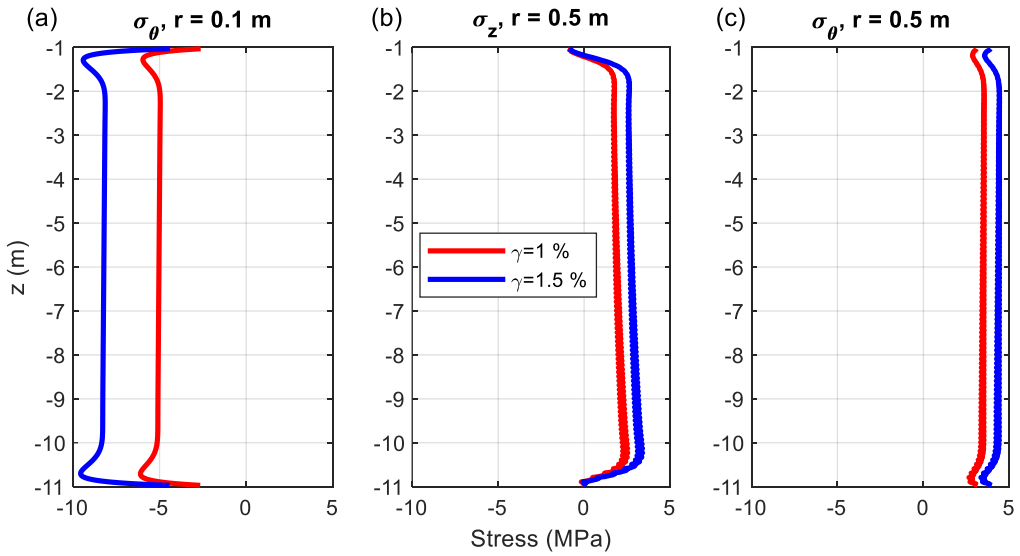

Figure 5.17: Stress distribution along z-direction for the pile design #3: (a) circumferential stress at inner skin; (b) vertical stress and (c) circumferential stress at outer skin.

Stress changing with time for the first 10 cycles at the inner and outer surface of the pile for pile design #3 is illustrated in this Figure 5.18. It follows a similar pattern discussed in the prior sections.

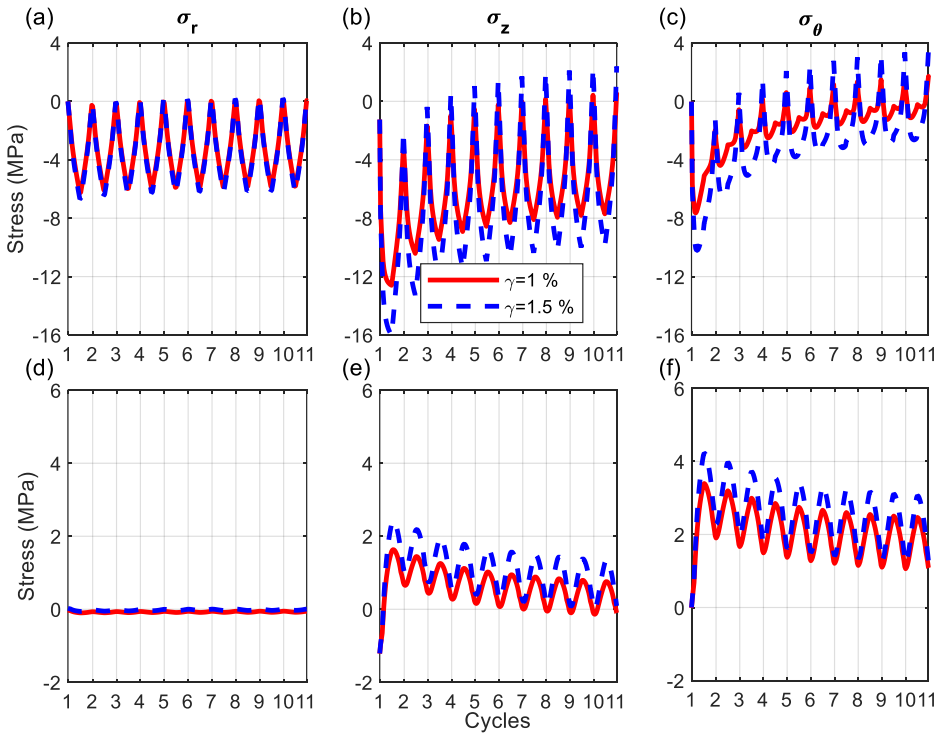

Figure 5.18: Stress varying with 10 cycles for (a)-(c) inner and (d)-(f) outer surface for the pile design #3.

Stress distribution along the r-direction at the middle and end of the different cycles for pile design #3 is shown in Figure 5.18. Radial stresses at the middle of all cycles induce compression. It shows an insignificant increase with the cycle. However, at the end of the cycles it generates compressive stresses at the 1st cycle only. Starting from the 13th cycle, it creates tensile stresses. Tensile stresses keep increasing with the cycle at the inner surface of the pile and reduce closer to the outer surface. Vertical stresses generate compression at the middle of the cycle. Small tensile stresses can be observed at the outer surface of the pile. At the end of the 1st cycle, this tendency is followed. However, starting from the 13th cycle tensile stresses at the inner surface of the pile can be noticed. They keep increasing with the cycle due to the residual stress effect. The same description can be applied to circumferential stresses at the end of the cycle as well. Vertical and circumferential stresses reach a maximum of around 4 and 5 MPa of tensile stresses at the end of the 365th cycle, correspondingly. Circumferential stresses at the middle of the 1st cycle start from compression. It gradually increases to tension. After reaching the transition cycle, pure tension stresses are generated. Transition cycles for γ=1% and γ=1.5% are the 13th and the 27th cycles, respectively. For d_{in}=300 mm, they are the 10th for γ=1% and the 20th cycle for γ=1.5%. For piles with d_{in}=400 mm, the transition cycle appeared to be the 5th cycle regardless of γ.

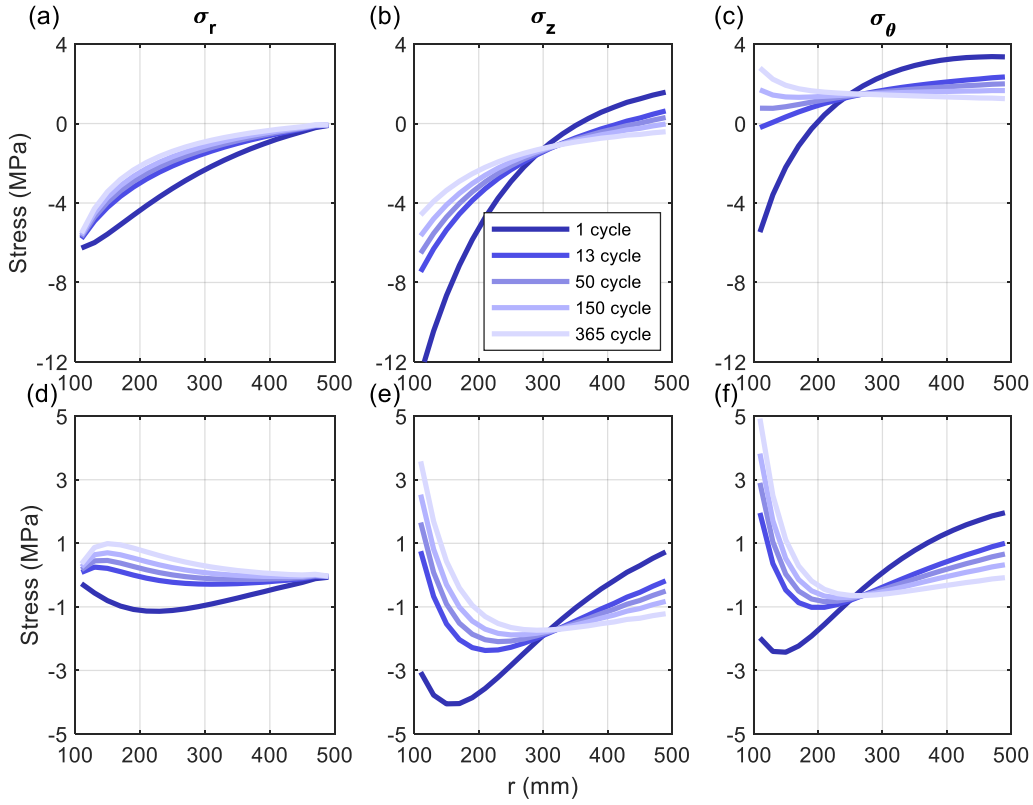

Figure 5.19: Stress distribution along r-direction at the (a)-(c) middle and (d)-(f) end of the different cycles for the pile design #3.

Figure 5.20 represents the stress profile along the z-direction at the inner and outer face of the pile for various cycles for pile design #3. At the inner side of the pile, compressive stresses are generated at the 1st cycle. Then, it is followed by tensile stresses increasing with cycles. This might be due to the residual stress effect. It reaches around 5 MPa of tensile stresses for both. At the outer skin, tensile stresses are generated at the 1st cycle. Starting from the 13th cycle, compressive stresses can be noticed.

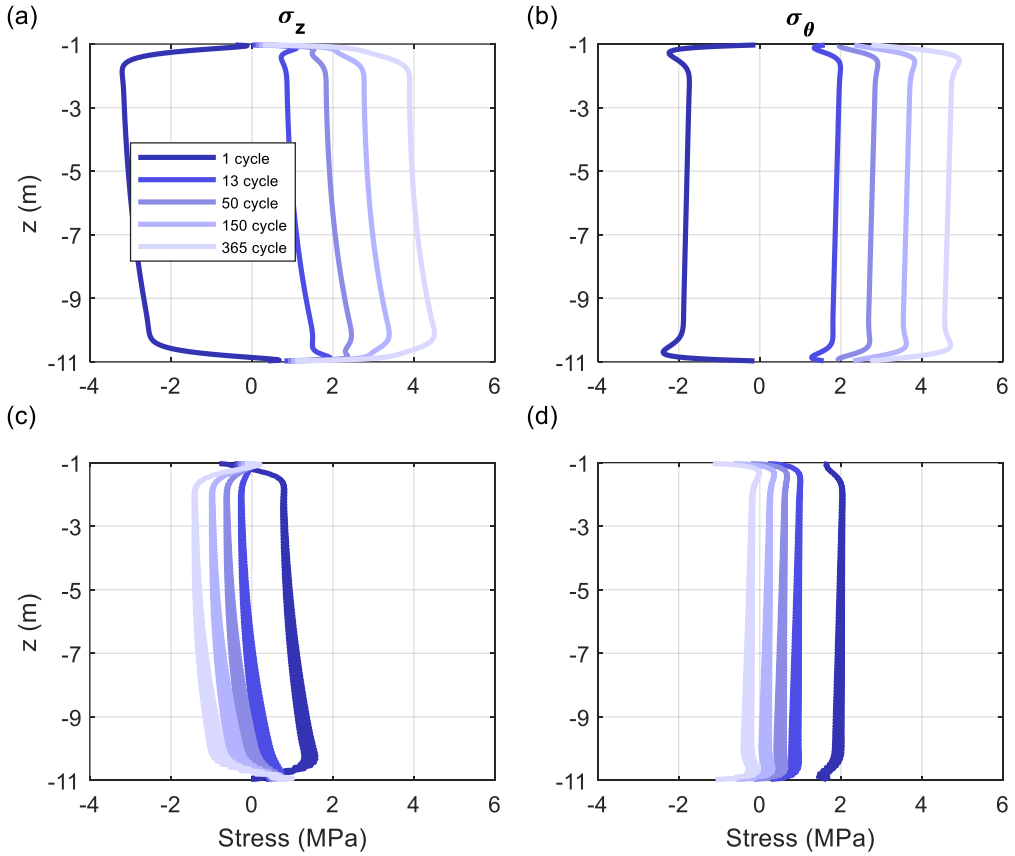

Figure 5.20: Stress distribution along z-direction for various cycles at the (a)-(b) inner and (c)-(d) outer surface for pile design #3.

Figure 5.21 demonstrates soil's stress and displacement profile along z-direction under combined loadings for pile design #3. A slight increase in lateral and friction stress can be noticed at the bottom of the pile in comparison to the original distribution. It keeps increasing with the cycle due to the residual temperature effect. This minor increase might be associated with the comparatively large wall thickness. Moreover, vertical displacement is reduced at the top of the pile from the original location to around 0.2 mm by the 365th cycle. At the bottom of the pile, a small increase can be observed as well. Other cases studied in this thesis follow a similar tendencies as well.

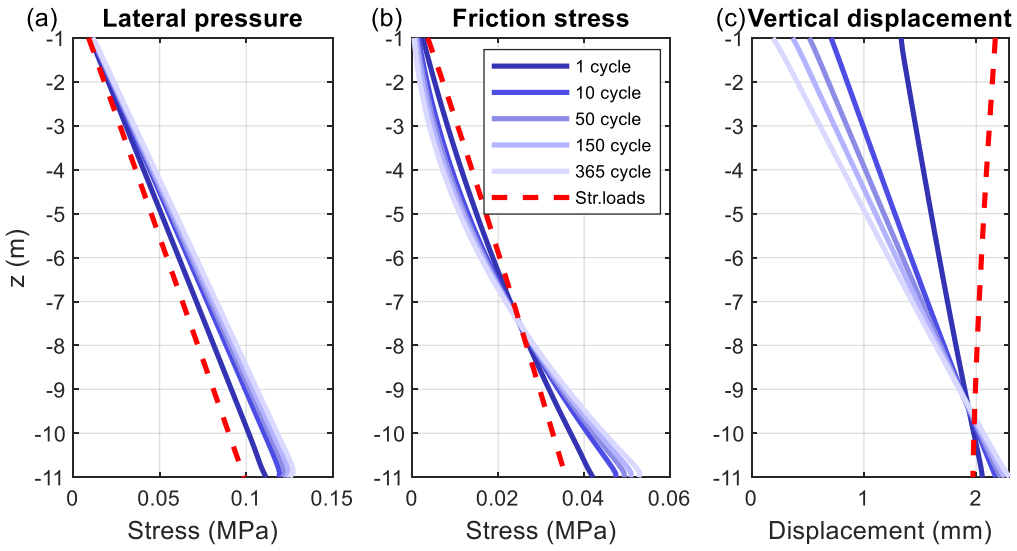

Figure 5.21: Soil stresses and displacement along z-direction for various cycles under (a)-(c) combined loadings for pile design #3.

5.4. Pile design #4

The stresses changing with one cycle at the inner and outer surface of the pile under combined loadings for pile design #4 are presented in Figure 5.22. Similar to the previous cases, radial stresses produce compressive stresses at both locations of the pile. At the outer surface, it reaches a negligible value of -0.04 MPa for γ=1% and -0.15 MPa for γ=1.5%. At the inner surface, combined loadings lead to compressive stress slightly lower than -6 MPa at the middle of the cycle. Vertical stress at the inner surface causes compressive stress of around -12 MPa and -16 MPa at the middle of the cycle for γ=1% and γ=1.5%, respectively. While at the outer surface, it produces slight tensile stress of 2-3 MPa. At the outer surface of the pile, circumferential stresses under the combined effect of temperature changes and internal air pressure result in 3.3-4.1 MPa of tensile stresses at the middle of the cycle. Whereas at the inner side, the minimum compressive stress is around -8 MPa at the beginning of the cycle and about -4 MPa at the middle of the cycle for γ=1%. For γ=1.5%, the minimum compressive stress is around -10 MPa at the beginning of the cycle and about -8 MPa at the middle of the cycle. As it was mentioned earlier, results for piles with different d_{in} can be found in Appendix A. They follow a similar pattern as discussed here.

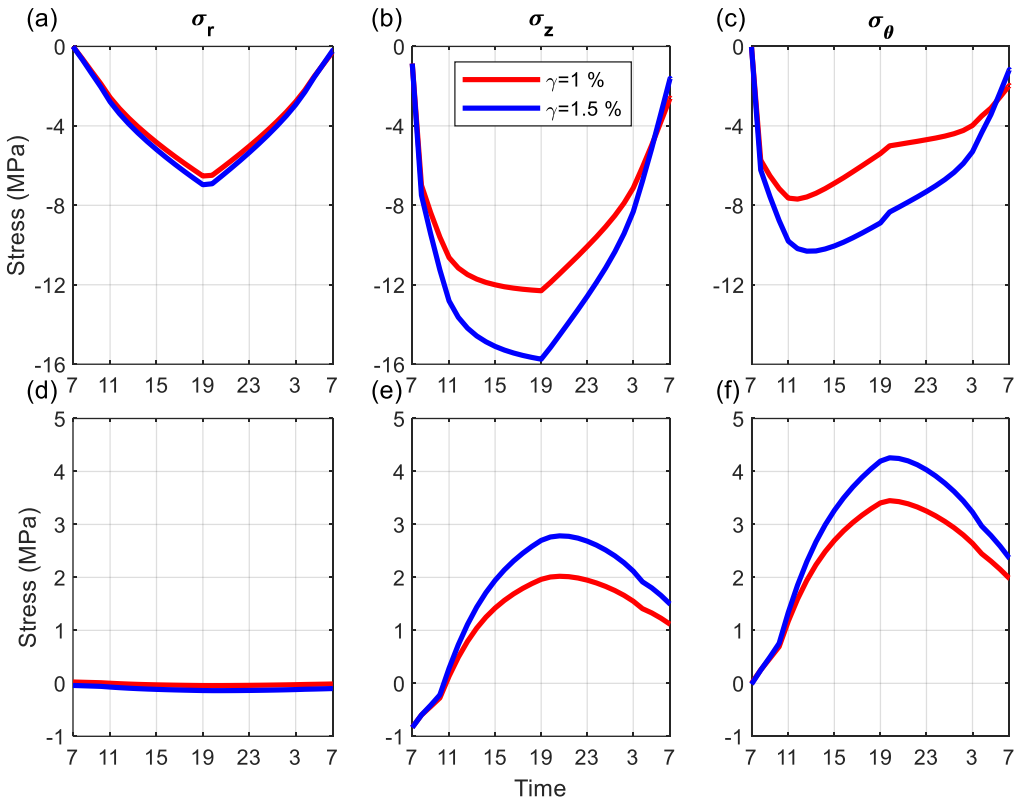

Figure 5.22: Stress varying with 24-hour time at the (a)-(c) inner and (d)-(f) outer surface for the pile design #4.

Figure 5.23 represents stress distribution along r-direction under combined loadings at the middle and end of the cycle for pile design #4. Radial stresses generate compression with the lowest of -1.2 MPa at the inner surface of the pile at the end of the cycle. Other stresses induce compressive stresses slowly transiting to tensile stresses as it moves away from the pile. The same trend is followed by the vertical stress at the middle of the cycle. It reaches about 2 MPa of tensile stress. Radial stresses at the middle of the cycle produce compressive stresses under combined loadings. It starts with -6 MPa at the inner skin and reaches 0 MPa at the outer side. Circumferential stresses at the middle of the cycle start with -4 MPa of compressive stresses at the inner side. It moderately transits to about 4 MPa of tensile stresses at the outer surface of the pile. A similar trend as it was discussed for other pile designs is followed here as well for other cases of γ and d_{in}.

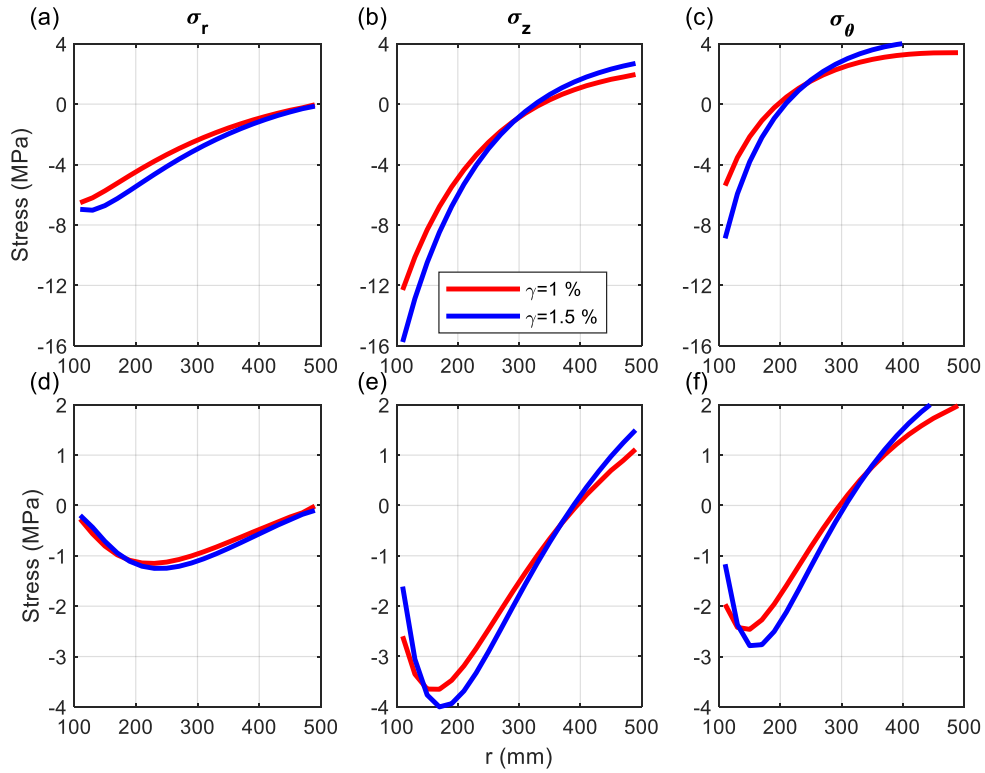

Figure 5.23: Stress distribution along r-direction at the (a)-(c) middle and (d)-(f) end of the cycle for the pile design #4.

Figure 5.24 demonstrates the stress profile along the longitudinal direction at different locations under combined effect for pile design #4. At the inner side of the pile, circumferential stresses produce compressive stresses of around -6 MPa. At the outer skin of the pile, both stresses produce approximately 3 and 3.6 MPa of tensile stresses, respectively. A similar trend as in other pile designs' case is followed here for other cases of γ and d_{in}.

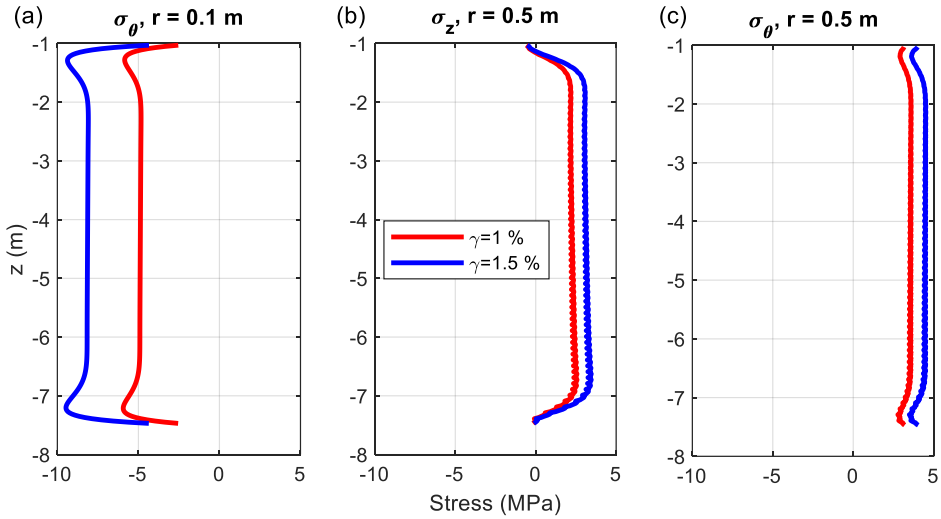

Figure 5.24: Stress distribution along z-direction for the pile design #4: (a) circumferential stress at inner skin; (b) vertical stress and (c) circumferential stress at outer skin.

Stress changing with time for the first 10 cycles at the inner and outer surface of the pile for pile design #4 is illustrated in this Figure 5.25. It follows a similar trend discussed in the previous sections.

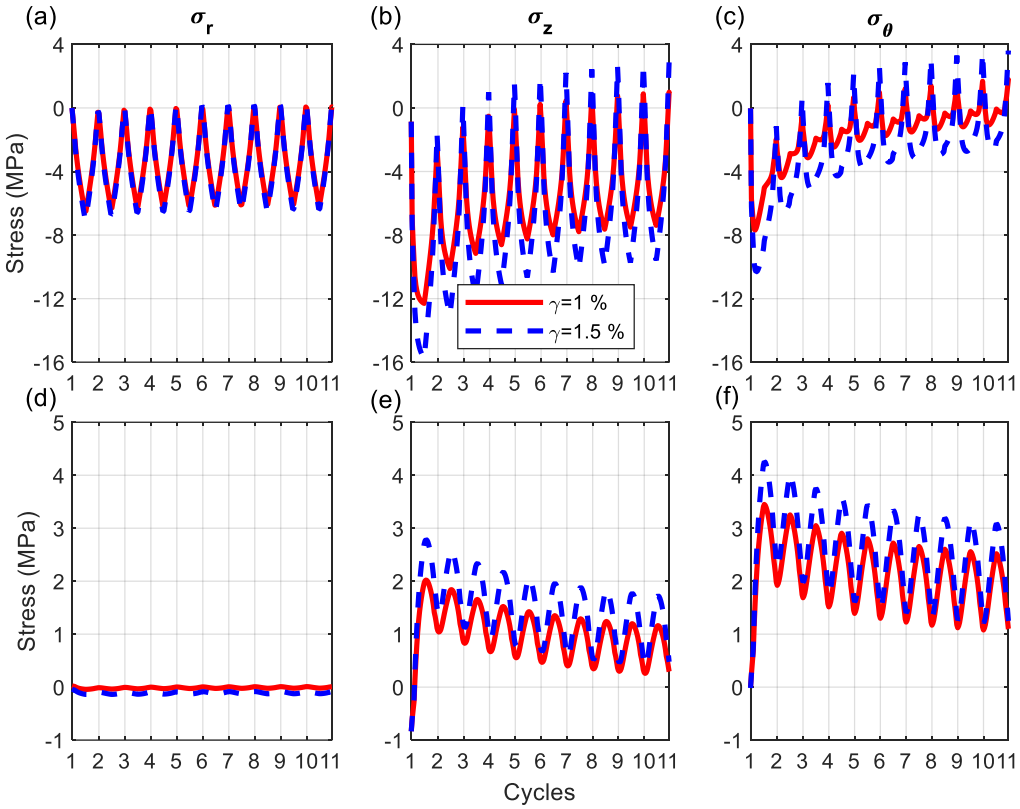

Figure 5.25: Stress varying with 10 cycles for (a)-(c) inner and (d)-(f) outer surface for the pile design #4.

Figure 5.26 demonstrates stress distribution along the radius at the middle and end of the different cycles for pile design #4. Radial stresses at the middle of all cycles induce compression. It shows an insignificant increase with the cycle. However, at the end of the cycles, it generates compressive stresses at the 1st cycle only. Starting from the 11th cycle, it produces tensile stresses. Tensile stresses increase with the cycle at the inner skin of the pile and reduce closer to the outer side. Vertical stresses produce compression at the middle of the cycle. Small tensile stresses can be observed at the outer surface of the pile. At the end of the 1st cycle, this pattern is also followed. However, starting from the 11th cycle tensile stresses at the inner surface of the pile can be observed. Their increase with the cycle can be associated with the residual stress effect. The same description can be applied to circumferential stresses at the end of the cycle as well. Vertical and circumferential stresses reach a maximum of around 4 and 6 MPa of tensile stresses at the end of the 365th cycle, respectively. Circumferential

stresses at the middle of the 1st cycle start from compression. It gradually increases to tension. After reaching the transition cycle (11th cycle), pure tension stresses are produced. For γ=1.5%, transition cycle appears further at the 22nd cycle. A similar tendency can be observed in the case of d_{in}=300 mm. However, for d_{in}=400 mm, the transition to pure tension happens at the 5th cycle regardless of γ.

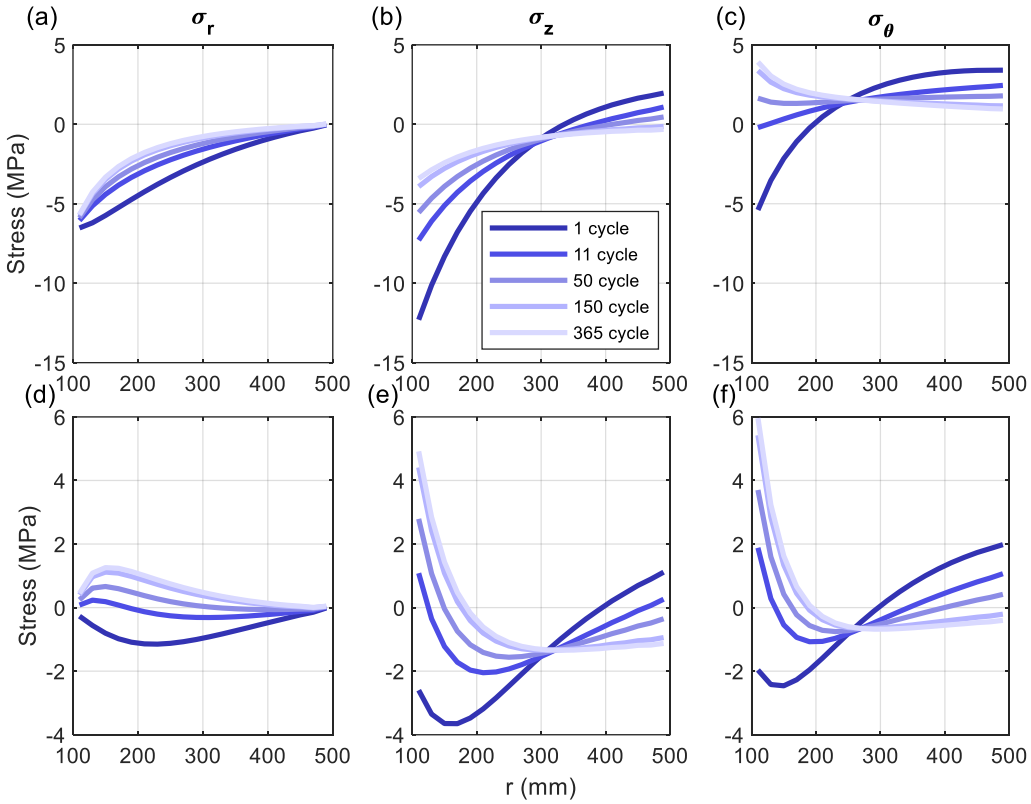

Figure 5.26: Stress distribution along r-direction at the (a)-(c) middle and (d)-(f) end of the different cycles for the pile design #4.

Figure 5.27 demonstrates the stress profile along the z-direction at the inner and outer face of the pile for various cycles for pile design #4. At the inner surface of the pile, compression stresses are generated at the 1st cycle. It is followed by tension stresses increasing with cycles. It reaches around 6 MPa of tensile stresses for both vertical and circumferential stresses. This might be due to the residual stress effect. At the outer skin, tensile stresses are generated at the 1st cycle. Starting from the 11th cycle, compressive stresses can be observed.

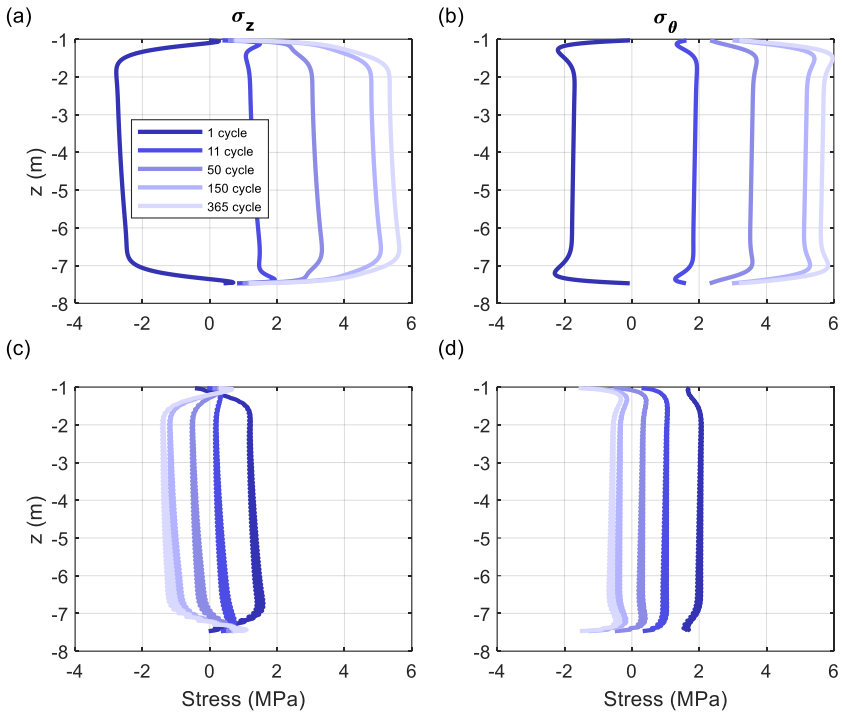

Figure 5.27: Stress distribution along z-direction for various cycles at the (a)-(b) inner and (c)-(d) outer surface for pile design #4.

Figure 5.28 represents soil's stress and displacement profile along z-direction under combined loadings for pile design #4. An insignificant increase of lateral and friction stress can be noticed at the bottom of the pile comparing to the original stress profile. This might be associated with the comparatively large wall thickness. It keeps increasing with the cycle due to the residual temperature effect. Moreover, vertical displacement is reduced at the top of the pile from the original location to around 0.8 mm by the 365th cycle. Piles with other d_{in} follow similar behavior as well.

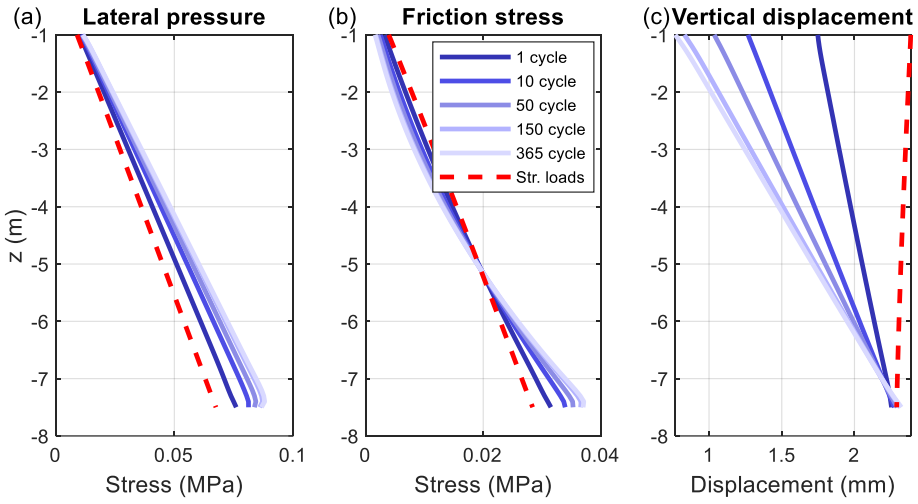

Figure 5.28: Soil stresses and displacement along z-direction for various cycles under (a)-(c) combined loadings for pile design #4.

5.5. Pile design #5

The stresses changing with one cycle at the inner and outer surface of the pile under combined loadings for pile design #5 are presented in Figure 5.29. Similarly, radial stresses demonstrate compressive stresses at both locations of the pile. It reaches a negligible value of -0.04 MPa for γ=1% and -0.15 MPa for γ=1.5% at the outer surface. It is slightly lower than -6 MPa at the middle of the cycle at the inner skin. Vertical stress at the inner surface causes compressive stress of around -12 MPa in the case of γ=1% and -16 MPa in the case of γ=1.5% at the middle of the cycle. At the same point in time, it generates slight tensile stress of 2-3 MPa at the outer surface. At the outer surface of the pile, circumferential stresses under the combined effect of temperature changes and internal air pressure result in 3.2-4.1 MPa of tensile stresses at the middle of the cycle. The minimum compressive stress is around -4 MPa at the inner side for γ=1%. For γ=1.5%, it is around -8 MPa. As it was mentioned earlier, results for piles with different d_{in} can be found in Appendix A. They follow a similar pattern as discussed above.

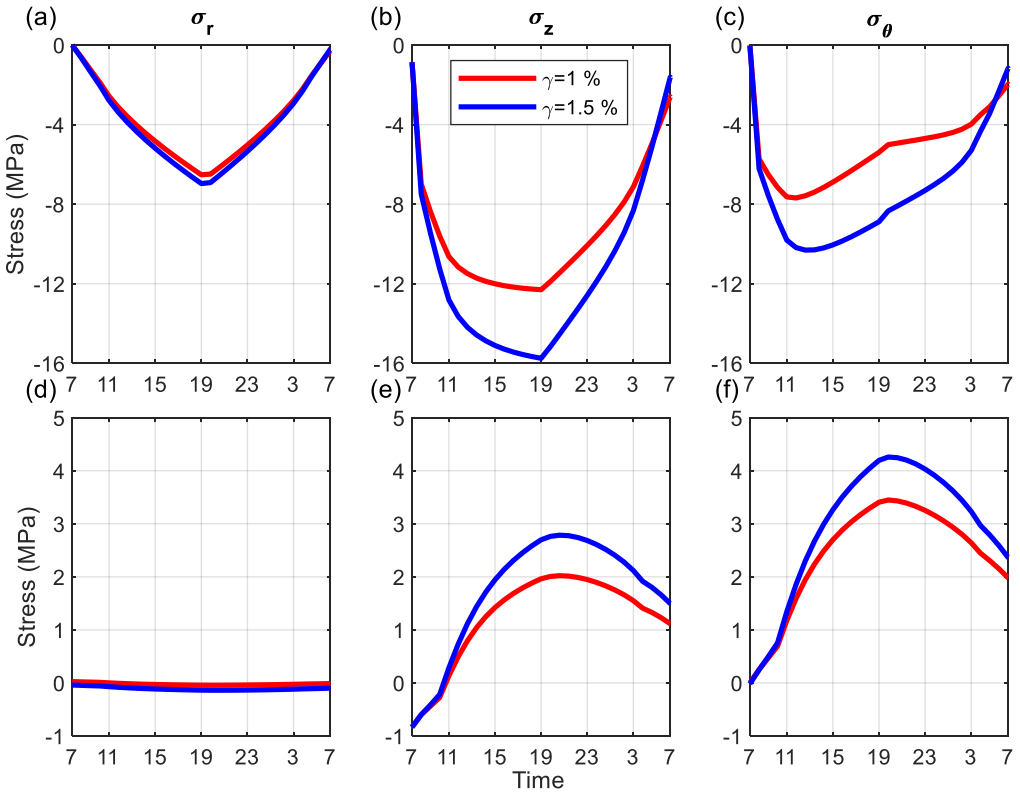

Figure 5.29: Stress varying with 24-hour time at the (a)-(c) inner and (d)-(f) outer surface for the pile design #5.

Figure 5.30 represents stress distribution along radius under the combined effect of temperature changes and internal air pressure at the middle and end of the cycle for pile design

#5. Radial stresses induce compressive stresses at the inner surface of the pile at the end of the cycle. Other stresses produce compressive stresses steadily transiting to tensile stresses as it moves away from the pile. The same trend is followed by the vertical stress at the middle of the cycle. It reaches about 2 MPa of tensile stress. Radial stresses at the middle of the cycle generate compressive stresses of -6 MPa at the inner skin and reach 0 MPa at the outer side. Circumferential stresses at the middle of the cycle start with compressive stresses at the inner side. It slowly transits to tensile stresses at the outer skin of the pile. A similar trend as it was discussed for other pile designs is followed here as well for other cases of γ and d_{in}.

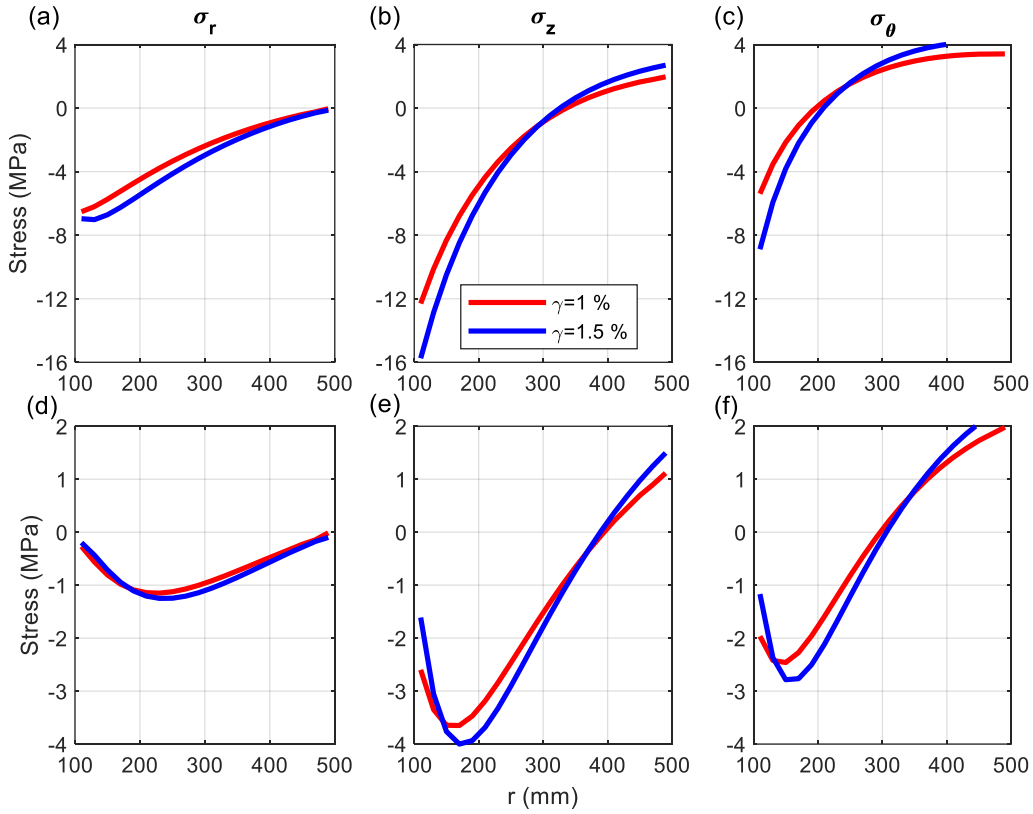

Figure 5.30: Stress distribution along r-direction at the (a)-(c) middle and (d)-(f) end of the cycle for the pile design #5.

The stress profile along the z-direction at different locations under the combined effect for pile design #5 is shown in Figure 5.31 below. At the inner side of the pile, circumferential stresses produce compressive stresses of approximately -6 MPa at the top and bottom parts of the pile. At the outer skin of the pile, both stresses generate approximately 3 and 3.6 MPa of tensile stresses, respectively. Similar patterns as was discussed for other pile designs can be observed for other cases of γ and d_{in}.

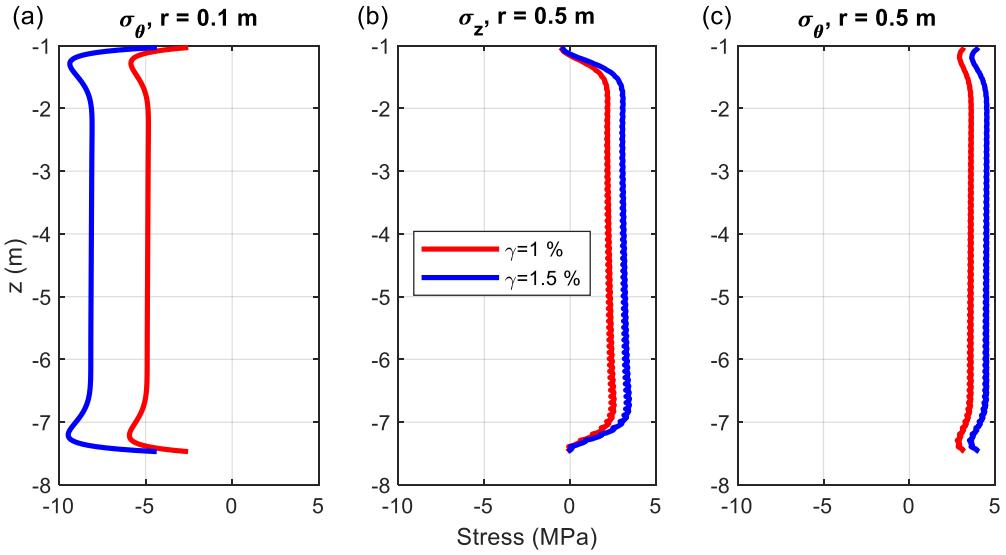

Figure 5.31: Stress distribution along z-direction for the pile design #5: (a) circumferential stress at inner skin; (b) vertical stress and (c) circumferential stress at outer skin.

Figure 5.32 shows the stress changing with time for the first 10 cycles at the inner and outer surface of the pile for pile design #5. A similar trend is followed as it was discussed in the previous cases.

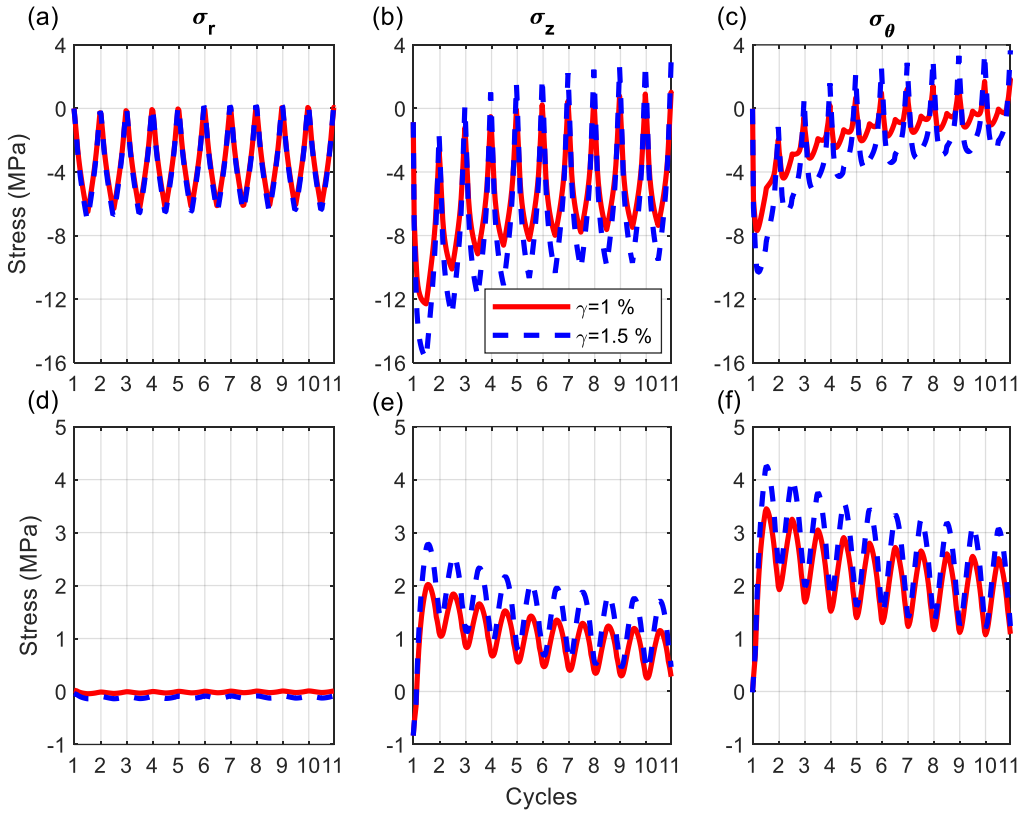

Figure 5.32: Stress varying with 10 cycles for (a)-(c) inner and (d)-(f) outer surface for the pile design #5.

Figure 5.33 illustrates stress distribution along r-direction at the middle and end of the different cycles for pile design #5. Radial stresses at the middle of all cycles generate compression. It shows an inconsiderable increase with the cycle. However, at the end of the cycles, it generates compressive stresses at the 1st cycle only. Starting from the 11th cycle, it produces tensile stresses. Tensile stresses increase with the cycle at the inner surface of the pile and decrease at the outer skin. Vertical stresses produce compression at the middle of the cycle. Small tensile stresses can be observed at the outer surface of the pile. At the end of the 1st cycle, this trend is also followed. However, starting from the 11th cycle tensile stresses can be observed at the inner surface of the pile. Their increase with the cycle can be associated with the residual stress effect. The same description can be applied to circumferential stresses at the end of the cycle as well. Vertical and circumferential stresses reach a maximum of around 4 and 6 MPa of tensile stresses at the end of the 365th cycle, respectively. Circumferential stresses at the middle of the 1st cycle start from compressive stresses and gradually increases to tensile stresses. After reaching the transition cycle (11th cycle), pure tension is induced. For γ=1.5%, pure tension occurs after the 19th cycle. For d_{in}=300 mm, these transition cycles happen at the 10th and the 15th cycle for γ=1% and γ=1.5%, respectively. In the case of piles with d_{in}=400 mm, it complies with previously mentioned patterns.

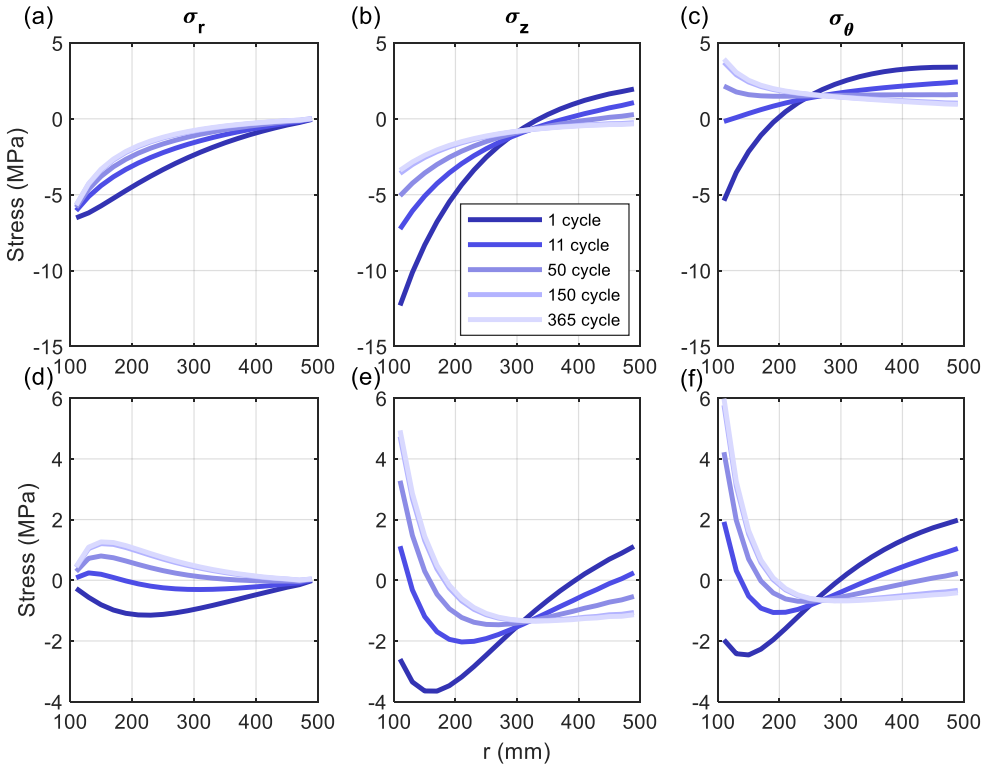

Figure 5.33: Stress distribution along r-direction at the (a)-(c) middle and (d)-(f) end of the different cycles for the pile design #5.

Figure 5.34 shows the stress profile along the longitudinal direction at the inner and outer face of the pile for various cycles for pile design #5. At the inner skin of the pile, compressive stresses are generated at the 1st cycle. It is followed by tension stresses increasing with cycles. This might be associated with the residual stress effect. It reaches around 6 MPa of tensile stresses for both vertical and circumferential stresses. At the outer side, tensile stresses are generated first. Compressive stresses can be observed starting from the transition cycle.

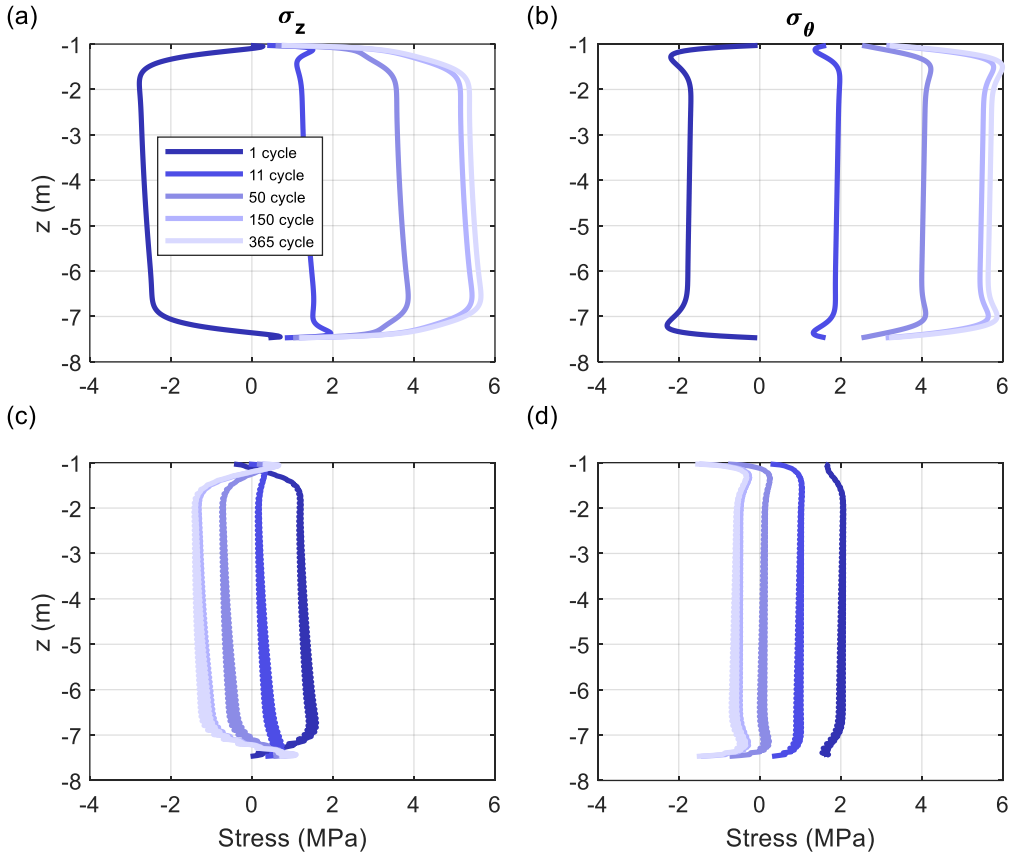

Figure 5.34: Stress distribution along z-direction for various cycles at the (a)-(b) inner and (c)-(d) outer surface for pile design #5.

Figure 5.35 shows soil's stress and displacement profile along z-direction under combined loadings for pile design #5. Minor increase of lateral and friction stress can be observed at the bottom of the pile comparing to the original stress profile. This inconsiderable increase might be associated with the comparatively large wall thickness. It increases with the cycle due to the residual temperature effect. Moreover, vertical displacement is decreased at the top of the pile from the original location to around 0.8 mm by the 365th cycle. Piles with other d_{in} follow similar behavior as well.

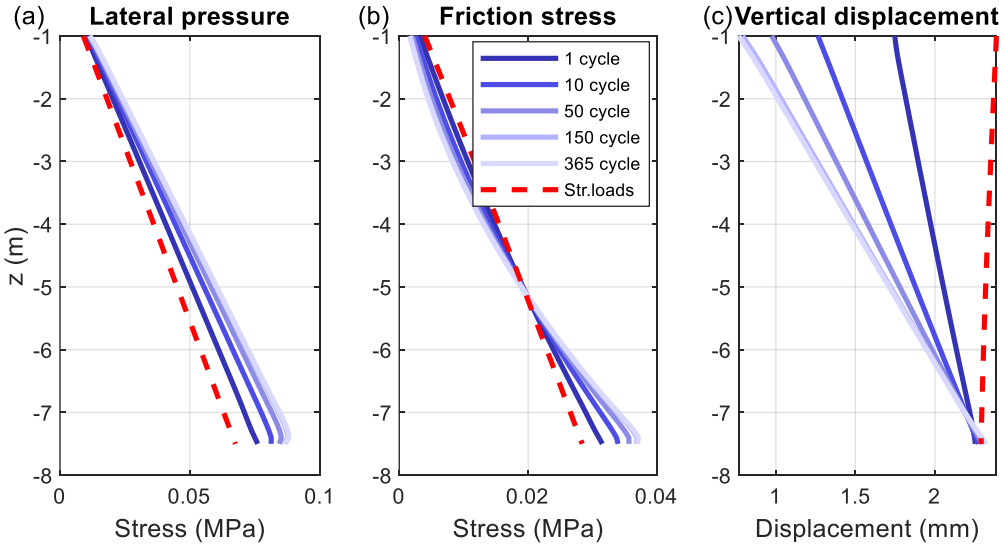

Figure 5.35: Soil stresses and displacement along z-direction for various cycles under (a)-(c) combined loadings for pile design #5.

Chapter 6 – Discussions and Design Recommendations

Once the results of thermal and thermal mechanical analyses are obtained, they can be used to make a judgment and identify key points of the study. Therefore, this section will describe the effect of different study parameters on the results of the study. Based on this information design recommendations will be given. Maximum allowable storage temperature named as design temperature will be tabulated for each case.

6.1. Parametric results

Figure 6.1 shows maximum stresses as well as the yield function changing with cycles for different d_{in}. According to Figure 6.1, radial stress generates low tensile stresses for all three different d_{in}. Pile with 200-mm d_{in} has shown the highest tensile stresses among other cases. However, vertical, and circumferential stresses produce higher tensile stresses and almost reach allowable tensile strength for the 200- and 400-mm energy storage piles. Interestingly, the 300-mm case demonstrates the lowest tensile stresses. As it was mentioned in Chapter 4, input temperature and pressure depend on different d_{in} as well. In this case, it reached a maximum of 33°C and 32°C for the 200- and 400-mm pile, whereas for the 300-mm pile it was slightly lower with 30°C. Thus, this might be the reason why the pile with d_{in}=300 mm has generated the lowest tensile stresses. A similar trend can be observed for the yield function as well.

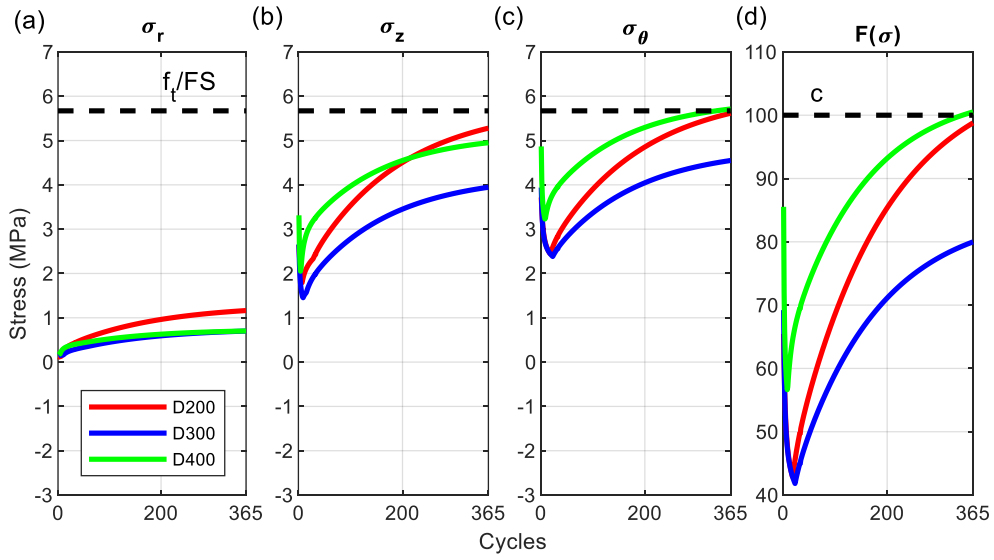

Figure 6.1: (a)-(c) Different maximum stresses and (d) yield function changing with cycles for various d_{in}.

Figure 6.2 demonstrates stress distribution along radial direction for different d_{in} at the middle and end of the 1st cycle. At the middle of the cycle, lower compressive stresses were

generated for the 200-mm pile at the inner surface of the pile. However, the magnitudes of stress became almost equal closer to the outer side regardless of d_{in}. At the end of the cycle, radial stresses also follow a similar trend closer to the outer surface. Whereas vertical and circumferential stresses demonstrate lower tensile stresses at the outer side as the pile gets thinner. Despite this, the difference was negligible with 2 MPa for d_{in}=200 mm and 1.5 MPa for d_{in}=400 mm.

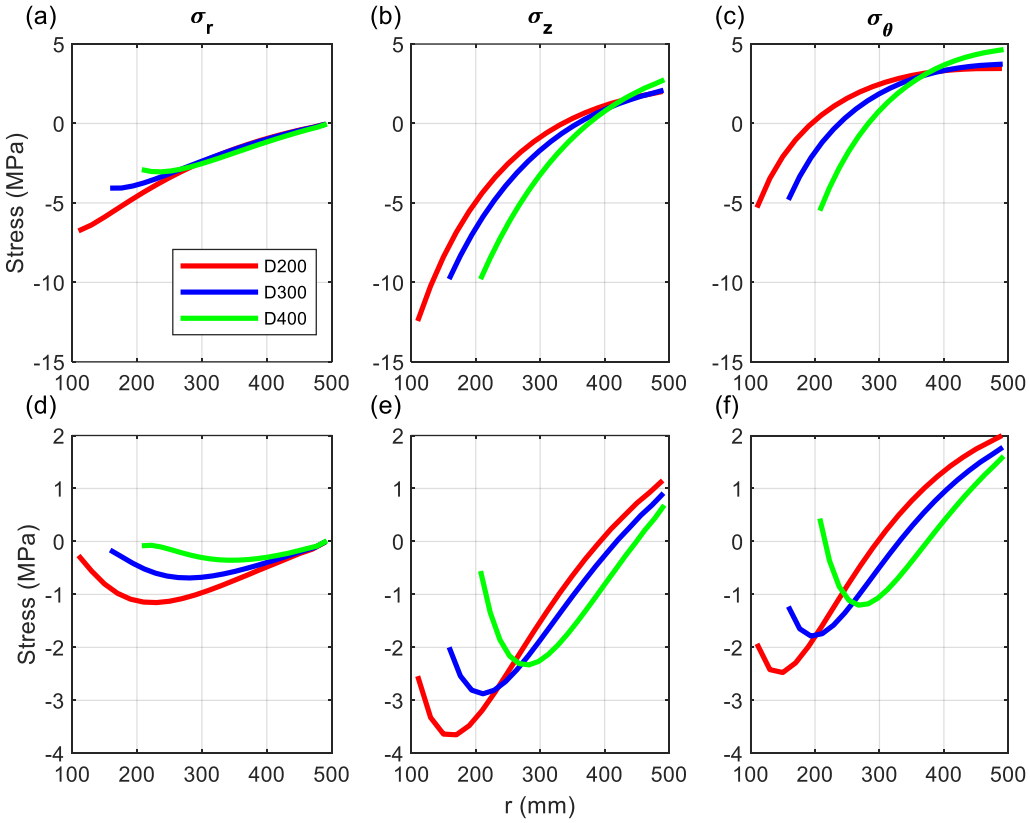

Figure 6.2: Stress distribution along radial direction at the (a)-(c) middle and (d)-(f) end of the 1st cycle for various d_{in}.

Maximum stresses and the yield function changing with cycles for different pile spacing are represented in the following Figure 6.3. As expected, the lower spacing between piles results in higher stresses, because faster heat transfer can be observed between adjacent piles with smaller pile spacing. This heat transfer happens due to thermal conduction between soil and pile.

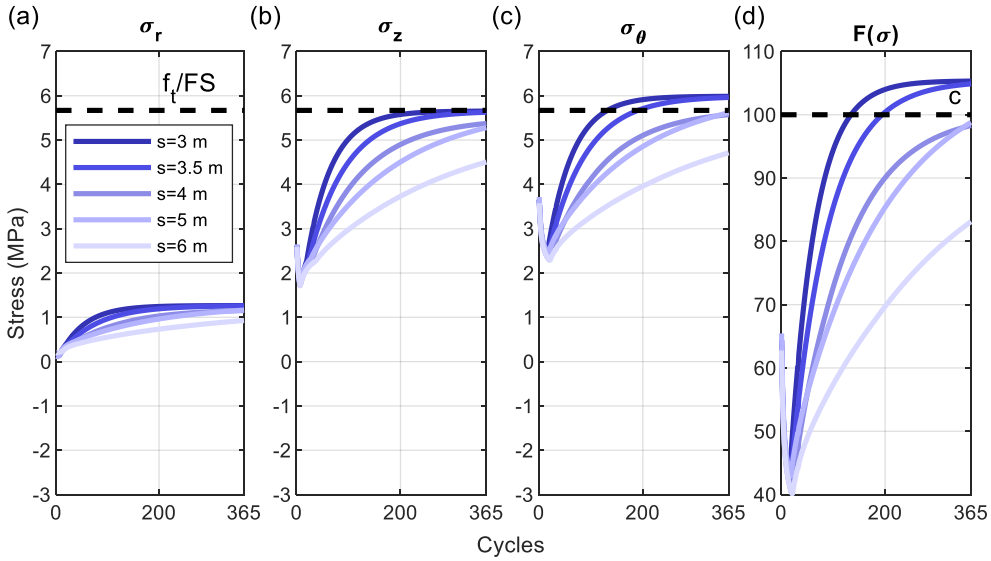

Figure 6.3: (a)-(c) Different maximum stresses and (d) yield function changing with cycles for various pile spacings.

Figure 6.4 illustrates the effect of different thermal expansion coefficients. In the case of radial stresses, the lowest coefficient results in higher stresses with a small deviation from other coefficients. Whereas for vertical stresses, a higher coefficient results in higher tensile stresses. Also, it should be noticed that a similar trend is not followed for circumferential stresses. The highest coefficient of 15×10^{-6}/°C generates the highest tensile stresses. However, the lowest tensile stresses are produced in the case of 12×10^{-6}/°C of thermal expansion coefficient. The lowest coefficient generated slightly higher tensile stresses in this case. A similar trend for circumferential stress is followed for yield function. The reason for this might be material compatibility between concrete and steel caps applied at the top and bottom of the pile. These steel caps also have the coefficient of thermal expansion of 12×10^{-6}/°C. Thus, it produces lower stresses when the same thermal expansion coefficient of concrete is used.

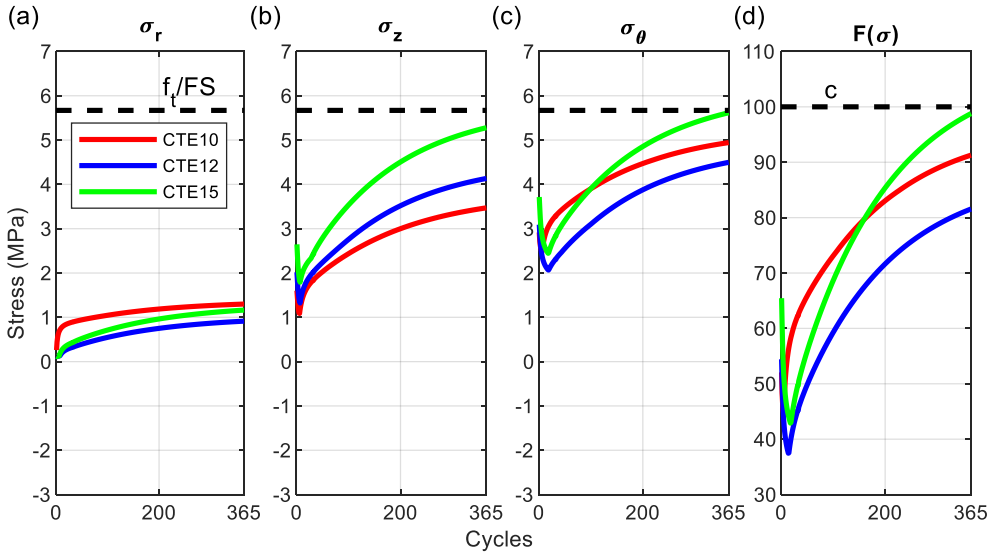

Figure 6.4: (a)-(c) Different maximum stresses and (d) yield function changing with cycles for various coefficients of thermal expansion.

Figure 6.5 demonstrates the effect of storage temperature and coefficient of thermal expansion on transition cycles (*N*). As it can be seen from Figure 6.5a, higher input temperature leads to slower transition. More time is needed to shift from the compression-tension zone to pure tension because of higher compressive stresses generated due to higher temperature changes. Figure 6.5b illustrates that a lower coefficient of thermal expansion results in faster transition to the pure tension zone. Thus, usage of concrete with a higher coefficient of thermal expansion will provide a slower transition to the pure transition zone.

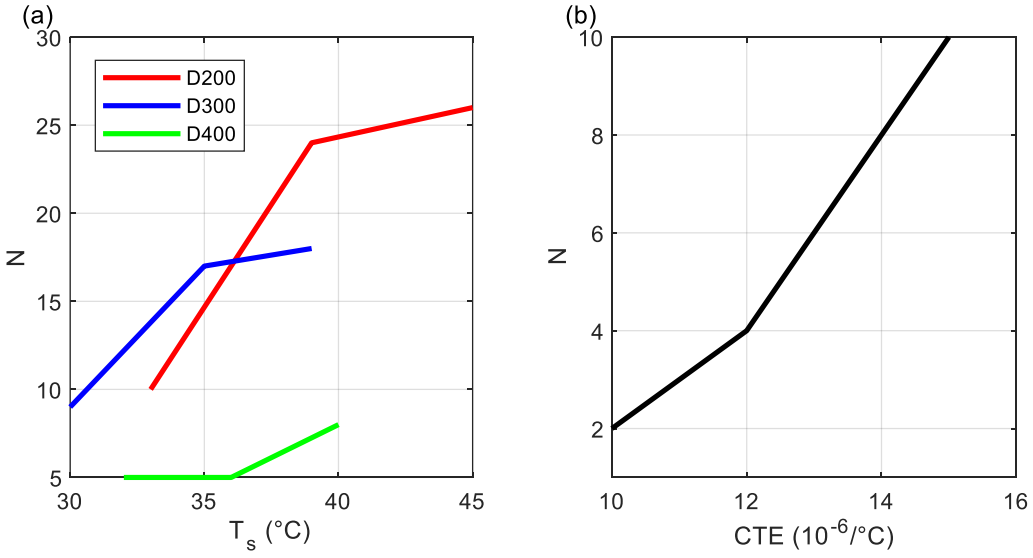

Figure 6.5: Transition cycles changing with different (a) storage temperature and (b) coefficient of thermal expansion.

6.2. Design recommendations

Figure 6.6 illustrates maximum stresses as well as the yield function changing with cycles, but for different T_s. As it was expected, higher input temperature results in higher stresses. This is associated with higher residual temperature remained from the former cycles. This cumulative effect results in high tensile stresses exceeding allowable tensile strength in the case of γ=1.5% and γ=2%. Using Figure 6.6 and 6.7, the design temperature for each pile design was identified through the interpolation so that the yield function will not exceed the allowable limit.

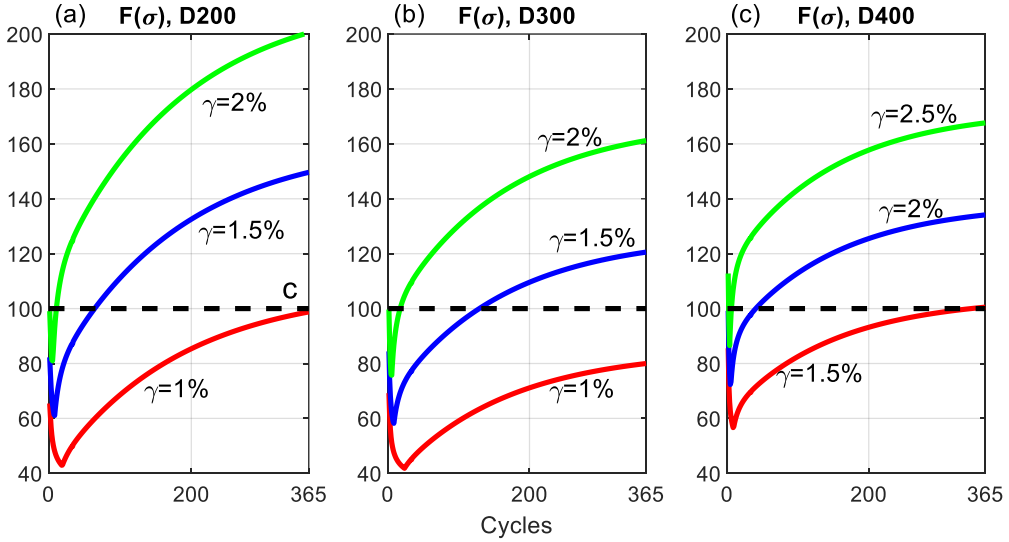

Figure 6.6: Yield function changing with cycles for pile design #1 for: (a) d_{in}=200 mm, (b) d_{in}=300 mm, (c) d_{in}=400 mm.

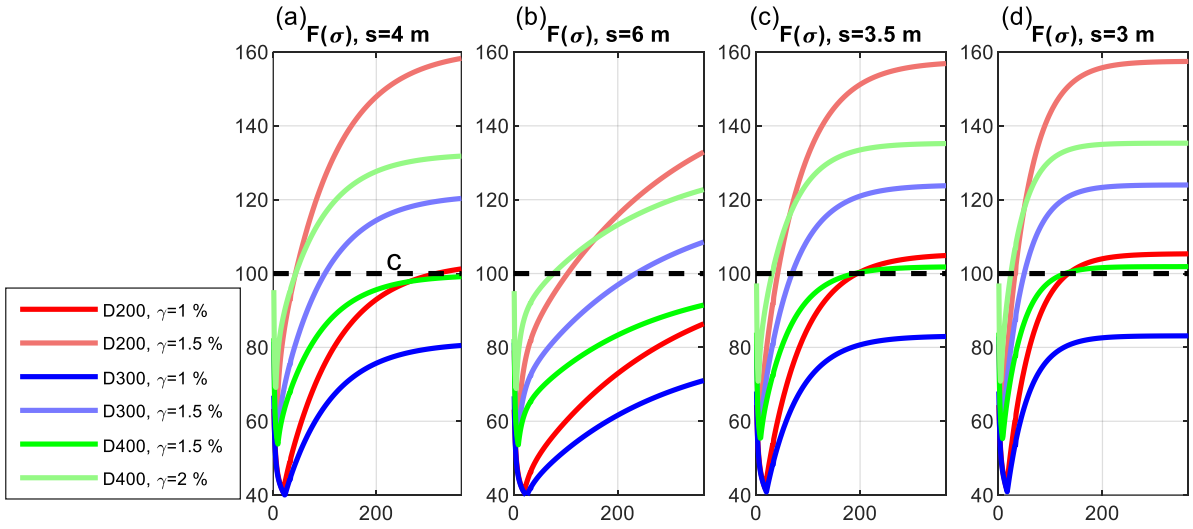

Figure 6.7: Yield function changing with cycles for: (a) pile design #2, (b) pile design #3, (c) pile design #4, (d) pile design #5.

Figure 6.8 demonstrates how the design temperature and transition cycle (N) change with different d_{in} for various pile spacings. A further arrangement of piles results in higher temperature allowed for storage according to Figure 6.8a. Moreover, this temperature allowed for storage reduces as the pile gets thinner. Furthermore, Figure 6.8b shows that the transition from compression-tension zone to pure tension zone appears to be faster as the pile gets thinner regardless of pile spacing.

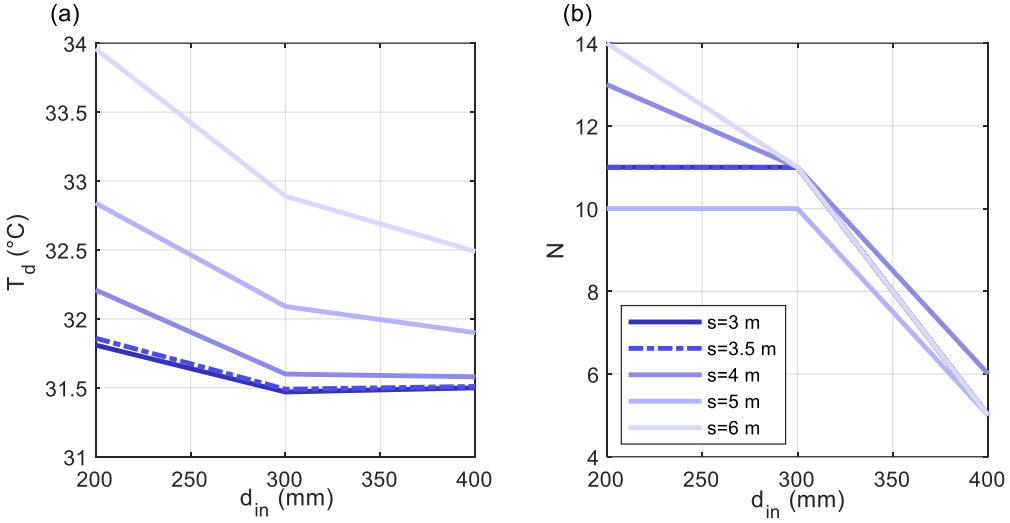

Figure 6.8: (a) Design temperature and (b) transition cycles changing with d_{in} for various pile spacings.

To sum up, maximum design temperatures (T_d) to be stored in the pile foundations for various thicknesses of the pile are tabulated below. As it can be noticed, it mostly lies in the range of approximately 31.5°C to 34°C. The corresponding design pressures are in the range of 6-7 MPa for d_{in}=200 mm, around 4 MPa for d_{in}=300 mm, and 2.5-3 MPa for d_{in}=400 mm. Furthermore, it is suggested to switch off and cool down energy storage piles every N day depending on chosen pile design to minimize the damaging effect on the structure.

Table 6.1: T_d and N for various pile design and inner diameter.

Pile design	d_{in}=200 mm			d_{in}=300 mm			d_{in}=400 mm		
	N	T_d (°C)	P_d (MPa)	N	T_d (°C)	P_d (MPa)	N	T_d (°C)	P_d (MPa)
#1 (s=5 m)	10	32.8	6.9	10	32.1	4.1	5	31.9	2.8
#2 (s=4 m)	13	32.2	6.2	11	31.6	3.8	6	31.6	2.6
#3 (s=6 m)	14	34.0	6.4	11	32.9	3.8	5	32.5	2.6
#4 (s=3.5 m)	11	31.9	6.6	11	31.5	3.9	5	31.5	2.7
#5 (s=3 m)	11	31.8	6.6	11	31.5	3.9	5	31.5	2.7

Chapter 7 – Conclusions

This thesis investigated the structural responses of the renewable energy storage piles under the combined effect of temperature changes and internal air pressure. Two steps of analytical studies were performed: (1) thermal analyses to identify temperature distributions inside concrete sections; and (2) thermal mechanical analyses to evaluate the structural responses. First, several conclusions can be drawn from the thermal analyses:

- The temperature changes, originated at the inner surface of the pile from the compressed air, penetrate through the pile section due to the thermal conduction and increase the temperature in the pile section.
- Residual temperatures were observed in the pile section at the end of each loading cycle. This residual temperature accumulates with the loading cycle and results in temperature increases in the pile section.
- Temperature distribution along the pile section changes with the loading cycle.
- The heat generated from adjacent piles can transfer through the soil layer to the pile via thermal conduction. This heat transfer increases the temperature in the pile, particularly for the cases with a small pile spacing.
- The heat transition in thinner piles happens to be faster than in thicker piles.

Second, conclusions of the thermal mechanical analyses are listed below:

- The internal air pressure results in circumferential tensile stresses. These tensile stresses have a maximum value at the inner surface and gradually reduce as moving to the outer surface. Whereas the thermal mechanical loading causes circumferential compressive stresses near the inner surface and circumferential tensile stresses near the outer surface. As a result, the maximum circumferential tensile stresses in the pile section under combined loading are smaller than the case under the internal air pressure.
- The thermal mechanical loading causes vertical tensile stresses in the pile section. This vertical tensile stress is smaller than the tensile circumferential stress. The combined biaxial tension stress still creates a less critical stress condition than the case under the internal air pressure according to the concrete damage theory under multi-axial stresses.
- The cyclic thermal loading causes residual stresses in the pile section. As the loading cycle increases, the residual effect reduces the compression stress at the inner surface

and eventually make it under tension after sufficient numbers of cycles. On the other hand, the residual effect reduces the tensile stress at the outer surface.

- The cyclic thermal loading causes the circumferential stress distribution changing from the compression-tension state into pure tension after the sufficient number of cycles.
- The combined loading has an insignificant effect on the lateral pressure and skin friction between the pile and soil due to the relatively large wall thickness.
- To avoid pure tension stress states inside the pile section, the piles with lower d_{in} have a larger limit on the number of days of continuous usage, while piles with greater d_{in} have a limit as low as 5 days.
- The lower spacing between piles results in larger thermal mechanical stresses in the pile section because faster heat transfer can be observed between adjacent piles with smaller pile spacing.
- Piles with a higher thermal expansion coefficient have larger thermal mechanical stresses but it allows a longer period of continuous usage before reaching the pure tension state.

Following design recommendations were made for the optimal storage temperature (design temperature) and the suggested continuous usage period:

- Design temperatures for all cases mostly lie in the range of approximately 31.5°C to 34°C.
- Design pressures for all cases are ranged from 2.6-6.9 MPa depending on d_{in}.
- It is suggested to switch off and cool down energy storage piles every *N (*ranged from 5-14*)* day depending on chosen pile design to avoid a pure tension state in the pile section.

In this thesis, the analytical models and simulations have several assumptions and limitations such as the thermal and thermal mechanical analysis were not coupled; nonlinearity in the concrete thermal and mechanical properties was not taken into consideration; the soil was simplified as discrete spring; the air temperature distributions inside the pile section were assumed to be uniform. Experimental work is recommended in the future to validate the simulation results.

References

[1] Tong, Z., Cheng, Z., & Tong, S. (2020). A review on the development of compressed air energy storage in China: Technical and economic challenges to commercialization. Renewable and Sustainable Energy Reviews, 135, 110178.

[2] Zhang, D., Kim, J., Tulebekova, S., Saliyev, D., & Lee, D. (2018). Structural responses of reinforced concrete pile foundations subjected to pressures from compressed air for renewable energy storage. International Journal of Concrete Structures and Materials, 12(1), 74.

[3] Cavallo, A. (2007). Controllable and affordable utility-scale electricity from intermittent wind resources and compressed air energy storage (CAES). Energy, 32(2), 120-127.

[4] Lund, H., & Salgi, G. (2009). The role of compressed air energy storage (CAES) in future sustainable energy systems. Energy conversion and management, 50(5), 1172-1179.

[5] Tulebekova, S., Zhang, D., Lee, D., Kim, J. R., Barissov, T., & Tsoy, V. (2019). Nonlinear responses of energy storage pile foundations with fiber reinforced concrete. Structural Engineering and Mechanics, 71(4), 363-375.

[6] Zhang, D., Mamesh, Z., Sailauova, D., Shon, C. S., Lee, D., & Kim, J. R. (2019). Temperature distributions inside concrete sections of renewable energy storage pile foundations. Applied Sciences, 9(22), 4776.

[7] Sailauova, D., Mamesh, Z., Zhang, D., Lee, D., Shon, C. S., & Kim, J. R. (2020). Group Pile Effect on Temperature Distributions inside Energy Storage Pile Foundations. Applied Sciences, 10(18), 6597.

[8] Hayter, Sheila J., and Alicen Kandt. Renewable energy applications for existing buildings. No. NREL/CP-7A40-52172. National Renewable Energy Lab.(NREL), Golden, CO (United States), 2011.

[9] Rugolo, J., & Aziz, M. J. (2012). Electricity storage for intermittent renewable sources. Energy & Environmental Science, 5(5), 7151-7160.

[10] Zhang, L., Ahmari, S., Sternberg, B., & Budhu, M. (2012). Feasibility study of compressed air energy storage using steel pipe piles. In GeoCongress 2012: State of the Art and Practice in Geotechnical Engineering (pp. 4272-4279).

[11] Tulebekova, S., Saliyev, D., Zhang, D., Kim, J. R., Karabay, A., Turlybek, A., & Kazybayeva, L. (2017, November). Preliminary analytical study on the feasibility of using reinforced concrete pile foundations for renewable energy storage by compressed air energy storage technology. In IOP Conference Series: Materials Science and Engineering; IOP Publishing Ltd.: London, UK (Vol. 271, pp. 12-23).

[12] Sabirova, A., Zhang, D., Kim, J., Nguyen, M., & Shon, C. (2016, August). Development of a reinforced concrete foundation system for renewable energy storage. In Proceedings of the 8th Asian Young geotechnical engineering conference (pp. 5-7).

[13] Breeze, P. (2018). Power system energy storage technologies. Academic Press.

[14] Ellabban, O., Abu-Rub, H., & Blaabjerg, F. (2014). Renewable energy resources: Current status, future prospects and their enabling technology. Renewable and Sustainable Energy Reviews, 39, 748-764.

[15] Di Donna, A., Loria, A. F. R., & Laloui, L. (2016). Numerical study of the response of a group of energy piles under different combinations of thermo-mechanical loads. Computers and Geotechnics, 72, 126-142.

[16] Faizal, M., Bouazza, A., McCartney, J. S., & Haberfield, C. (2019). Effects of cyclic temperature variations on thermal response of an energy pile under a residential building. Journal of Geotechnical and Geoenvironmental Engineering, 145(10), 04019066.

[17] Laloui, L., Nuth, M., & Vulliet, L. (2006). Experimental and numerical investigations of the behaviour of a heat exchanger pile. International journal for numerical and analytical methods in geomechanics, 30(8), 763-781.

[18] Murphy, K. D., McCartney, J. S., & Henry, K. S. (2015). Evaluation of thermo-mechanical and thermal behavior of full-scale energy foundations. Acta Geotechnica, 10(2), 179-195.

[19] The Green Age (2020). Compressed Air Energy Storage. https://www.thegreenage.co.uk/tech/compressed-air-energy-storage/. Accessed 28 September 2020.

[20] Al-Shemmeri, T. (2010). Engineering thermodynamics. Bookboon.

[21] Das, B. M. (Ed.). (2010). Geotechnical engineering handbook. J. Ross publishing.

[22] Graybeal, B. A. (2006). Material property characterization of ultra-high performance concrete (No. FHWA-HRT-06-103). United States. Federal Highway Administration. Office of Infrastructure Research and Development.

[23] Yang, I. H., & Park, J. (2019). Mechanical and Thermal Properties of UHPC Exposed to High-Temperature Thermal Cycling. Advances in Materials Science and Engineering, 2019.

[24] Kersten, M. S. (1949). Thermal properties of soils.

[25] Abu-Hamdeh, N. H. (2003). Thermal properties of soils as affected by density and water content. Biosystems engineering, 86(1), 97-102.

[26] Thomas, H. R., & Rees, S. W. (2009). Measured and simulated heat transfer to foundation soils. Géotechnique, 59(4), 365-375.

[27] Brandl, H. (2006). Energy foundations and other thermo-active ground structures. Géotechnique, 56(2), 81-122.

[28] Engineering ToolBox, (2003). Young's Modulus - Tensile and Yield Strength for common Materials. [online] Available at: https://www.engineeringtoolbox.com/young-modulus-d_417.html [Accessed 19 March 2021].

[29] Engineering ToolBox, (2008). Poisson's ratio. [online] Available at: https://www.engineeringtoolbox.com/poissons-ratio-d_1224.html [Accessed 19 March 2021].

[30] Cverna, F. (Ed.). (2002). ASM Ready Reference: Thermal properties of metals. Asm International.

[31] API (2002). Recommended practice for planning, designing and constructing fixed offshore platforms—working stress design. API recommended practice report 2A-WSD. American Petroleum Institute, December.

[32] Dowell, J. C. (2008). A method for predicting mobilization of resistance for micropiles used in slope stabilization applications.

[33] Lee, J., & Fenves, G. L. (1998). Plastic-damage model for cyclic loading of concrete structures. Journal of engineering mechanics, 124(8), 892-900.

Appendices

Appendix A – Thermal Mechanical Analyses

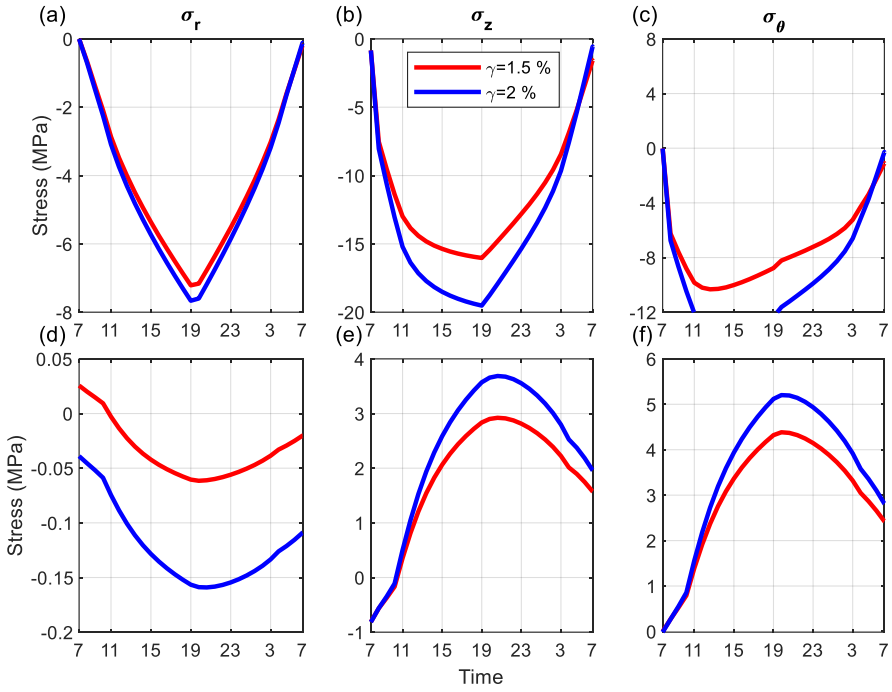

Figure A.1 Stress varying with 24-hour time at the (a)-(c) inner and (d)-(f) outer surface for the pile design #1 for d_{in}=200 mm.

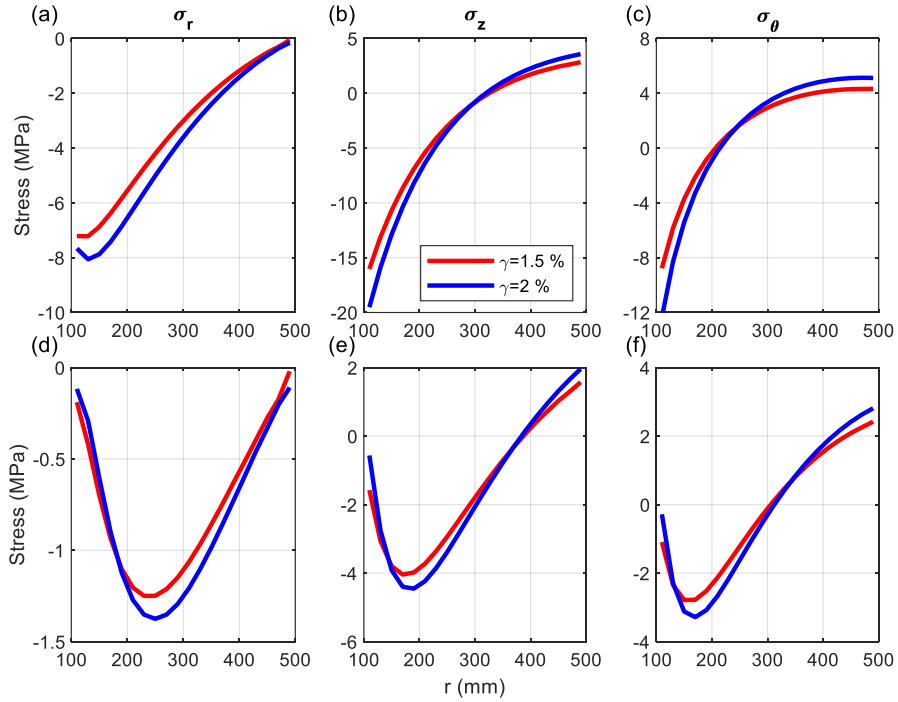

Figure A.2 Stress distribution along r-direction at the (a)-(c) middle and (d)-(f) end of the cycle for the pile design #1 for d_{in}=200 mm.

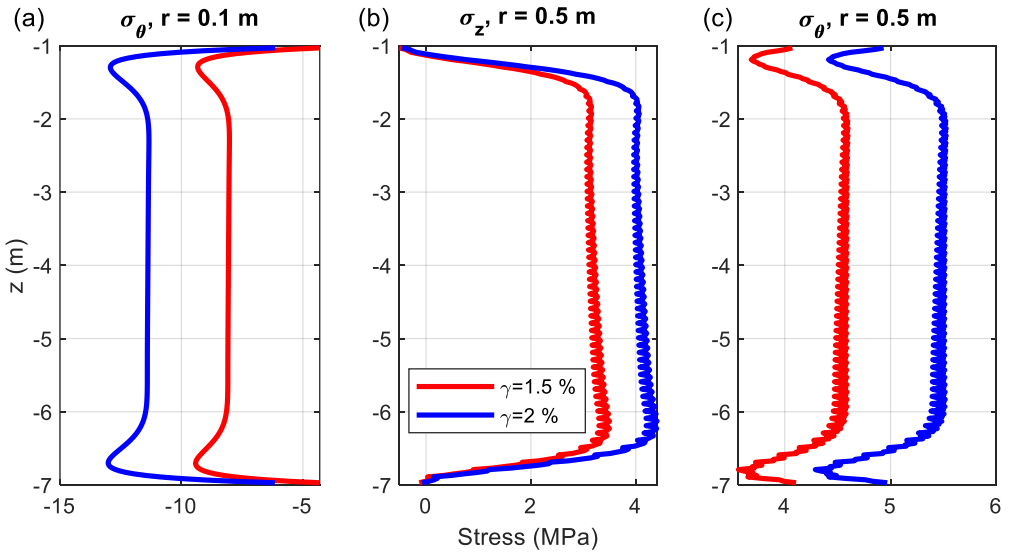

Figure A.3 Stress distribution along z-direction for various cycles at the (a)-(b) inner and (c)-(d) outer surface for pile design #1 for d_{in}=200 mm.

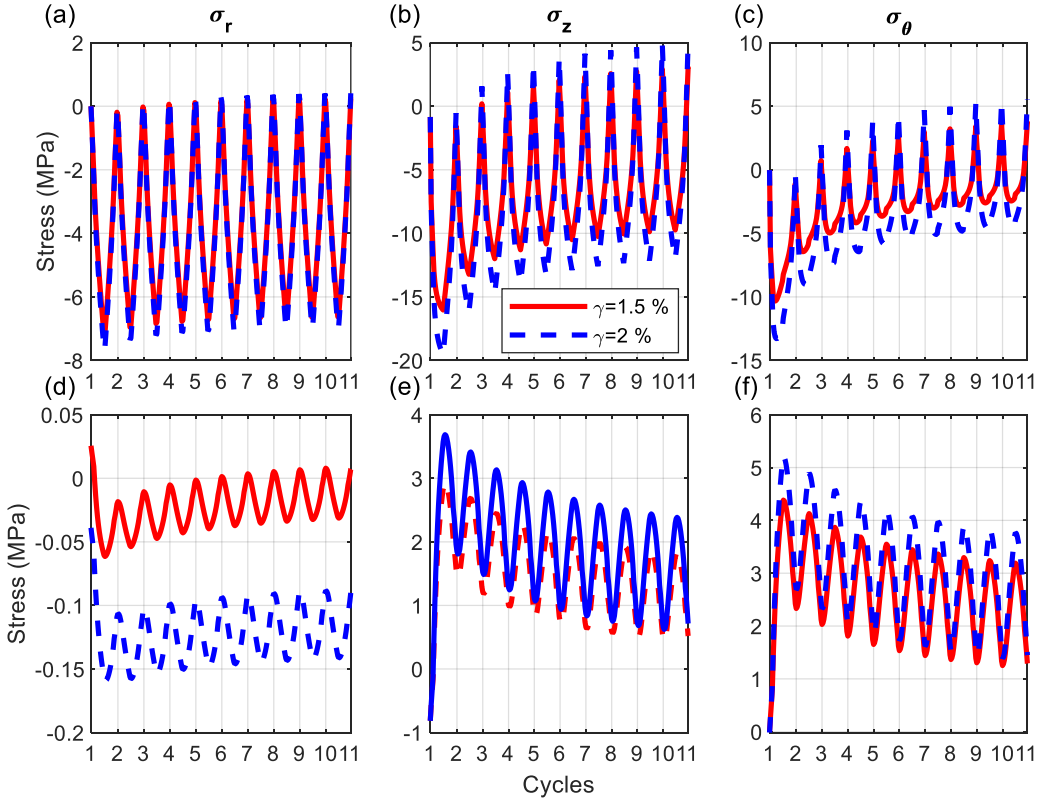

Figure A.4 Stress varying with 10 cycles for (a)-(c) inner and (d)-(f) outer surface for the pile design #1 for d_{in}=200 mm.

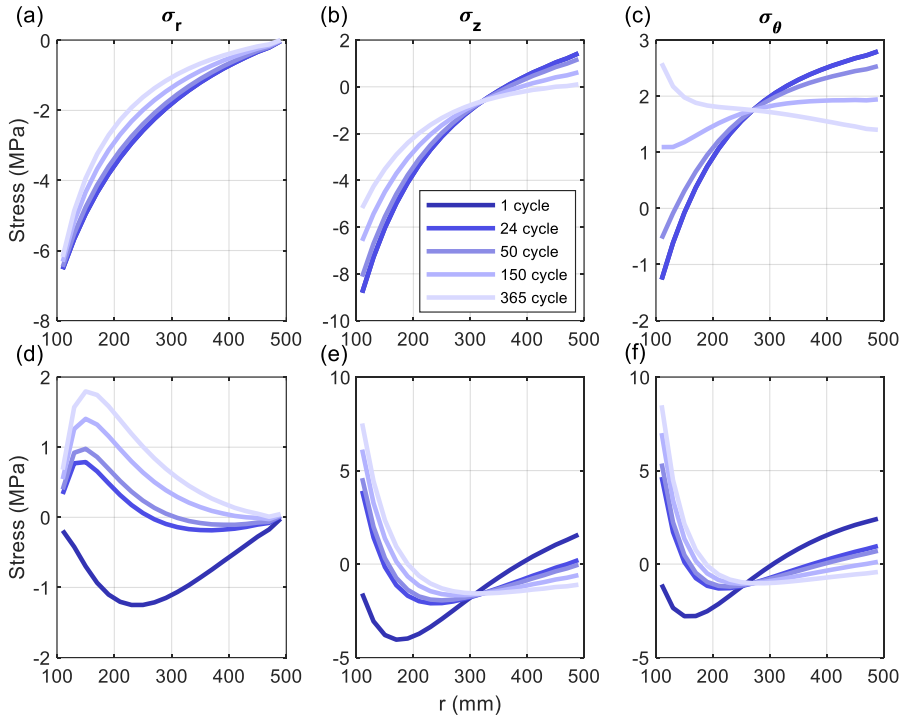

Figure A.5 Stress distribution along r-direction at the (a)-(c) middle and (d)-(f) end of the different cycles for the pile design #1 for γ=1.5%, d_{in}=200 mm.

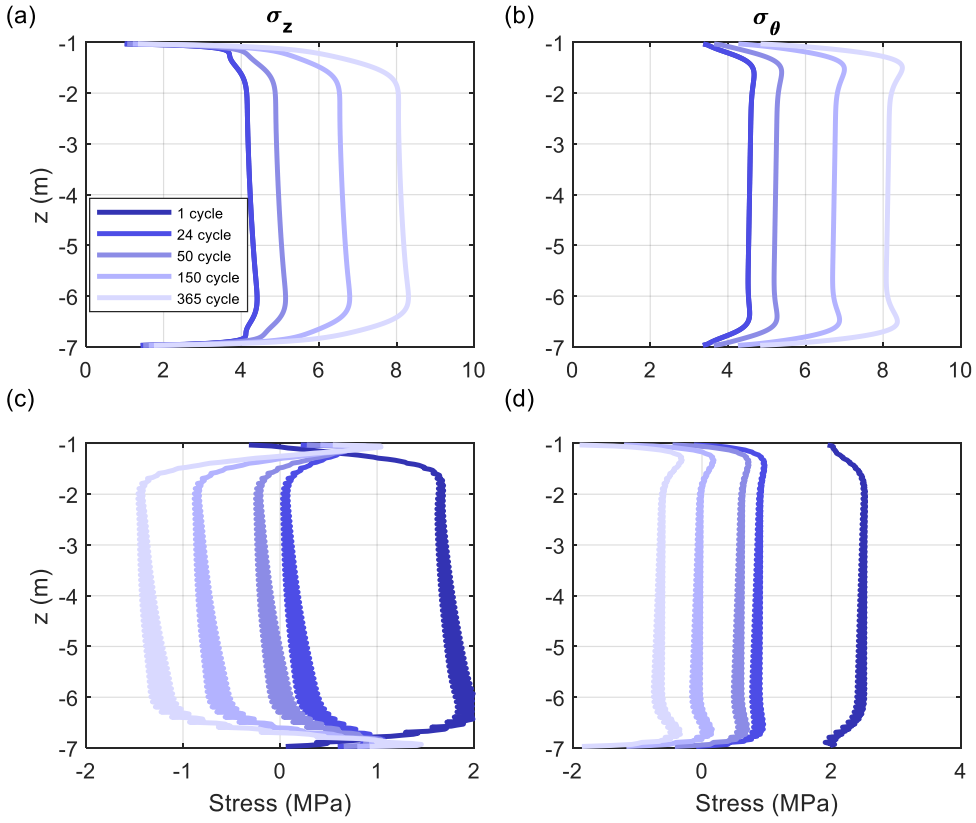

Figure A.6 Stress distribution along z-direction for various cycles at the (a)-(b) inner and (c)-(d) outer surface for pile design #1 for γ=1.5%, d_{in}=200 mm.

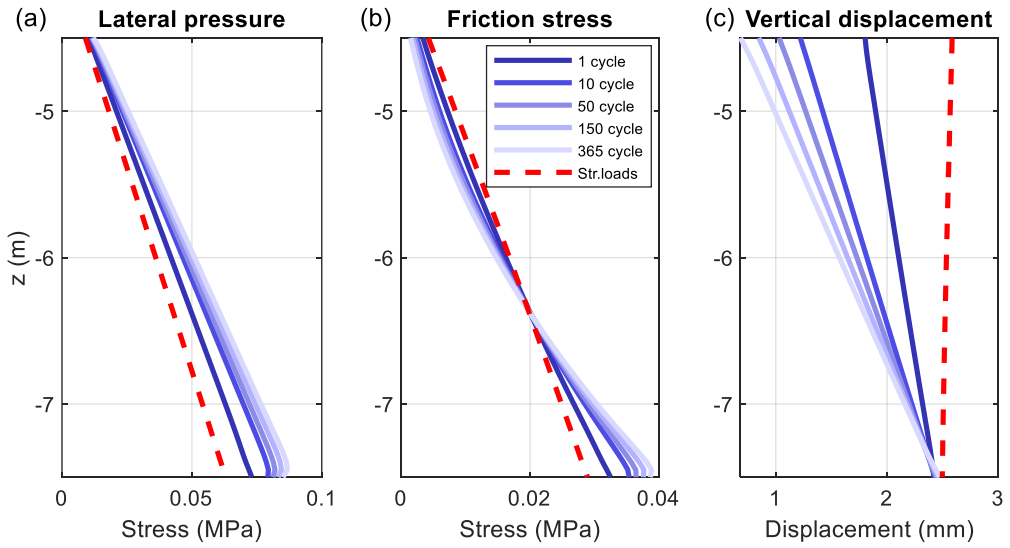

Figure A.7 Soil stresses and displacement along z-direction for various cycles under (a)-(c) combined loadings for pile design #1 for γ=1.5%, d_{in}=200 mm.

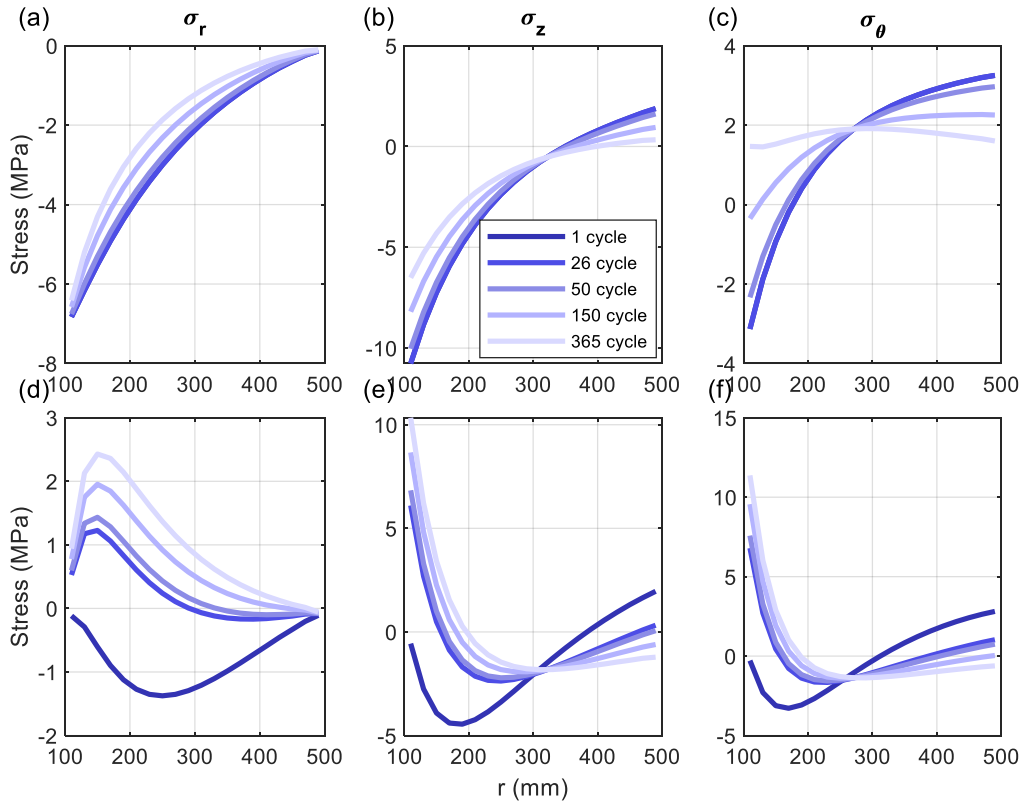

Figure A.8 Stress distribution along r-direction at the (a)-(c) middle and (d)-(f) end of the different cycles for the pile design #1 for γ=2%, d_{in}=200 mm.

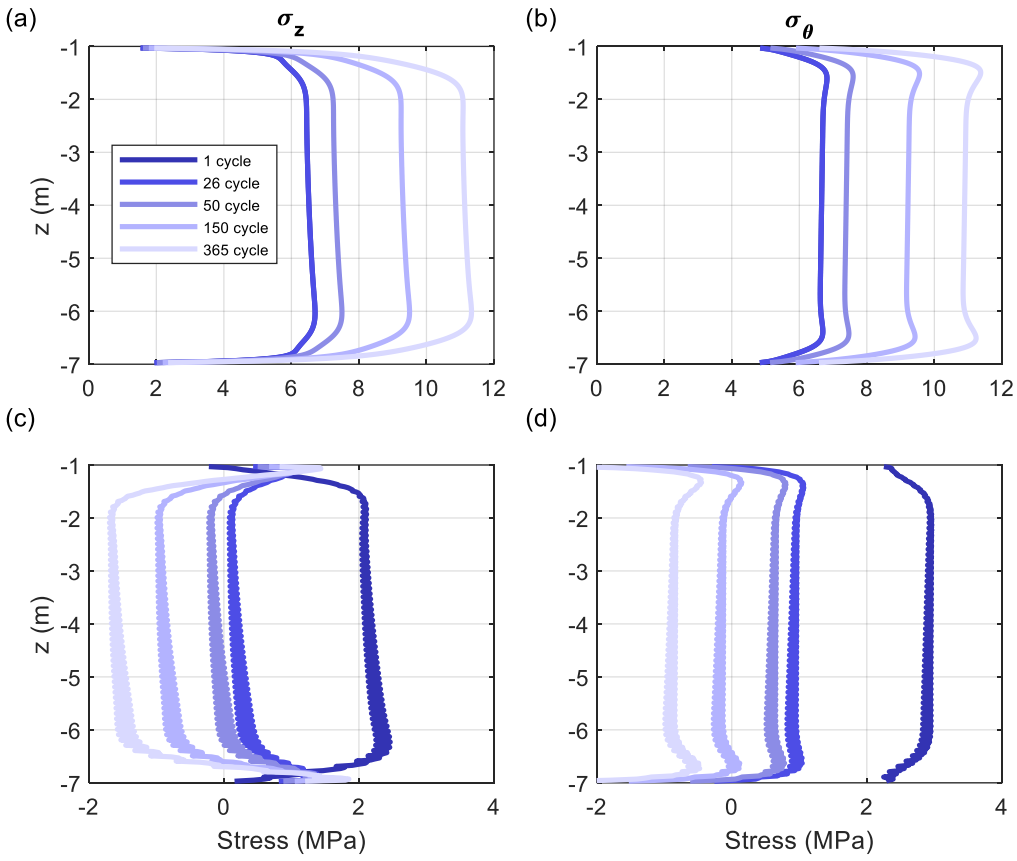

Figure A.9 Stress distribution along z-direction for various cycles at the (a)-(b) inner and (c)-(d) outer surface for pile design #1 for γ=2%, d_{in}=200 mm.

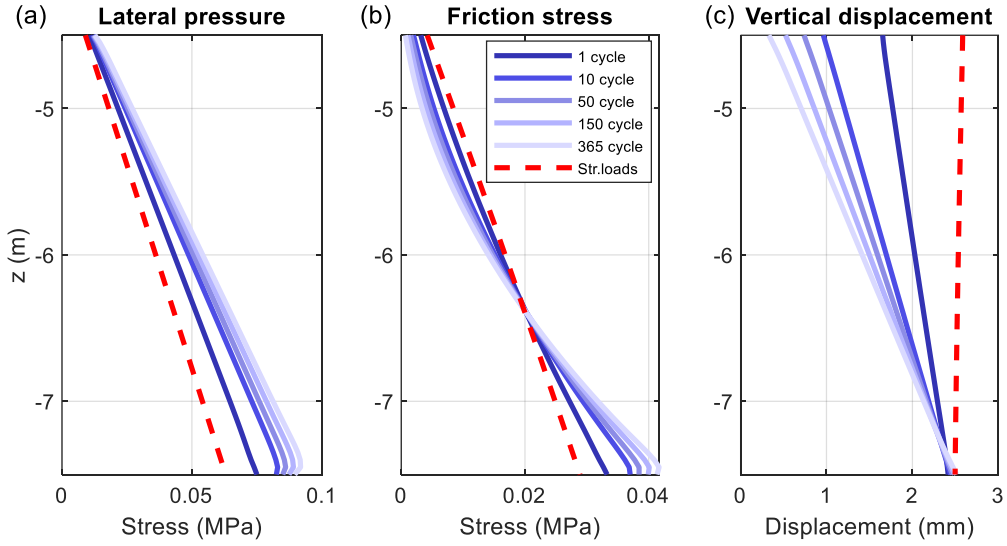

Figure A.10 Soil stresses and displacement along z-direction for various cycles under (a)-(c) combined loadings for pile design #1 for γ=2%, d_{in}=200 mm.

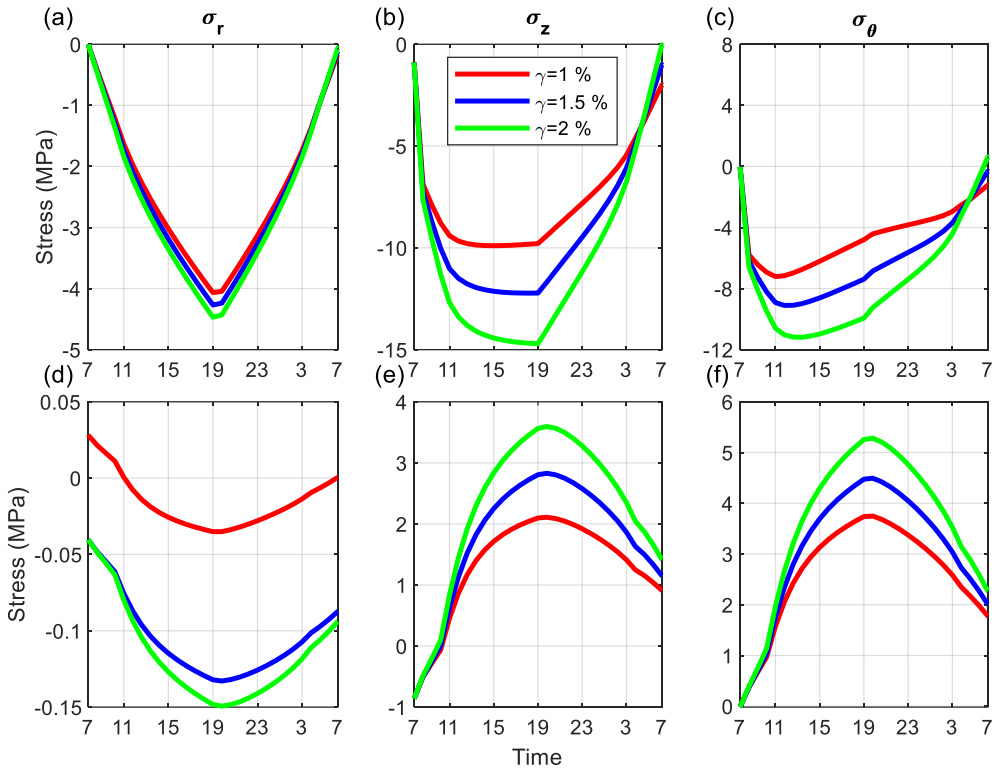

Figure A.11 Stress varying with 24-hour time at the (a)-(c) inner and (d)-(f) outer surface for the pile design #1 for d_{in}=300 mm.

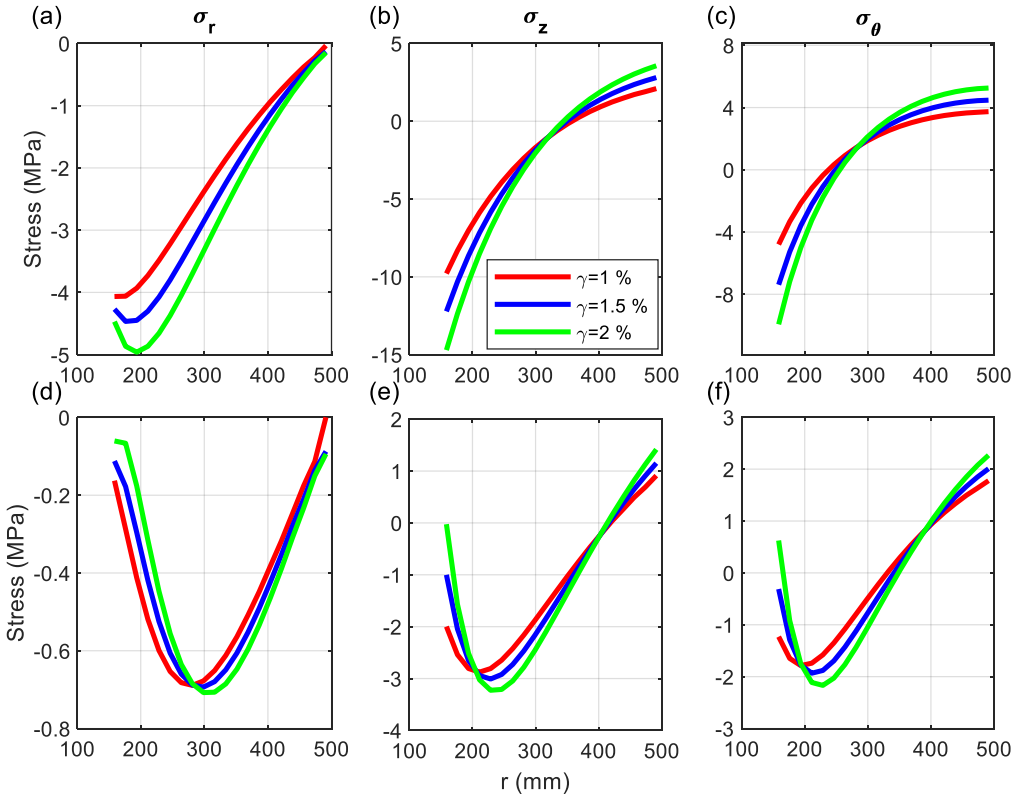

Figure A.12 Stress distribution along r-direction at the (a)-(c) middle and (d)-(f) end of the cycle for the pile design #1 for d_{in}=300 mm.

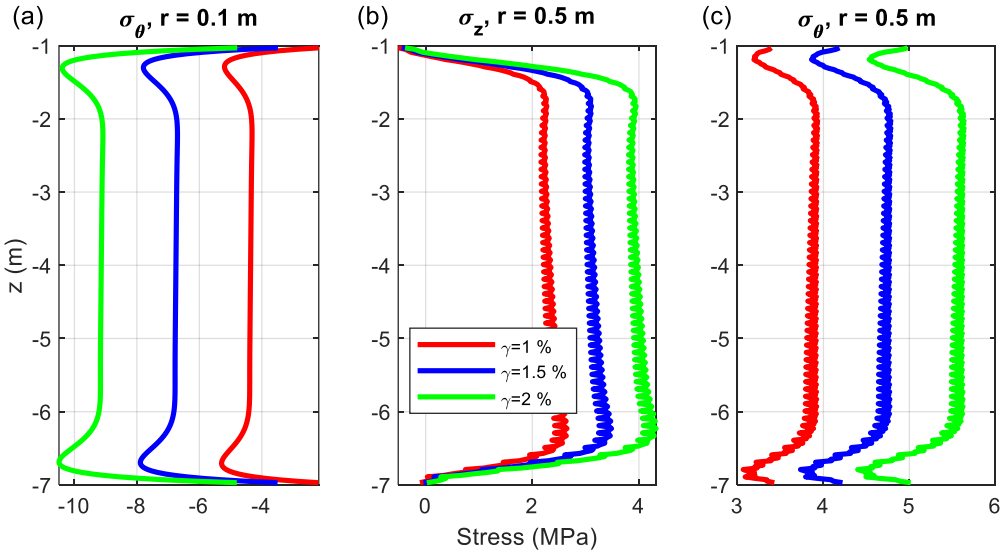

Figure A.13 Stress distribution along z-direction for various cycles at the (a)-(b) inner and (c)-(d) outer surface for pile design #1 for d_{in}=300 mm.

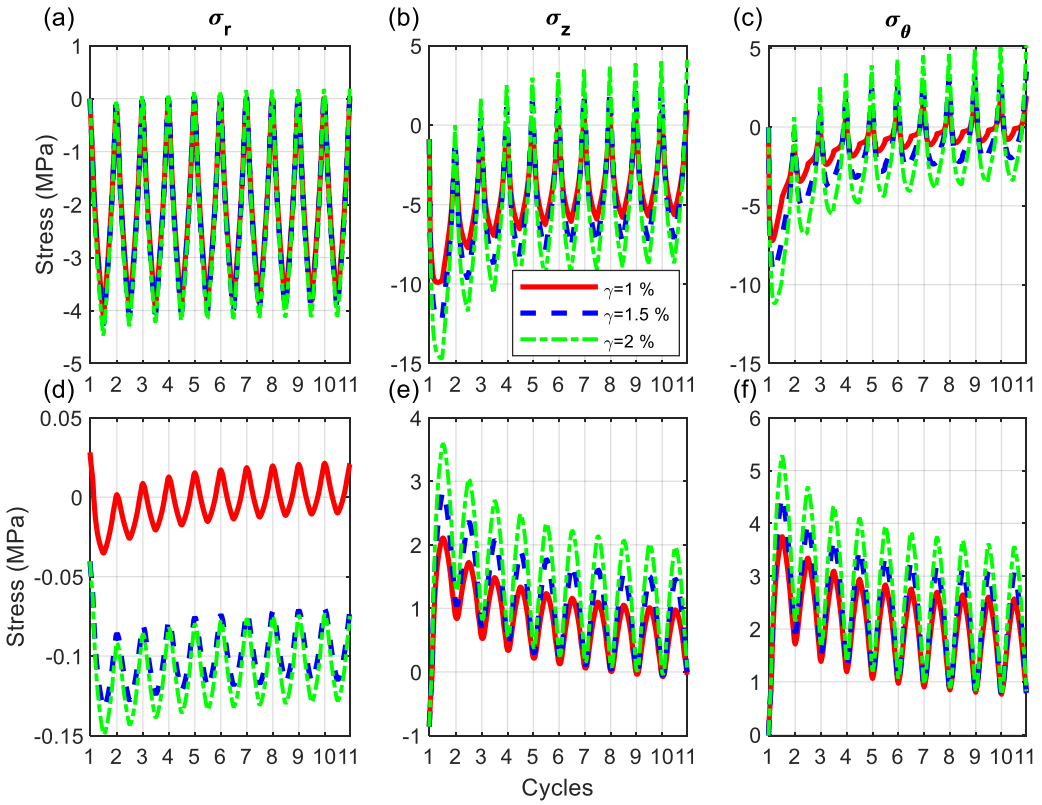

Figure A.14 Stress varying with 10 cycles for (a)-(c) inner and (d)-(f) outer surface for the pile design #1 for d_{in}=300 mm.

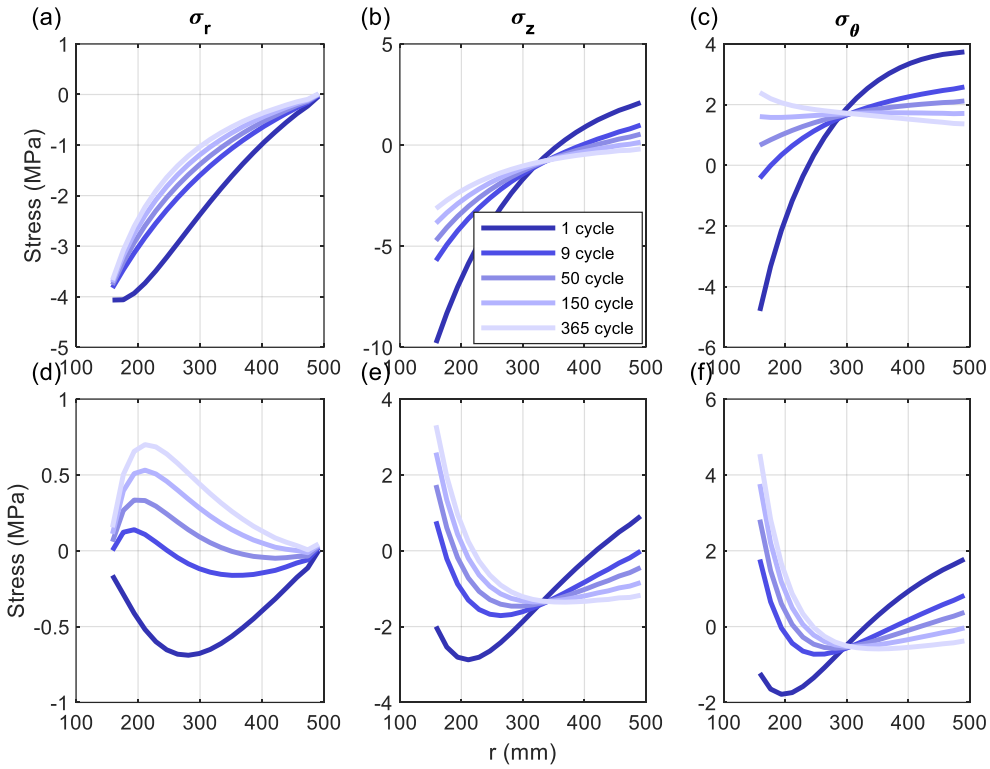

Figure A.15 Stress distribution along r-direction at the (a)-(c) middle and (d)-(f) end of the different cycles for the pile design #1 for γ=1%, d_{in}=300 mm.

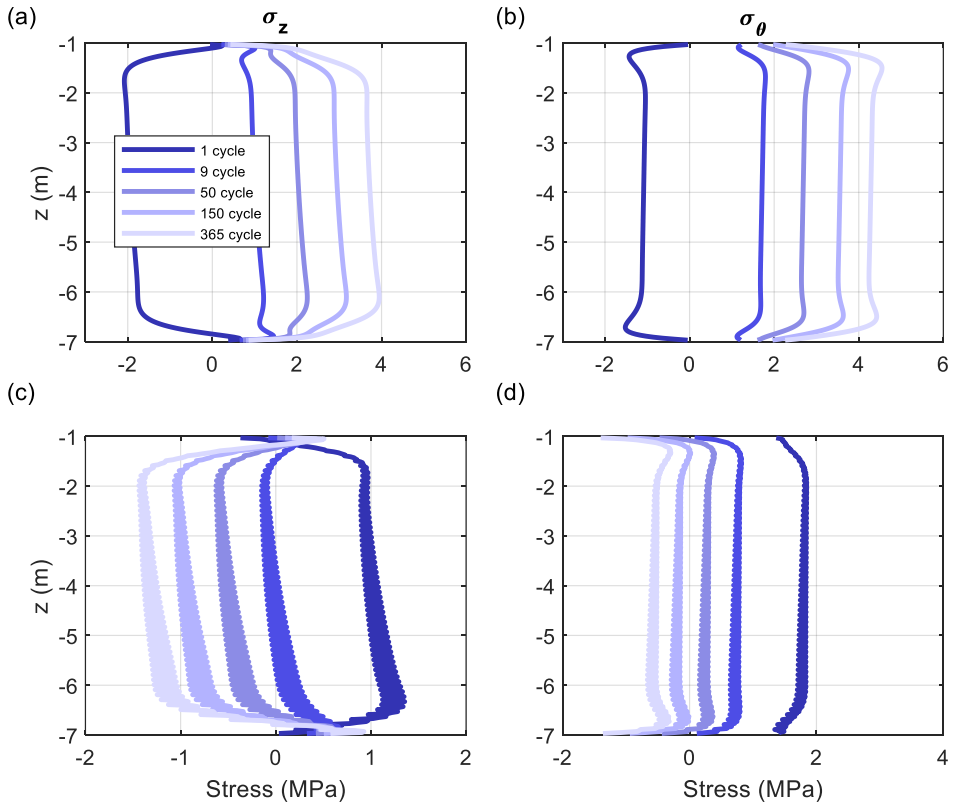

Figure A.16 Stress distribution along z-direction for various cycles at the (a)-(b) inner and (c)-(d) outer surface for pile design #1 for γ=1%, d_{in}=300 mm.

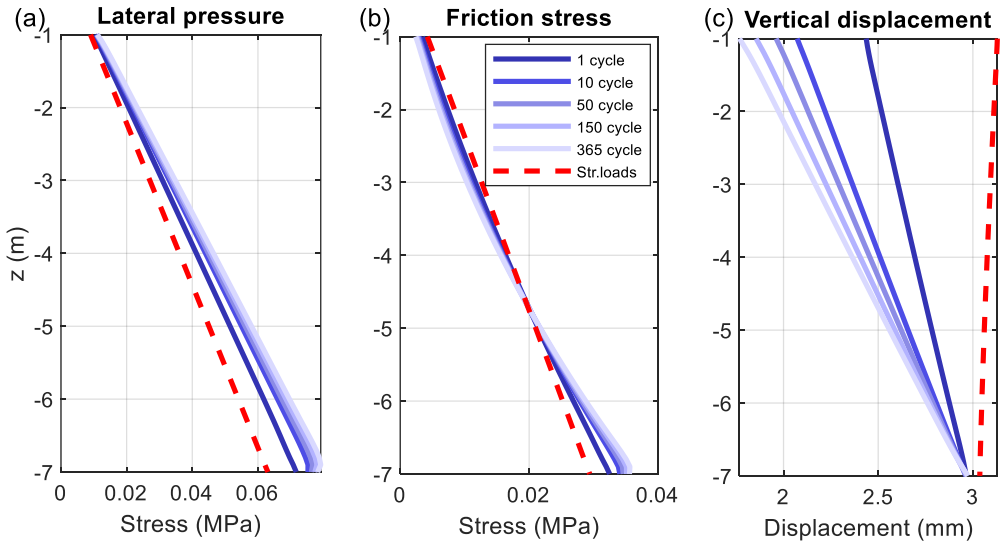

Figure A.17 Soil stresses and displacement along z-direction for various cycles under (a)-(c) combined loadings for pile design #1 for γ=1%, d_{in}=300 mm.

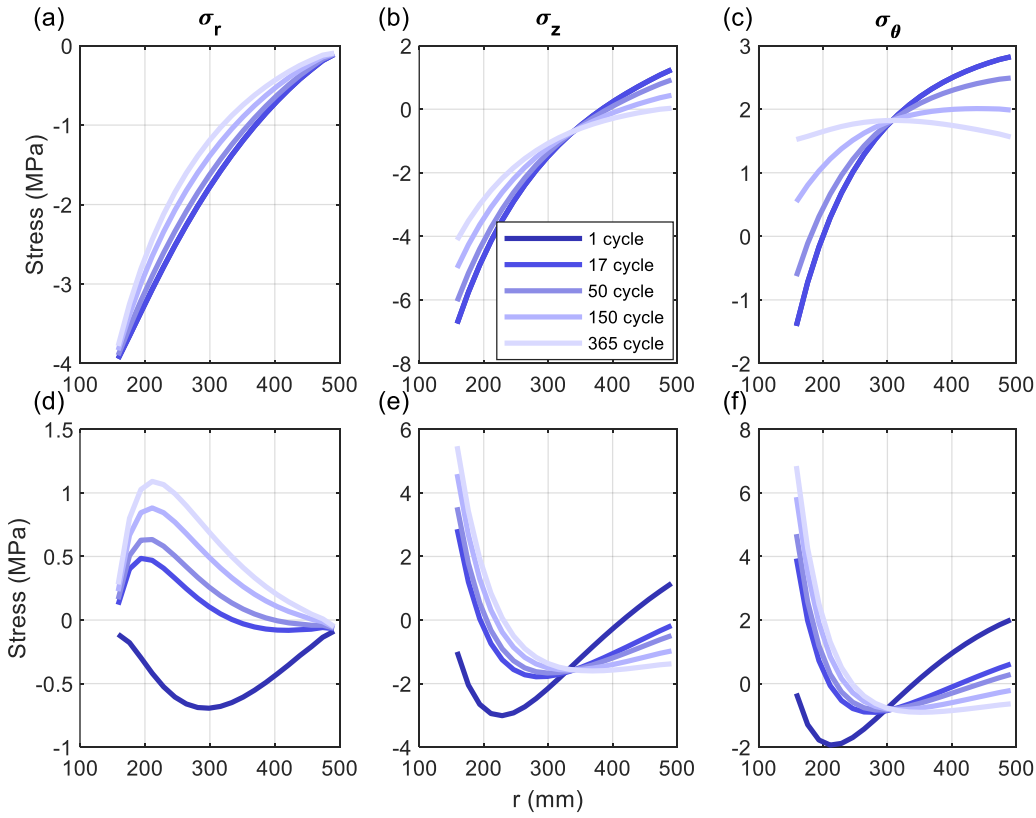

Figure A.18 Stress distribution along r-direction at the (a)-(c) middle and (d)-(f) end of the different cycles for the pile design #1 for γ=1.5%, d_{in}=300 mm.

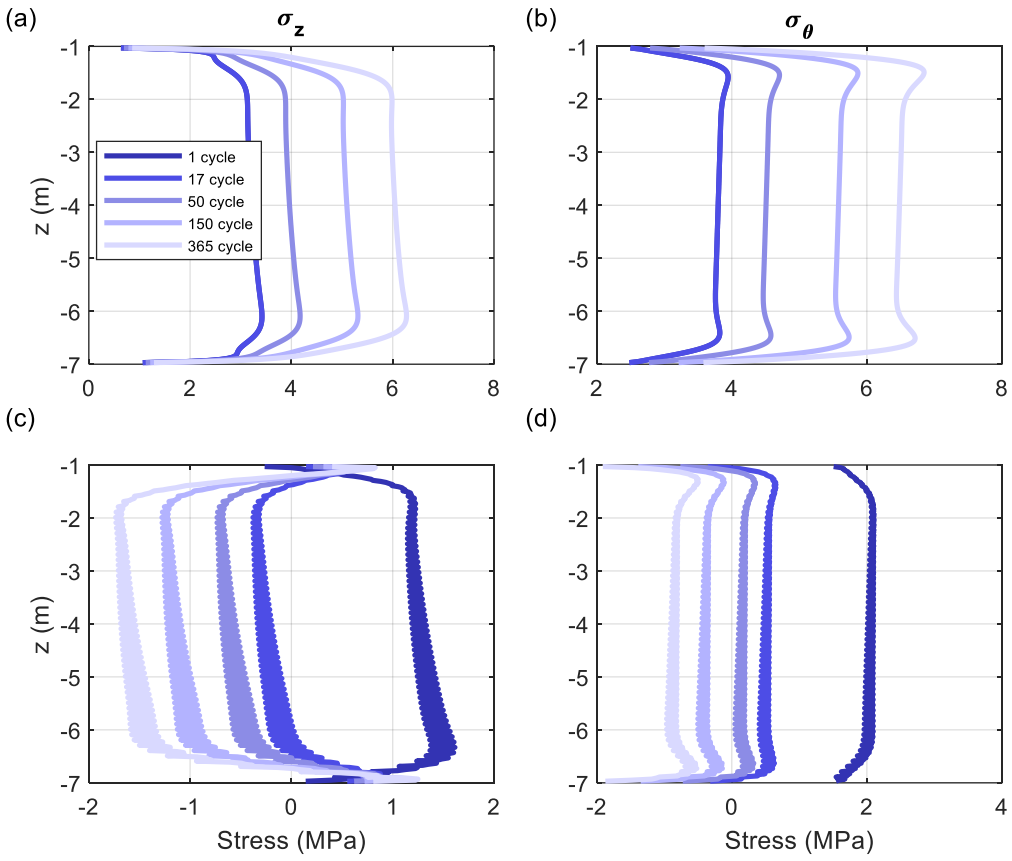

Figure A.19 Stress distribution along z-direction for various cycles at the (a)-(b) inner and (c)-(d) outer surface for pile design #1 for γ=1.5%, d_{in}=300 mm.

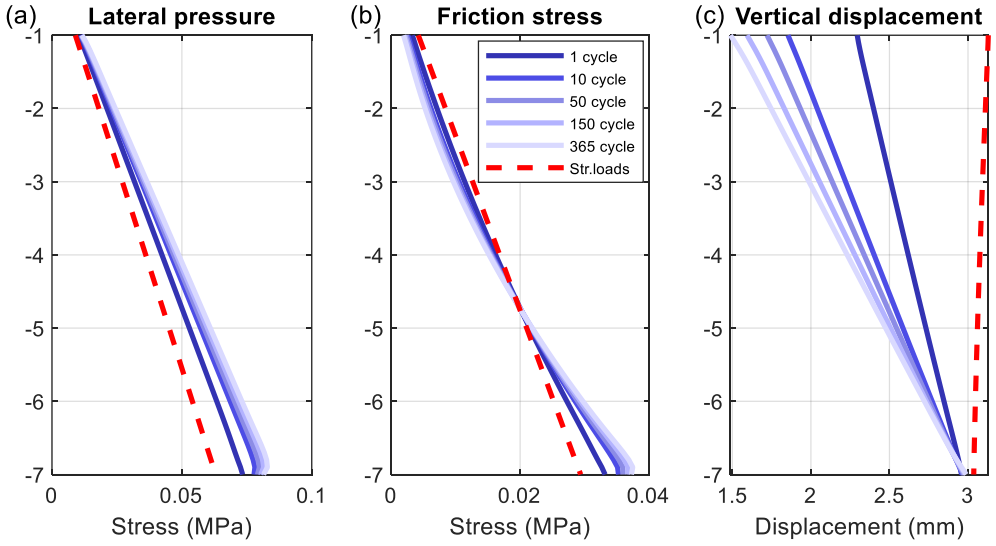

Figure A.20 Soil stresses and displacement along z-direction for various cycles under (a)-(c) combined loadings for pile design #1 for γ=1.5%, d_{in}=300 mm.

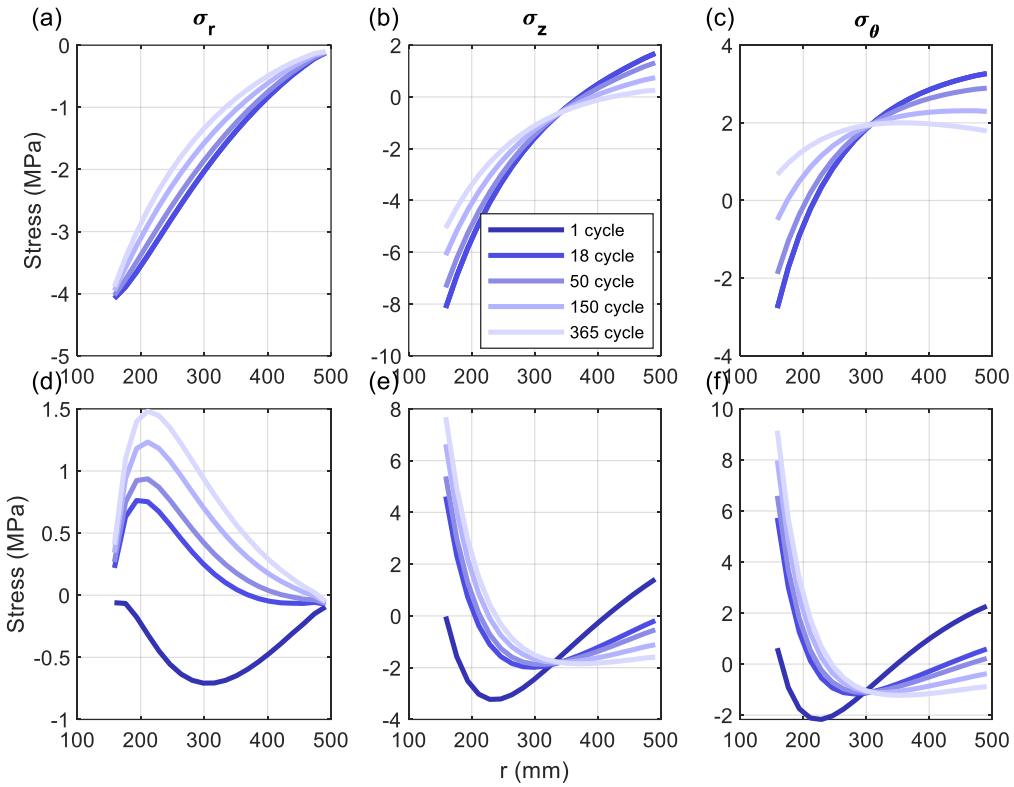

Figure A.21 Stress distribution along r-direction at the (a)-(c) middle and (d)-(f) end of the different cycles for the pile design #1 for γ=2%, d_{in}=300 mm.

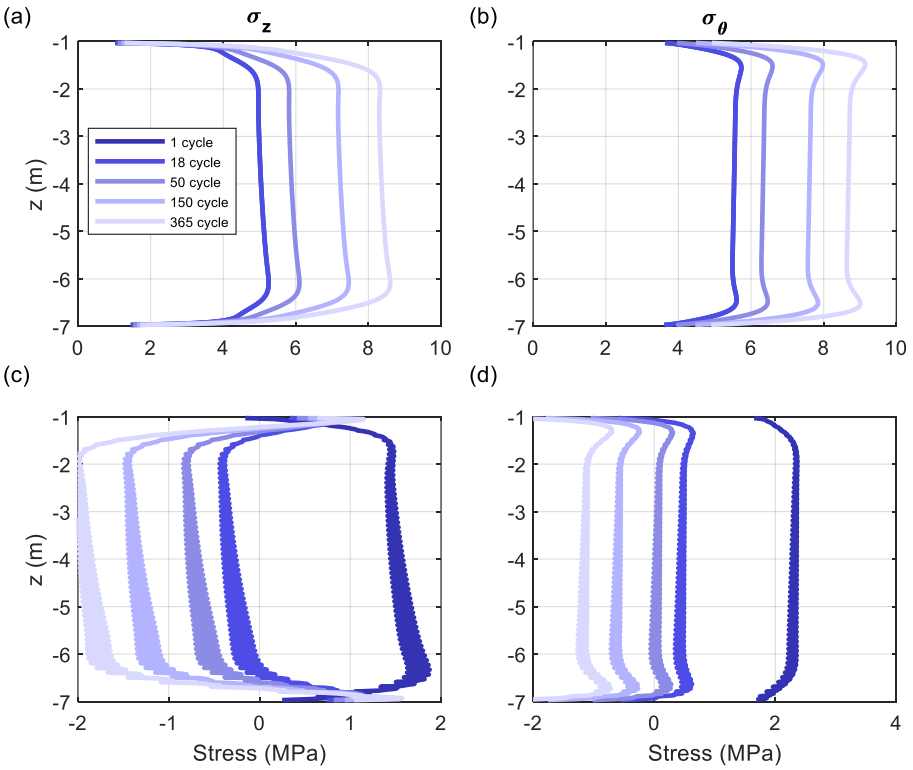

Figure A.22 Stress distribution along z-direction for various cycles at the (a)-(b) inner and (c)-(d) outer surface for pile design #1 for γ=2%, d_{in}=300 mm.

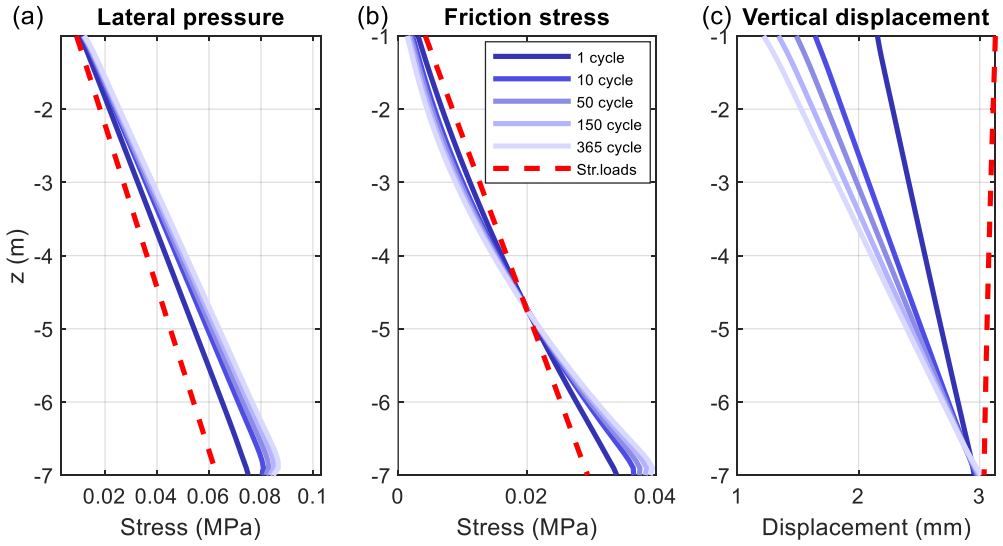

Figure A.23 Soil stresses and displacement along z-direction for various cycles under (a)-(c) combined loadings for pile design #1 for γ=2%, d_{in}=300 mm.

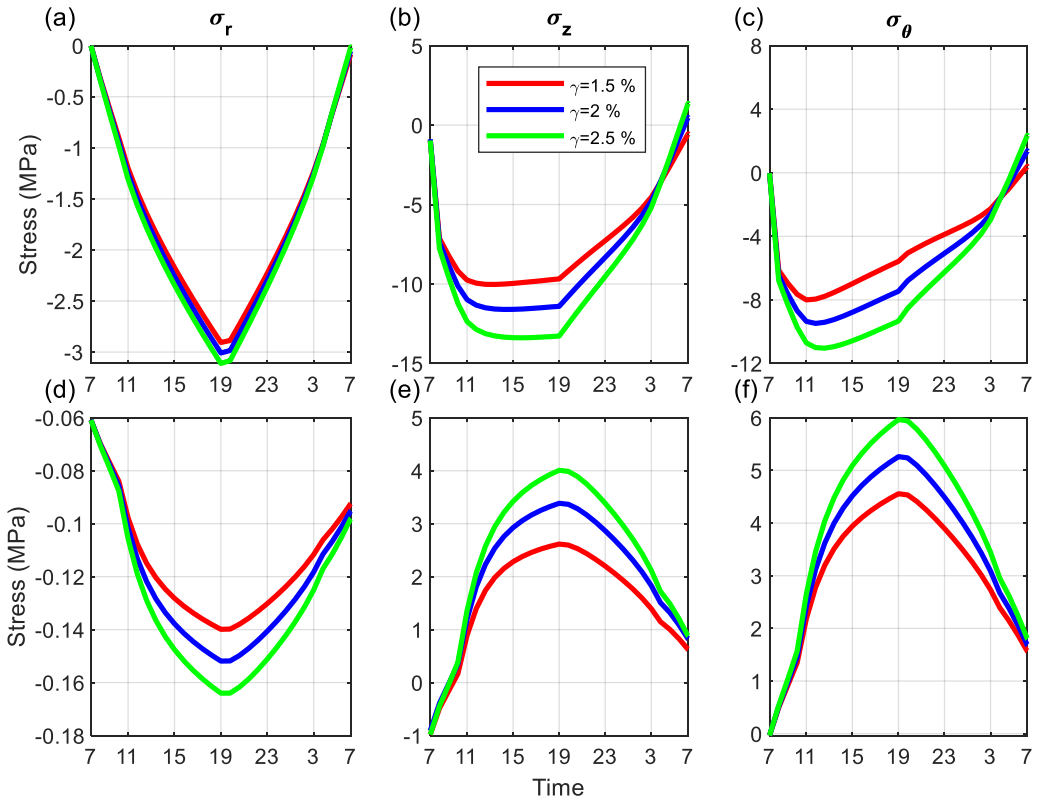

Figure A.24 Stress varying with 24-hour time at the (a)-(c) inner and (d)-(f) outer surface for the pile design #1 for d_{in}=400 mm.

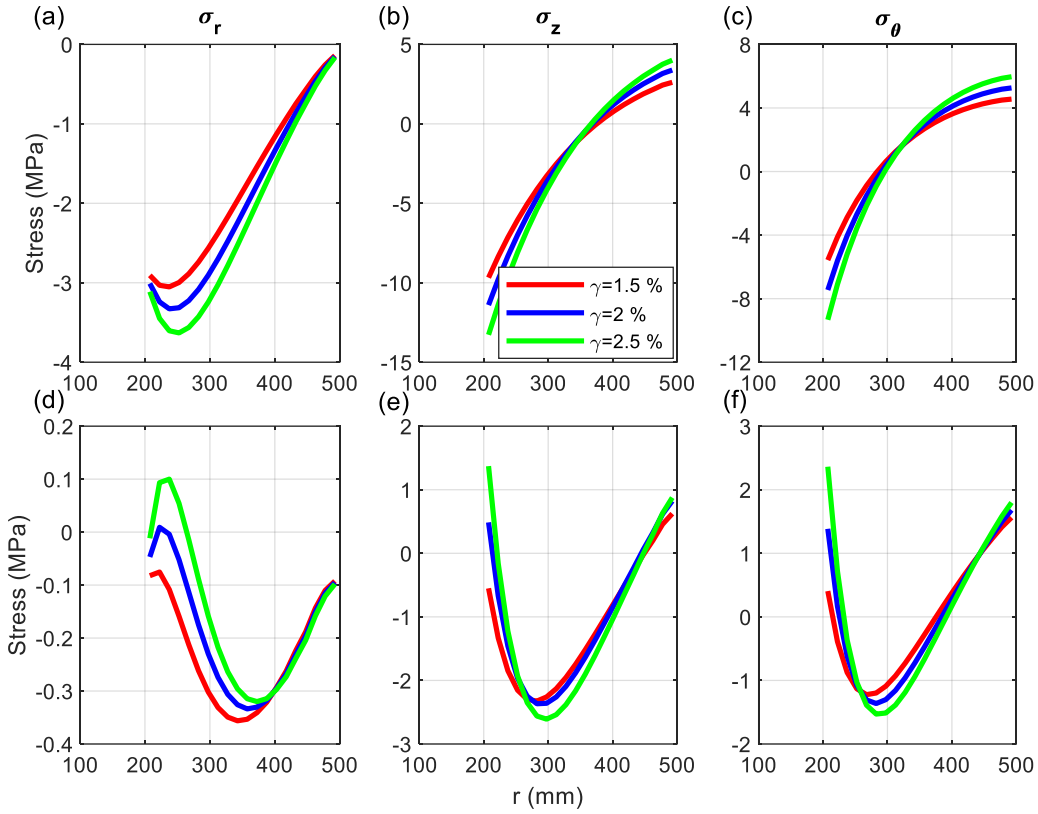

Figure A.25 Stress distribution along r-direction at the (a)-(c) middle and (d)-(f) end of the cycle for the pile design #1 for d_{in}=400 mm.

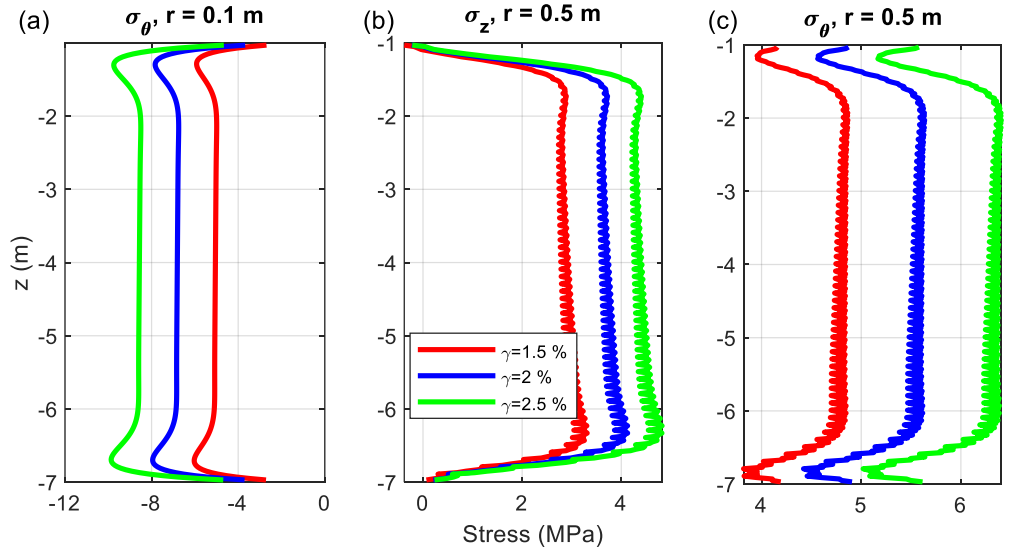

Figure A.26 Stress distribution along z-direction for various cycles at the (a)-(b) inner and (c)-(d) outer surface for pile design #1 for d_{in}=400 mm.

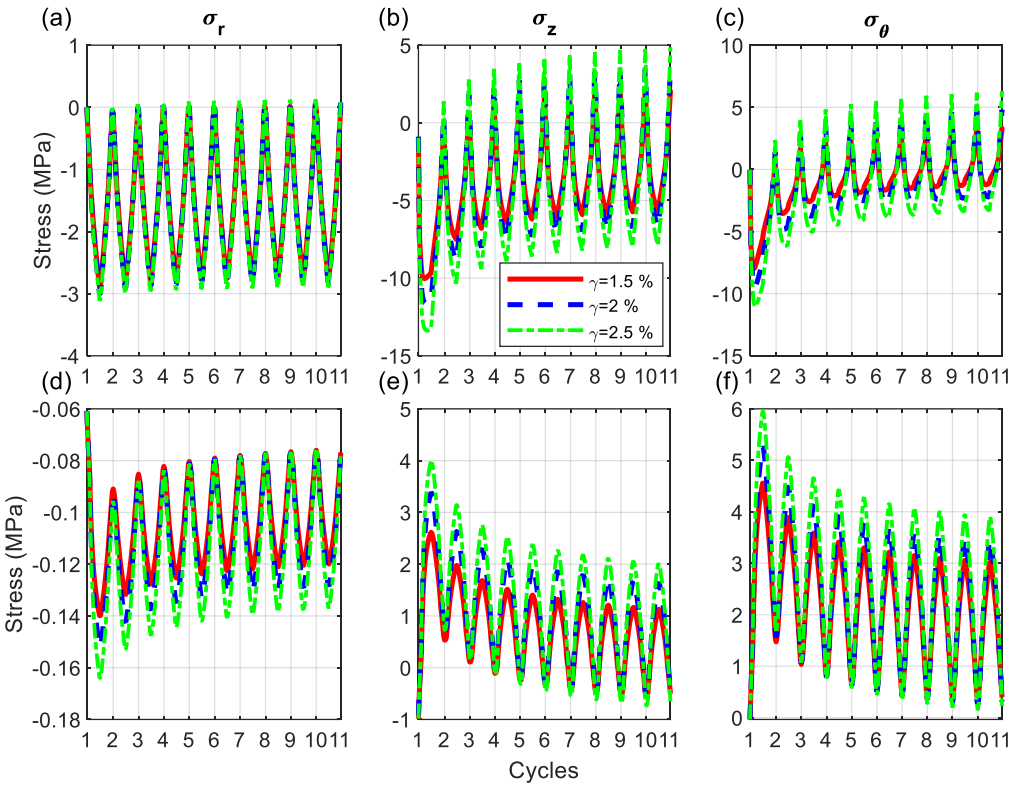

Figure A.27 Stress varying with 10 cycles for (a)-(c) inner and (d)-(f) outer surface for the pile design #1 for d_{in}=400 mm.

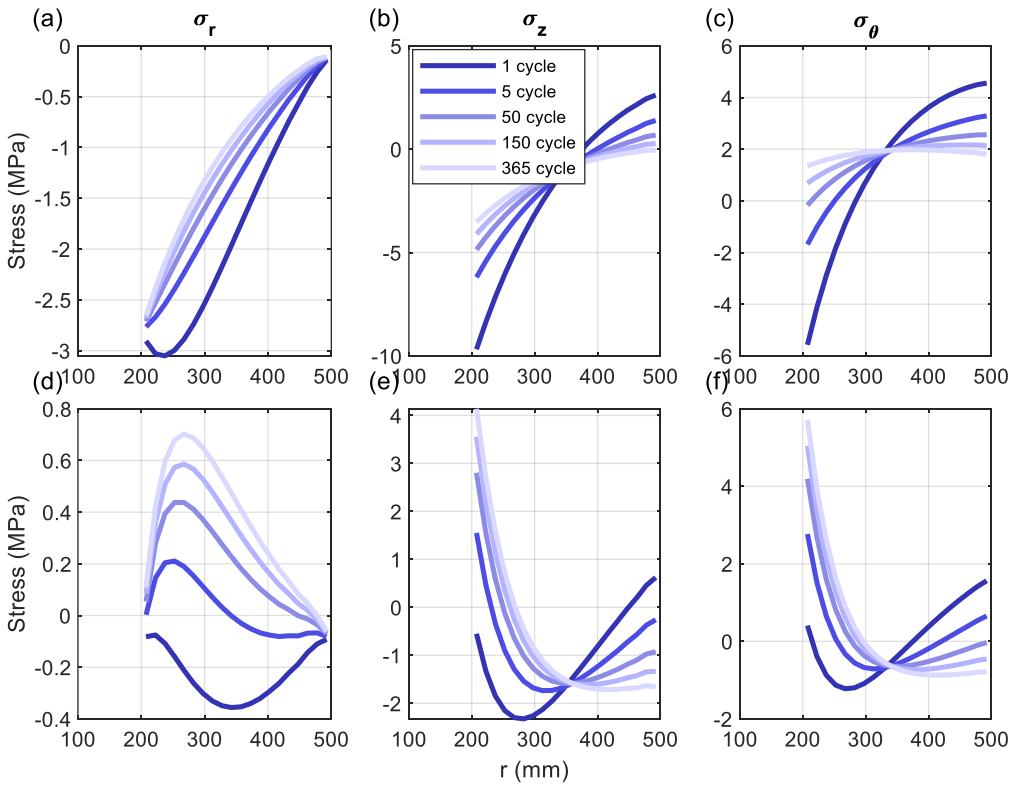

Figure A.28 Stress distribution along r-direction at the (a)-(c) middle and (d)-(f) end of the different cycles for the pile design #1 for γ=1.5%, d_{in}=400 mm.

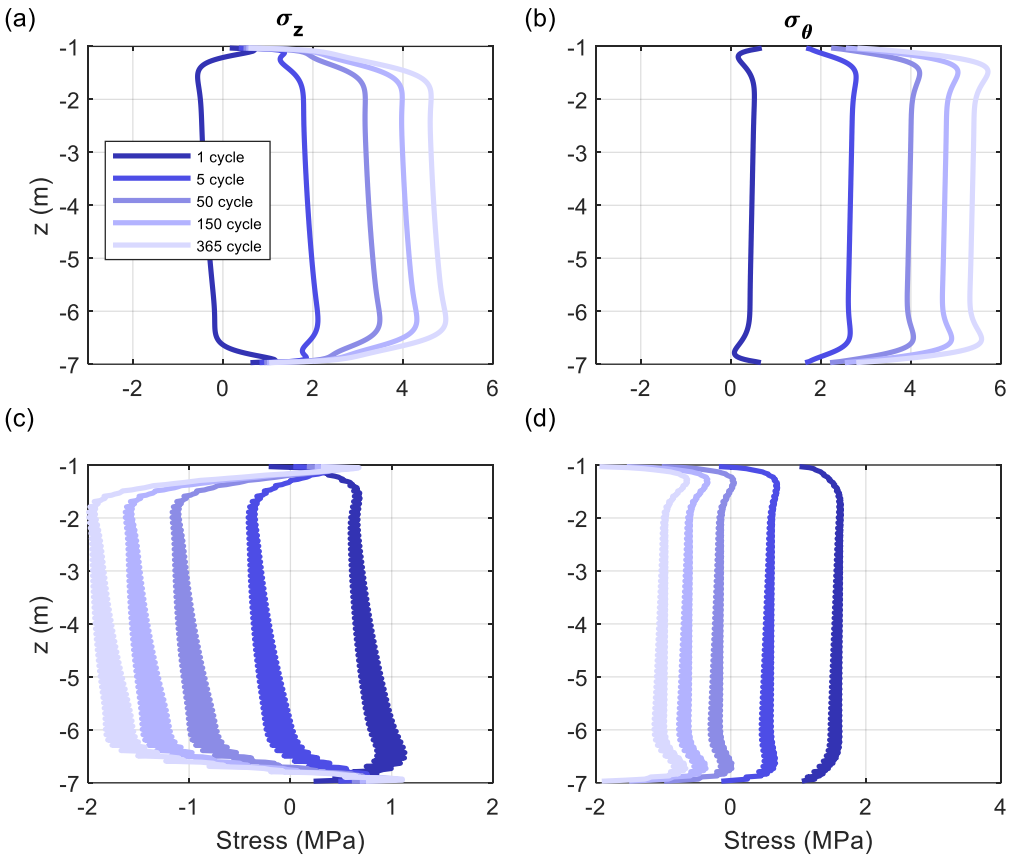

Figure A.29 Stress distribution along z-direction for various cycles at the (a)-(b) inner and (c)-(d) outer surface for pile design #1 for γ=1.5%, d_{in}=400 mm.

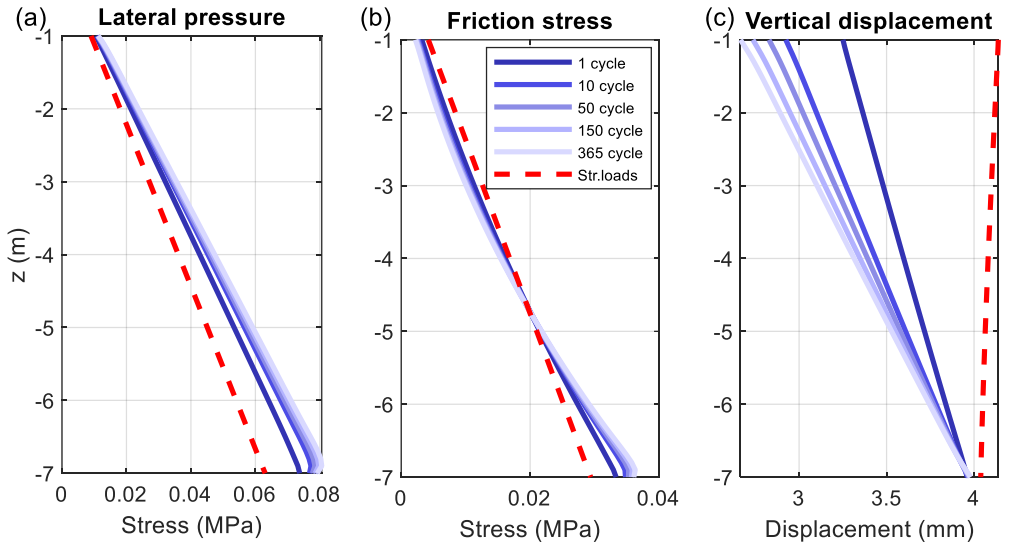

Figure A.30 Soil stresses and displacement along z-direction for various cycles under (a)-(c) combined loadings for pile design #1 for γ=1.5%, d_{in}=400 mm.

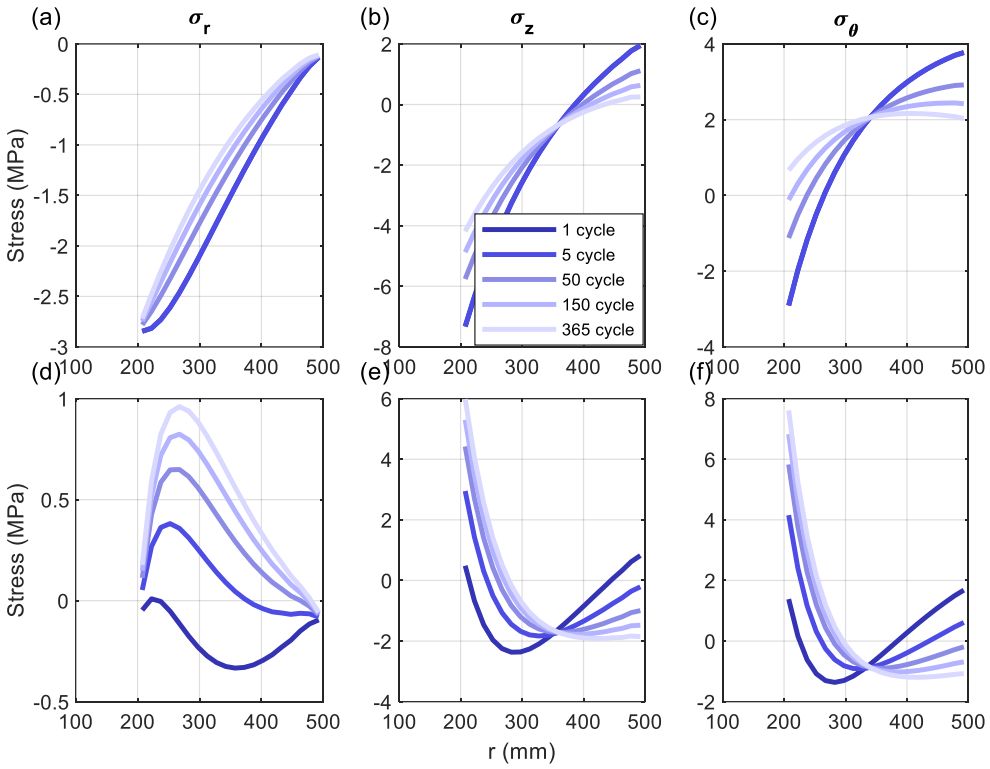

Figure A.31 Stress distribution along r-direction at the (a)-(c) middle and (d)-(f) end of the different cycles for the pile design #1 for γ=2%, d_{in}=400 mm.

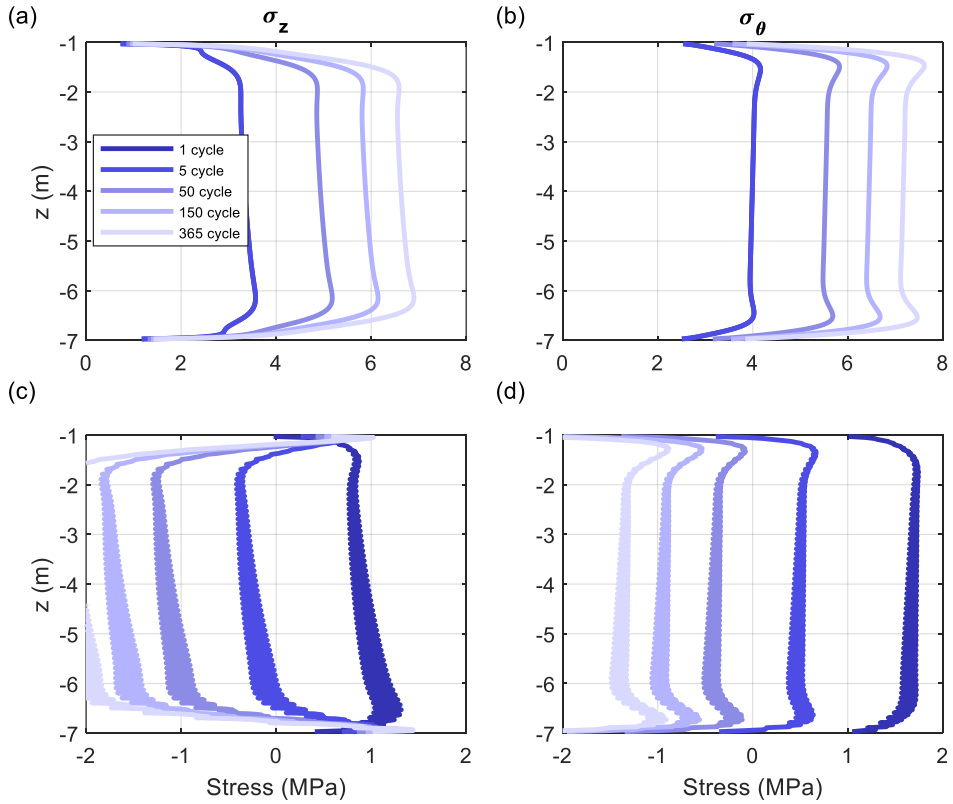

Figure A.32 Stress distribution along z-direction for various cycles at the (a)-(b) inner and (c)-(d) outer surface for pile design #1 for γ=2%, d_{in}=400 mm.

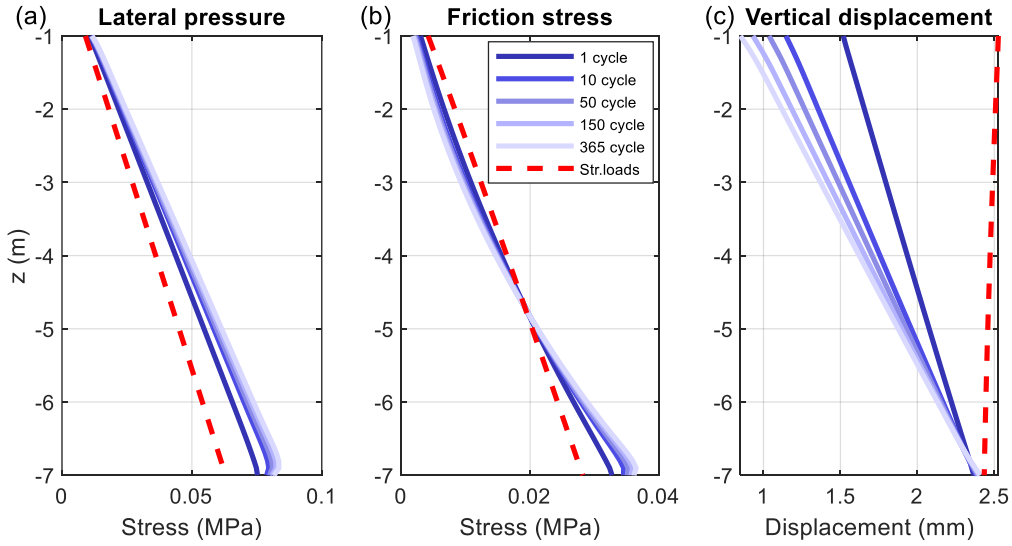

Figure A.33 Soil stresses and displacement along z-direction for various cycles under (a)-(c) combined loadings for pile design #1 for γ=2%, d_{in}=400 mm.

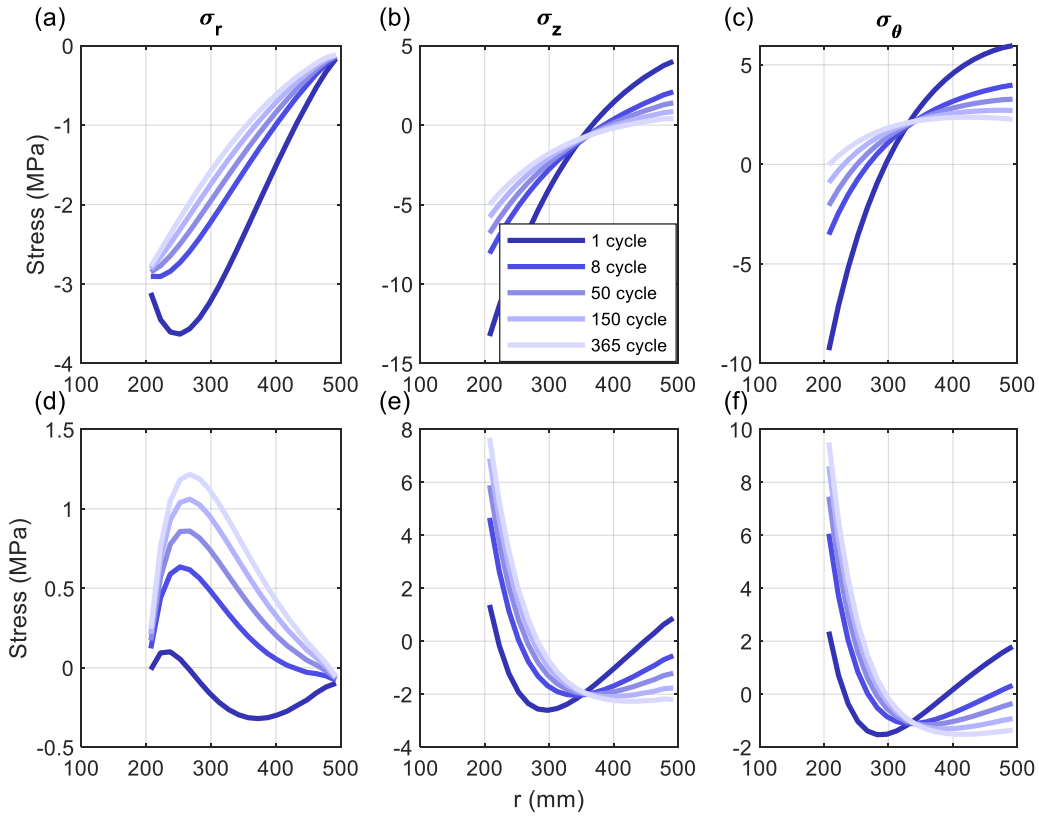

Figure A.34 Stress distribution along r-direction at the (a)-(c) middle and (d)-(f) end of the different cycles for the pile design #1 for γ=2.5%, d_{in}=400 mm.

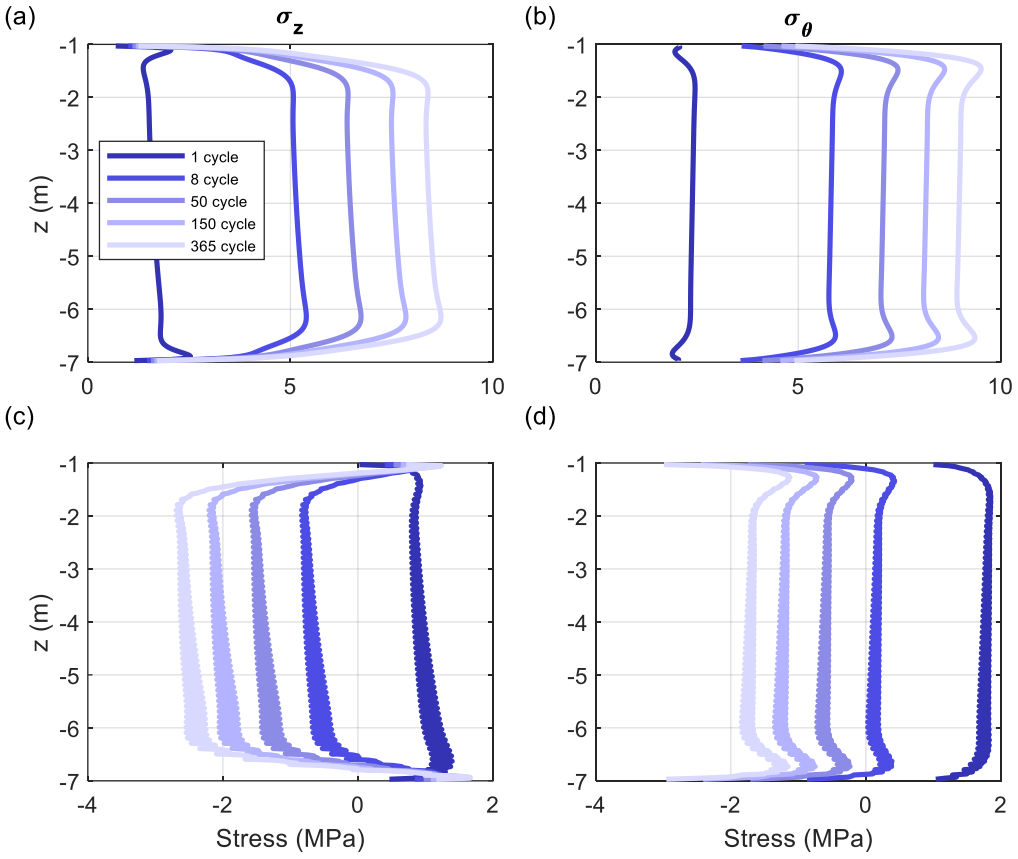

Figure A.35 Stress distribution along z-direction for various cycles at the (a)-(b) inner and (c)-(d) outer surface for pile design #1 for γ=2.5%, d_{in}=400 mm.

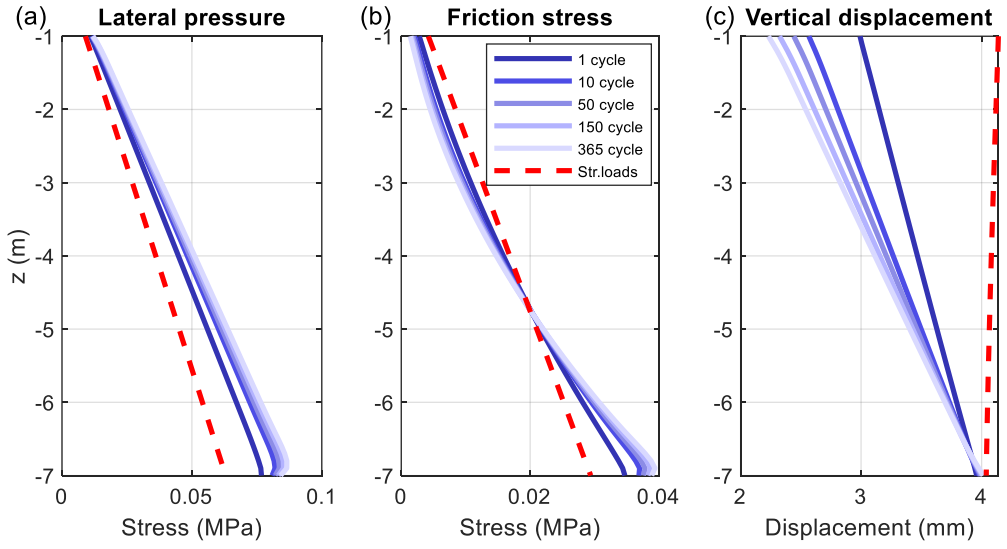

Figure A.36 Soil stresses and displacement along z-direction for various cycles under (a)-(c) combined loadings for pile design #1 for γ=2.5%, d_{in}=400 mm.

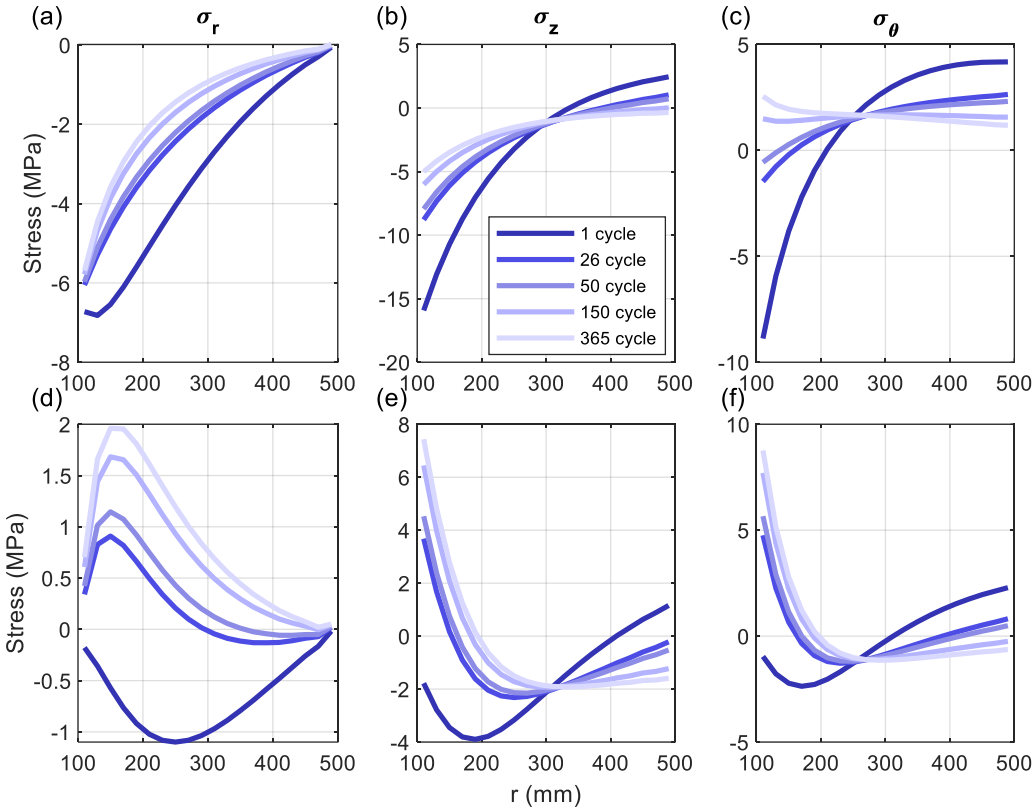

Figure A.37 Stress distribution along r-direction at the (a)-(c) middle and (d)-(f) end of the different cycles for the pile design #2 for γ=1.5%, d_{in}=200 mm.

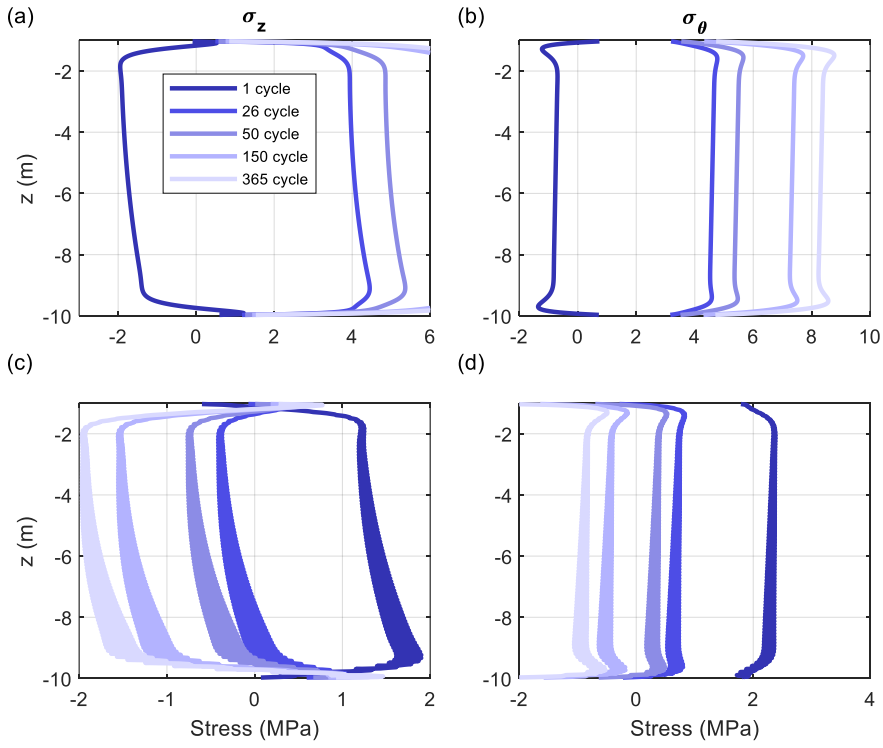

Figure A.38 Stress distribution along z-direction for various cycles at the (a)-(b) inner and (c)-(d) outer surface for pile design #2 for γ=1.5%, d_{in}=200 mm.

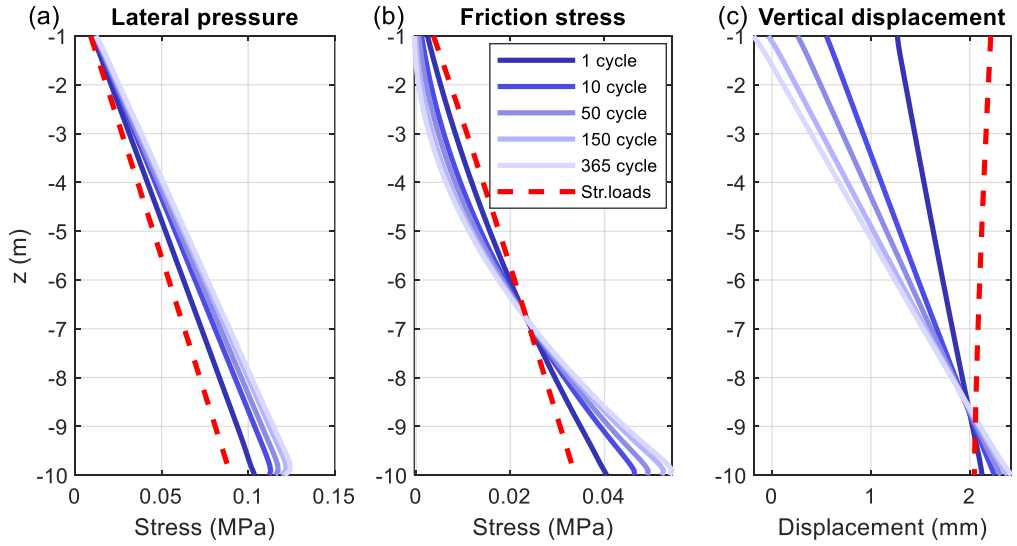

Figure A.39 Soil stresses and displacement along z-direction for various cycles under (a)-(c) combined loadings for pile design #2 for γ=1.5%, d_{in}=200 mm.

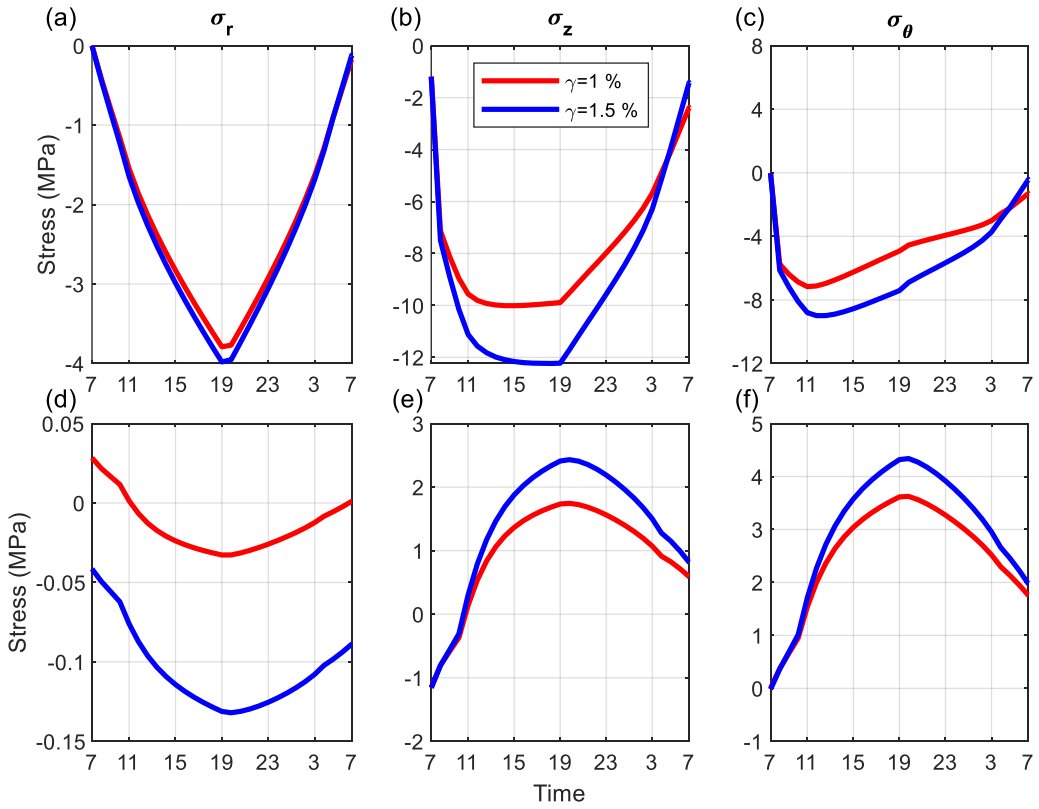

Figure A.40 Stress varying with 24-hour time at the (a)-(c) inner and (d)-(f) outer surface for the pile design #2 for d_{in}=300 mm.

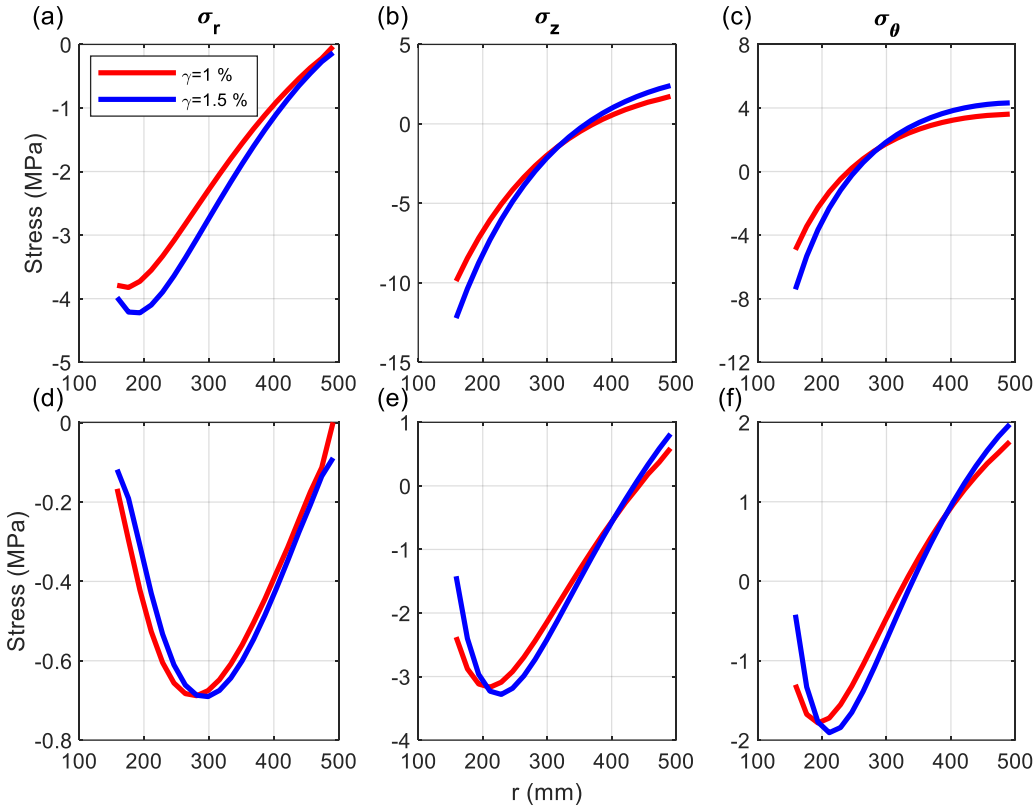

Figure A.41 Stress distribution along r-direction at the (a)-(c) middle and (d)-(f) end of the cycle for the pile design #2 for d_{in}=300 mm.

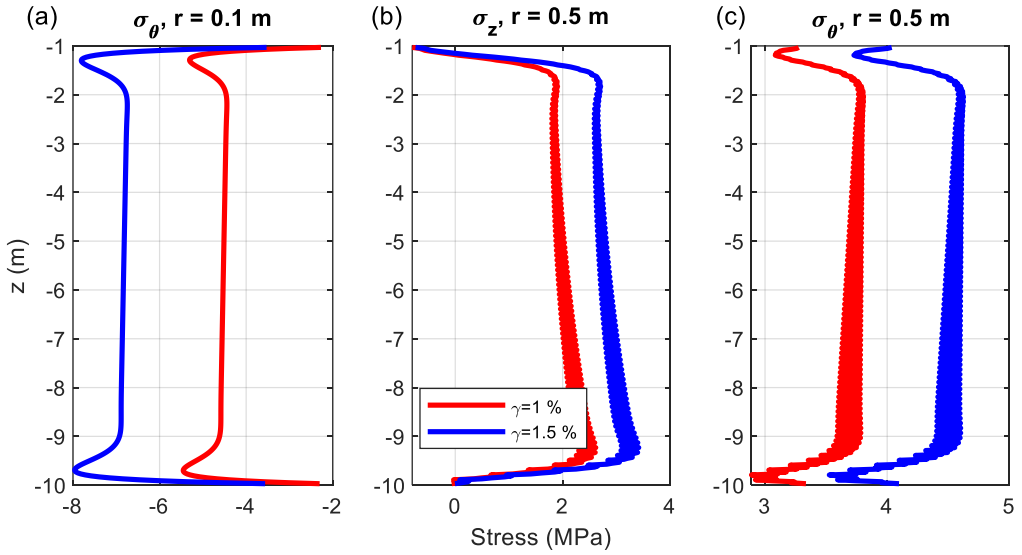

Figure A.42 Stress distribution along z-direction for various cycles at the (a)-(b) inner and (c)-(d) outer surface for pile design #2 for d_{in}=300 mm.

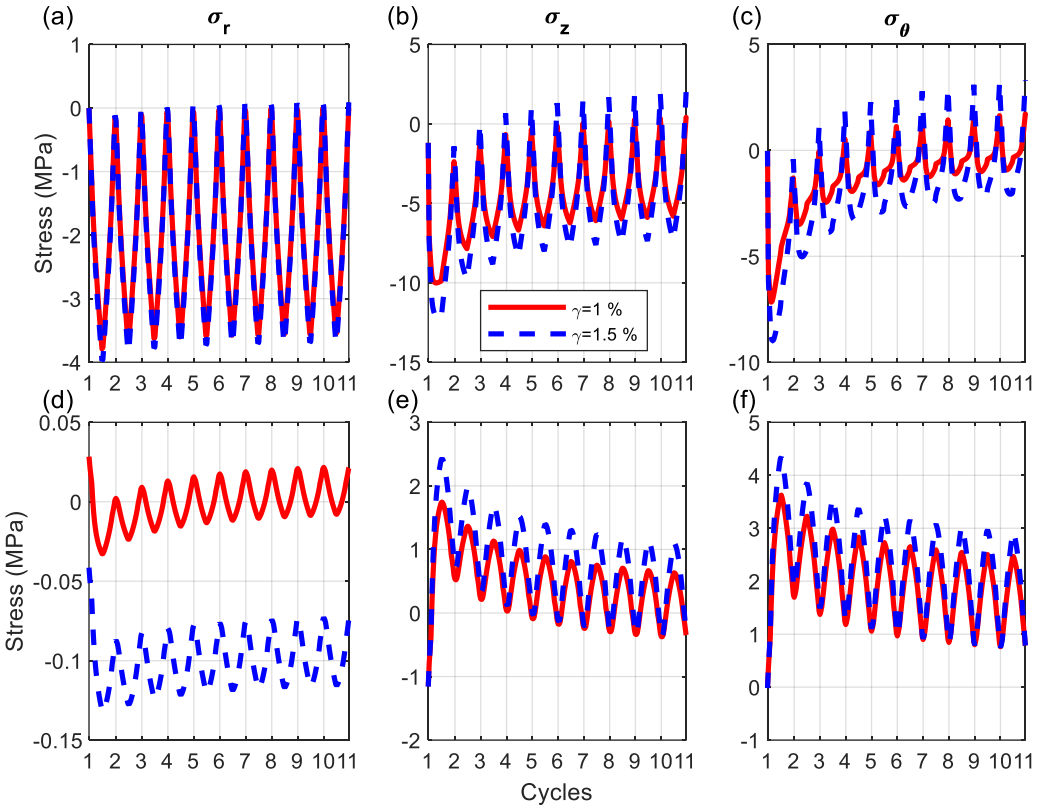

Figure A.43 Stress varying with 10 cycles for (a)-(c) inner and (d)-(f) outer surface for the pile design #2 for d_{in}=300 mm.

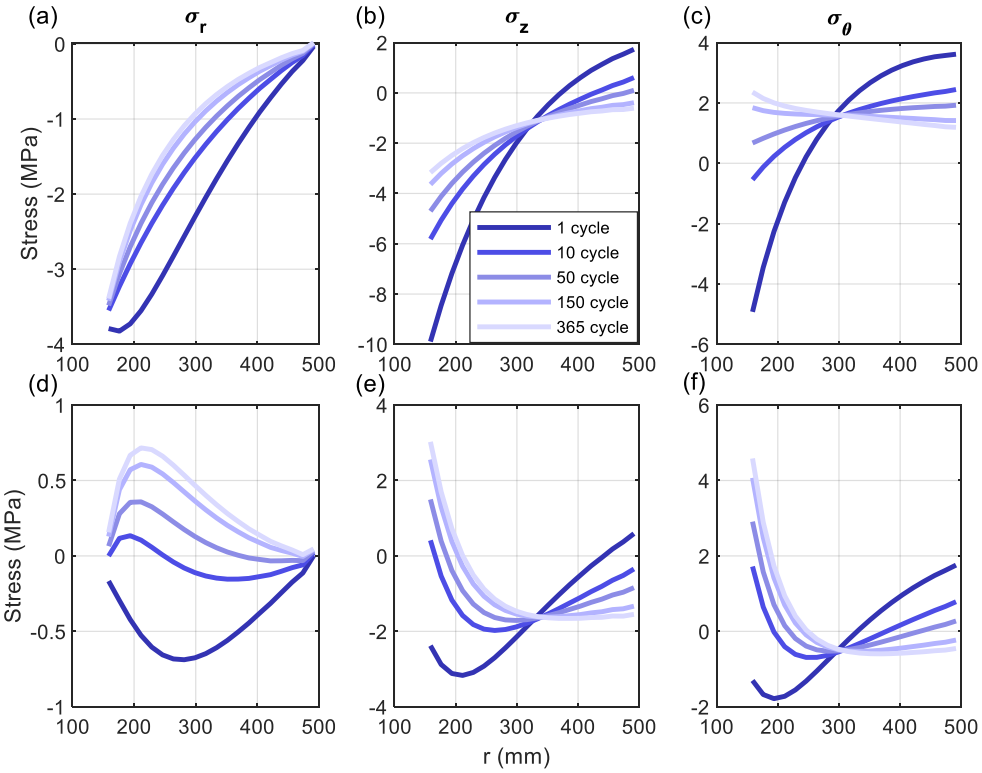

Figure A.44 Stress distribution along r-direction at the (a)-(c) middle and (d)-(f) end of the different cycles for the pile design #2 for γ=1%, d_{in}=300 mm.

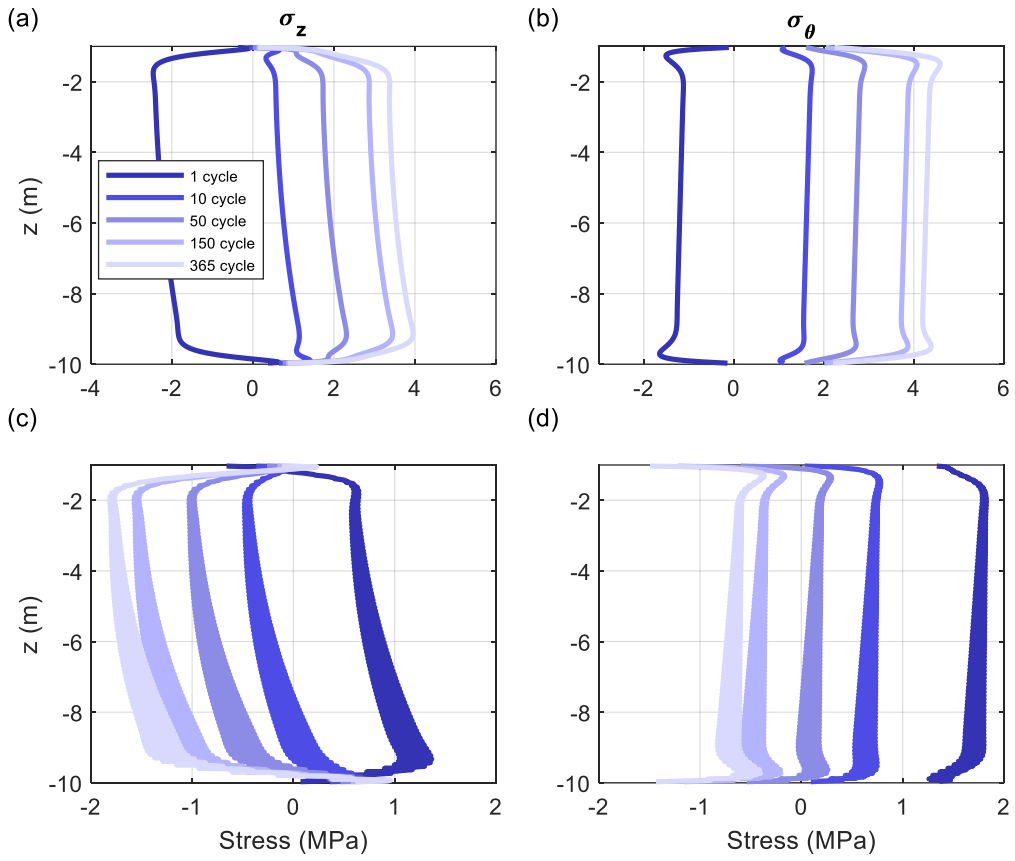

Figure A.45 Stress distribution along z-direction for various cycles at the (a)-(b) inner and (c)-(d) outer surface for pile design #2 for γ=1%, d_{in}=300 mm.

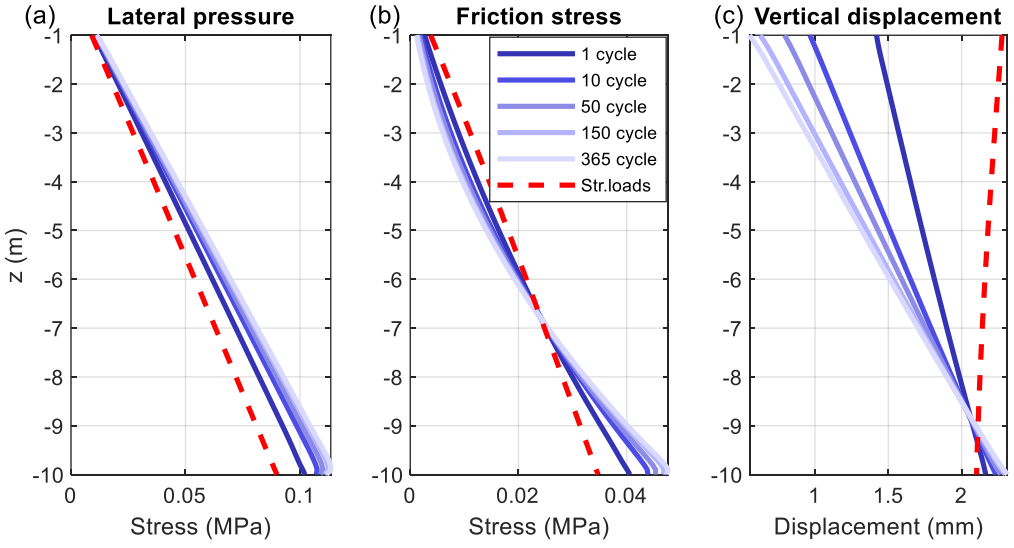

Figure A.46 Soil stresses and displacement along z-direction for various cycles under (a)-(c) combined loadings for pile design #2 for γ=1%, d_{in}=300 mm.

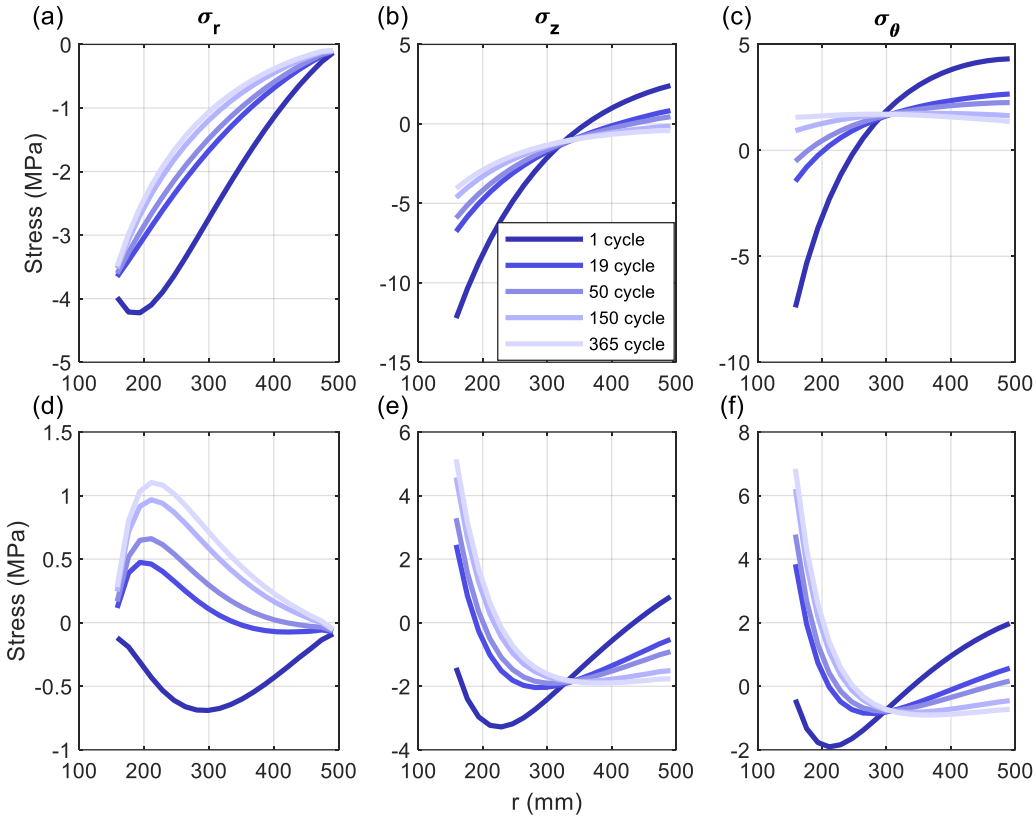

Figure A.47 Stress distribution along r-direction at the (a)-(c) middle and (d)-(f) end of the different cycles for the pile design #2 for γ=1.5%, d_{in}=300 mm.

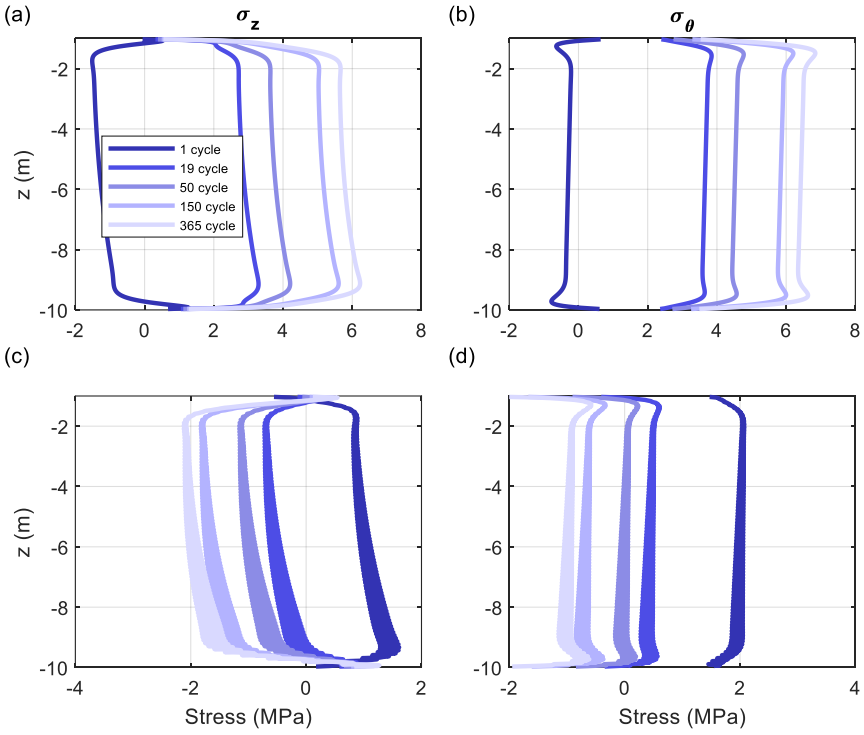

Figure A.48 Stress distribution along z-direction for various cycles at the (a)-(b) inner and (c)-(d) outer surface for pile design #2 for γ=1.5%, d_{in}=300 mm.

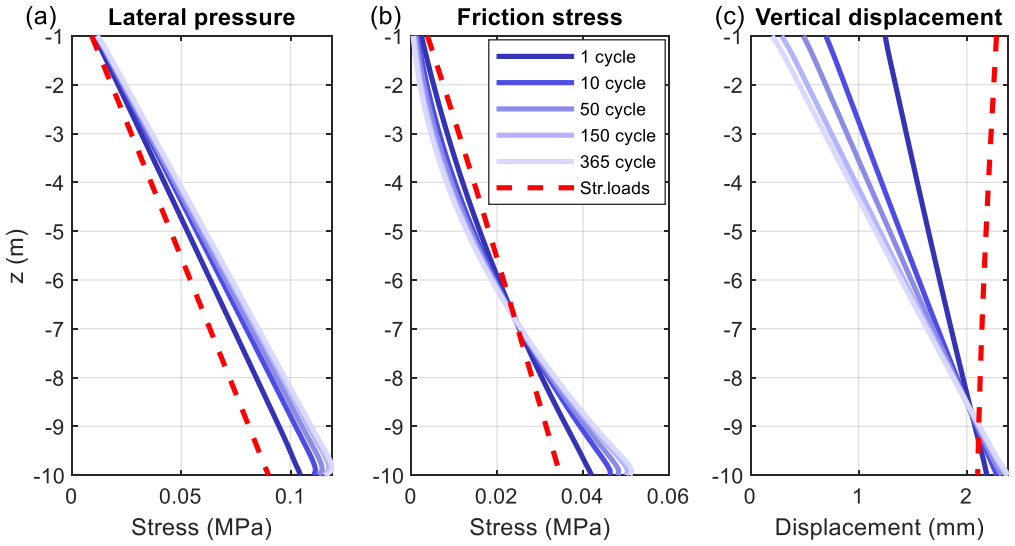

Figure A.49 Soil stresses and displacement along z-direction for various cycles under (a)-(c) combined loadings for pile design #2 for γ=1.5%, d_{in}=300 mm.

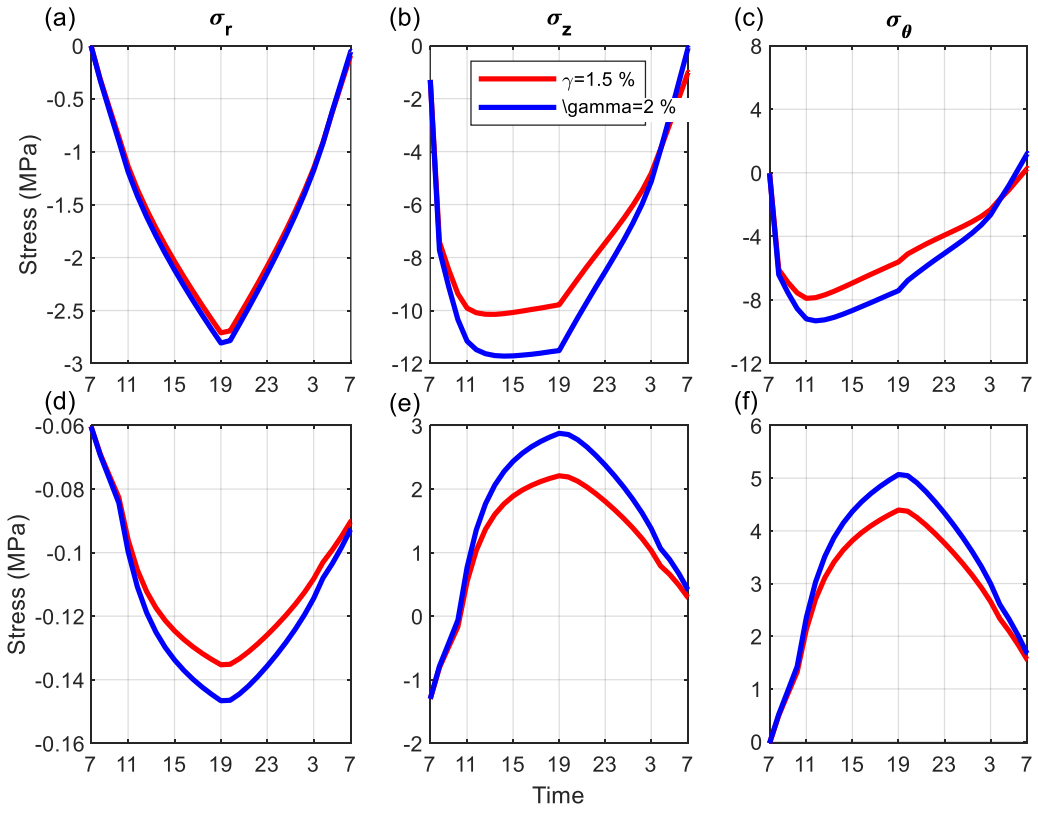

Figure A.50 Stress varying with 24-hour time at the (a)-(c) inner and (d)-(f) outer surface for the pile design #2 for d_{in}=400 mm.

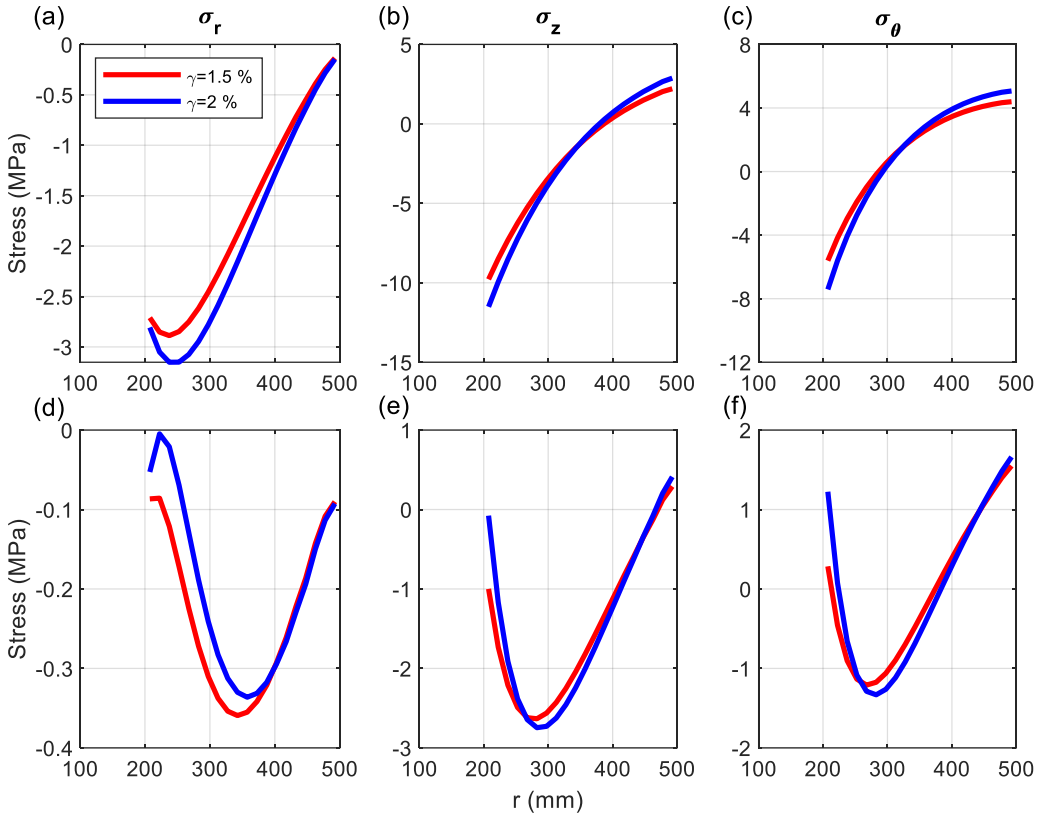

Figure A.51 Stress distribution along r-direction at the (a)-(c) middle and (d)-(f) end of the cycle for the pile design #2 for d_{in}=400 mm.

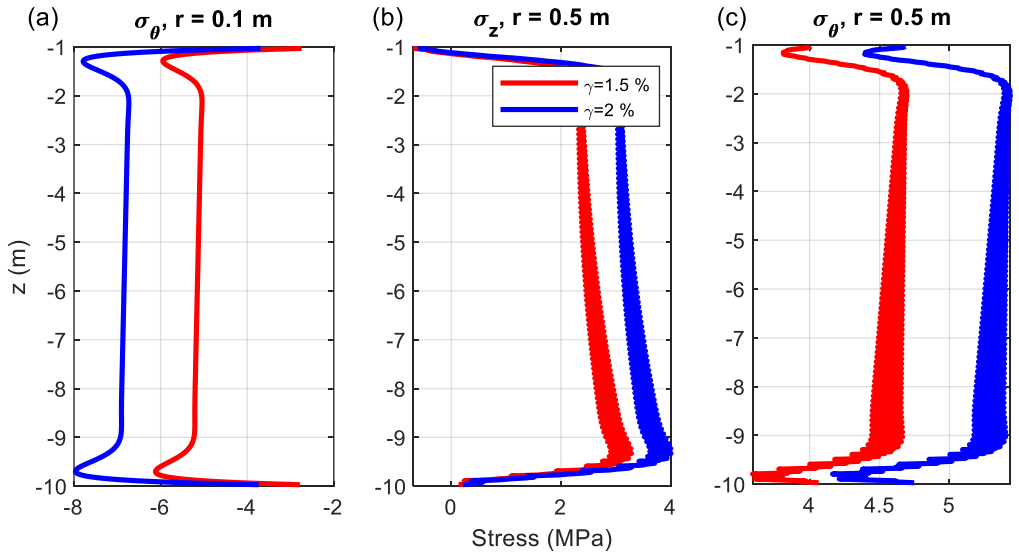

Figure A.52 Stress distribution along z-direction for various cycles at the (a)-(b) inner and (c)-(d) outer surface for pile design #2 for d_{in}=400 mm.

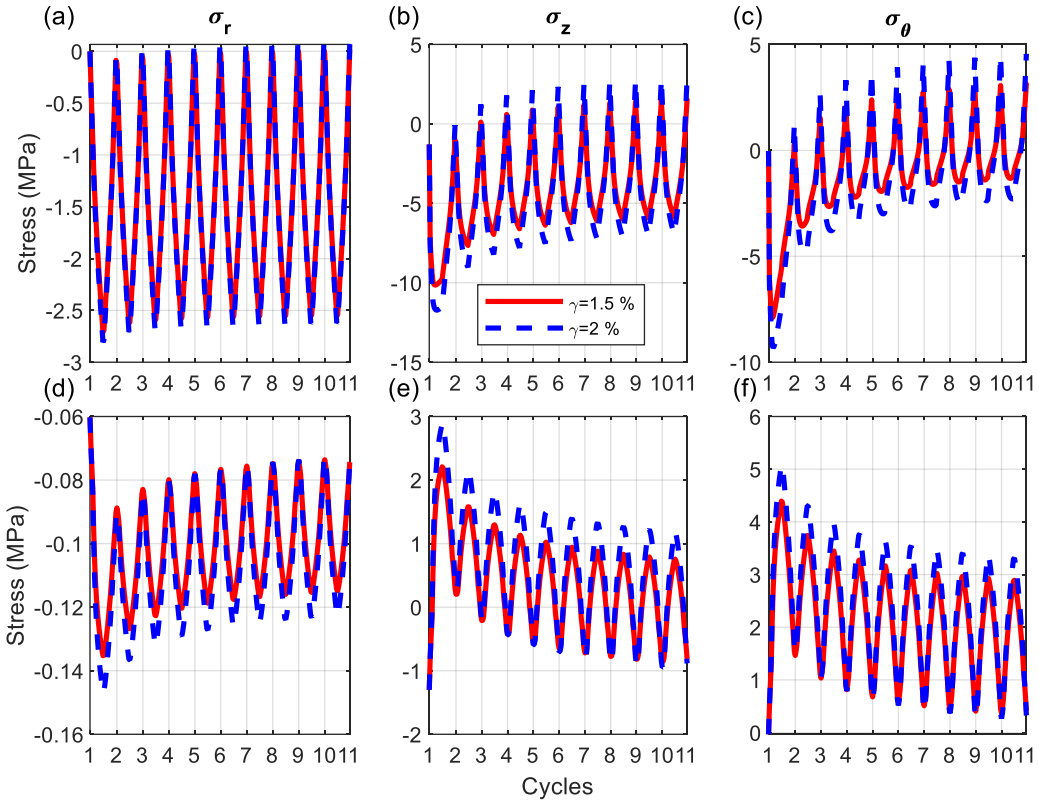

Figure A.53 Stress varying with 10 cycles for (a)-(c) inner and (d)-(f) outer surface for the pile design #2 for d_{in}=400 mm.

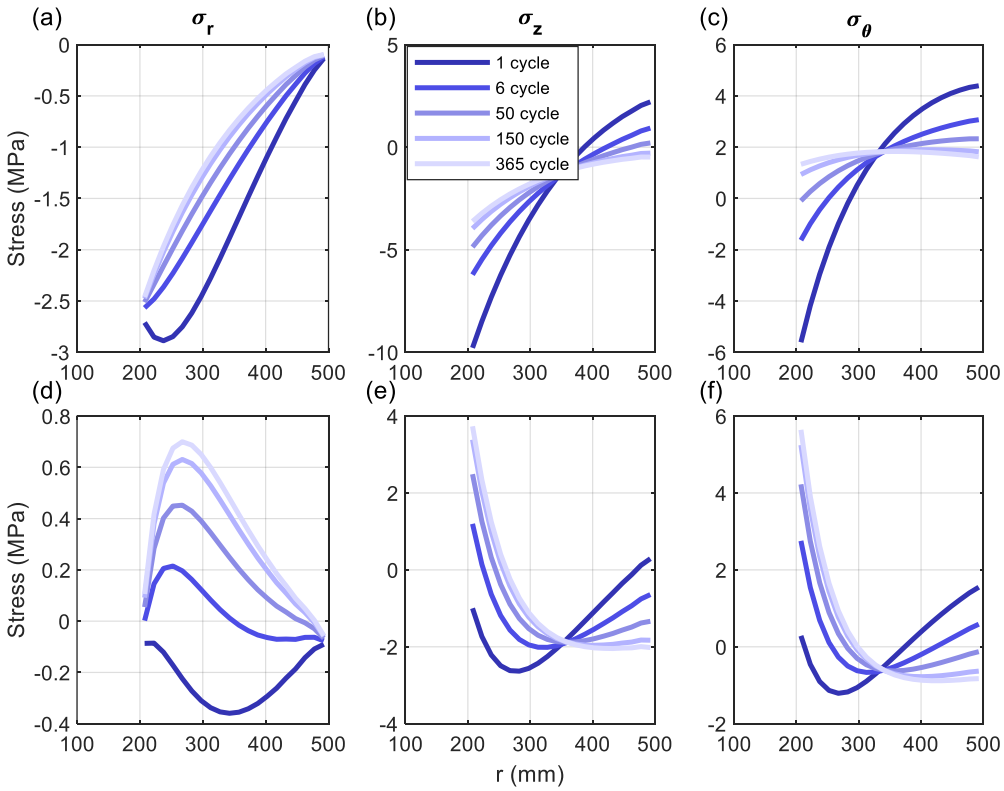

Figure A.54 Stress distribution along r-direction at the (a)-(c) middle and (d)-(f) end of the different cycles for the pile design #2 for γ=1.5%, d_{in}=400 mm.

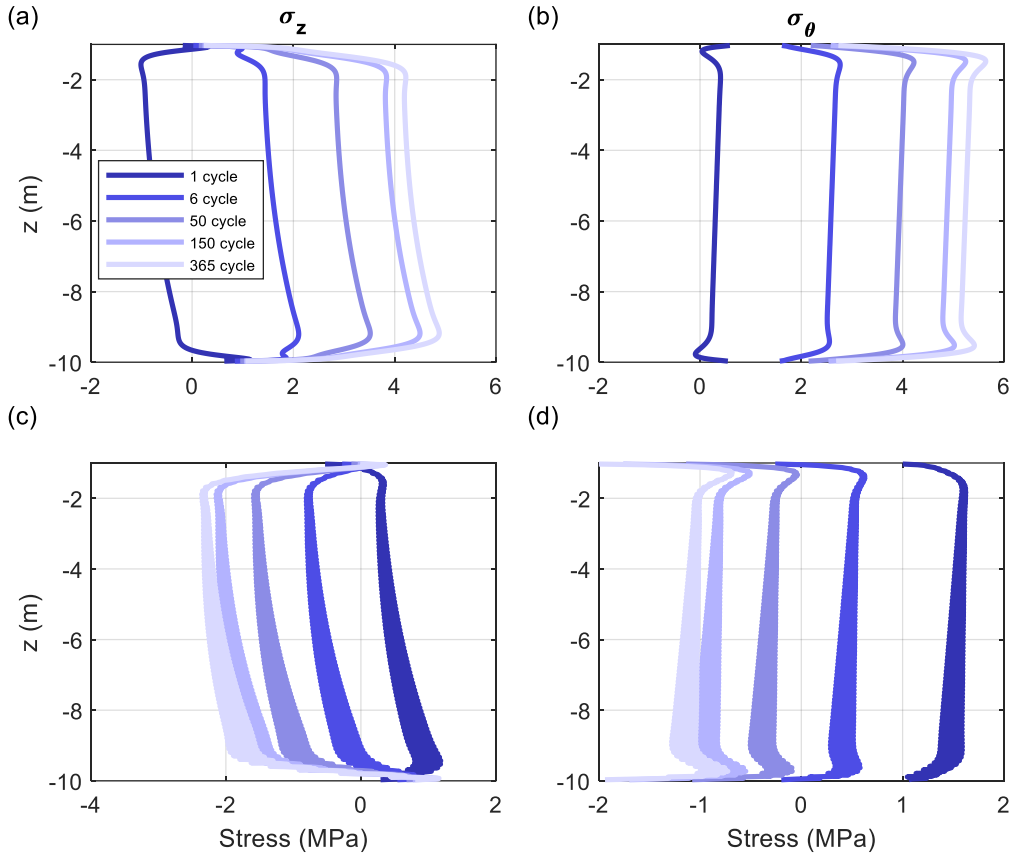

Figure A.55 Stress distribution along z-direction for various cycles at the (a)-(b) inner and (c)-(d) outer surface for pile design #2 for γ=1.5%, d_{in}=400 mm.

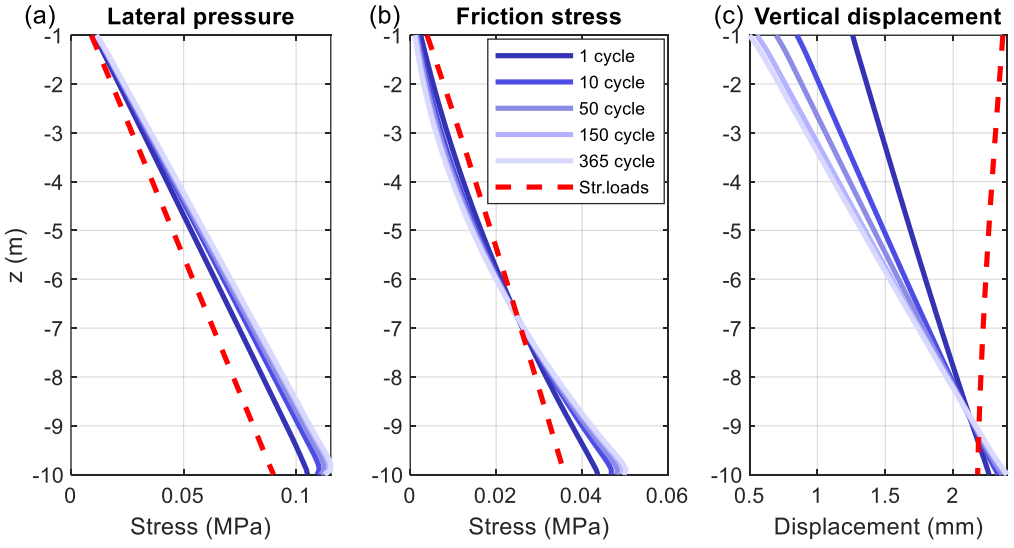

Figure A.56 Soil stresses and displacement along z-direction for various cycles under (a)-(c) combined loadings for pile design #2 for γ=1.5%, d_{in}=400 mm.

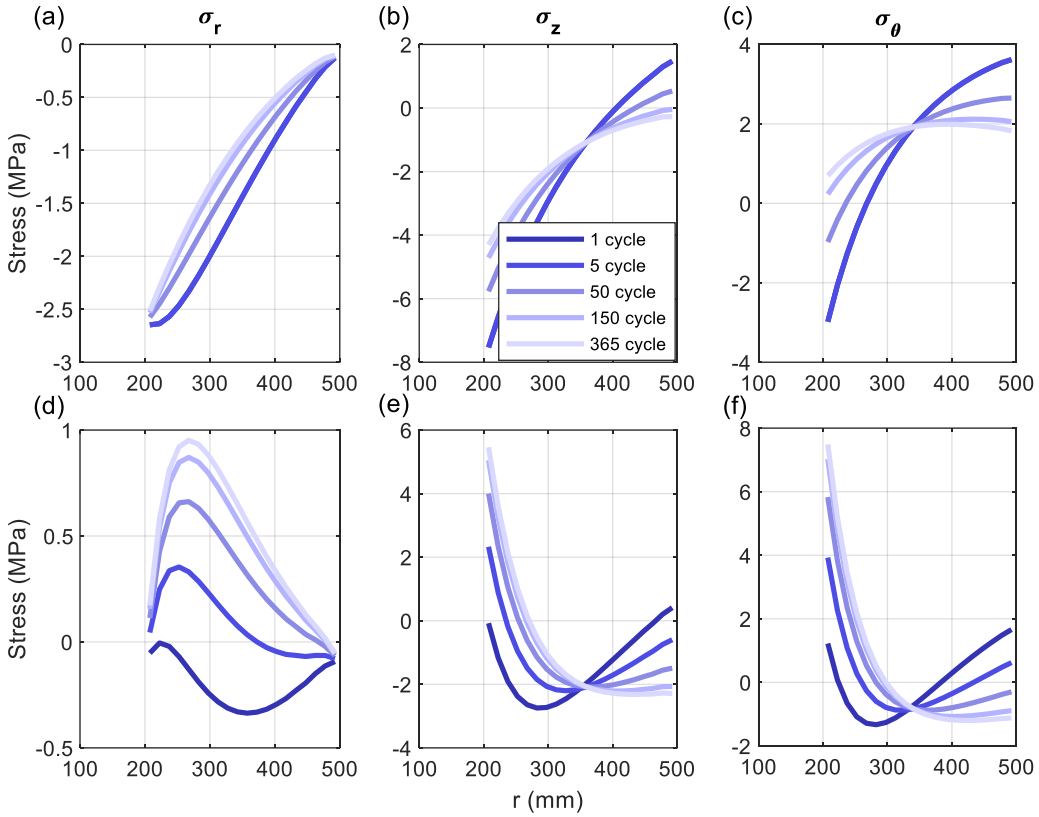

Figure A.57 Stress distribution along r-direction at the (a)-(c) middle and (d)-(f) end of the different cycles for the pile design #2 for γ=2%, d_{in}=400 mm.

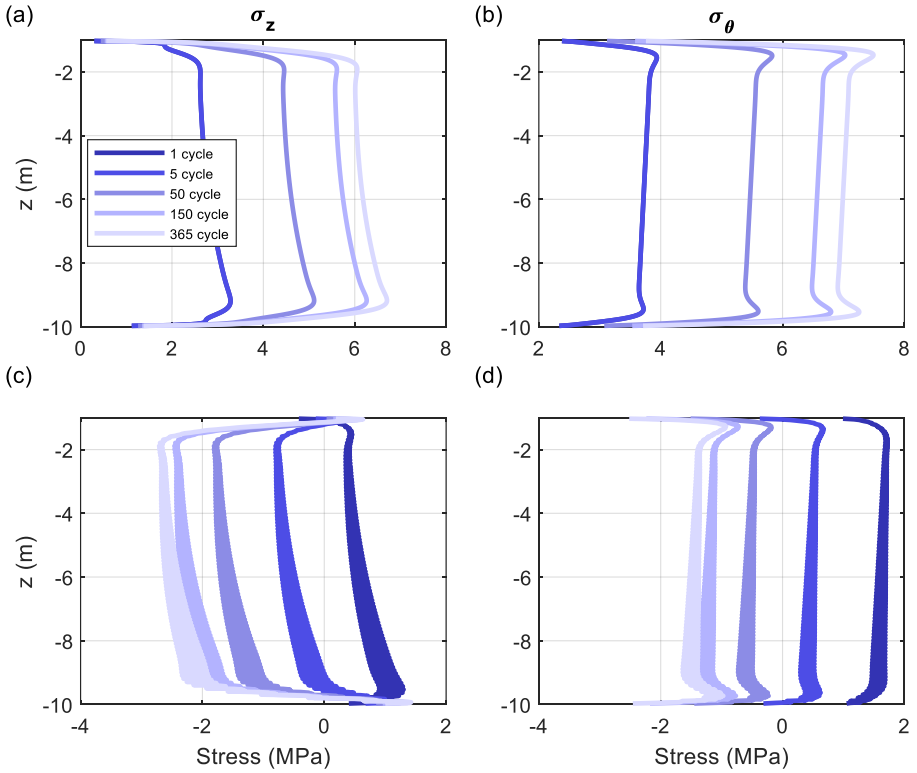

Figure A.58 Stress distribution along z-direction for various cycles at the (a)-(b) inner and (c)-(d) outer surface for pile design #2 for γ=2%, d_{in}=400 mm.

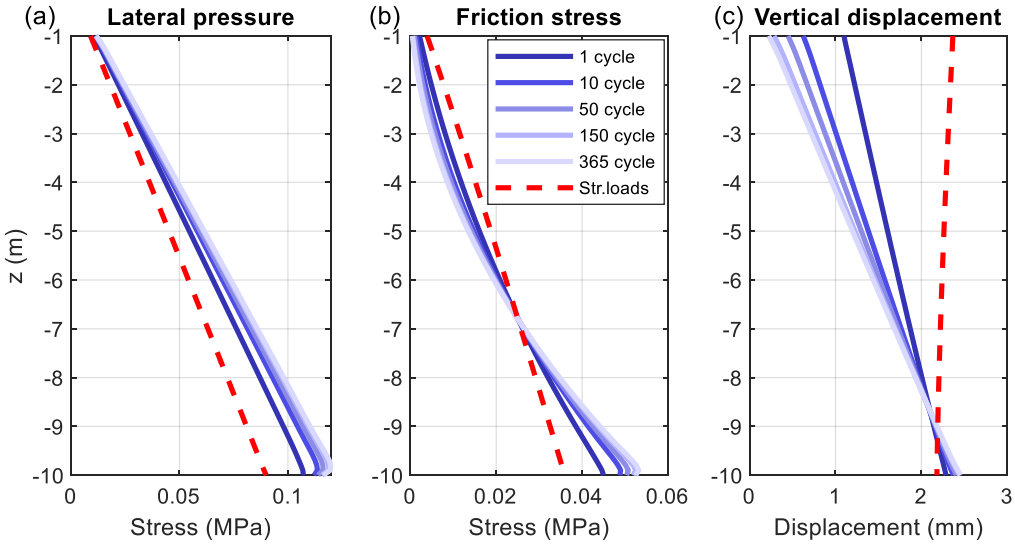

Figure A.59 Soil stresses and displacement along z-direction for various cycles under (a)-(c) combined loadings for pile design #2 for γ=2%, d_{in}=400 mm.

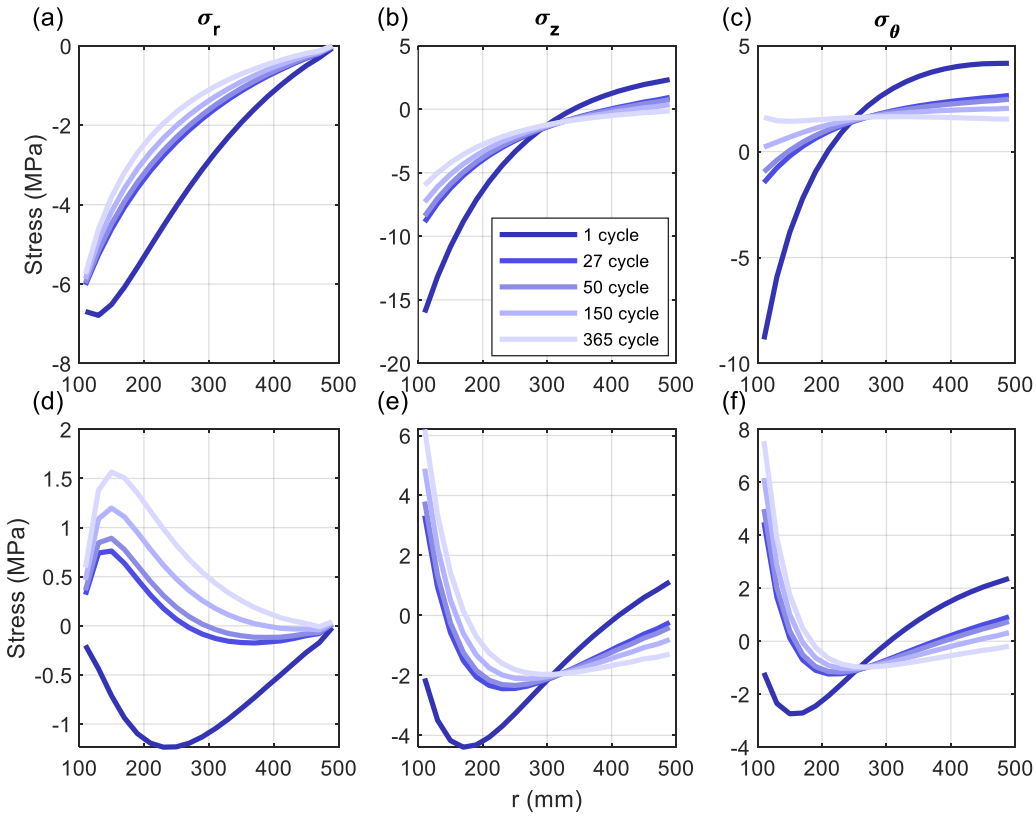

Figure A.60 Stress distribution along r-direction at the (a)-(c) middle and (d)-(f) end of the different cycles for the pile design #3 for γ=1.5%, d_{in}=200 mm.

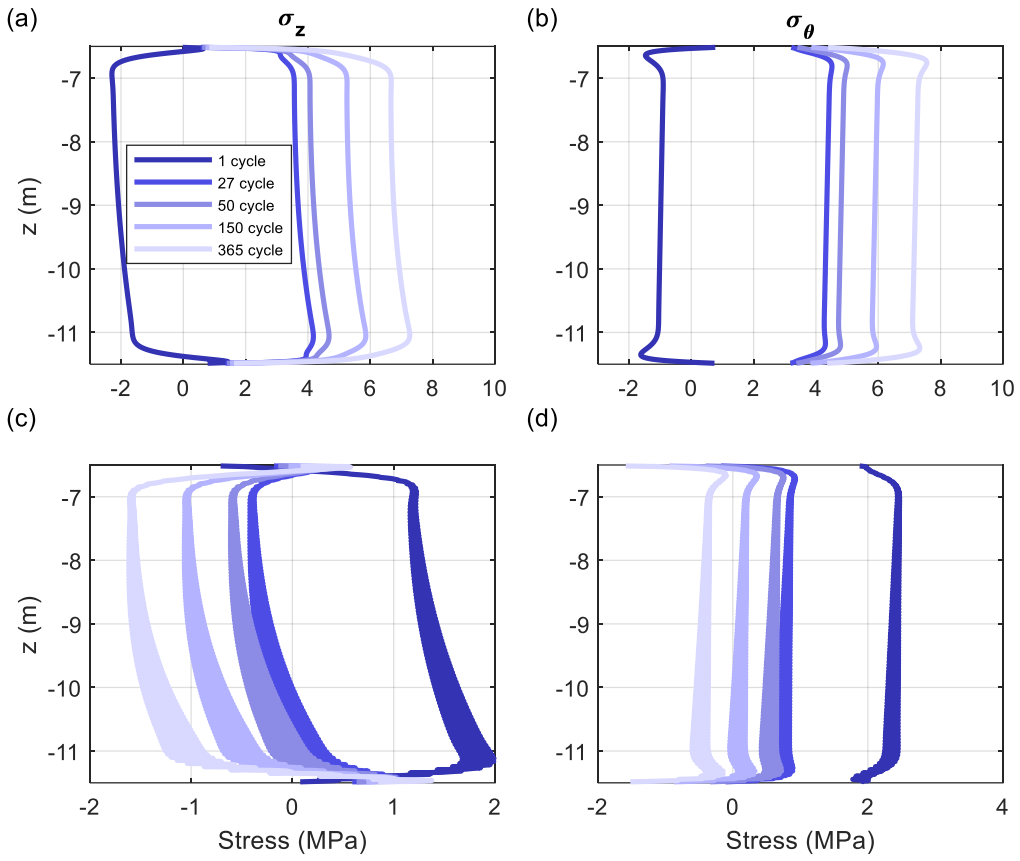

Figure A.61 Stress distribution along z-direction for various cycles at the (a)-(b) inner and (c)-(d) outer surface for pile design #3 for γ=1.5%, d_{in}=200 mm.

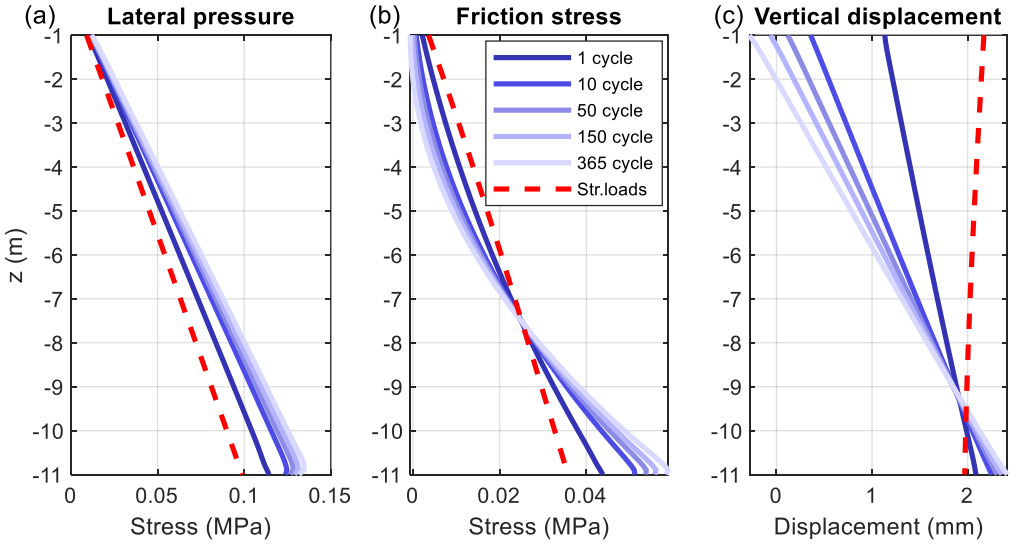

Figure A.62 Soil stresses and displacement along z-direction for various cycles under (a)-(c) combined loadings for pile design #3 for γ=1.5%, d_{in}=200 mm.

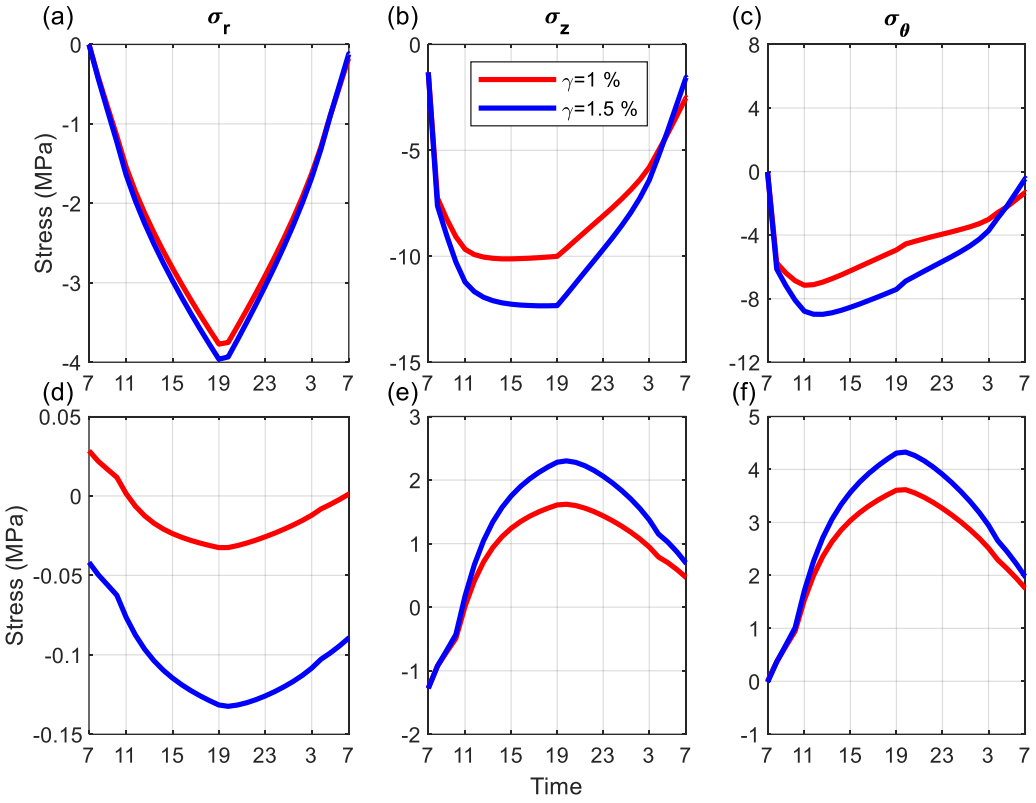

Figure A.63 Stress varying with 24-hour time at the (a)-(c) inner and (d)-(f) outer surface for the pile design #3 for d_{in}=300 mm.

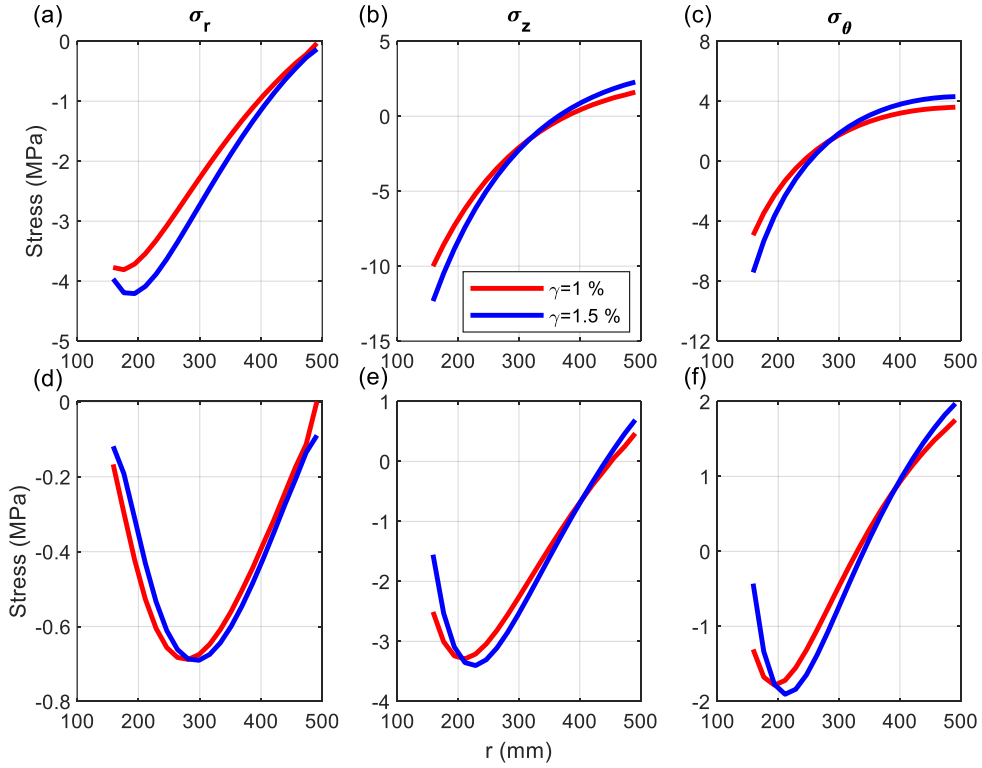

Figure A.64 Stress distribution along r-direction at the (a)-(c) middle and (d)-(f) end of the cycle for the pile design #3 for d_{in}=300 mm.

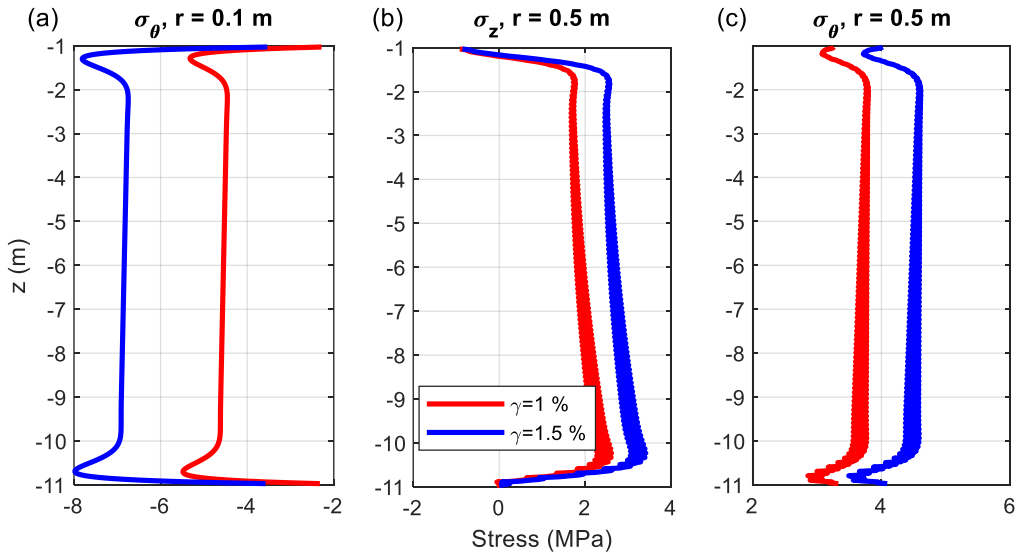

Figure A.65 Stress distribution along z-direction for various cycles at the (a)-(b) inner and (c)-(d) outer surface for pile design #3 for d_{in}=300 mm.

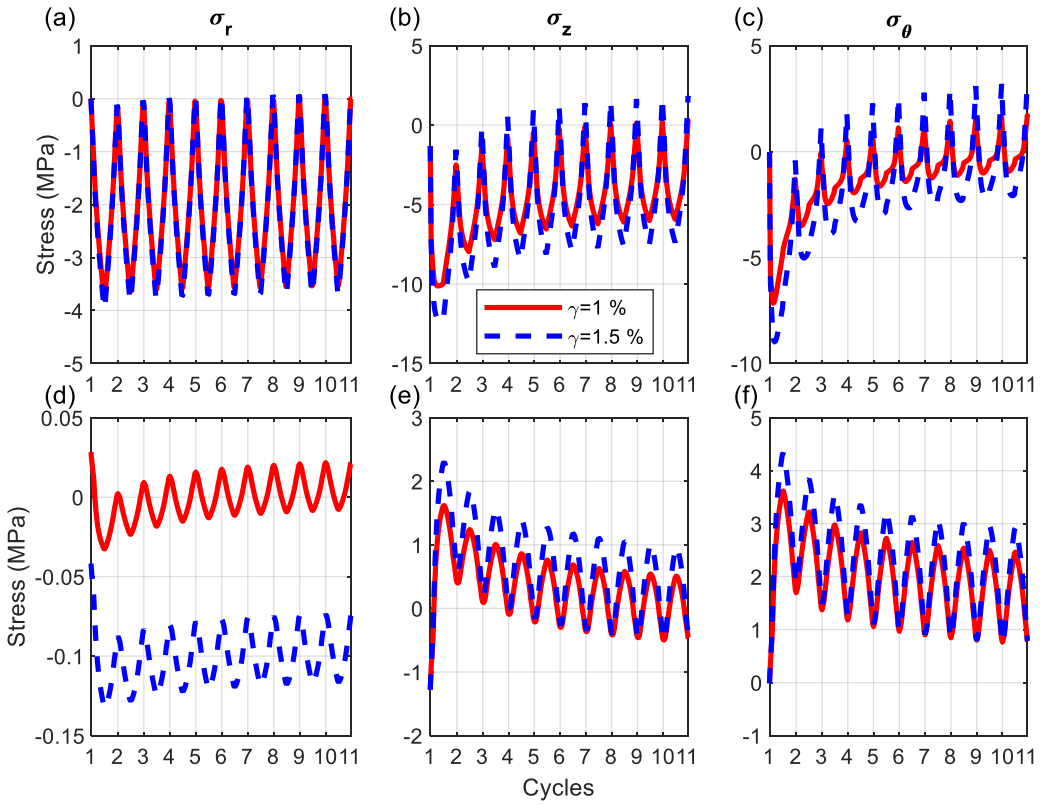

Figure A.66 Stress varying with 10 cycles for (a)-(c) inner and (d)-(f) outer surface for the pile design #3 for d_{in}=300 mm.

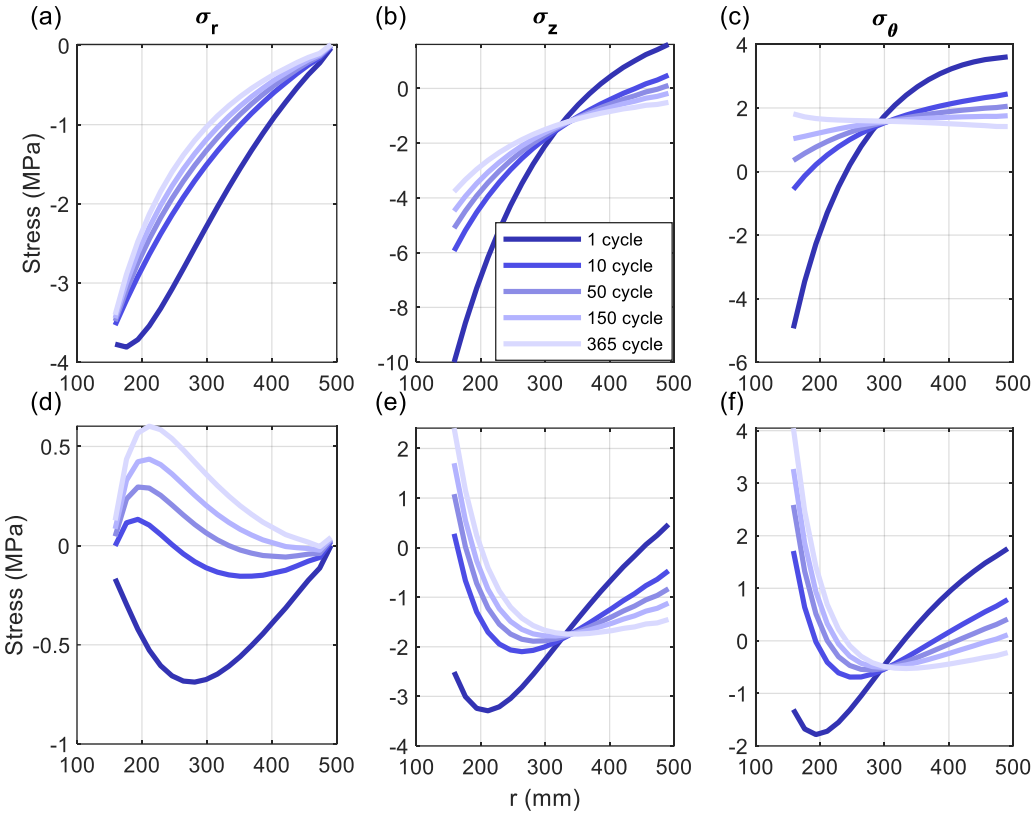

Figure A.67 Stress distribution along r-direction at the (a)-(c) middle and (d)-(f) end of the different cycles for the pile design #3 for γ=1 %, d_{in}=300 mm.

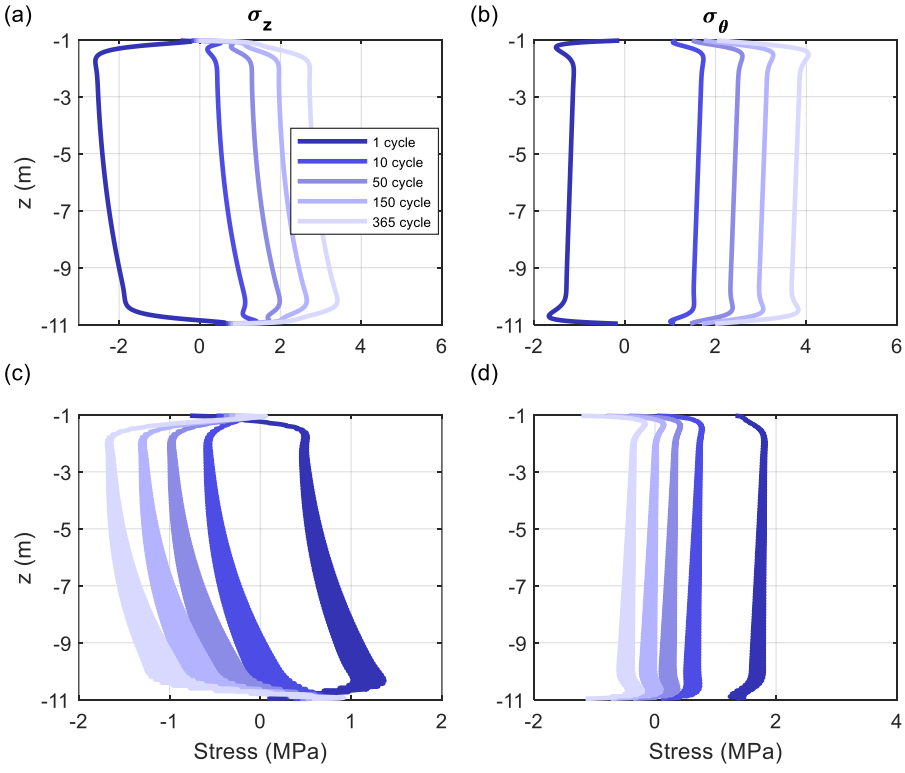

Figure A.68 Stress distribution along z-direction for various cycles at the (a)-(b) inner and (c)-(d) outer surface for pile design #3 for γ=1%, d_{in}=300 mm.

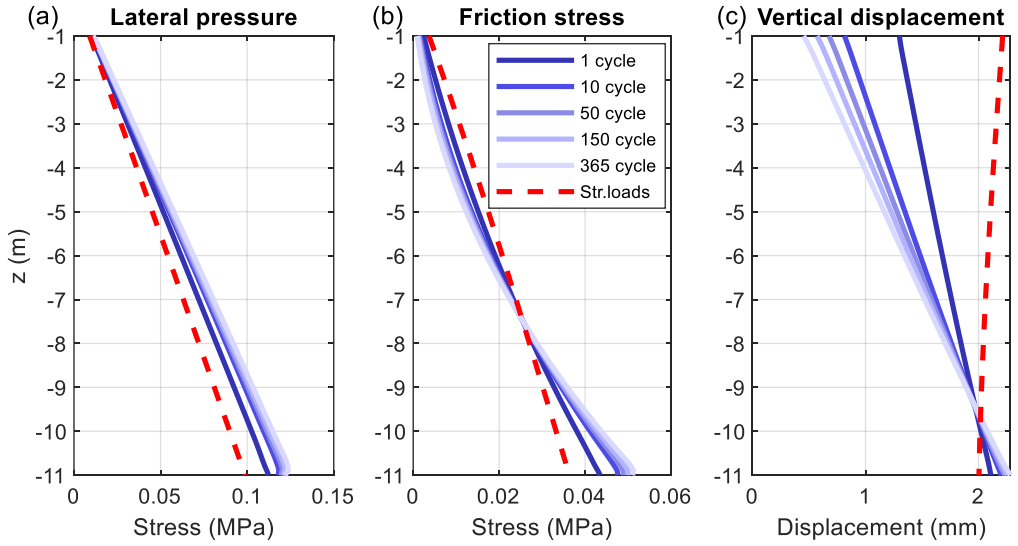

Figure A.69 Soil stresses and displacement along z-direction for various cycles under (a)-(c) combined loadings for pile design #3 for γ=1%, d_{in}=300 mm.

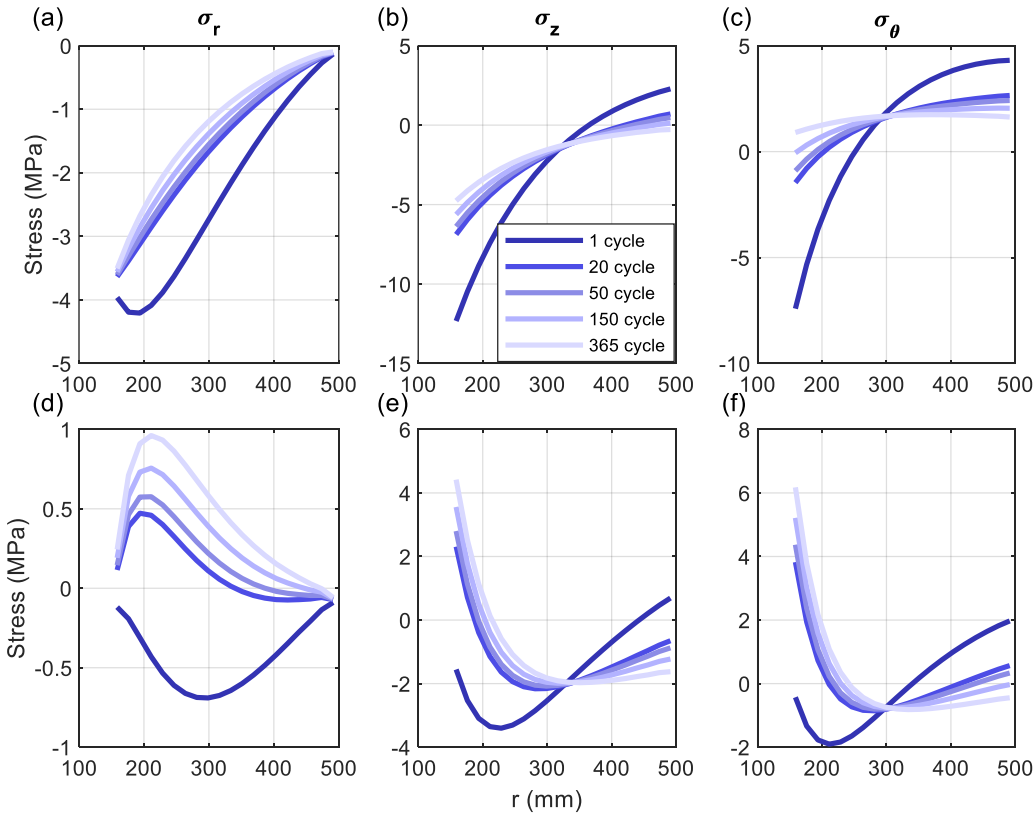

Figure A.70 Stress distribution along r-direction at the (a)-(c) middle and (d)-(f) end of the different cycles for the pile design #3 for γ=1.5 %, d_{in}=300 mm.

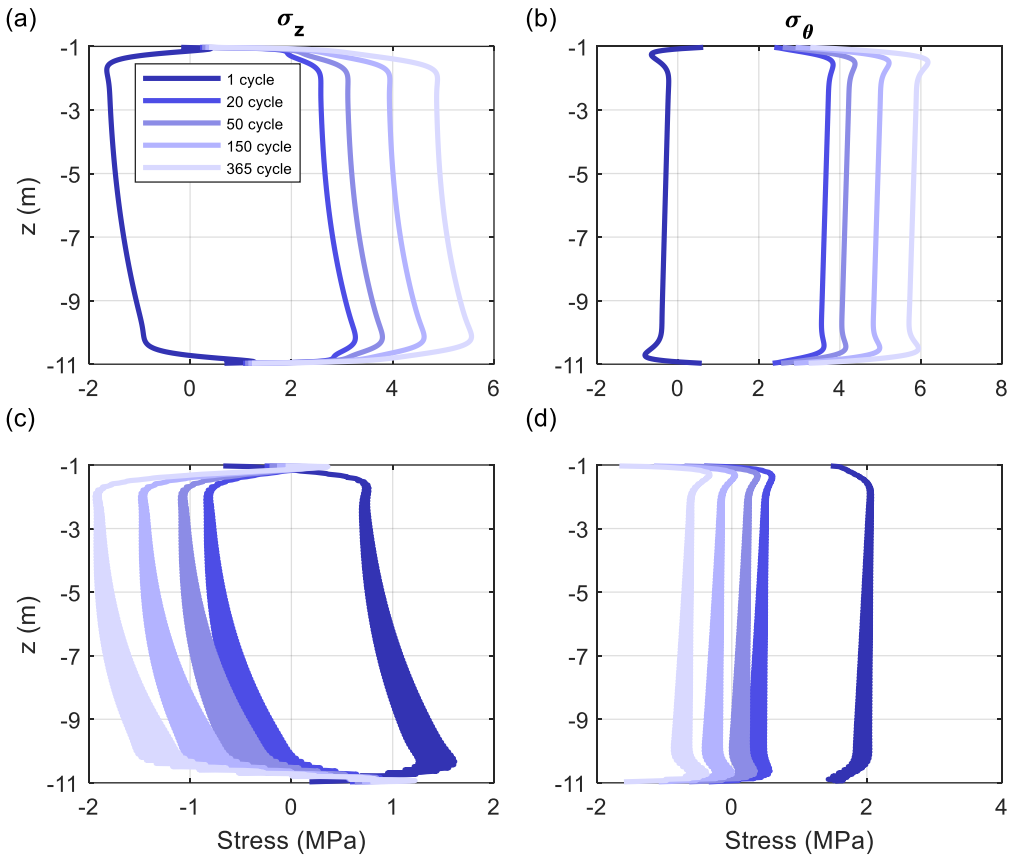

Figure A.71 Stress distribution along z-direction for various cycles at the (a)-(b) inner and (c)-(d) outer surface for pile design #3 for γ=1.5%, d_{in}=300 mm.

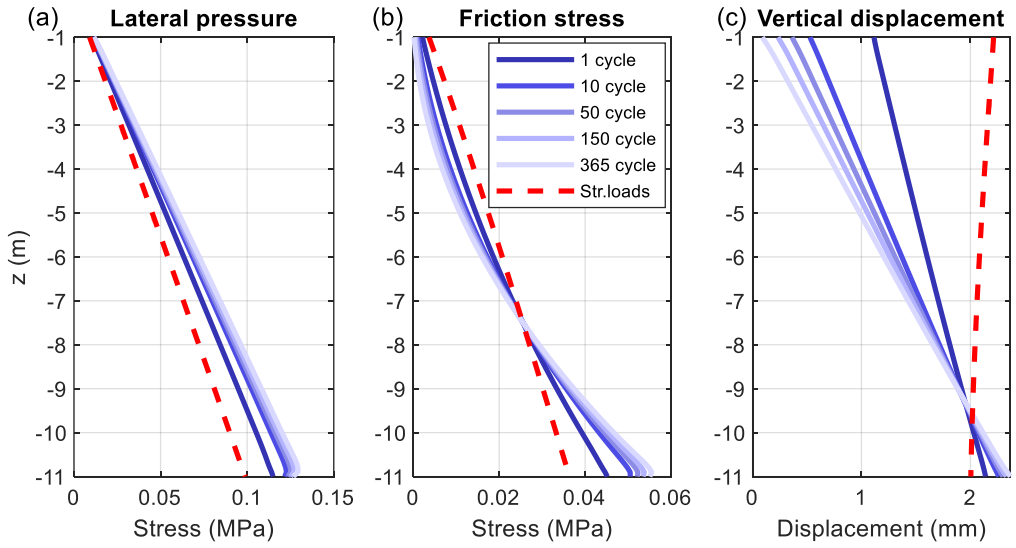

Figure A.72 Soil stresses and displacement along z-direction for various cycles under (a)-(c) combined loadings for pile design #3 for γ=1.5%, d_{in}=300 mm.

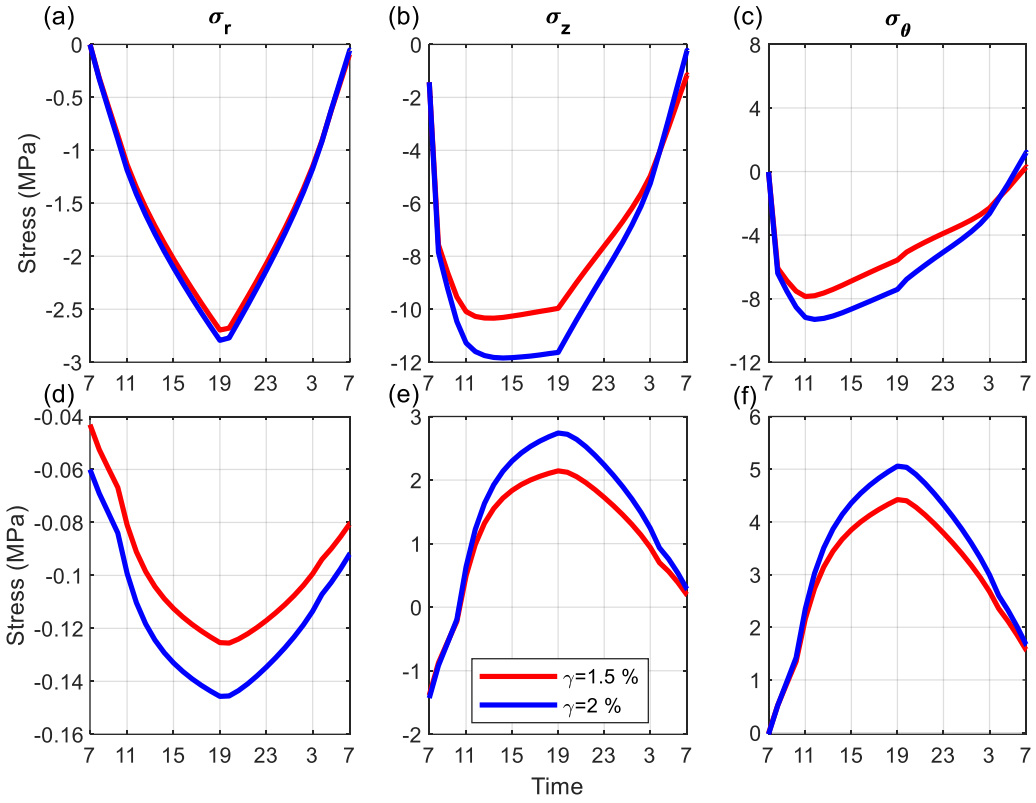

Figure A.73 Stress varying with 24-hour time at the (a)-(c) inner and (d)-(f) outer surface for the pile design #3 for d_{in}=400 mm.

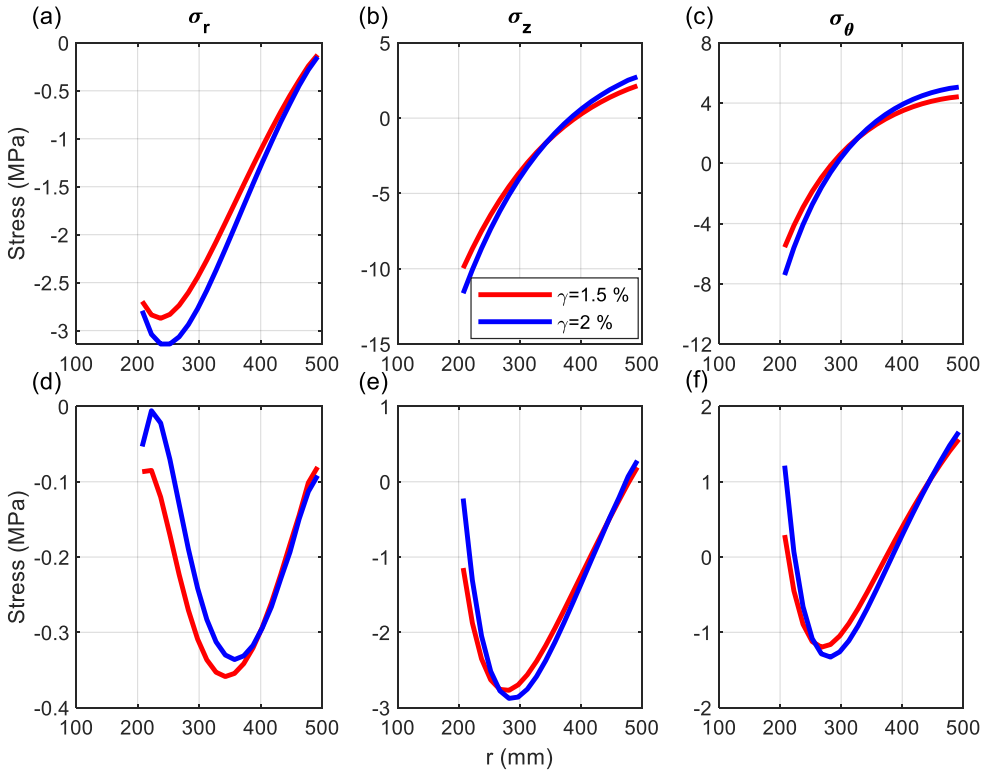

Figure A.74 Stress distribution along r-direction at the (a)-(c) middle and (d)-(f) end of the cycle for the pile design #3 for d_{in}=400 mm.

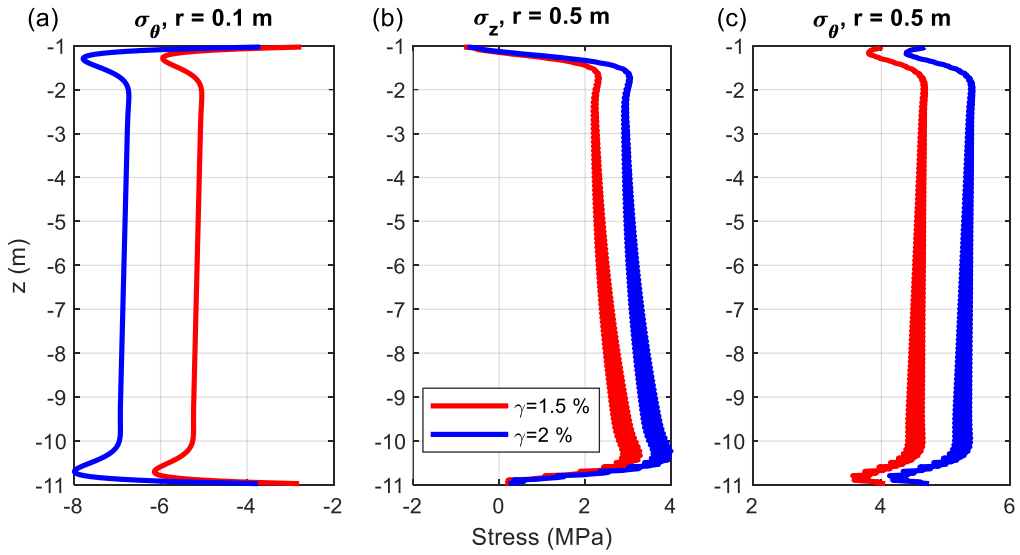

Figure A.75 Stress distribution along z-direction for various cycles at the (a)-(b) inner and (c)-(d) outer surface for pile design #3 for d_{in}=400 mm.

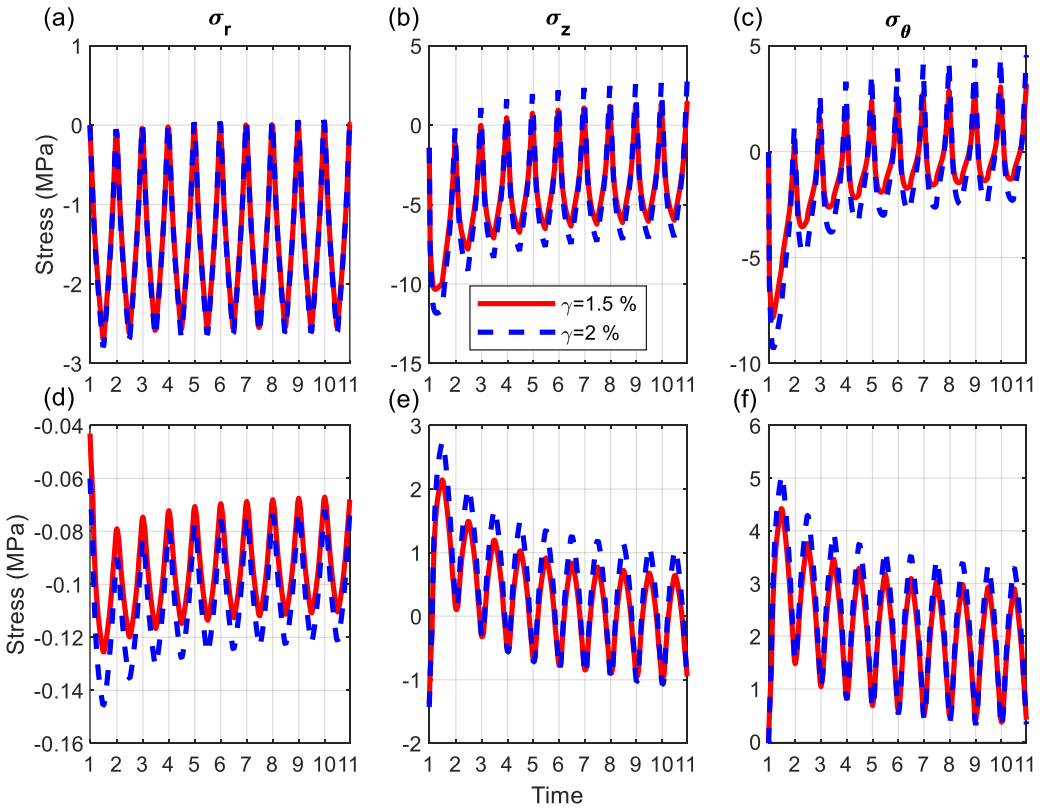

Figure A.76 Stress varying with 10 cycles for (a)-(c) inner and (d)-(f) outer surface for the pile design #3 for d_{in}=400 mm.

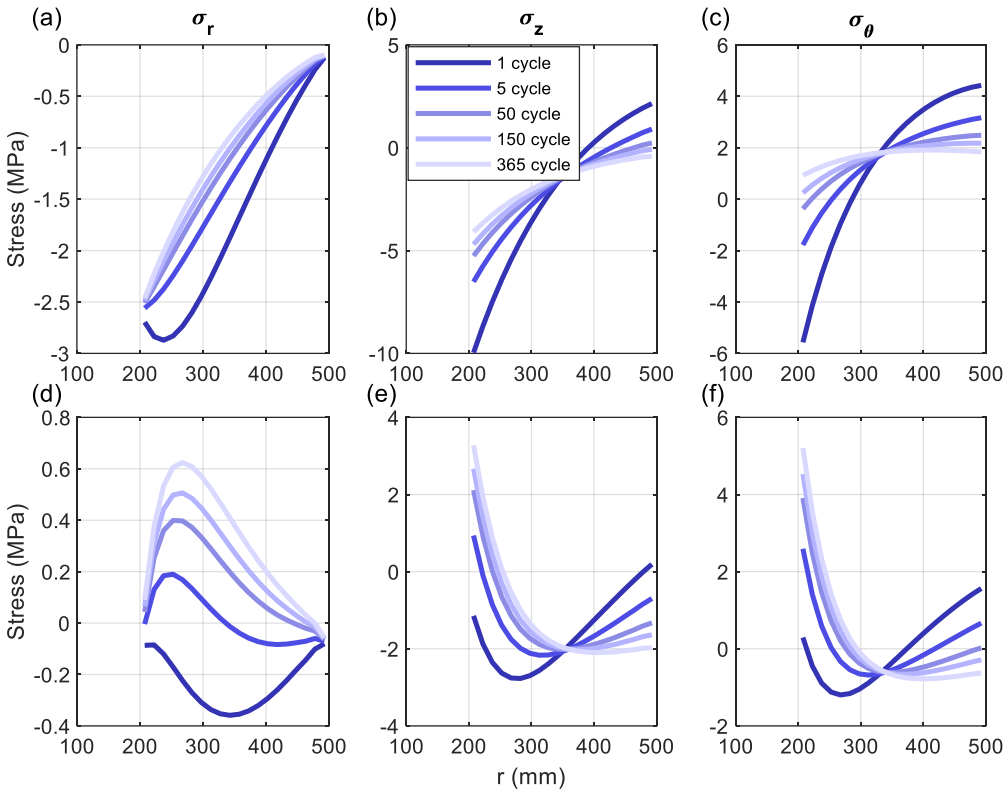

Figure A.77 Stress distribution along r-direction at the (a)-(c) middle and (d)-(f) end of the different cycles for the pile design #3 for γ=1.5%, d_{in}=400 mm.

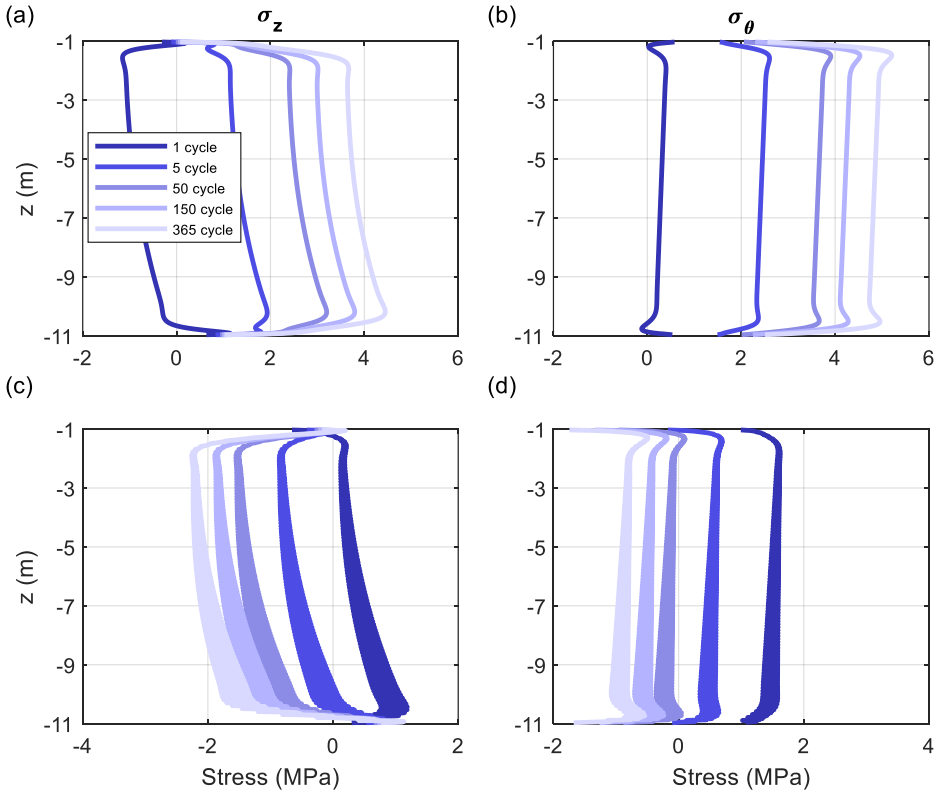

Figure A.78 Stress distribution along z-direction for various cycles at the (a)-(b) inner and (c)-(d) outer surface for pile design #3 for γ=1.5%, d_{in}=400 mm.

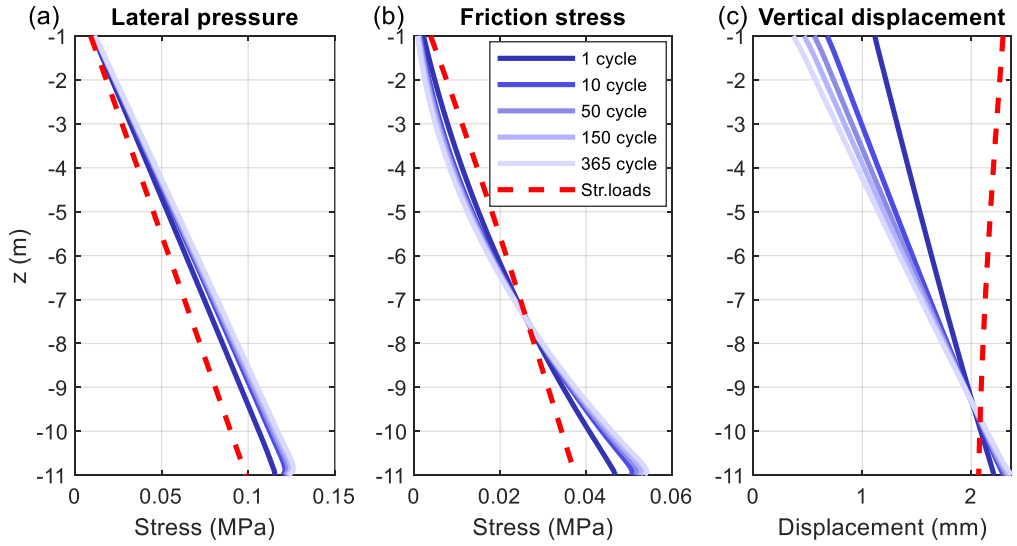

Figure A.79 Soil stresses and displacement along z-direction for various cycles under (a)-(c) combined loadings for pile design #3 for γ=1.5%, d_{in}=400 mm.

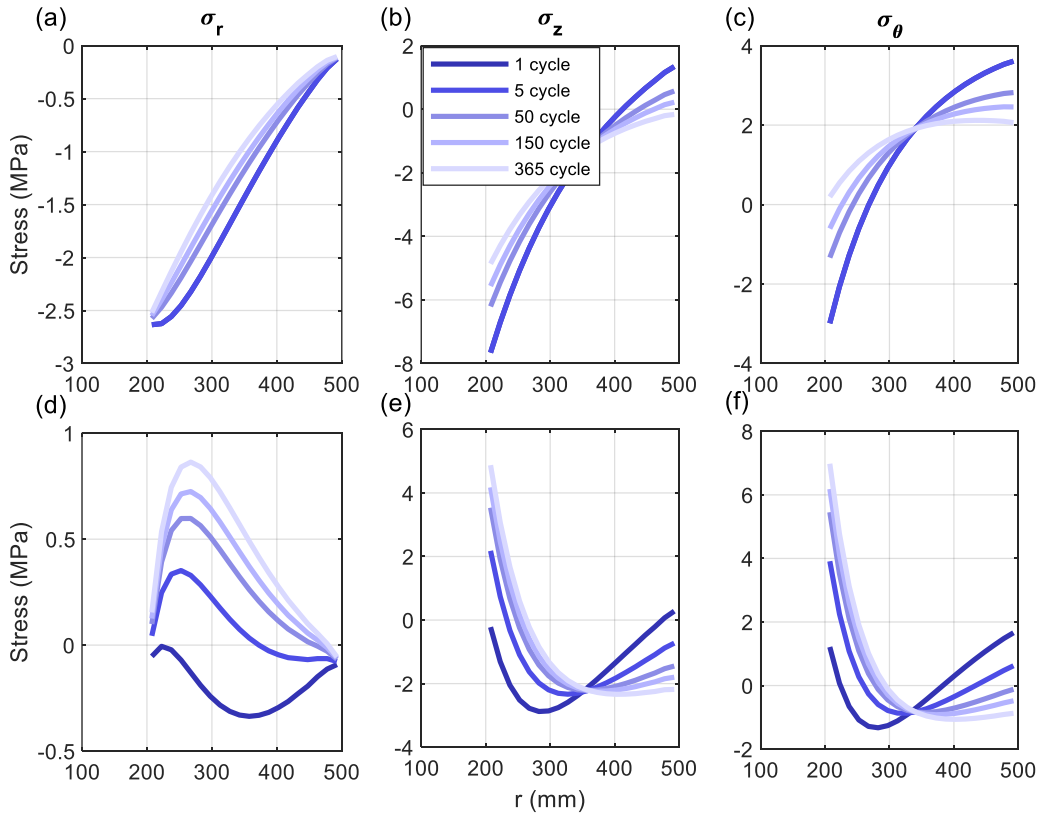

Figure A.80 Stress distribution along r-direction at the (a)-(c) middle and (d)-(f) end of the different cycles for the pile design #3 for γ=2%, d_{in}=400 mm.

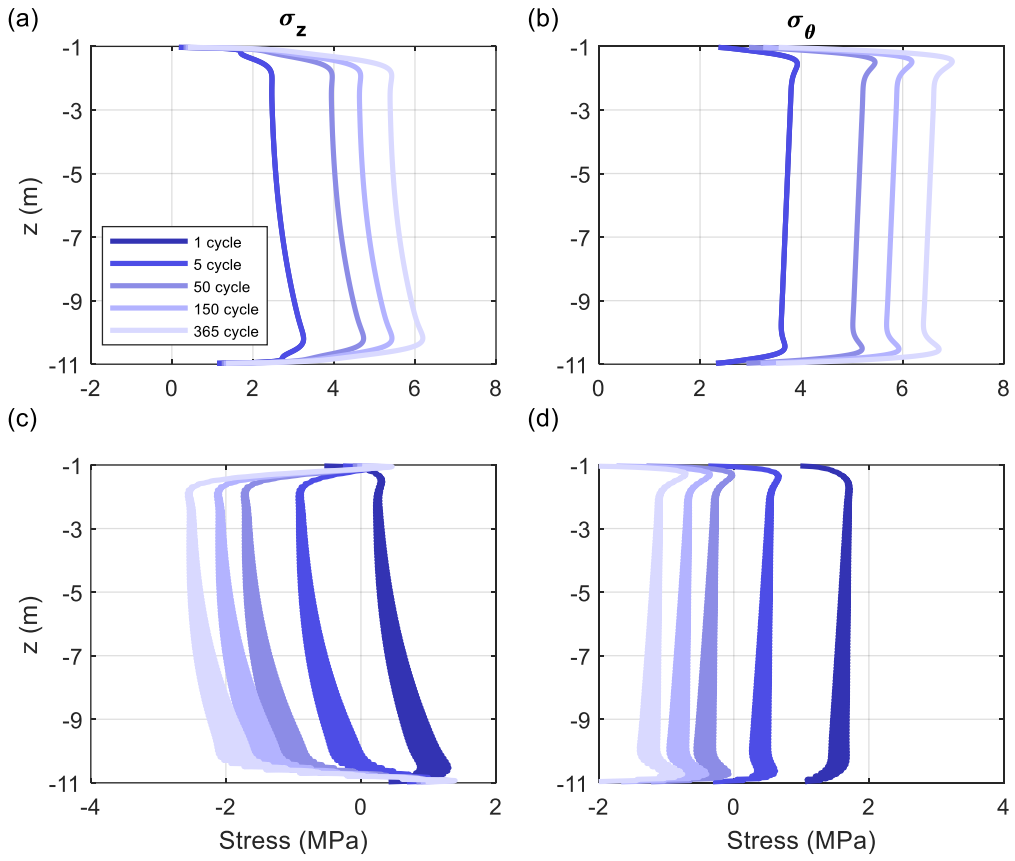

Figure A.81 Stress distribution along z-direction for various cycles at the (a)-(b) inner and (c)-(d) outer surface for pile design #3 for γ=2%, d_{in}=400 mm.

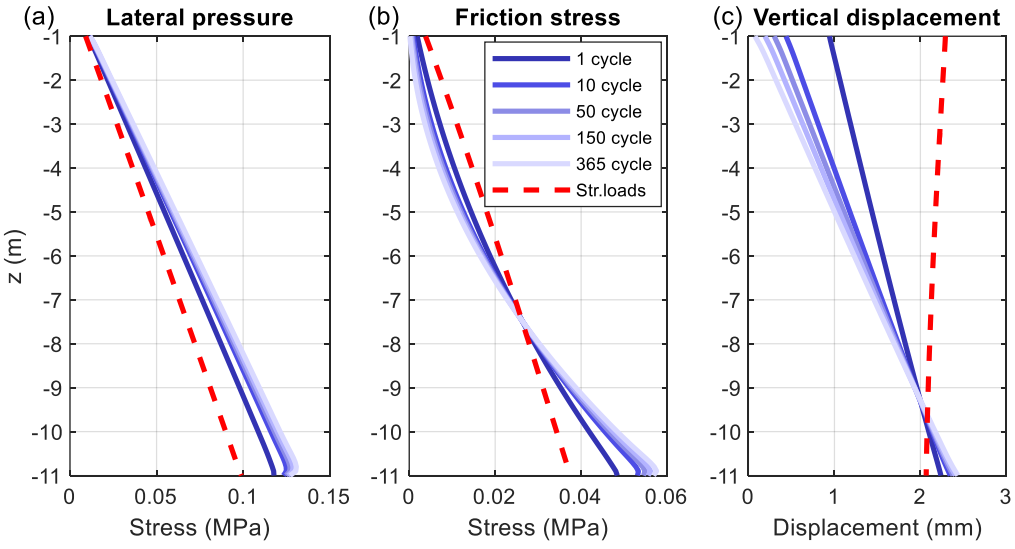

Figure A.82 Soil stresses and displacement along z-direction for various cycles under (a)-(c) combined loadings for pile design #3 for γ=2%, d_{in}=400 mm.

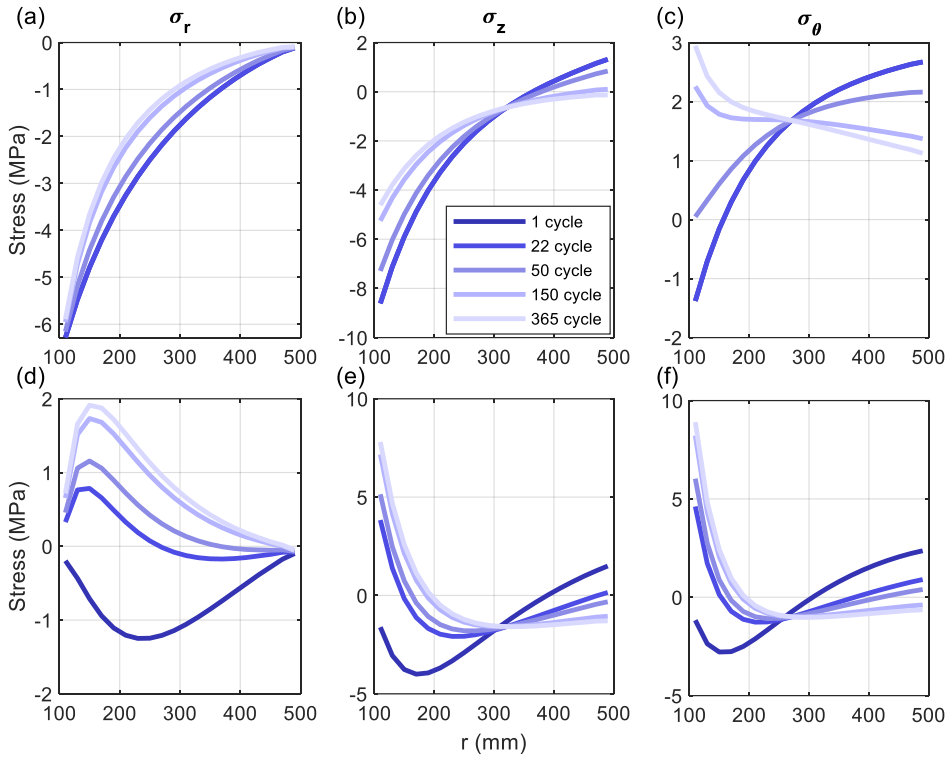

Figure A.83 Stress distribution along r-direction at the (a)-(c) middle and (d)-(f) end of the different cycles for the pile design #4 for γ=1.5%, d_{in}=200 mm.

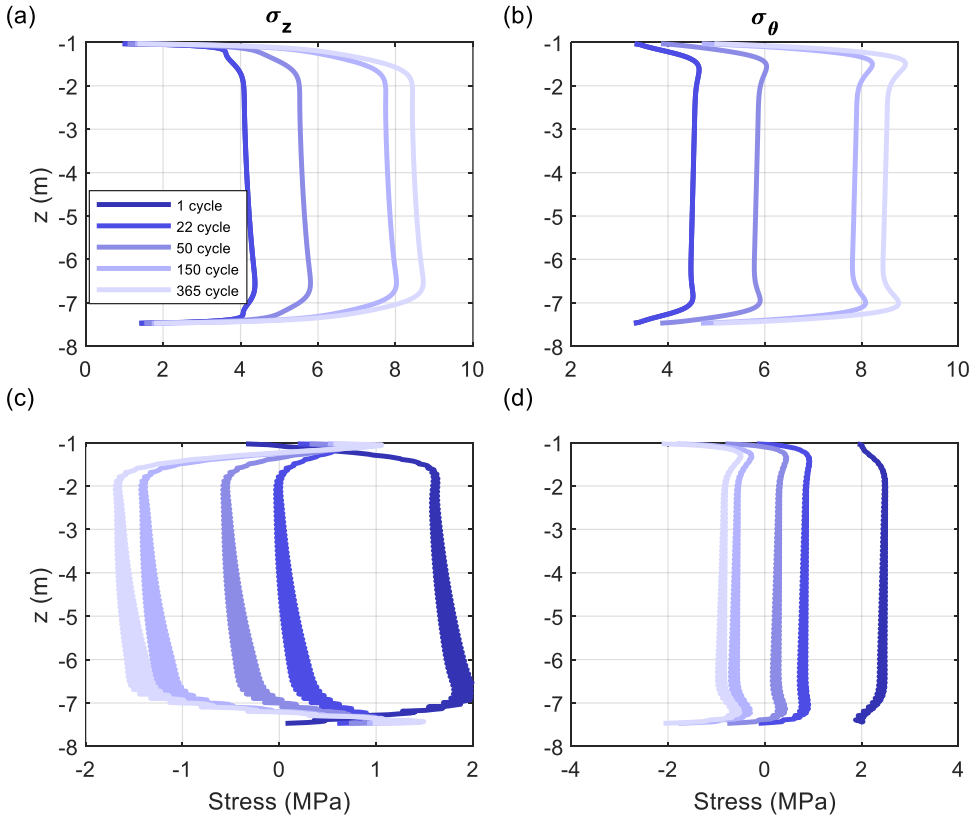

Figure A.84 Stress distribution along z-direction for various cycles at the (a)-(b) inner and (c)-(d) outer surface for pile design #4 for γ=1.5%, d_{in}=200 mm.

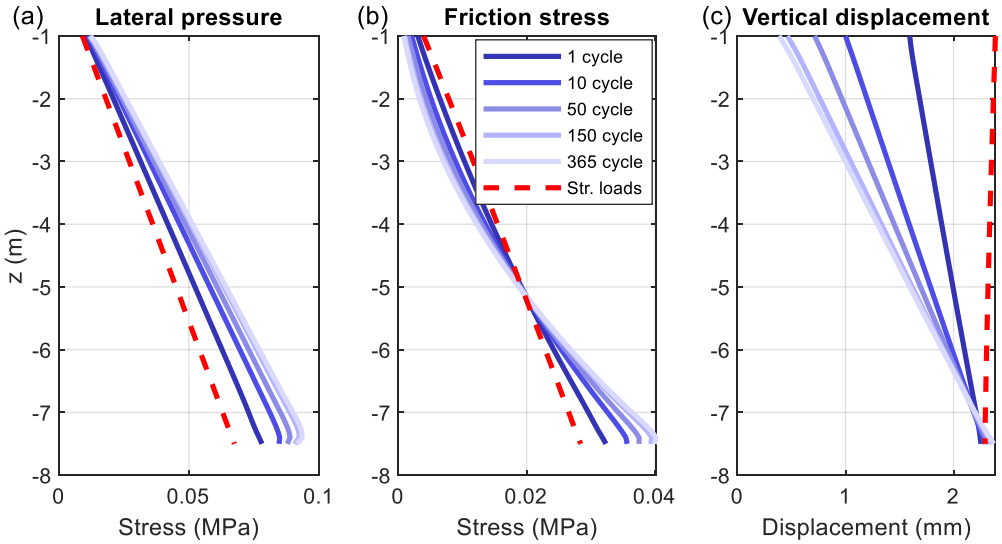

Figure A.85 Soil stresses and displacement along z-direction for various cycles under (a)-(c) combined loadings for pile design #4 for γ=1.5%, d_{in}=200 mm.

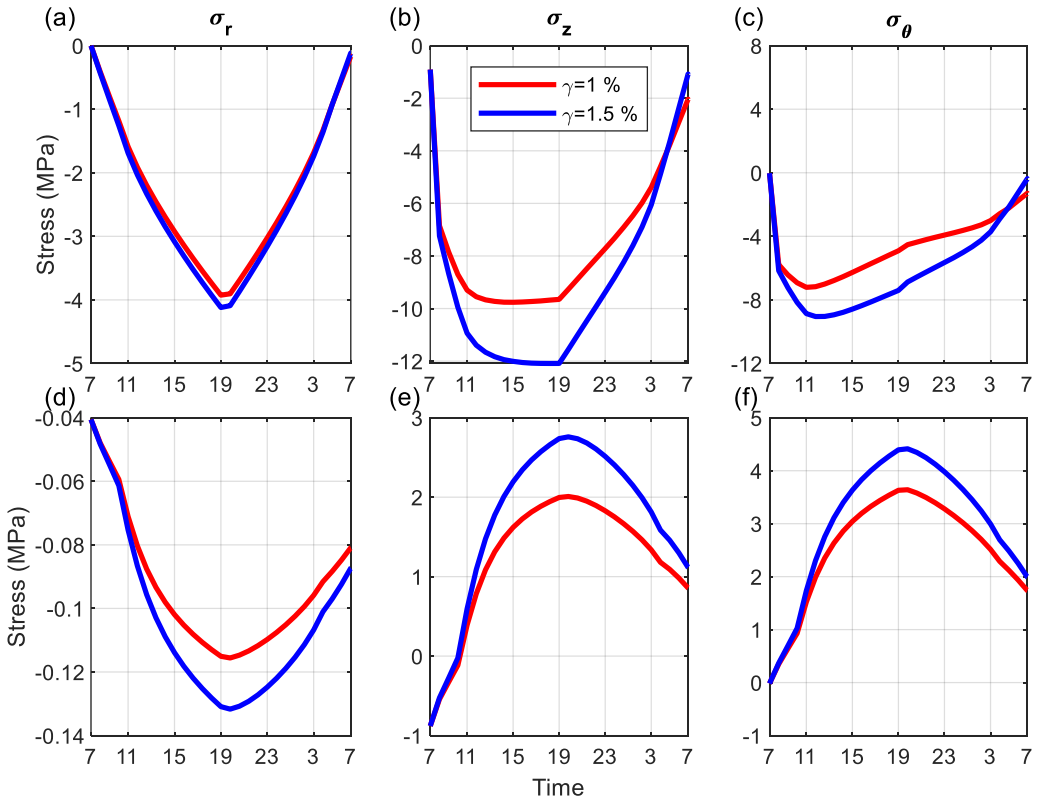

Figure A.86 Stress varying with 24-hour time at the (a)-(c) inner and (d)-(f) outer surface for the pile design #4 for d_{in}=300 mm.

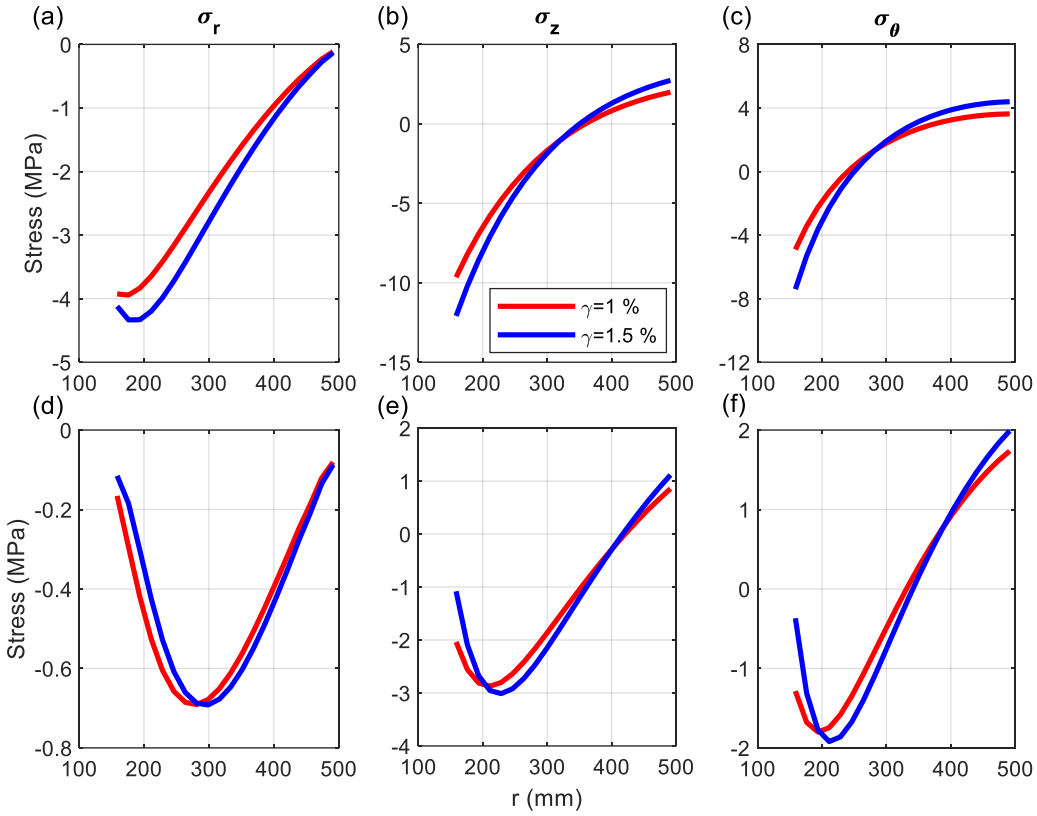

Figure A.87 Stress distribution along r-direction at the (a)-(c) middle and (d)-(f) end of the cycle for the pile design #4 for d_{in}=300 mm.

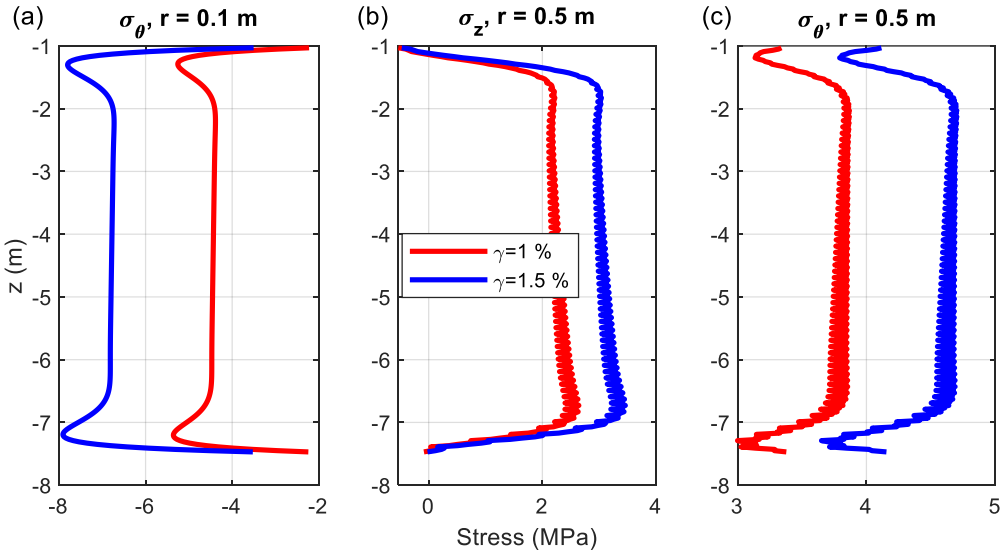

Figure A.88 Stress distribution along z-direction for various cycles at the (a)-(b) inner and (c)-(d) outer surface for pile design #4 for d_{in}=300 mm.

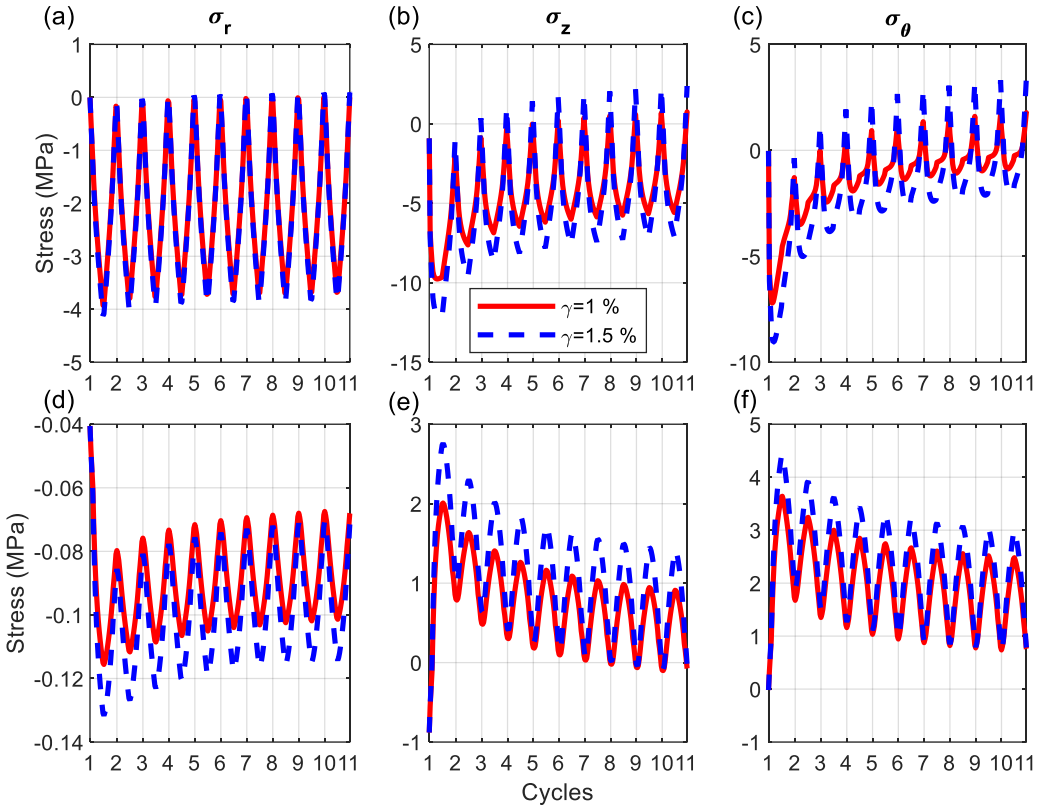

Figure A.89 Stress varying with 10 cycles for (a)-(c) inner and (d)-(f) outer surface for the pile design #4 for d_{in}=300 mm.

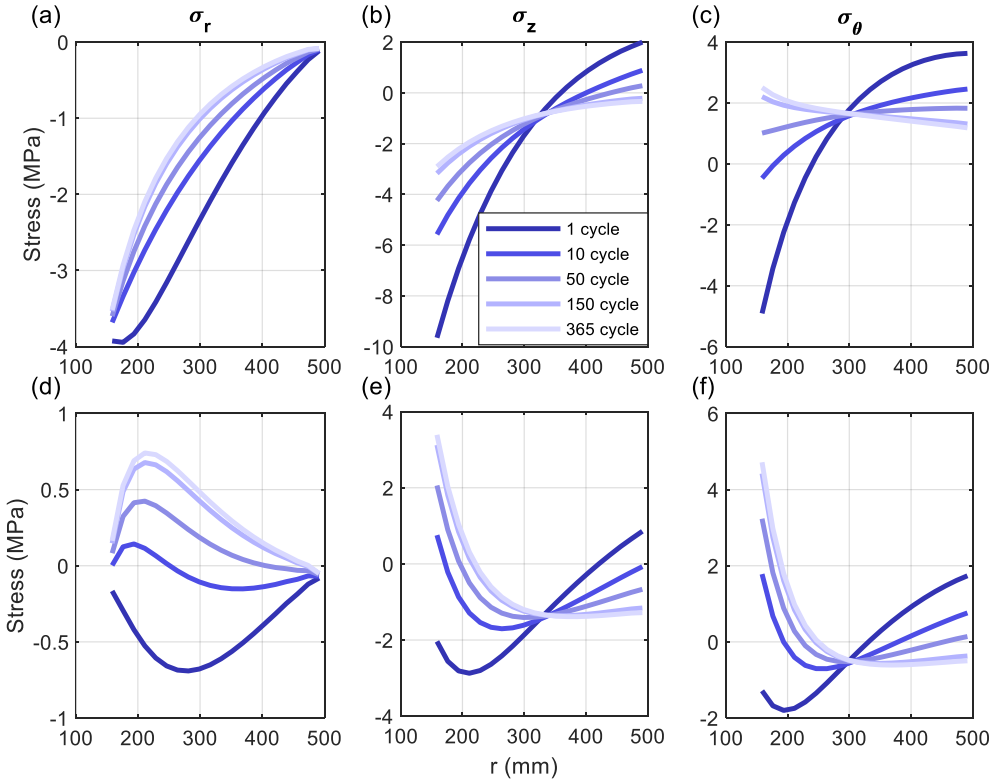

Figure A.90 Stress distribution along r-direction at the (a)-(c) middle and (d)-(f) end of the different cycles for the pile design #4 for γ=1%, d_{in}=300 mm.

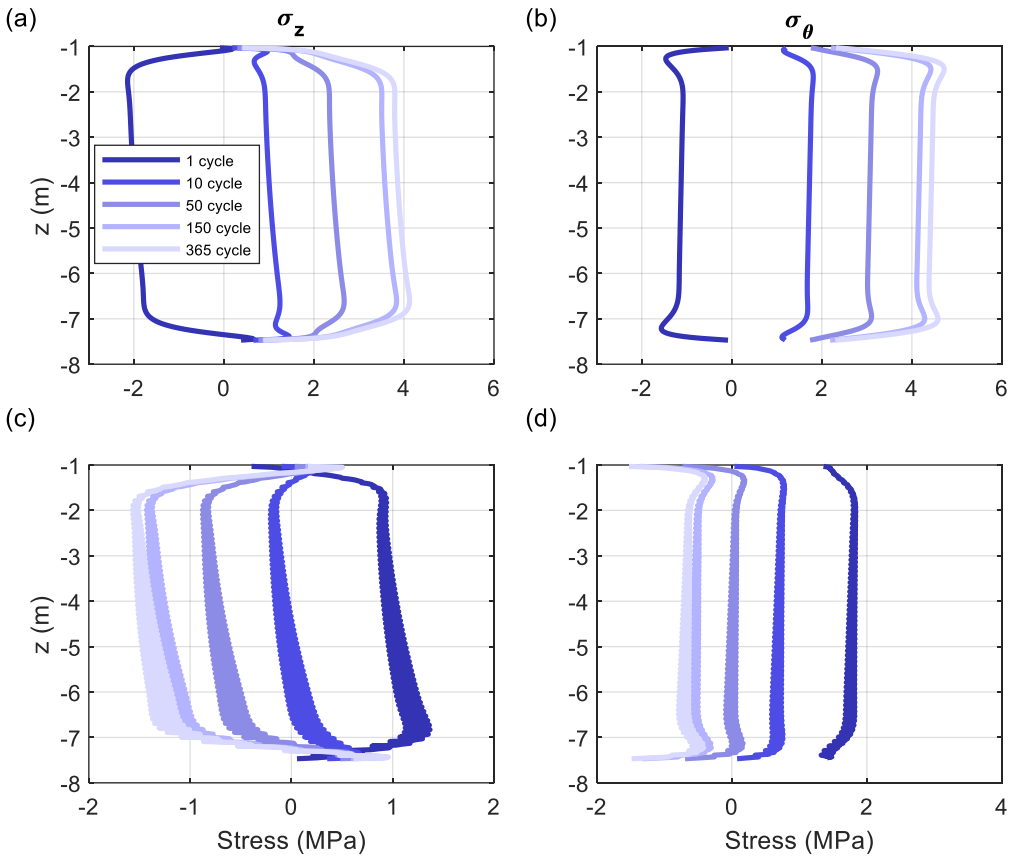

Figure A.91 Stress distribution along z-direction for various cycles at the (a)-(b) inner and (c)-(d) outer surface for pile design #4 for γ=1%, d_{in}=300 mm.

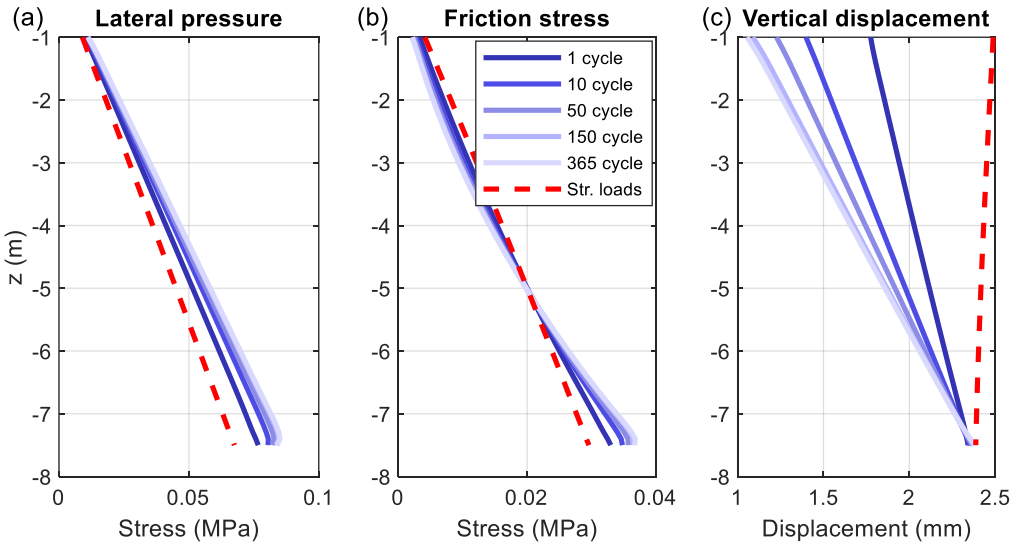

Figure A.92 Soil stresses and displacement along z-direction for various cycles under (a)-(c) combined loadings for pile design #4 for γ=1%, d_{in}=300 mm.

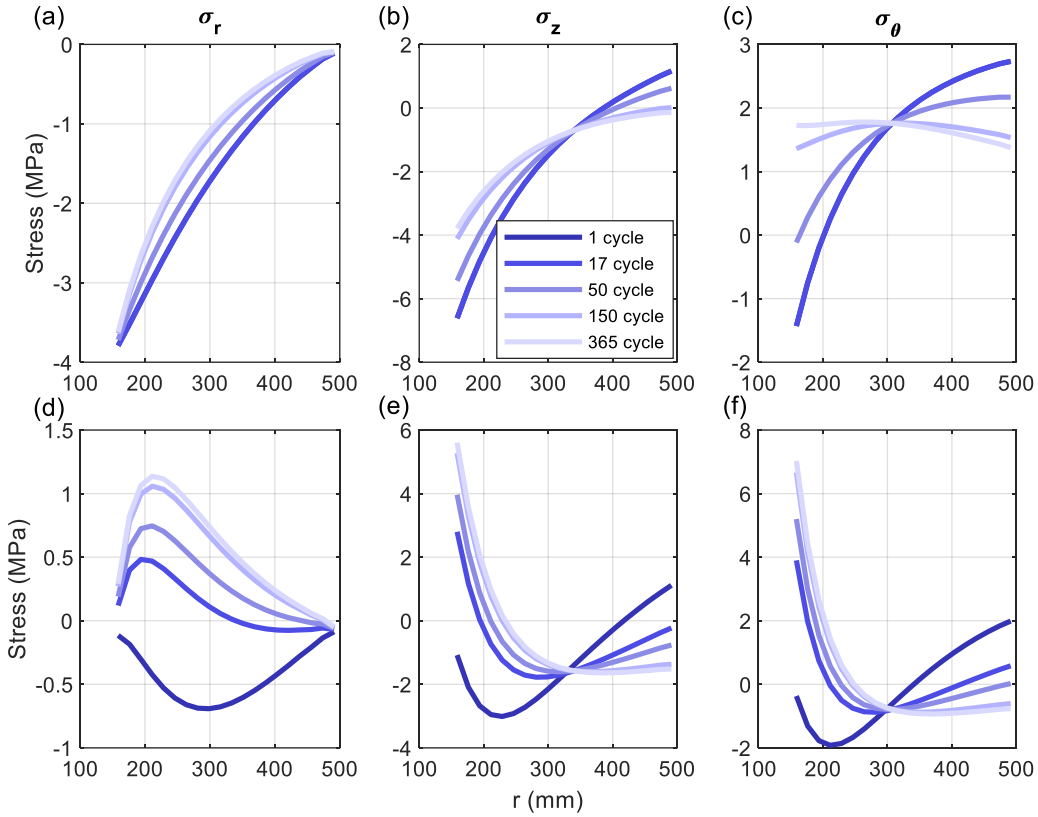

Figure A.93 Stress distribution along r-direction at the (a)-(c) middle and (d)-(f) end of the different cycles for the pile design #4 for γ=1.5%, d_{in}=300 mm.

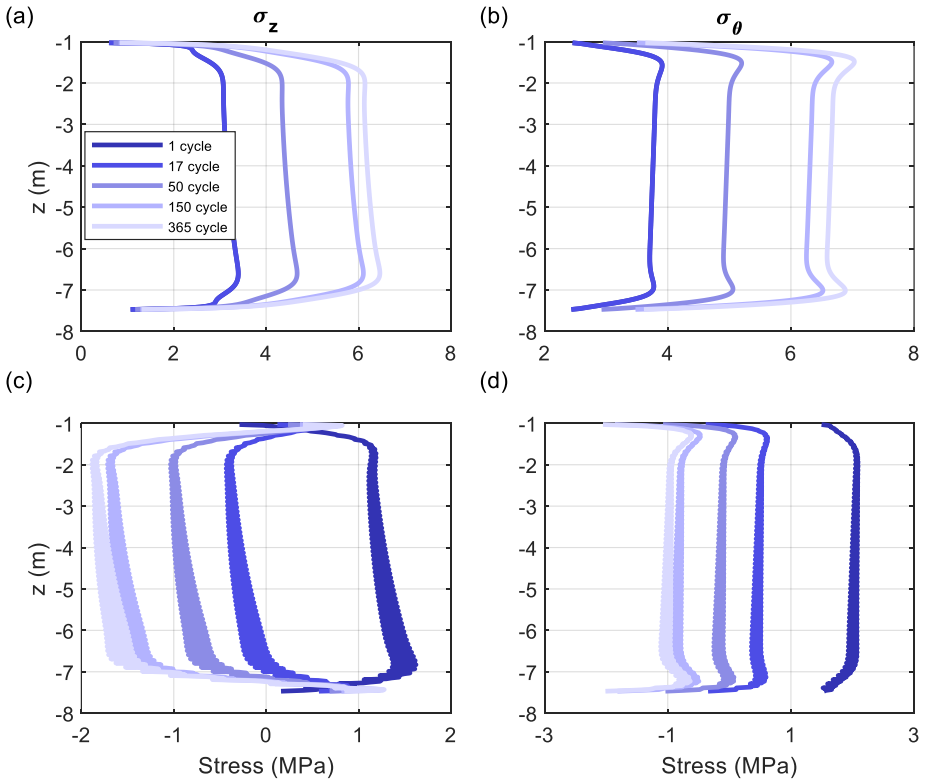

Figure A.94 Stress distribution along z-direction for various cycles at the (a)-(b) inner and (c)-(d) outer surface for pile design #4 for γ=1.5%, d_{in}=300 mm.

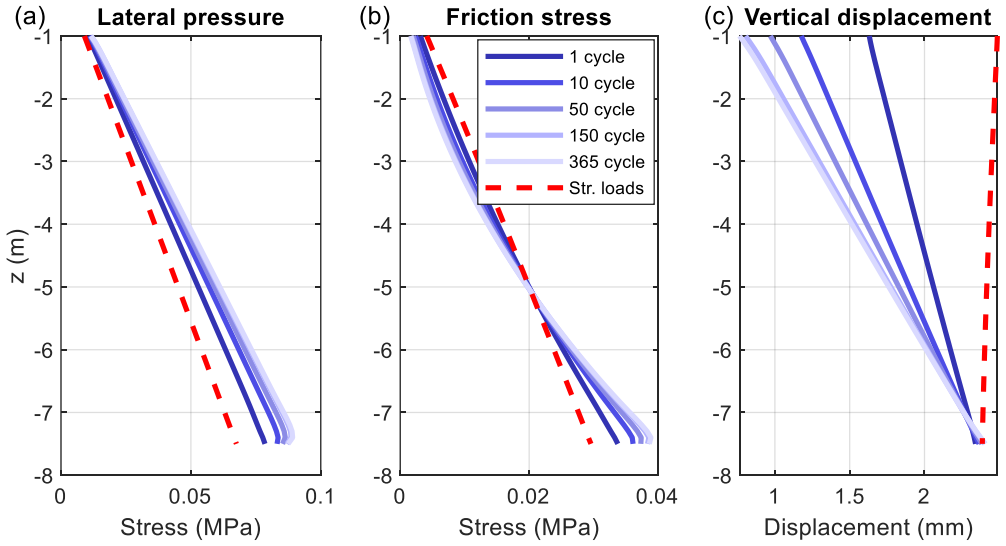

Figure A.95 Soil stresses and displacement along z-direction for various cycles under (a)-(c) combined loadings for pile design #4 for γ=1.5%, d_{in}=300 mm.

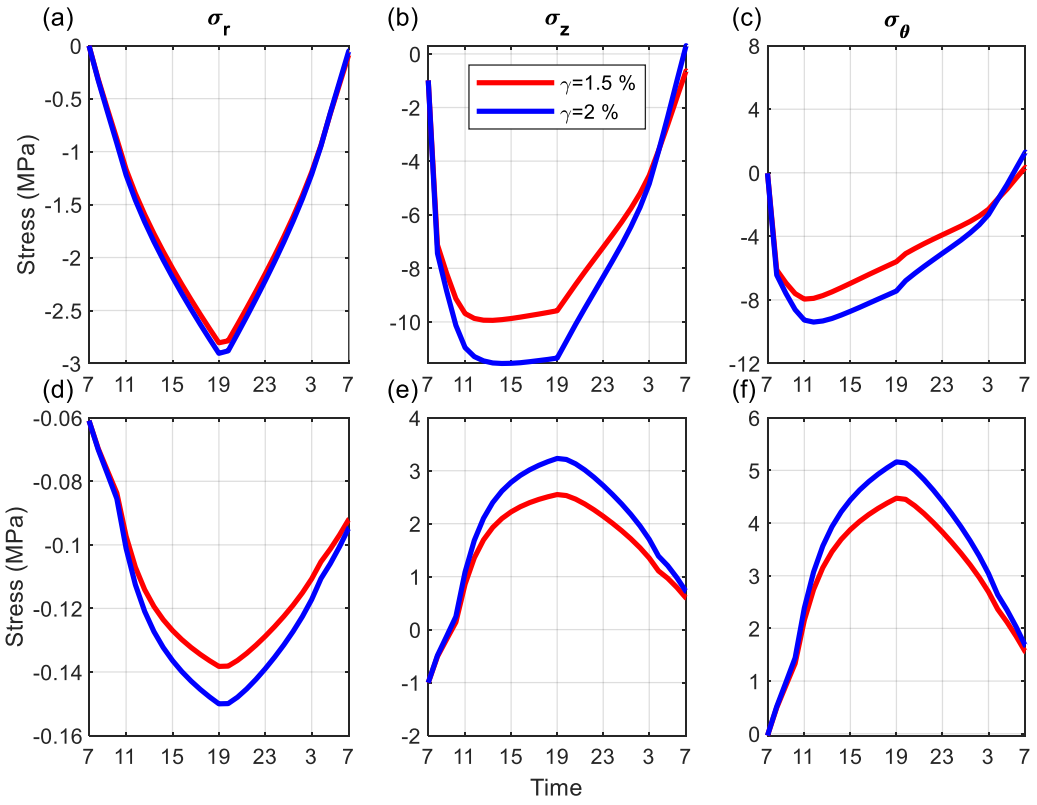

Figure A.96 Stress varying with 24-hour time at the (a)-(c) inner and (d)-(f) outer surface for the pile design #4 for d_{in}=400 mm.

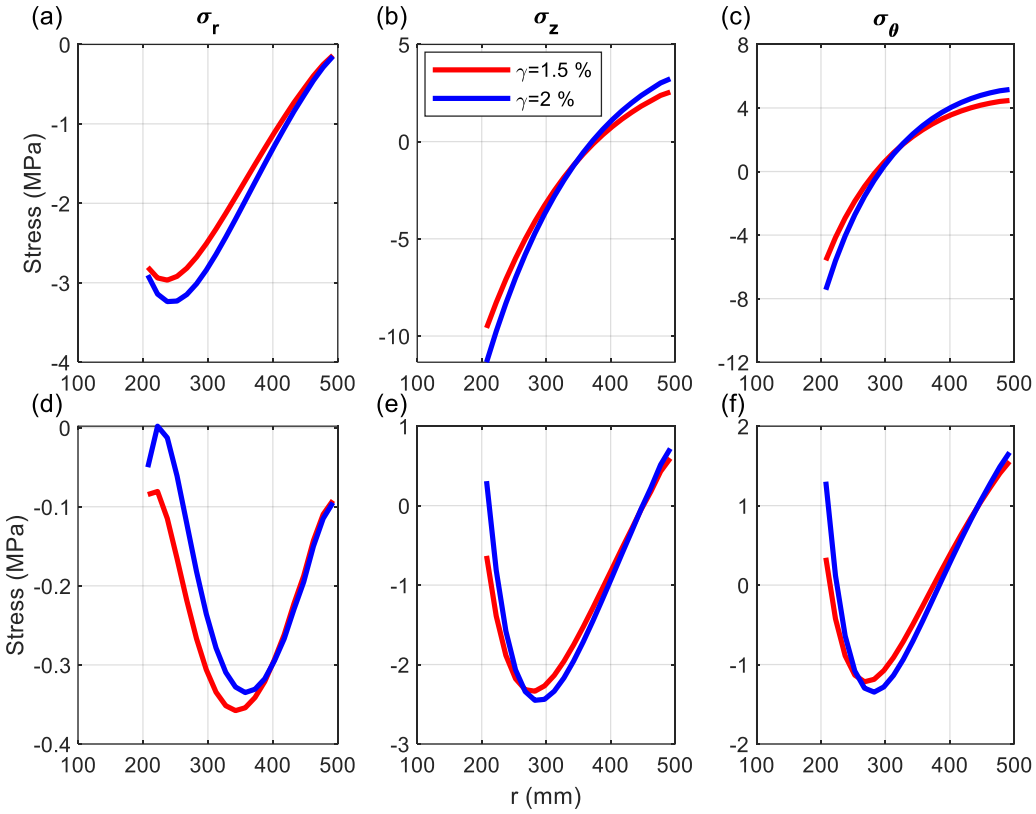

Figure A.97 Stress distribution along r-direction at the (a)-(c) middle and (d)-(f) end of the cycle for the pile design #4 for d_{in}=400 mm.

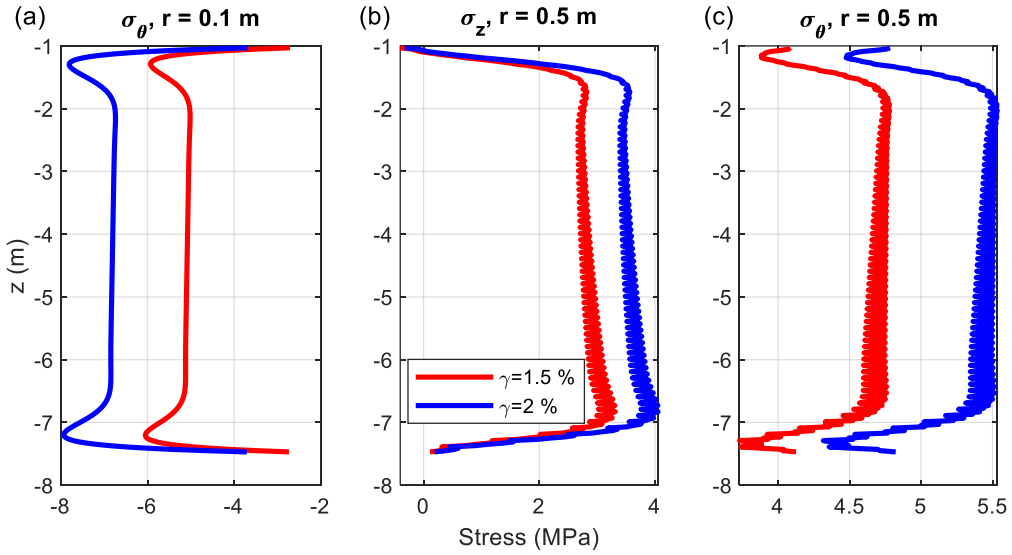

Figure A.98 Stress distribution along z-direction for various cycles at the (a)-(b) inner and (c)-(d) outer surface for pile design #4 for d_{in}=400 mm.

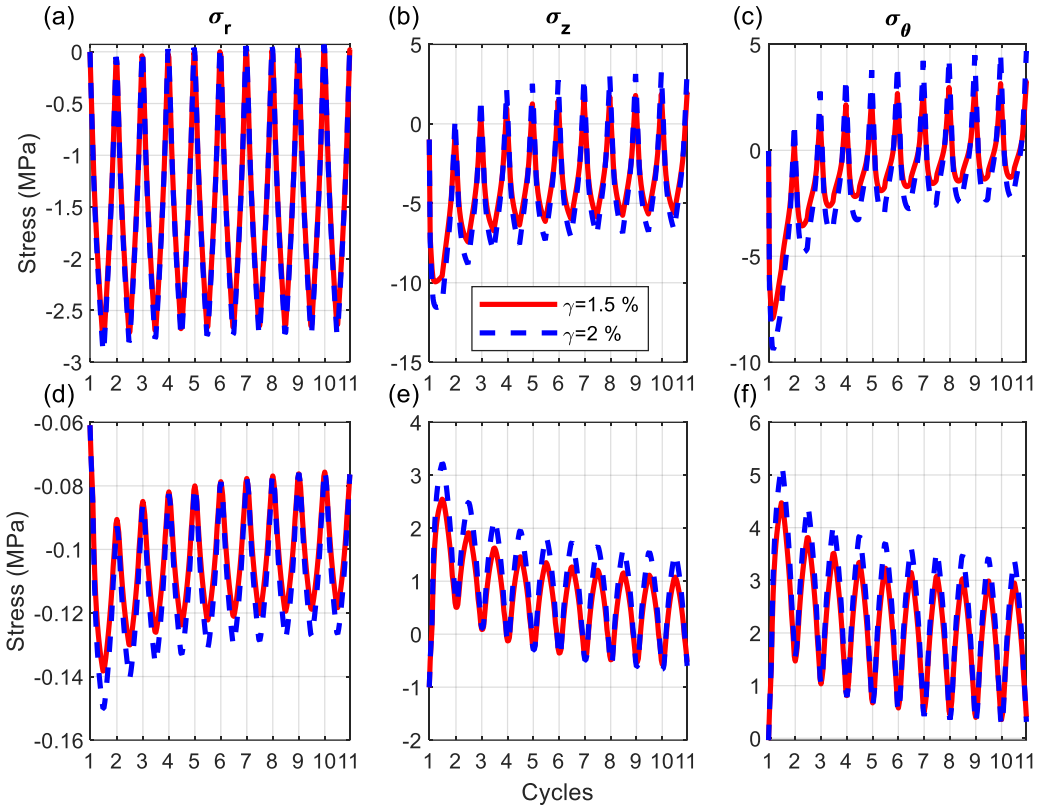

Figure A.99 Stress varying with 10 cycles for (a)-(c) inner and (d)-(f) outer surface for the pile design #4 for d_{in}=400 mm.

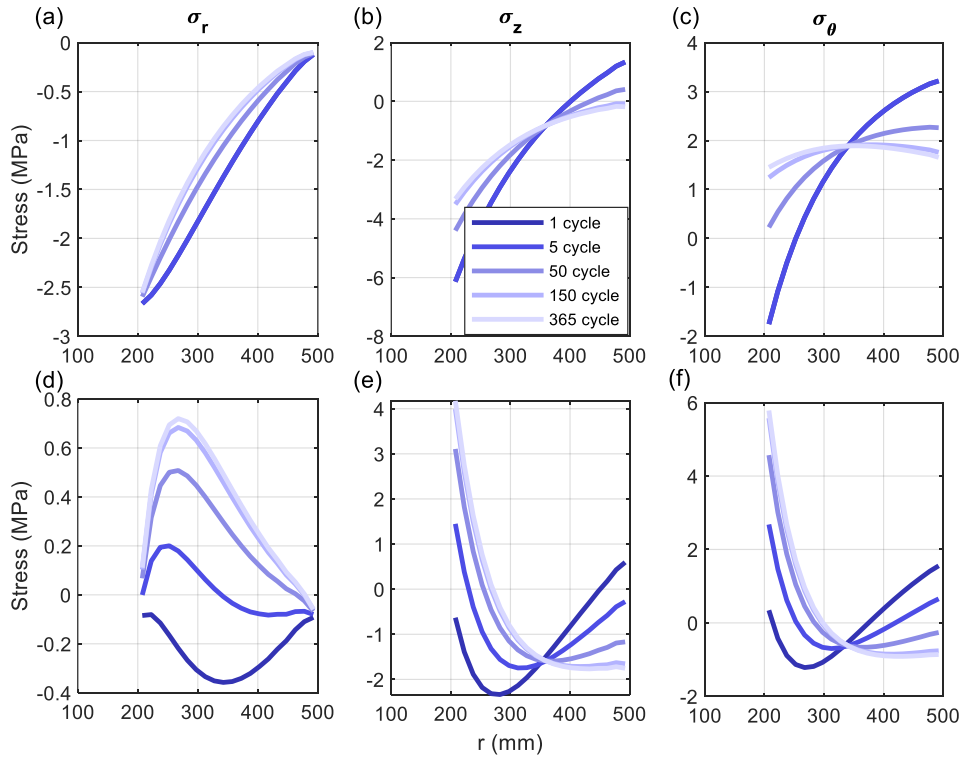

Figure A.100 Stress distribution along r-direction at the (a)-(c) middle and (d)-(f) end of the different cycles for the pile design #4 for γ=1.5%, d_{in}=400 mm.

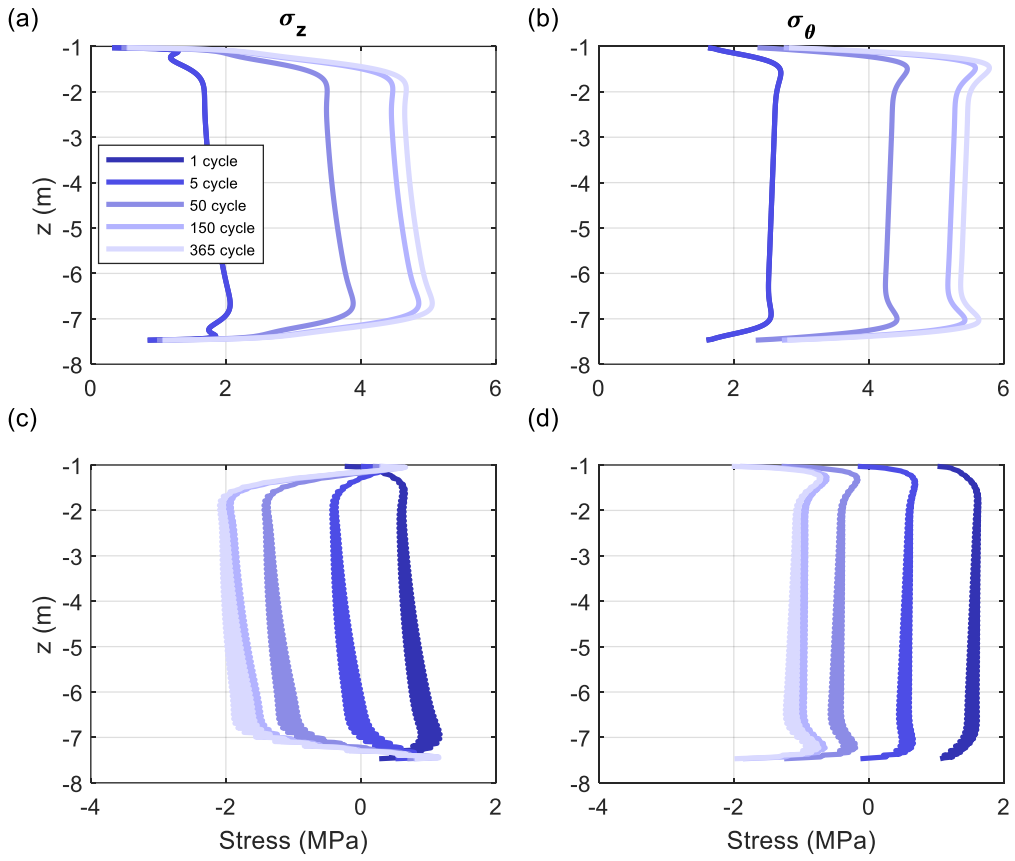

Figure A.101 Stress distribution along z-direction for various cycles at the (a)-(b) inner and (c)-(d) outer surface for pile design #4 for γ=1.5%, d_{in}=400 mm.

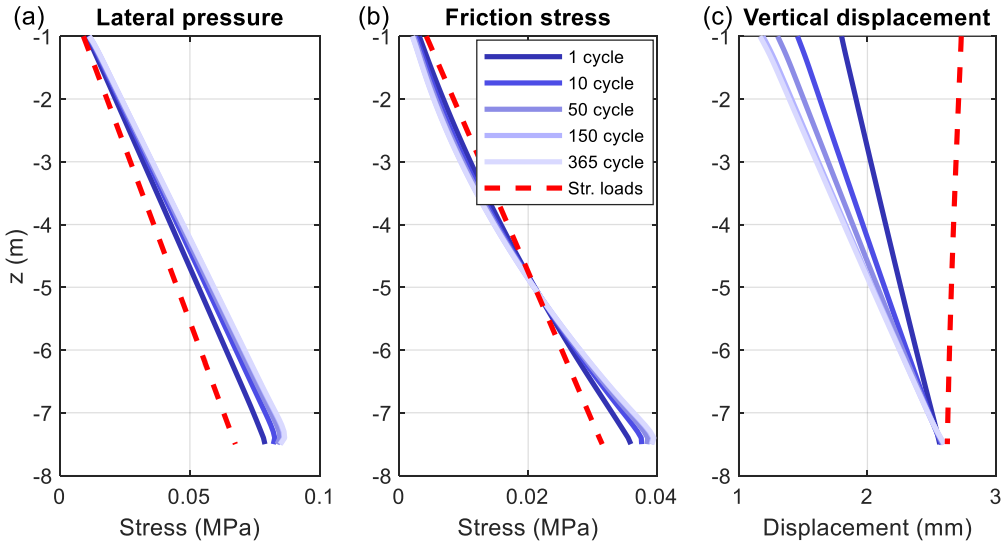

Figure A.102 Soil stresses and displacement along z-direction for various cycles under (a)-(c) combined loadings for pile design #4 for γ=1.5%, d_{in}=400 mm.

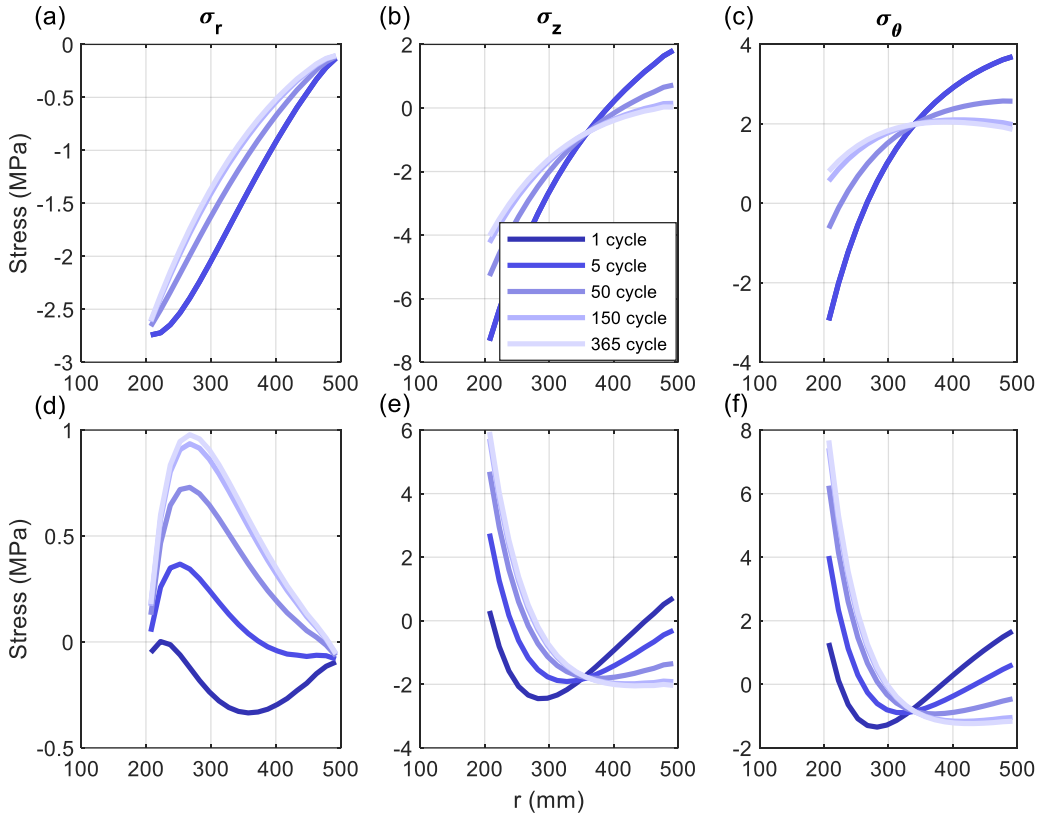

Figure A.103 Stress distribution along r-direction at the (a)-(c) middle and (d)-(f) end of the different cycles for the pile design #4 for γ=2%, d_{in}=400 mm.

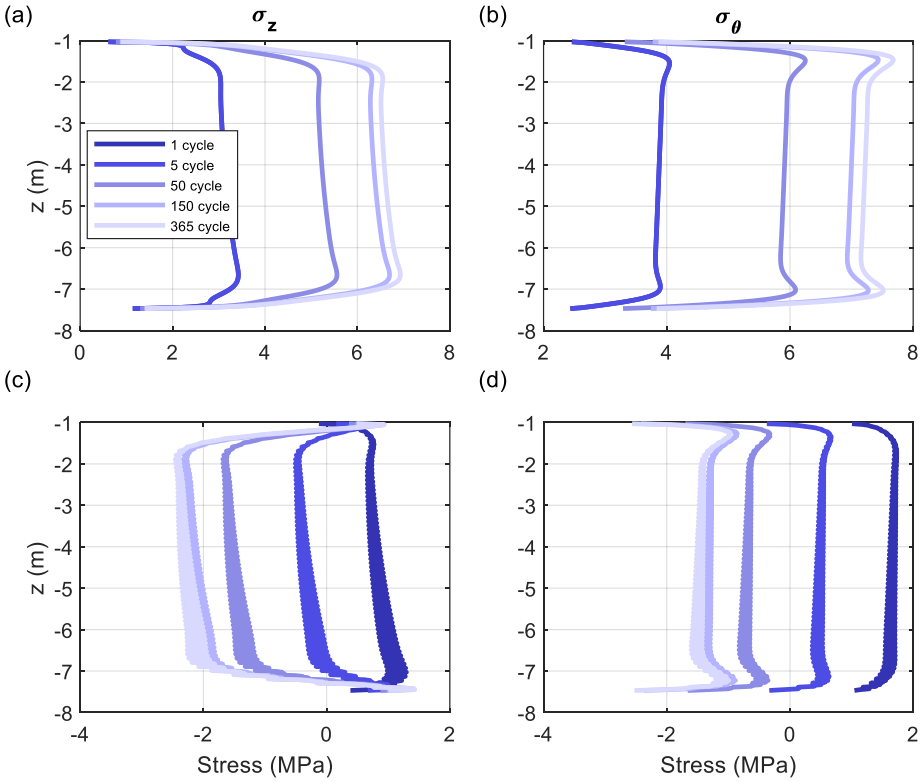

Figure A.104 Stress distribution along z-direction for various cycles at the (a)-(b) inner and (c)-(d) outer surface for pile design #4 for γ=2%, d_{in}=400 mm.

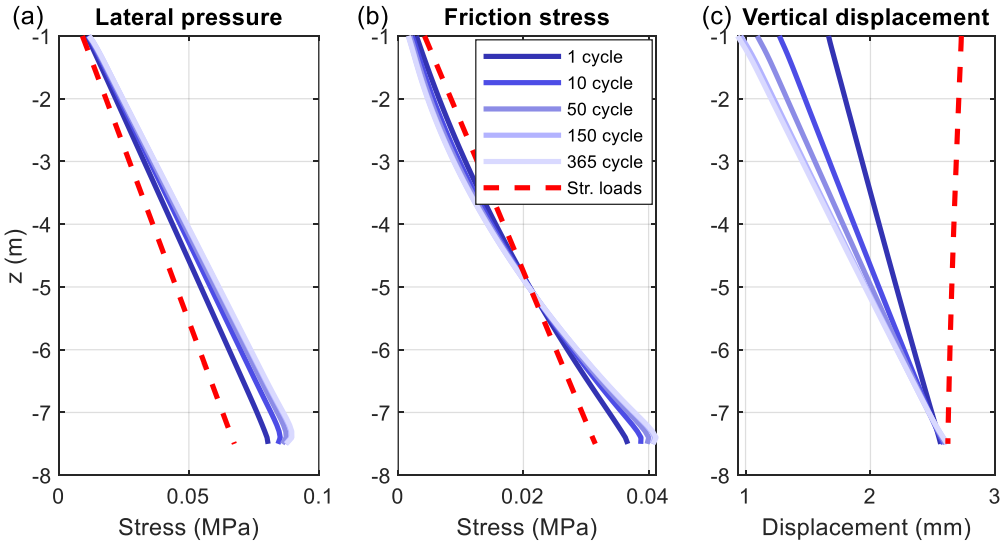

Figure A.105 Soil stresses and displacement along z-direction for various cycles under (a)-(c) combined loadings for pile design #4 for γ=2%, d_{in}=400 mm.

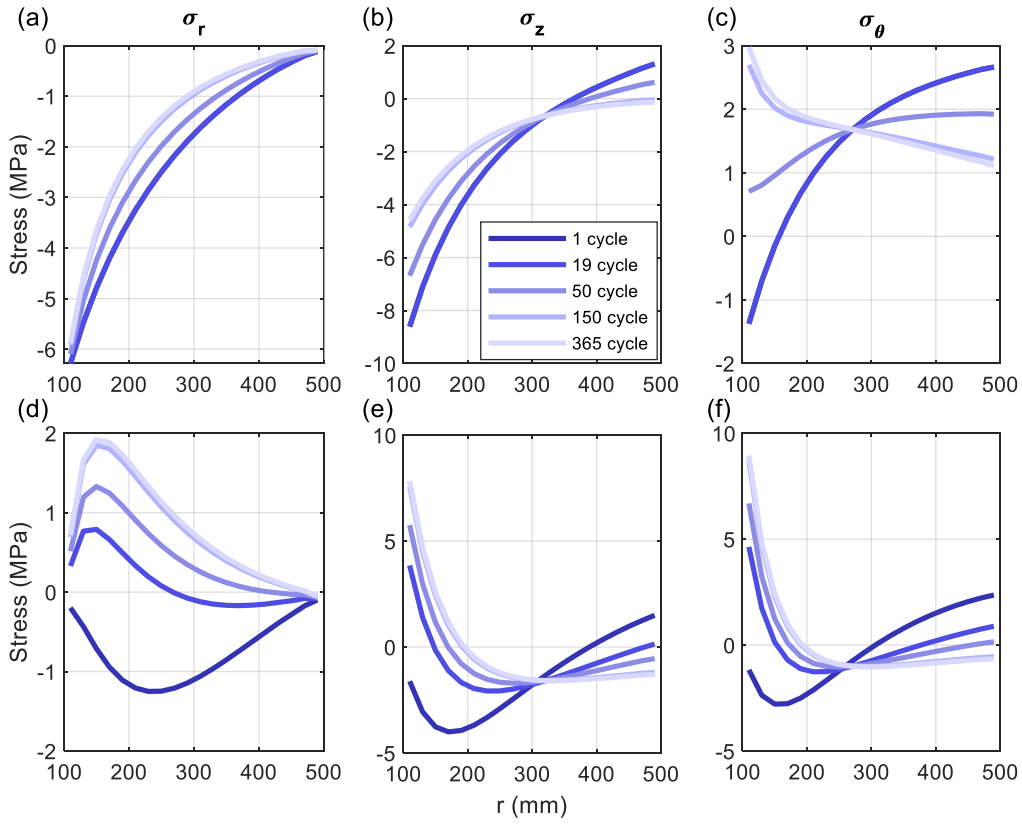

Figure A.106 Stress distribution along r-direction at the (a)-(c) middle and (d)-(f) end of the different cycles for the pile design #5 for γ=1%, d_{in}=200 mm.

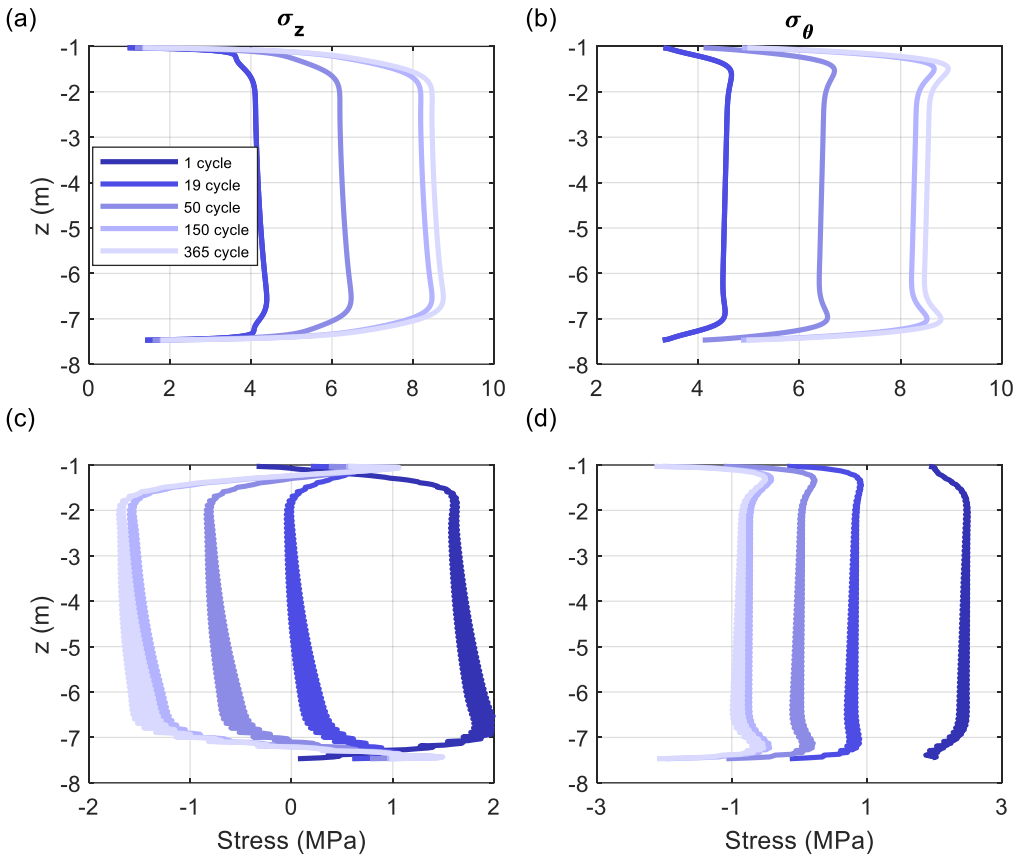

Figure A.107 Stress distribution along z-direction for various cycles at the (a)-(b) inner and (c)-(d) outer surface for pile design #5 for γ=1%, d_{in}=200 mm.

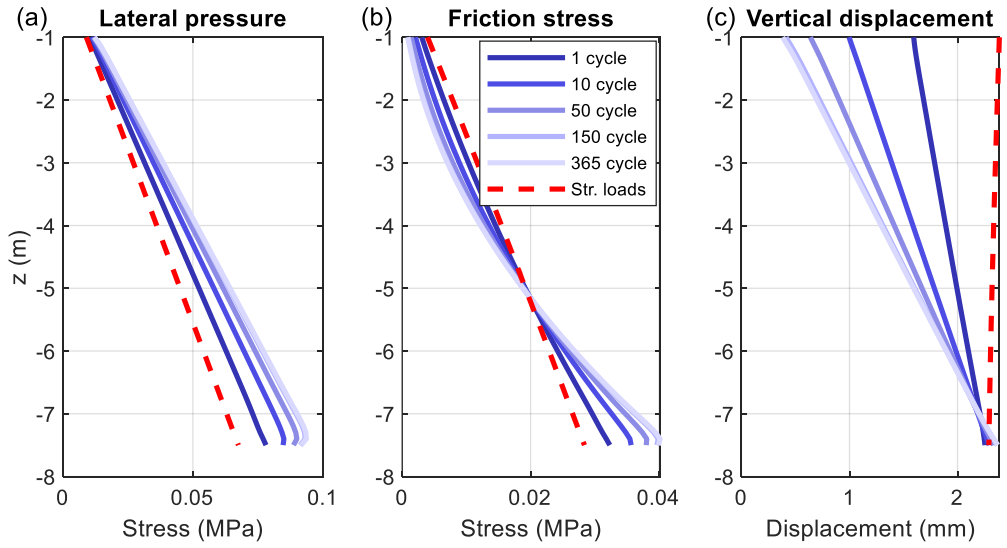

Figure A.108 Soil stresses and displacement along z-direction for various cycles under (a)-(c) combined loadings for pile design #5 for γ=1%, d_{in}=200 mm.

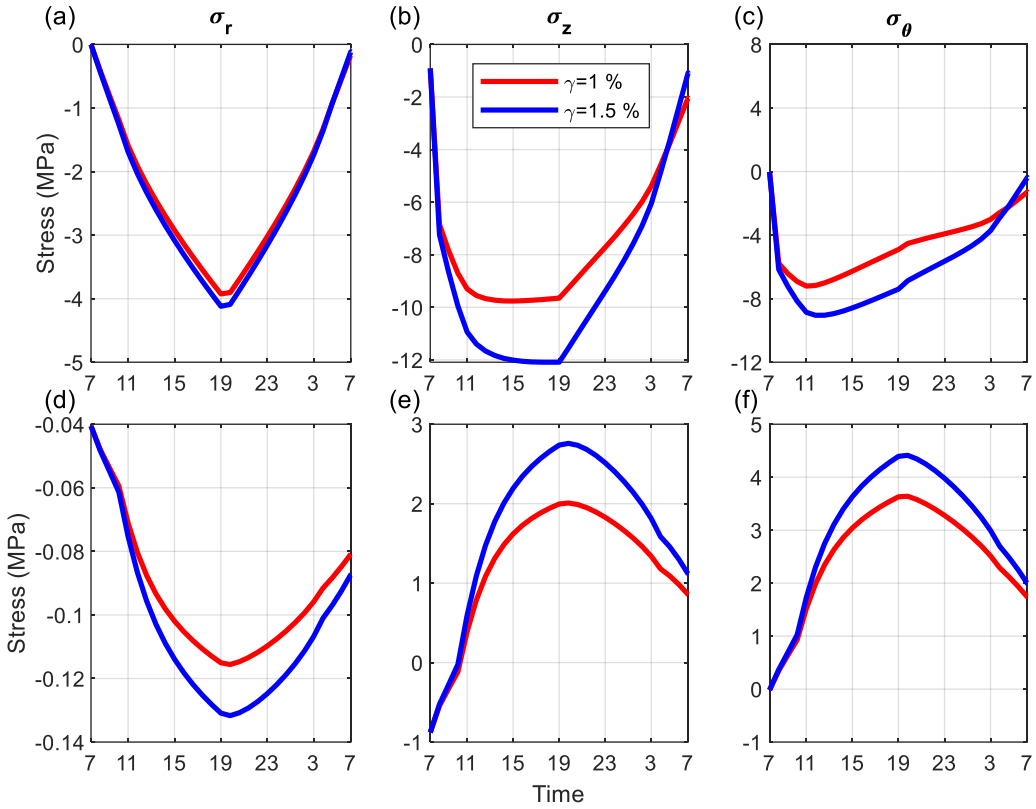

Figure A.109 Stress varying with 24-hour time at the (a)-(c) inner and (d)-(f) outer surface for the pile design #5 for d_{in}=300 mm.

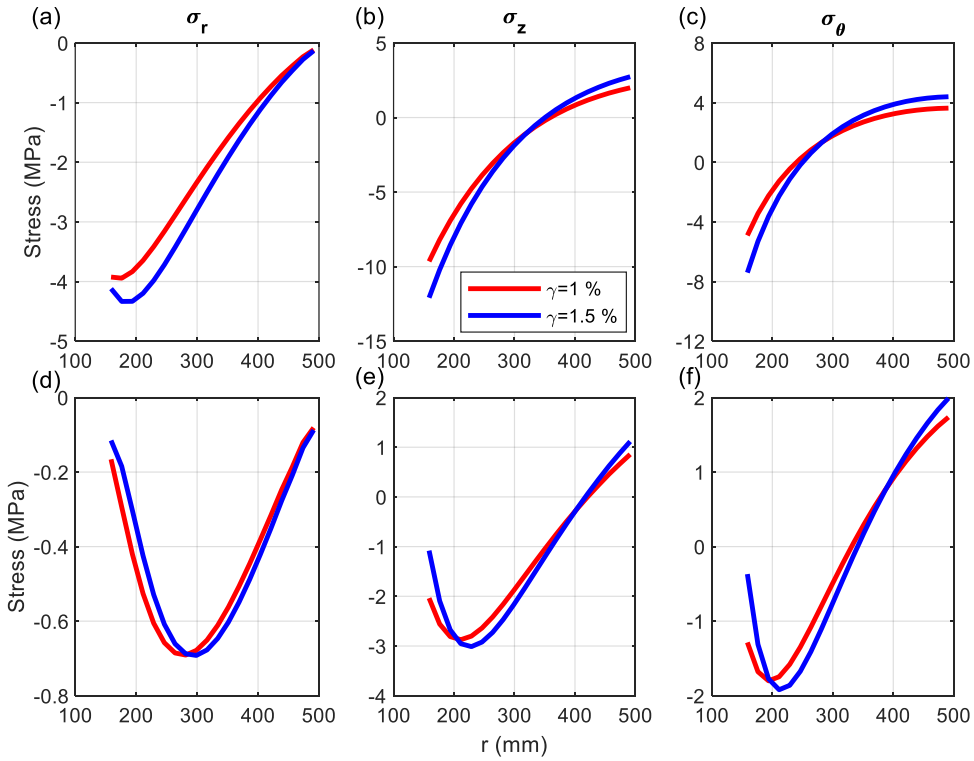

Figure A.110 Stress distribution along r-direction at the (a)-(c) middle and (d)-(f) end of the cycle for the pile design #5 for d_{in}=300 mm.

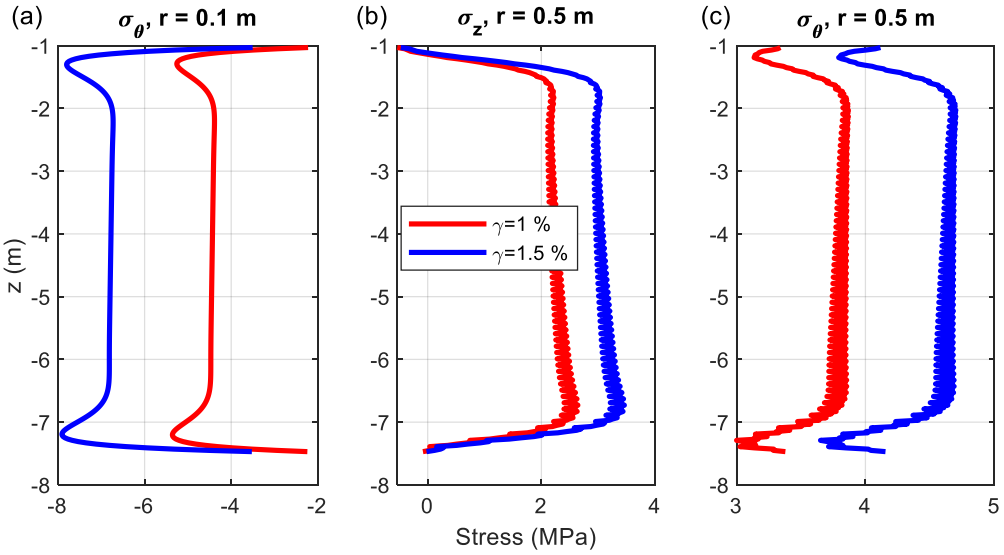

Figure A.111 Stress distribution along z-direction for various cycles at the (a)-(b) inner and (c)-(d) outer surface for pile design #5 for d_{in}=300 mm.

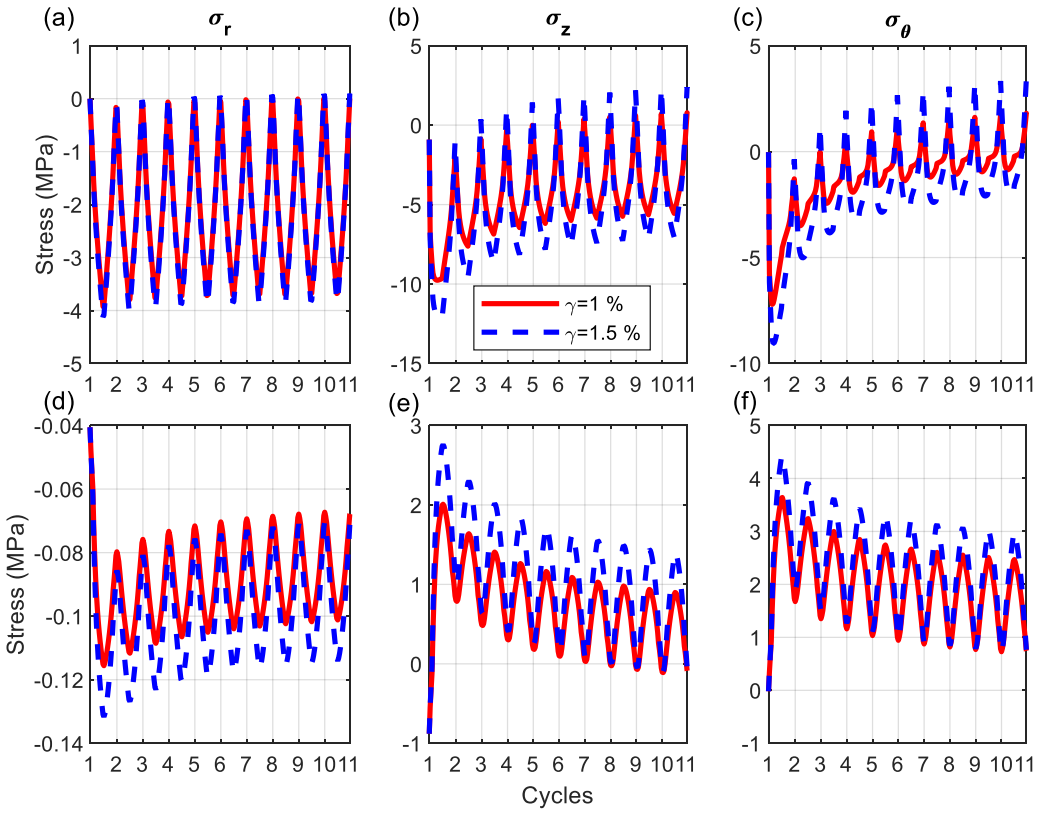

Figure A.112 Stress varying with 10 cycles for (a)-(c) inner and (d)-(f) outer surface for the pile design #5 for d_{in}=300 mm.

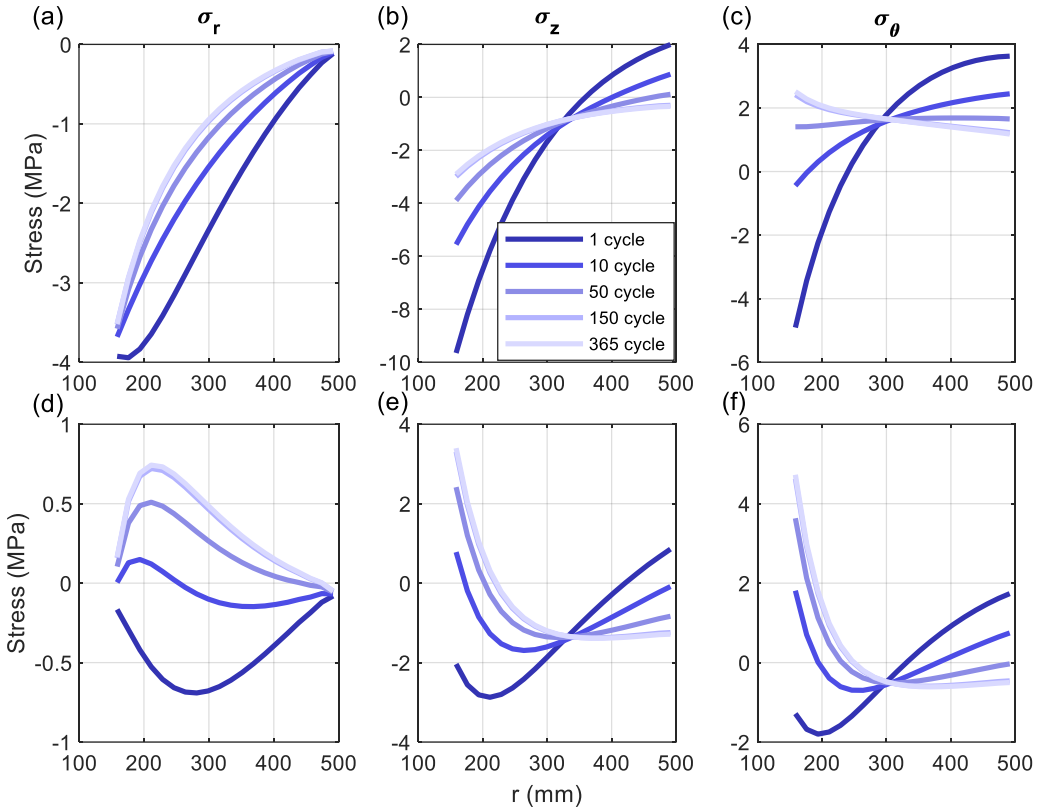

Figure A.113 Stress distribution along r-direction at the (a)-(c) middle and (d)-(f) end of the different cycles for the pile design #5 for γ=1%, d_{in}=300 mm.

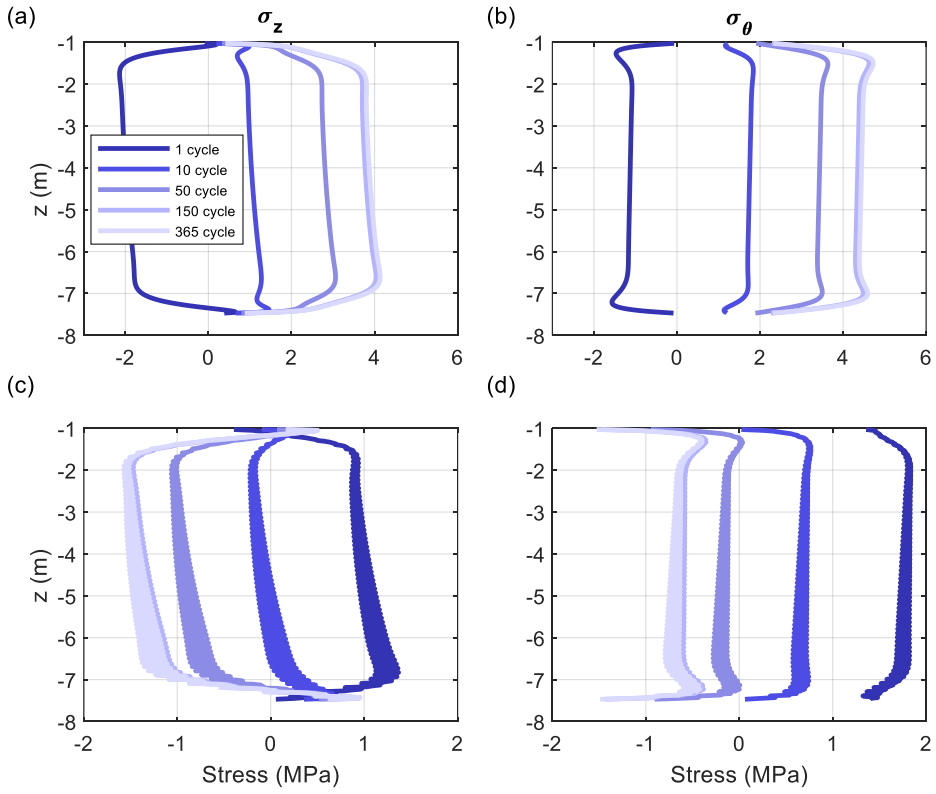

Figure A.114 Stress distribution along z-direction for various cycles at the (a)-(b) inner and (c)-(d) outer surface for pile design #5 for γ=1%, d_{in}=300 mm.

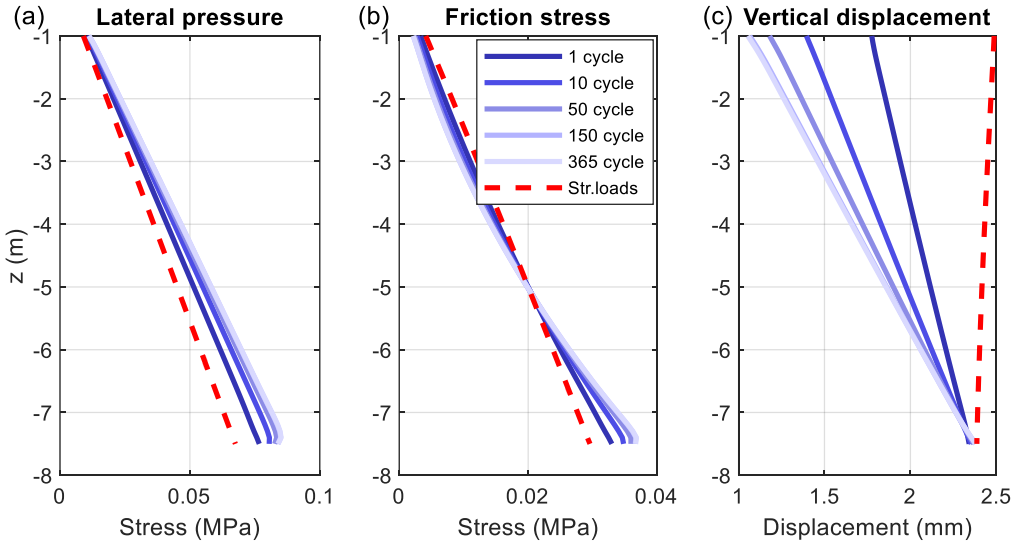

Figure A.115 Soil stresses and displacement along z-direction for various cycles under (a)-(c) combined loadings for pile design #5 for γ=1%, d_{in}=300 mm.

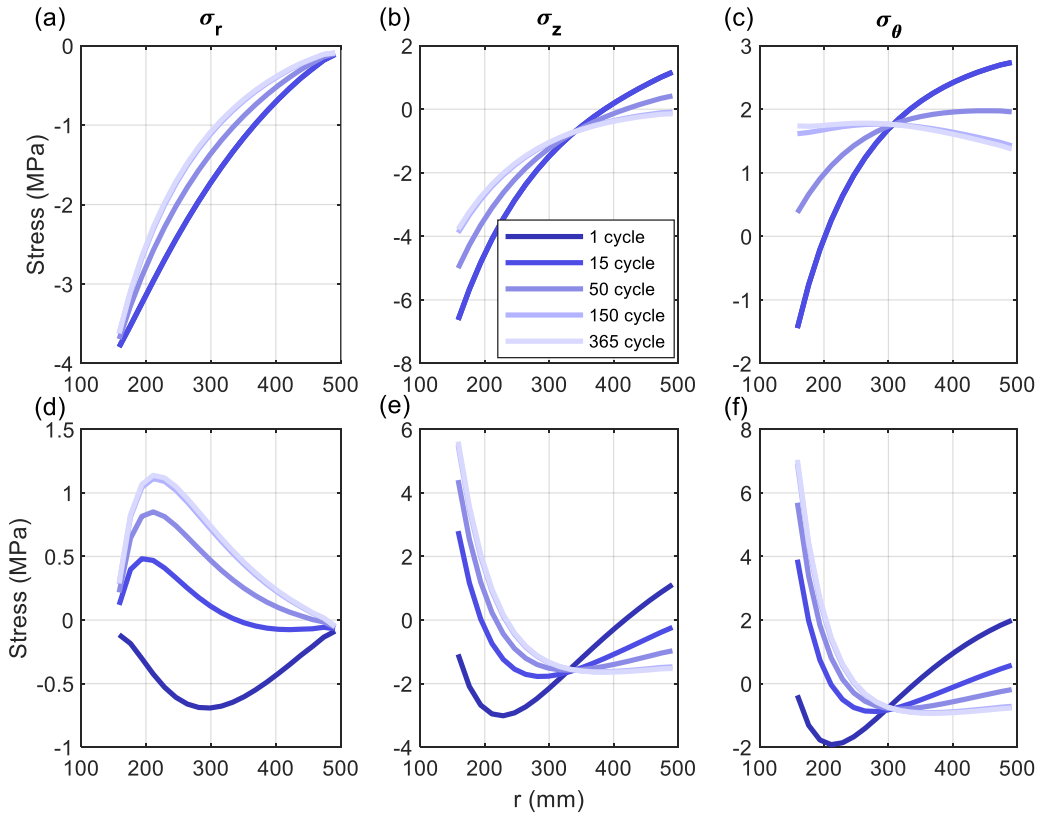

Figure A.116 Stress distribution along r-direction at the (a)-(c) middle and (d)-(f) end of the different cycles for the pile design #5 for γ=1.5%, d_{in}=300 mm.

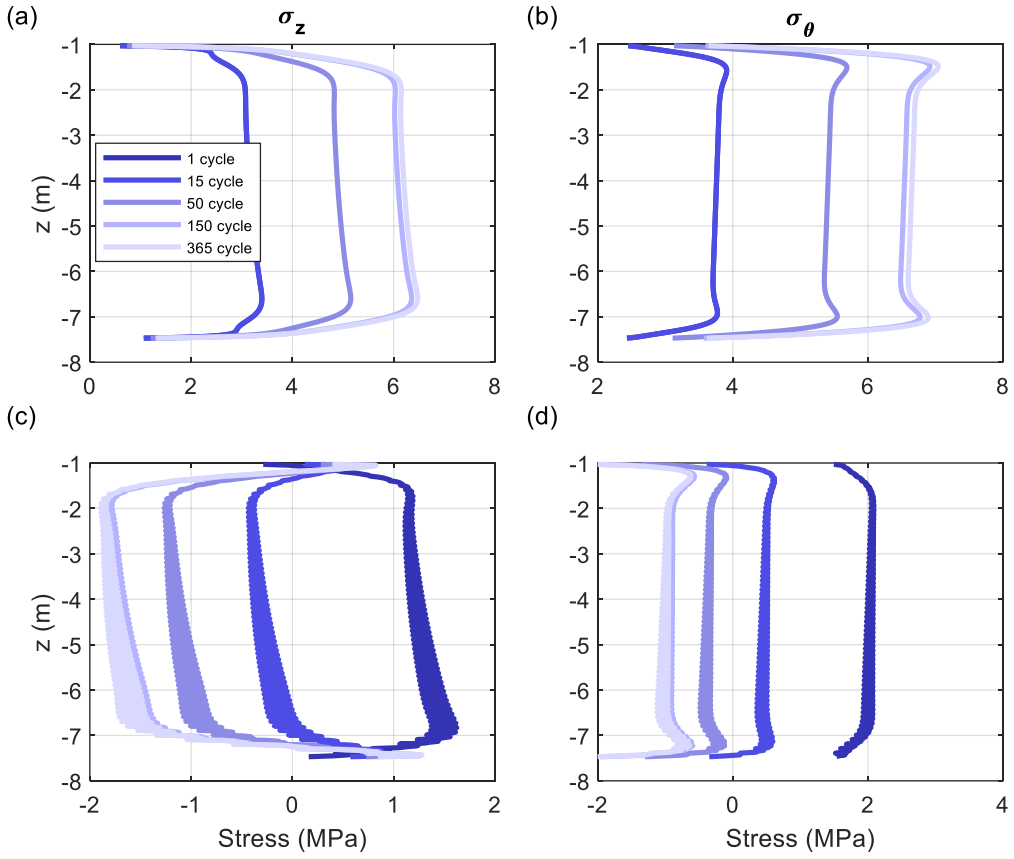

Figure A.117 Stress distribution along z-direction for various cycles at the (a)-(b) inner and (c)-(d) outer surface for pile design #5 for γ=1.5%, d_{in}=300 mm.

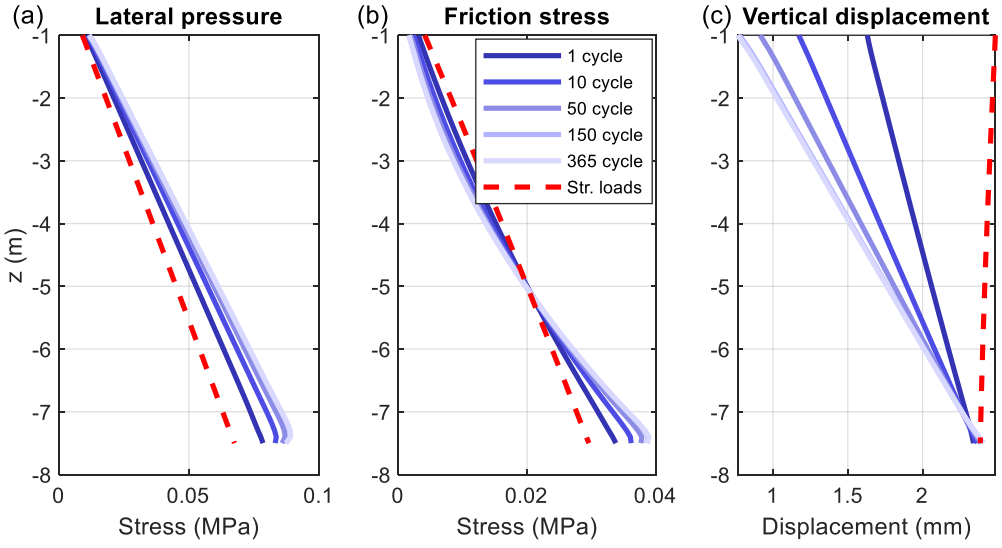

Figure A.118 Soil stresses and displacement along z-direction for various cycles under (a)-(c) combined loadings for pile design #5 for γ=1.5%, d_{in}=300 mm.

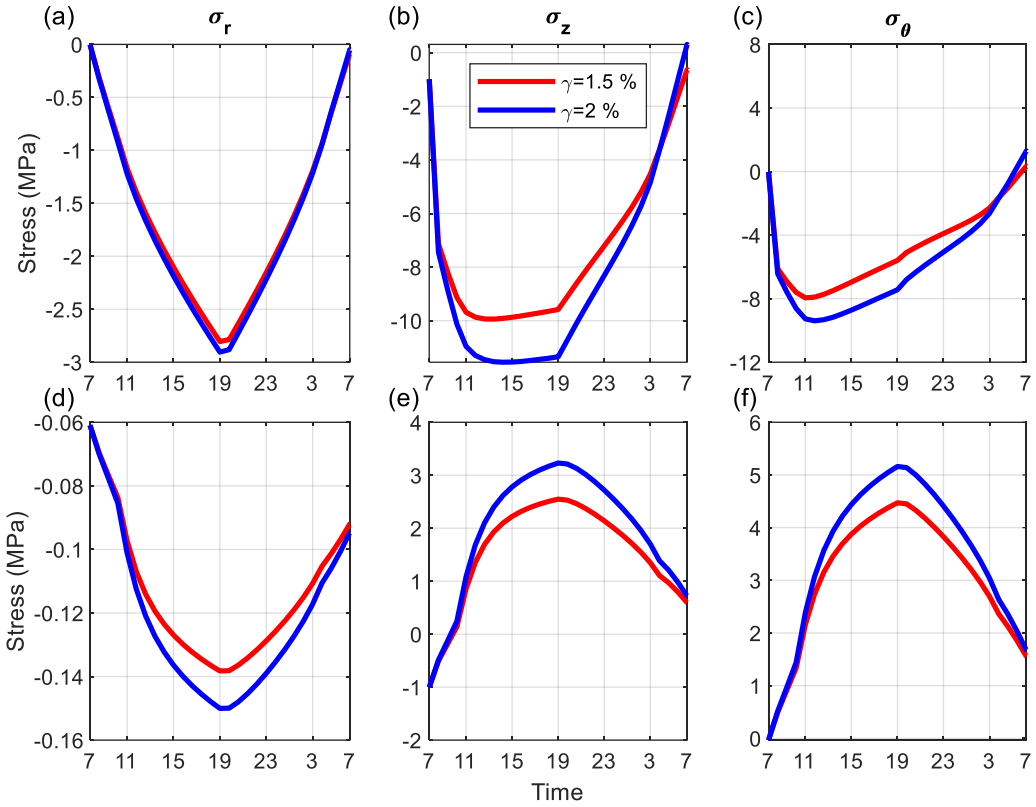

Figure A.119 Stress varying with 24-hour time at the (a)-(c) inner and (d)-(f) outer surface for the pile design #5 for d_{in}=400 mm.

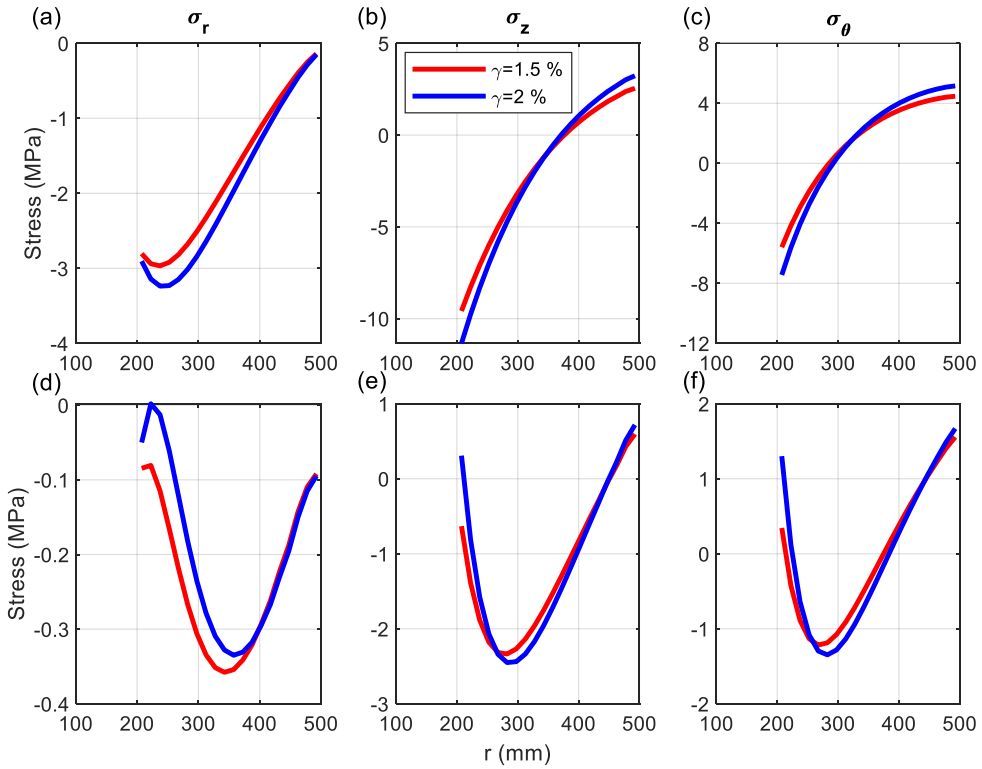

Figure A.120 Stress distribution along r-direction at the (a)-(c) middle and (d)-(f) end of the cycle for the pile design #5 for d_{in}=400 mm.

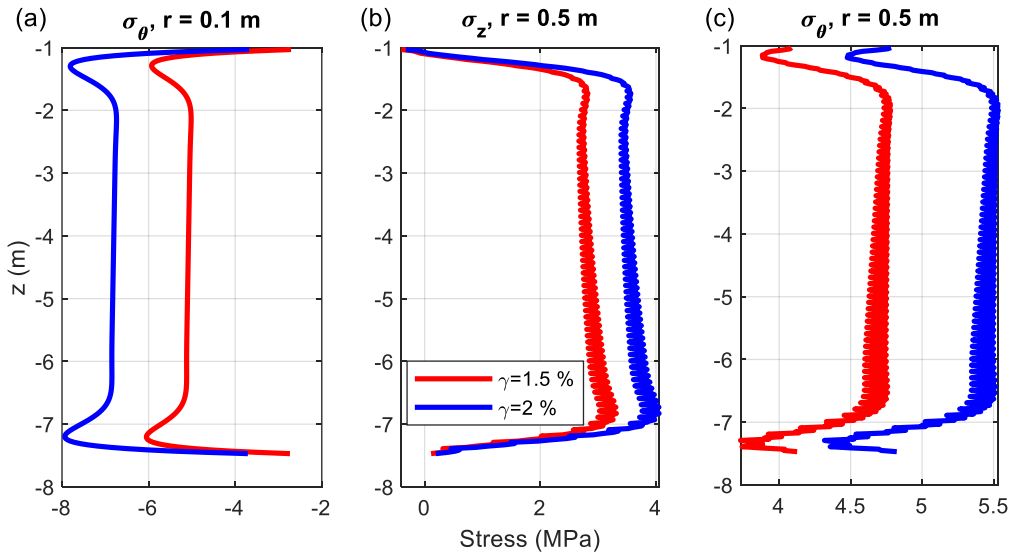

Figure A.121 Stress distribution along z-direction for various cycles at the (a)-(b) inner and (c)-(d) outer surface for pile design #5 for d_{in}=400 mm.

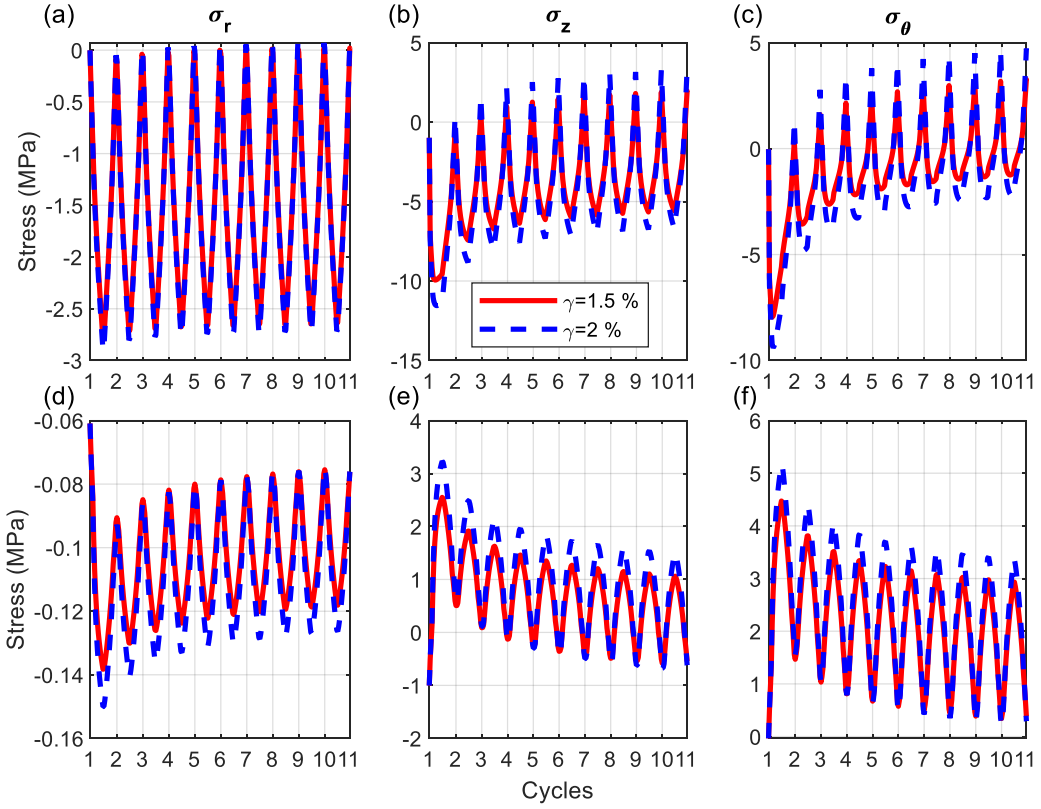

Figure A.122 Stress varying with 10 cycles for (a)-(c) inner and (d)-(f) outer surface for the pile design #5 for d_{in}=400 mm.

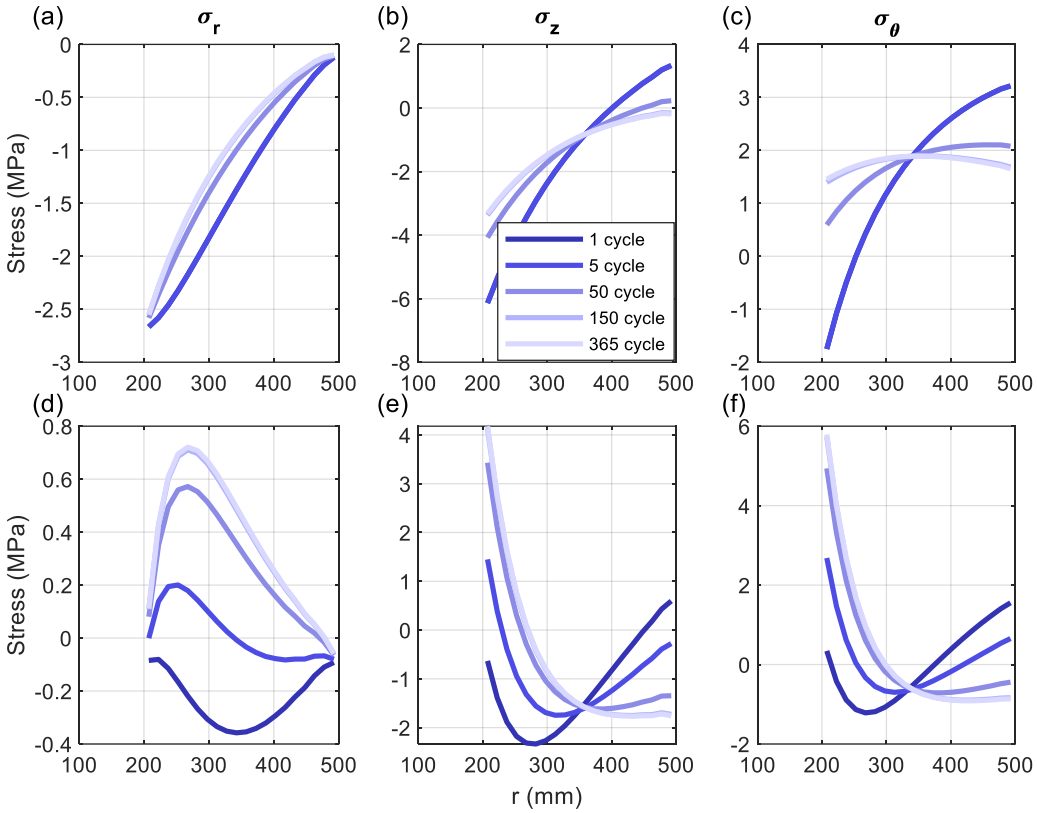

Figure A.123 Stress distribution along r-direction at the (a)-(c) middle and (d)-(f) end of the different cycles for the pile design #5 for γ=1.5%, d_{in}=400 mm.

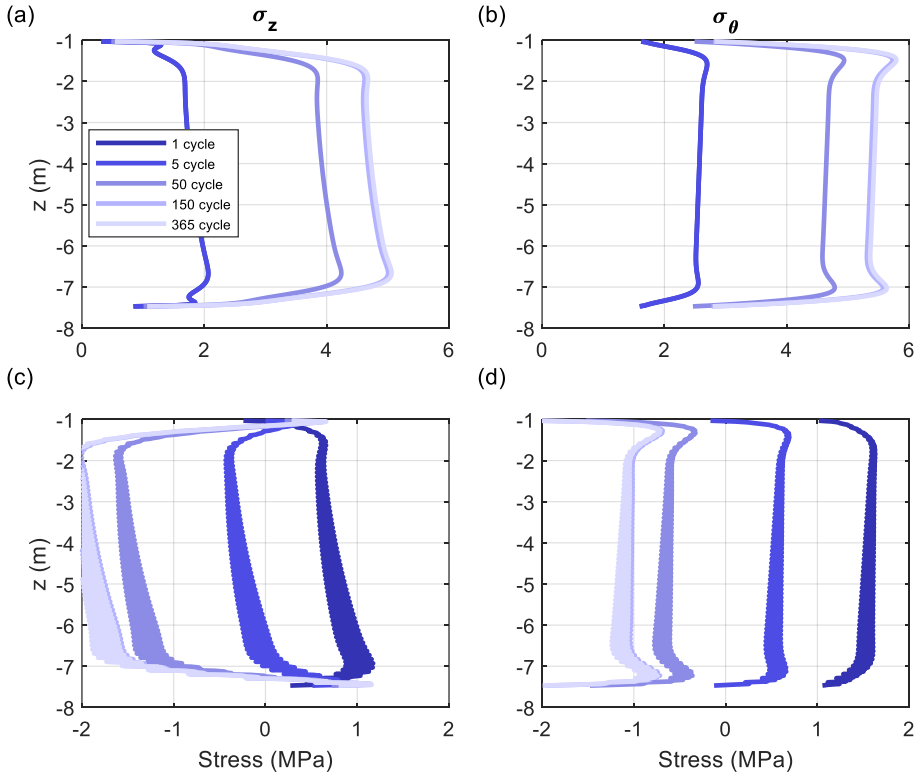

Figure A.124 Stress distribution along z-direction for various cycles at the (a)-(b) inner and (c)-(d) outer surface for pile design #5 for γ=1.5%, d_{in}=400 mm.

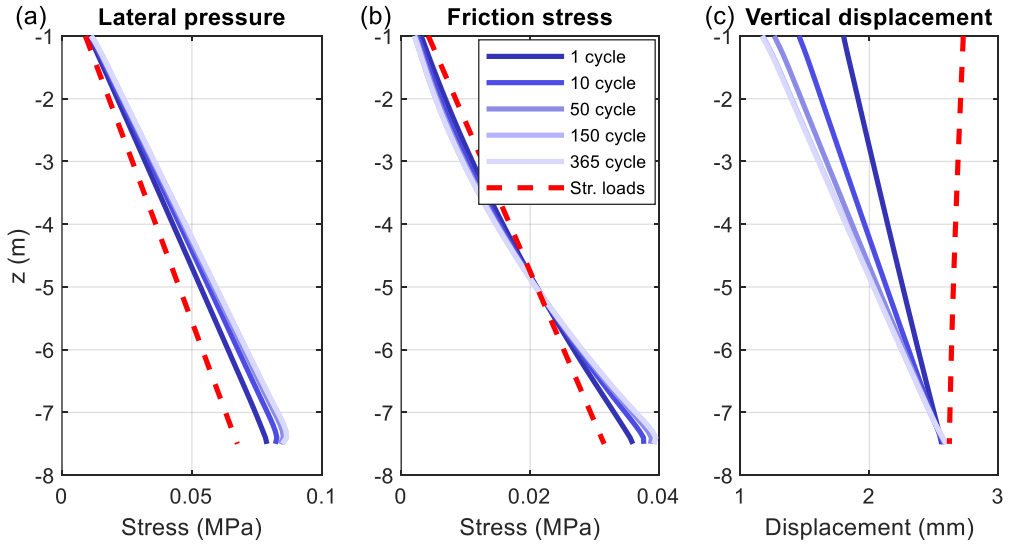

Figure A.125 Soil stresses and displacement along z-direction for various cycles under (a)-(c) combined loadings for pile design #5 for γ=1.5%, d_{in}=400 mm.

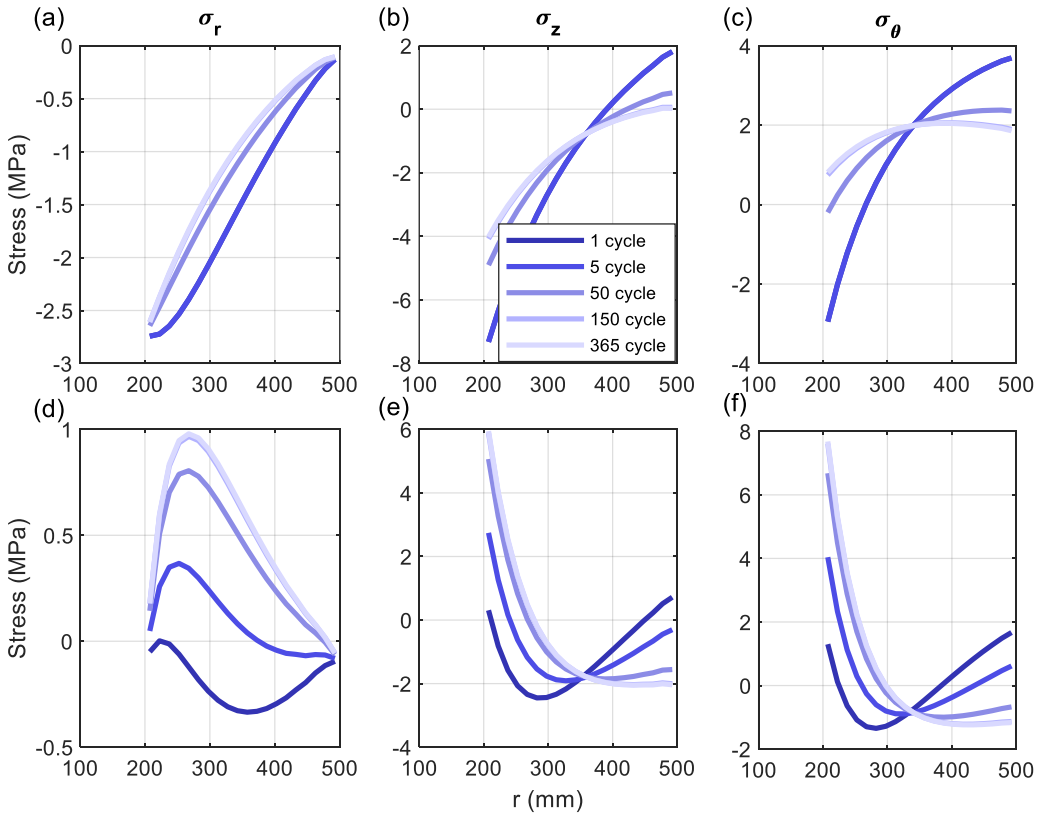

Figure A.126 Stress distribution along r-direction at the (a)-(c) middle and (d)-(f) end of the different cycles for the pile design #5 for γ=2%, d_{in}=400 mm.

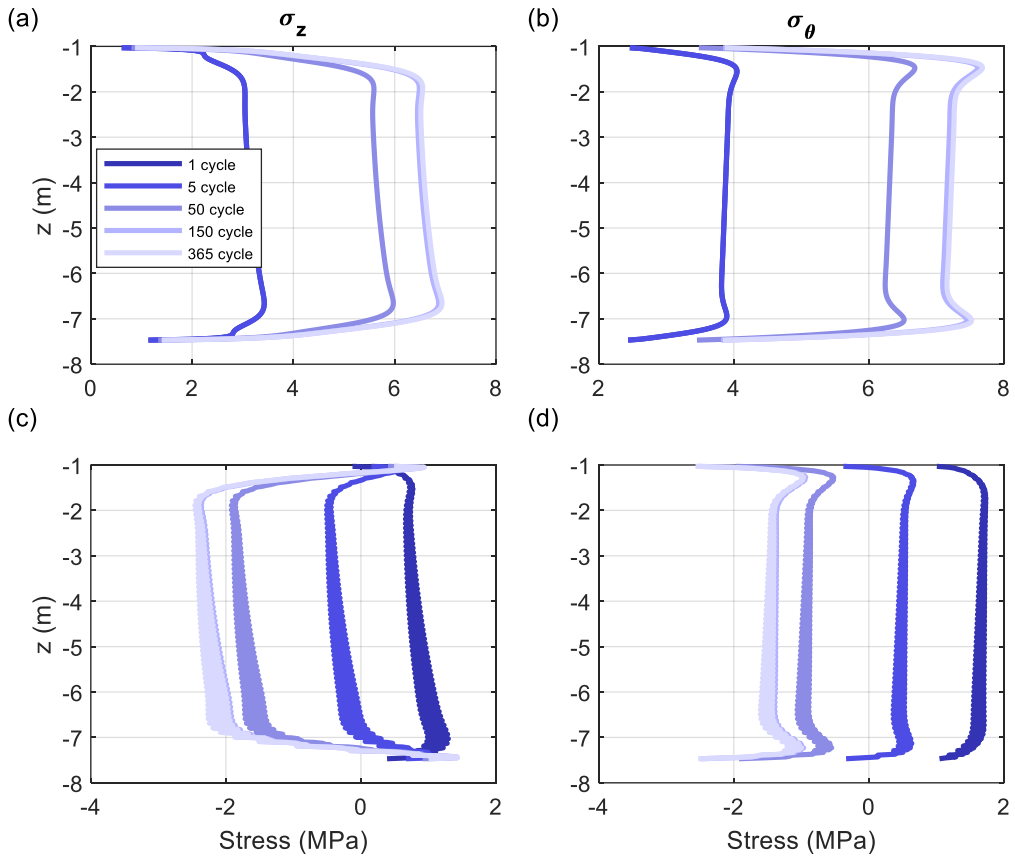

Figure A.127 Stress distribution along z-direction for various cycles at the (a)-(b) inner and (c)-(d) outer surface for pile design #5 for γ=2%, d_{in}=400 mm.

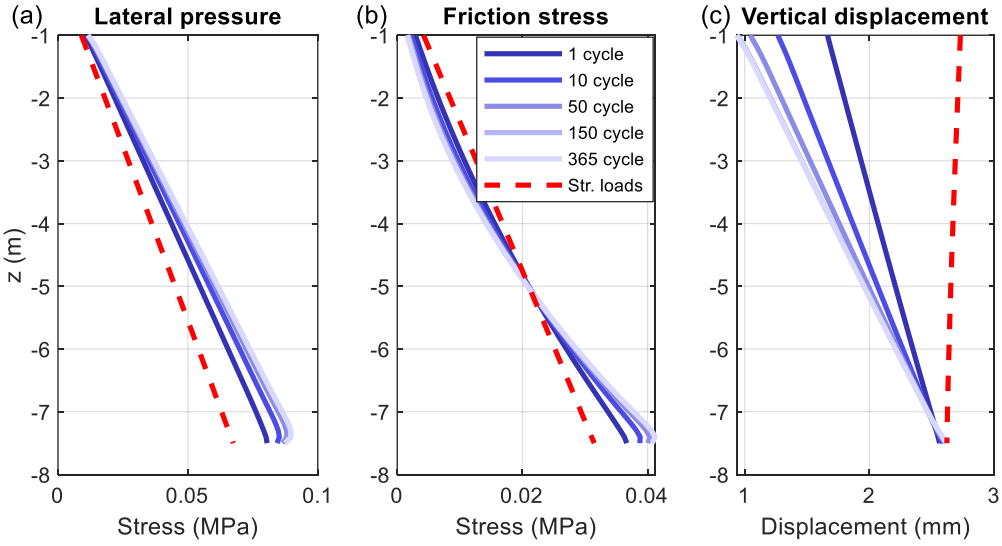

Figure A.128 Soil stresses and displacement along z-direction for various cycles under (a)-(c) combined loadings for pile design #5 for γ=2%, d_{in}=400 mm.

Appendix B – Details of the Analytical Model

Defining the parameters of the model

```
**Parameter
*parameter
Es=45550.0
Es_st=200000.0
Pr=0.2
Pr_st=0.3
CTE=0.000015
CTE_st=0.000012
Lp=6000.
Hb=1000.
```

Application of the material properties

```
** MATERIALS
*Material, name=Material-1
*Elastic
<Es>, <Pr>
*Expansion
<CTE>
*Material, name=Steel
*Elastic
<Es_st>, <Pr_st>
*Expansion
<CTE_st>
```

Modeling of lateral springs

```
*Element, TYPE=GAPUNI, ELSET=Conele1
6001, 6321, 6322
*GAP, ELSET=Conele1
-0.3708435816187234, 1, 0, 0, 157079.6327
*SURFACE BEHAVIOR, PRESSURE-OVERCLOSURE=TABULAR
0.0, 0.0
0.007294222118866172, 0.3
0.014436358001323249, 0.6
0.0234843634983797, 1.0
0.04234459835991136, 2.0
0.054999437947920886, 3.0
0.06249966916445039, 4.0
0.06662208527471214, 5.0
0.06991378028508959, 7.0
0.07048388894185545, 8.0
0.0707725392001814, 9.0
0.07091824588353797, 10.0
0.07102867124215156, 12.0
0.07105666400682896, 14.0
0.07106375499570368, 16.0
```

0.07106555091887787, 18.0
0.07106600574817039, 20.0
0.07106615983930595, 30.0
0.0710661599998326, 40.0
0.07106615999999982, 50.0
*Friction, ELASTIC SLIP=2.54
<Mu>

Modeling of end bearing springs

*Element, TYPE=GAPUNI, ELSET=end1
6062, 6383, 1
*GAP, ELSET=end1
<Agap>, 0, 1, 0, 6283.185307
*SURFACE BEHAVIOR, PRESSURE-OVERCLOSURE=TABULAR
0.0, 0.0
0.40919700328814734, 2.0
0.8183940065762947, 13.0
1.227591009864442, 42.0
1.4731092118373303, 73.0
1.6367880131525894, 100.0
1.638, 1000.0
*FRICTION, ROUGH

Application of the pressure and temperature loadings

*Step, name=Step-1, nlgeom=NO, inc=1
*Static
1, 1
*Dsload
Surf-2, P, 0.10099999999999999
*Temperature
inner, 21.73
set120, 17.4201
set140, 14.7266
set160, 13.2635
set180, 12.5506
set200, 12.2292
set220, 12.0923
set240, 12.0362
set260, 12.0139
set280, 12.0053
set300, 12.002
set320, 12.0007
set340, 12.0003
set360, 12.0001
set380, 12.0
set400, 12.0
set420, 12.0
set440, 12.0
set460, 12.0

set480, 12.0
outer, 12.0
*Restart, write, frequency=0
*Output, field, variable=PRESELECT
*Output, history, variable=PRESELECT
*End Step